Green Chemistry and Sustainable Technology

Ji Chen *Editor*

Application of Ionic Liquids on Rare Earth Green Separation and Utilization

Springer

Green Chemistry and Sustainable Technology

Aims and Scope

The series *Green Chemistry and Sustainable Technology* aims to present cutting-edge research and important advances in green chemistry, green chemical engineering and sustainable industrial technology. The scope of coverage includes (but is not limited to):

- Environmentally benign chemical synthesis and processes (green catalysis, green solvents and reagents, atom-economy synthetic methods etc.)
- Green chemicals and energy produced from renewable resources (biomass, carbon dioxide etc.)
- Novel materials and technologies for energy production and storage (bio-fuels and bioenergies, hydrogen, fuel cells, solar cells, lithium-ion batteries etc.)
- Green chemical engineering processes (process integration, materials diversity, energy saving, waste minimization, efficient separation processes etc.)
- Green technologies for environmental sustainability (carbon dioxide capture, waste and harmful chemicals treatment, pollution prevention, environmental redemption etc.)

The series *Green Chemistry and Sustainable Technology* is intended to provide an accessible reference resource for postgraduate students, academic researchers and industrial professionals who are interested in green chemistry and technologies for sustainable development.

More information about this series at http://www.springer.com/series/11661

Ji Chen
Editor

Application of Ionic Liquids on Rare Earth Green Separation and Utilization

Springer

Editor
Ji Chen
State Key Laboratory of Rare Earth Resources Utilization
Changchun Institute of Applied Chemistry
Chinese Academy of Sciences
Changchun, China

ISSN 2196-6982 ISSN 2196-6990 (electronic)
Green Chemistry and Sustainable Technology
ISBN 978-3-662-47509-6 ISBN 978-3-662-47510-2 (eBook)
DOI 10.1007/978-3-662-47510-2

Library of Congress Control Number: 2015951081

Springer Heidelberg New York Dordrecht London

Printed on acid-free paper

Springer-Verlag GmbH Berlin Heidelberg is part of Springer Science+Business Media (www.springer.com)

Preface

Recently, with the rapid development of science and technology, rare earth plays a vital role both in economy and society, which is largely relying on their unique electronic structure and physicochemical properties. As functional materials, rare earth compounds are widely used in electric, magnetic, optical, and catalytic fields. The world's attention about rare earth separation and recovery from both rare earth ores and secondary resources dramatically increased in recent years. However, there are some serious environmental considerations in rare earth separation procedure such as mining, refining, and recycling in the current industry. The environmental challenge of rare earth separation restricted the development of rare earth industry. For example, the strictest new regulation about "Emission Standards of Rare Earth Industrial Pollutants" is issued by the Ministry of Environment Protection (MEP) of China in 2011. People have to recheck the traditional industrial separation processes and look for the new substitutions of traditional diluents and extractants. Moreover, the separation of transplutonium actinides and rare earth in fission products is still one of the most challenging aspects of advanced nuclear fuel partitioning schemes.

Facing such a grim situation, traditional methods show some inherent disadvantages and ionic liquids as "green solvents" display unique properties. Ionic liquids have a great potential to provide novel intensified separation and purification technologies, which will make significant contributions to establish the sustainable processes in the future processing industry. In the last 10 years, the mutual development of ionic liquids and rare earth is attracting more and more attention from both academic and industrial communities.

The objective in preparing this book is to provide a complete understanding of the background and utilization of ionic liquids in rare earth field – from introduction (Part I) and chemistry of ionic liquids with rare earth (Part II) to ionic liquids for the extraction and separation of rare earth (Part III) and electrodeposition of rare earth metal in ionic liquids (Part IV) and further to the utilization of ionic liquids on rare earth materials (Part V). The order of 9 chapters reflects a logical journey from

basic knowledge to application. And this book gives a systematical review in the application of ionic liquids on rare earth green separation and utilization.

This book was prepared by a team of scientists who have made remarkable achievements in innovative research of both rare earth and ionic liquids. I am firmly convinced that this book will open the horizon and provide an excellent platform for future collaborations in this new realm.

We hope this book will be useful to wider professionals working with ionic liquids, rare earth separation, and production of the rare earth materials including chemists and metallurgists in rare earth industry, research agencies, government, and universities including graduate students.

Finally, I want to show my sincere thanks to the colleagues who have participated in the writing of this book, especially Professor Robin D. Rogers who gave generous recommendation and important contribution to this book. Without the great effort of each author, there is no successful accomplishment of this book.

Changchun, China J. Chen

Contents

Part I Introduction

1 Ionic Liquids in the Context of Rare Earth Separation and Utilization 3
Ji Chen and Jiangling Gao

Part II Chemistry of Ionic Liquids with Rare Earth

2 Using Crystal Structures of Ionic Compounds to Explore Complexation and Extraction of Rare Earth Elements in Ionic Liquids 21
Steven P. Kelley, J. Seth Nuss, and Robin D. Rogers

Part III Ionic Liquids for the Extraction and Separation of Rare Earth

3 Separating Rare-Earth Elements with Ionic Liquids 45
Nada Mehio, Huimin Luo, Chi-Linh Do-Thanh, Xiaoqi Sun, Yinglin Shen, Jason R. Bell, and Sheng Dai

4 Ionic Liquid-Based Extraction and the Application to Liquid Membrane Separation of Rare Earth Metals 73
Fukiko Kubota, Jian Yang, and Masahiro Goto

5 Application of Ionic Liquid Extractants on Rare Earth Green Separation 85
Hualing Yang, Ji Chen, Hongmin Cui, Wei Wang, Li Chen, and Yu Liu

Part IV Electrodeposition of Rare Earth Metal in Ionic Liquids

6 Electrodeposition of Rare Earth Metal in Ionic Liquids 117
Masahiko Matsumiya

Part V Utilization of Ionic Liquids on Rare Earth Materials

7 Ionic Liquids and Rare Earth Soft Luminescent Materials 157
Huanrong Li, Yige Wang, Tianren Wang, and Zhiqiang Li

8 Photofunctional Rare Earth Materials Based on Ionic Liquids . . . 179
Bing Yan

9 Ionic Liquid-Assisted Hydrothermal Synthesis of Rare Earth Luminescence Materials 207
Yanhua Song, Yuefeng Deng, Ji Chen, and Haifeng Zou

Contributors

Jason R. Bell Energy and Transportation Sciences Division, Oak Ridge National Laboratory, Oak Ridge, TN, USA

Ji Chen State Key Laboratory of Rare Earth Resources Utilization, Changchun Institute of Applied Chemistry, Chinese Academy of Sciences, Changchun, China

Li Chen State Key Laboratory of Rare Earth Resources Utilization, Changchun Institute of Applied Chemistry, Chinese Academy of Sciences, Changchun, China

Hongmin Cui State Key Laboratory of Rare Earth Resources Utilization, Changchun Institute of Applied Chemistry, Chinese Academy of Sciences, Changchun, China

Sheng Dai Department of Chemistry, The University of Tennessee, Knoxville, TN, USA

Chemical Sciences Division, Oak Ridge National Laboratory, Oak Ridge, TN, USA

Yuefeng Deng State Key Laboratory of Rare Earth Resources Utilization, Changchun Institute of Applied Chemistry, Chinese Academy of Sciences, Changchun, China

Chi-Linh Do-Thanh Department of Chemistry, The University of Tennessee, Knoxville, TN, USA

Jiangling Gao State Key Laboratory of Rare Earth Resources Utilization, Changchun Institute of Applied Chemistry, Chinese Academy of Sciences, Changchun, China

Masahiro Goto Department of Applied Chemistry, Graduate School of Engineering, Kyushu University, Fukuoka, Japan

Center for Future Chemistry, Kyushu University, Fukuoka, Japan

Steven P. Kelley Department of Chemistry, The University of Alabama, Tuscaloosa, AL, USA

Fukiko Kubota Department of Applied Chemistry, Graduate School of Engineering, Kyushu University, Fukuoka, Japan

Huanrong Li School of Chemical Engineering and Technology, Hebei University of Technology, Tianjin, China

Zhiqiang Li School of Chemical Engineering and Technology, Hebei University of Technology, Tianjin, China

Yu Liu State Key Laboratory of Rare Earth Resources Utilization, Changchun Institute of Applied Chemistry, Chinese Academy of Sciences, Changchun, China

Huimin Luo Energy and Transportation Sciences Division, Oak Ridge National Laboratory, Oak Ridge, TN, USA

Masahiko Matsumiya Graduate School of Environment and Information Sciences, Yokohama National University, Yokohama, Japan

Nada Mehio Department of Chemistry, The University of Tennessee, Knoxville, TN, USA

J. Seth Nuss Department of Chemistry, The University of Alabama, Tuscaloosa, AL, USA

Robin D. Rogers Department of Chemistry, McGill University, Montreal, QC, Canada

Yinglin Shen Chemical Sciences Division, Oak Ridge National Laboratory, Oak Ridge, TN, USA

Yanhua Song College of Chemistry, Jilin University, Changchun, China

Xiaoqi Sun Chemical Sciences Division, Oak Ridge National Laboratory, Oak Ridge, TN, USA

Tianren Wang School of Chemical Engineering and Technology, Hebei University, Tianjin, China

Yige Wang School of Chemical Engineering and Technology, Hebei University of Technology, Tianjin, China

Wei Wang State Key Laboratory of Rare Earth Resources Utilization, Changchun Institute of Applied Chemistry, Chinese Academy of Sciences, Changchun, China

Bing Yan Department of Chemistry, Tongji University, Shanghai, China

Jian Yang Department of Applied Chemistry, Graduate School of Engineering, Kyushu University, Fukuoka, Japan

Hualing Yang State Key Laboratory of Rare Earth Resources Utilization, Changchun Institute of Applied Chemistry, Chinese Academy of Sciences, Changchun, China

School of Chemistry and Chemical Engineering, Nantong University, Nantong, China

Haifeng Zou College of Chemistry, Jilin University, Changchun, China

Part I
Introduction

Chapter 1
Ionic Liquids in the Context of Rare Earth Separation and Utilization

Ji Chen and Jiangling Gao

Abstract With the rapid development of science and technology, rare earths (REs) are playing a vital role in economic and social development due to their unique electronic structure and physicochemical properties. REs are widely used in lighting, electrical, and magnetic field as a crucially strategic resource. Being the upstream of the RE industry supply chain, RE separation is crucial throughout the whole industry. The primary issues about RE separation are reviewed in this chapter. Conventional organic solvent extractants expose some inherent questions in the long-term application, while ionic liquids as "green solvents" show great potential in the separation processes. This chapter also overviewed RE resources in the world and the issues associated with these separation processes. A brief introduction to ionic liquid-based RE functional materials has been also made.

Keywords RE separation • RE resources • RE separation history • Defects of conventional organic extractants • Uniqueness of ionic liquids • Solid-liquid separation systems • Ionic liquid-based RE functional materials

1.1 Rare Earths

The rare earths (REs) are a group of chemically similar elements in the entire periodic table, consisting of scandium (Sc), yttrium (Y), and the lanthanides. The lanthanides are the series of elements with atomic numbers from 57 to 71, including lanthanum (La), cerium (Ce), praseodymium (Pr), neodymium (Nd), samarium (Sm), europium (Eu), gadolinium (Gd), terbium (Tb), dysprosium (Dy), holmium (Ho), erbium (Er), thulium (Tm), ytterbium (Yb), and lutetium (Lu).

Based on the electronic structure and physicochemical properties, REs can be classified as light REs and heavy REs. Light REs are also called "cerium subgroup," including La, Ce, Pr, Nd, Sm, Eu, and Gd. Heavy REs are also called "yttrium

J. Chen (✉) • J. Gao
State Key Laboratory of Rare Earth Resources Utilization, Changchun Institute of Applied Chemistry, Chinese Academy of Sciences, 5625 Renmin Street, Changchun 130022, China
e-mail: jchen@ciac.ac.cn; jlgao@ciac.ac.cn

J. Chen (ed.), *Application of Ionic Liquids on Rare Earth Green Separation and Utilization*, Green Chemistry and Sustainable Technology,
DOI 10.1007/978-3-662-47510-2_1

subgroup," comprising Tb, Dy, Ho, Er, Tm, Yb, Lu, and Y. Sc is a highly dispersed element, which is not classified in it.

As a crucially strategic resource, REs play a vital role in economic and social development. Over the past several decades, applications of REs have grown dramatically owing to their unique electronic structure and chemical properties. Meanwhile, the high value of these elements depends on the effective separation into high-purity compounds. Due to extremely similar electronic configurations, separation of individual REs is a daunting task.

RE separation is in the upstream of the RE industry supply chain, which is crucial throughout the RE industry. The subsequent subjects are all based on it because of the demand of raw materials, especially for lighting, electrical, and magnetic products, such as Nd-Fe-B magnets, phosphors, metal alloys, etc. Generally, RE separation comprises decomposing the minerals and separating the individual REs, which involves not only the separation of naturally co-occurring REs from each other but also the operation that results in impurity removal, i.e., the separation of REs and coexistent non-REs, such as thorium (Th), fluoride (F), and phosphate (P). Consequently, effective separation processes in the broad sense involve (1) high-purity products to provide high-quality raw materials, (2) comprehensive utilization of RE resources, and (3) minimum environmental impact to meet the national emission standard.

1.2 Overview of REs Resources and Associated Issues

As mentioned above, REs are widely distributed in the earth's crust, which include primary and paragenetic resources. Meanwhile, REs existing in secondary resources and nuclear fuels are important as well. The following introduction is based on the four main sources of REs and the issues associated with separation processes.

1.2.1 Primary Resource

The minerals of REs occur in various geological environments, and primary resource plays an exclusive role. The most representative primary resources are bastnasite, monazite, and ion-absorbed RE deposit. Bastnasite and monazite are the predominant minerals of light REs, while ion-absorbed RE deposit is the predominant mineral of heavy REs. Owing to their unique properties and recently strained supply, more countries were involved in the exploitation of REs. Then, a brief description of the present situation is as follows.

1.2.1.1 Bastnasite

As a fluorocarbonate of the cerium group REs, bastnasite is the most important RE resource in the world. Bayan Obo mixed ore, located in Inner Mongolia of China,

mainly consists of bastnasite and monazite, which is the largest RE deposit. Due to the characteristic of this resource, the separation process differs from other pure bastnasites. To utilize the associated and trace nuclide Th, reasonable separation and recovery are also required. As a valuable nuclear and a long-half-life element, Th doesn't belong to REs, but is found to be mainly associated with RE resources. The high-temperature roasting by concentrated H_2SO_4 only decomposed and recovered REs, while Th and others were abandoned without efficient treatment. Therefore, efficient method is urgently needed to separate REs and associated F, P, and Th. Recently, a new method using changeable valence of Ce is explored, which co-extract and recover Ce(IV), F, and P from H_2SO_4 leaching liquor, leading to favorable conditions for the subsequent separation of Th(IV) and RE(III) [1].

The world's second largest light RE deposit, Mountain Pass carbonatite deposit in California of the USA, has the highest grade. This deposit was found when seeking for uranium (U), and the increasing demand of Eu for color television in the 1960s accelerated the mining process. Mountain Pass made an important contribution to the world's technology development and also established a guiding status for subsequent RE industry. The processing step used at Mountain Pass is based on solvent extraction, and purified $Eu_2\ O_3$ is obtained by reduction on account of the variability of Eu's valence [2]. The main drawback is the extremely low grade of heavy REs and no reasonable processing line of Th. Ultimately, environmental costs and pressure cause the halt in 2002. Due to US domestic demand, Mountain Pass was claimed to resume in 2012.

Concluding from the above, it is required not only to achieve effective extraction of REs, Ce, and associated valuable elements Th, F, and P but also to decrease the residue and wastewater and simplify the separation process of bastnasite. Ultimately, both highly pure individual RE oxides and comprehensive utilization of resources are achieved.

1.2.1.2 Monazite

As the second largest segment of light RE resource, monazite is a phosphate mineral which contains REs and radioactive elements U and Th. The attraction of monazite originated from the demand of U, and monazite has long been the principal ore of REs until 1965, when production of bastnasite exceeded monazite production. Monazite was found in many geological environments, especially in Australia. Previously, with the limited demand for Th and environmental concerns associated with the radioactivity, some monazite producers had to cease. Nowadays, a global mining boom appears to alleviate the supply-demand problem. Mount Weld RE deposit in Western Australia, a second concentration plant, started operation in 2013, and the separation and smelting factory is built in Kuantan, Malaysia, which is expected to meet about one-third of the RE global demand. Basic information is shown in Tables 1.1 and 1.2.

Table 1.1 Components of some important RE concentrates

	REO	ThO_2	U_3O_8	F	P_2O_5	Reserve/Mt	Grade/%
Mixed ore [2, 3]							
Bayan Obo, Inner Mongolia, China	60	0.2–0.3	–	7–8	6–7	48	5–6
Bastnasite							
Mountain Pass, CA, USA [2]	55–60	0.1	–	4	0.9	2.58	8–9
Maoniuping, Sichuan, China [1, 2]	60	0.2–0.3	–	8–10	–	2.00	3–5
Monazite							
Mount Weld, Australia [4]	55–68	1.1	0.1–0.3	0.2–1.7	19–30	0.8	9.7
Ion-absorbed RE deposits							
Xunwu, Longnan, Jiangxi, China [5]	92	0.002	0.032	–	–	0.35	0.1–0.2

Table 1.2 RE content of different minerals [6]

	Mixed ore	Bastnasite	Monazite	Ion-absorbed RE deposits	
REs	Bayan Obo mixed ore, China	Mountain Pass, USA	Mount Weld, Australia	Xunwu, China	Longnan, China
Y	0.27	0.09	Trace	8.00	65.00
La	27.27	32.25	26.00	43.4	1.82
Ce	48.73	49.17	51.00	2.40	0.4
Pr	5.13	4.35	4.00	9.00	0.7
Nd	16.63	12.02	15.00	31.70	3.00
Sm	1.24	0.79	1.80	3.90	2.80
Eu	0.21	0.12	0.4	0.5	0.10
Gd	0.4	0.17	1.00	3.00	6.90
Tb	Trace	trace	0.1	Trace	1.30
Dy	0.1	trace	0.2	Trace	6.70
Ho	Trace	trace	0.1	Trace	1.60
Er	Trace	trace	0.2	trace	4.90
Tm	Trace	trace	Trace	trace	0.7
Yb	Trace	trace	0.1	0.3	2.50
Lu	Trace	Trace	Trace	0.1	0.4
Total	100	100	100	100	100

1.2.1.3 Ion-Absorbed RE Deposit

It is known that the distributions of REs contained in minerals vary a lot and the heavy REs are relatively scarce, such as Tb, Dy, and Ho ~ Lu. In reality, these heavy REs may not be used in a large content, but they are crucial to the function of the products. For example, as alloying additions to Nd-Fe-B magnets, Dy is extensively used due to its resistance to coercive force and demagnetization at elevated temperatures. Also for Lu, the embedded Lu is critical to the crystals' function, such as lutetium oxyorthosilicate scintillator in PET-CT and Lu-CeF_3 as the best electromagnetic energy equipment applied in Hadron Collider. Based on the importance for advanced technologies and no substitutions, an increasing demand for heavy REs is inevitable.

Being an unusual type of RE ore, ion-absorbed RE deposit is the most significant primary heavy RE resource, which is found mainly in South China. Detailed information about ion-absorbed RE deposit is in Table 1.2. Unlike the separation of light REs, the widely used 2-ethylhexyl phosphoric acid mono(2-ethylhexyl) ester (P507) system has low separation factor values for heavy REs, and there is a great challenge to strip heavy REs completely (especially for Tm, Yb, Lu). Thus, new extraction systems are urgently needed to obtain higher separation factors for heavy REs, achieve complete extraction, and lower the consumption of acid and base.

Table 1.3 Recycling potentials for REs

RE application	Estimated RE stocks in 2020 (tons)	Estimated average lifetime (years)	Estimated RE old scrap in 2020 (tons)
Magnets	300,000	15	20,000
Lamp phosphors	25,000	6	4167
Nickel-metal-hydride batteries	50,000	10	5000
Total	375,000	–	29,167

Reprinted from Ref. [7], Copyright 2015, with permission from Elsevier

1.2.2 Secondary Resource

With the dramatically increasing application, global RE consumption has exhibited significant growth in recent years. As an important nonrenewable natural resource, a stable supply of RE raw materials is crucial. In addition to mineral resource, secondary resource also has tremendous potential. It is estimated that the current recycling rates of REs are less than 1 %. An assessment of recycling potential global REs for the year 2020 is outlined, which includes most extensively used permanent magnets, nickel-metal-hydride batteries, and lamp phosphors, as shown in Table 1.3. The so-called urban mining can make a significant contribution to the overall RE supply, which means the process to recover the compounds and materials from products at their end of life. Recently, with large amounts of RE accumulation in "urban mines" and highlighted supply problems, the recycling of urban mining has become an important source for stabilizing supplies, especially for the regions without sufficient economic and/or operational primary RE deposits. On the other hand, RE recycling is so meaningful which can not only balance the REs' supply and demand relation but also reduce environmental pollution. Overall, the transition from a linear to a circular approach is the most effective strategy in the future.

The main characteristic of secondary resource is the widely dispersed RE concentrations, from 0.1 to 30 %, and no radioactive Th and U compared with the primary ores. Similarly, they contain abundant Nd and Dy. Thus, what is urgently needed in RE recycling is a highly selective and efficient extractant which can obtain individual REs and useful concomitant elements at the same time.

1.2.3 Advanced Nuclear Fuel System

With increasing concern for the global environmental problem, low-carbon energy plays a vital role in the world energy market. Nuclear energy has unparalleled advantages such as high energy density and low greenhouse gas emission. However, disposal of the high-level radioactive waste became the most challenging aspect of advanced nuclear fuel system. In recent years, transmutation of actinides has been proposed to effectively reduce the environmental hazards of nuclear

waste, but some REs, especially Sm, Eu, and Gd, have high thermal neutron capture cross sections, which limit the efficiency of transmutation in reactors. Thus, to achieve better transmutation, the separation of REs with actinides from fission products is critical. Owing to the similar ionic radii and similar chemical properties, the separation process is contesting.

Based on the separation of REs/actinides, the most significant issue accompanied is high radiation stability, both in extractant and dilute. The crucial factor "economy" becomes less important compared with other RE civilian industrial separation systems.

1.3 Separation History of REs

In 1886, the demand of Th opened the prelude of RE industry. Before the 1920s, the major separation method is fractional crystallization. During World War II, it was found that ion exchange method used to separate U can also be used to separate adjacent REs. Until the 1950s, solvent extraction is applied to RE separation. Due to the obvious advantages of simple operation, mild process conditions, and fast, continuous, and economical handling of large quantities of materials, solvent extraction gradually replaced the ion exchange. Up to now, the separation and purification of REs have heavily relied on solvent extraction, which became the predominant RE separation technology, but there also exit some unignorable issues relating to the environment. The following introduction is based on both dilute and extractant.

1.3.1 Hazardous Issues Associated with Organic Dilute

Solvent extraction of REs is similar to other two-phase extraction processes, which need an abundance of nonpolar organic dilutes (or solvents). In RE hydrometallurgy, the most widely used dilutes are kerosene and n-heptane, which are used to dissolve and dilute organic extractants to reduce the viscosity of the extracted complexes, but most organic solvents are highly volatile and flammable. Therefore, strict standards for fire and explosion are severely needed in industrial process. Unfortunately, tragedy still happened. *Inner Mongolia Baotou Steel Rare-Earth* announced that one of its metallurgical factories caught a fire on June 7, 2007 [8]. After that, the factory took approximately 4 months to resume normal operations. Furthermore, one of the significant reasons for the fire is that a large amount of kerosene was used in the RE separation factory.

Overall, the large-scale use of volatile solvents is a great threat to safe operation, not only because of their toxic and flammable nature but also due to the obvious health problems associated with them. Therefore, it is crucial to seek safer replacements, for which nonvolatile and nonflammable solvents are preferred.

1.3.2 Overview of the Defects of Organic Extractant

Since the 1950s, numerous extractants have been investigated for the RE separation. The structures of some typical extractants are listed in Fig. 1.1. Peppard et al. first reported the extraction of REs with di(2-ethylhexyl) phosphoric acid (P204) in 1957, which obtained higher adjacent separation factor value ($\beta = 2.5$, HCl medium) than the TBP-HNO_3 system ($\beta = 1.5$) [9]. In the 1960s, Molycorp, Inc., in the USA, first applied P204 to RE industrial separation, which formed the first generation of industrial extraction technique. Then, Shanghai Institute of Organic Chemistry, Chinese Academy of Sciences (CAS), successfully synthesized P507 on an industrial scale in the 1980s, and Changchun Institute of Applied Chemistry of CAS completed a systematic study of extraction and separation of REs based on P507. Hereafter, the second generation of RE industrial separation by P507 is most widely used in China. P507 system is superior to P204 because of its high β value, high extraction capacity, and easy stripping.

Saponification In RE hydrometallurgy, P507 needs to be saponified by $NH_3 \cdot H_2O$, NaOH, or $Ca(OH)_2$ not only to break hydrogen bonds in the dimers of extractant but also to keep the acidity of aqueous phase and enhance the cation exchange of REs. However, this will undoubtedly produce an abundance of corresponding ammonia nitrogen, Na^+, or Ca^{2+} wastewater. The extraction mechanism of RE(III) by acid

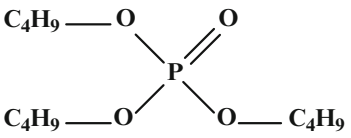

tributyl phosphate
(TBP)

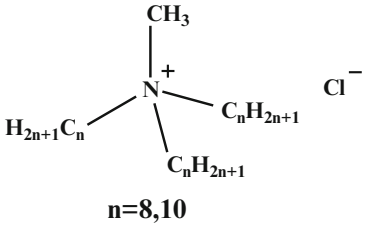

trialkylmethylammonium chloride
(Aliquat 336)

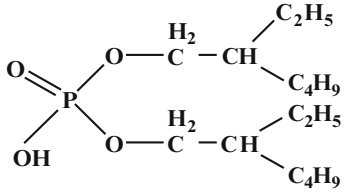

di(2-ethylhexyl) phosphoric acid
(P204)

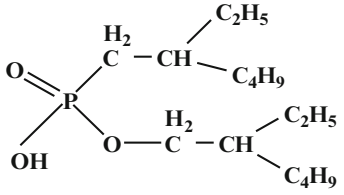

2-ethylhexyl phosphoric acid mono
(2-ethylhexyl) ester (P507)

Fig. 1.1 Structure of some important extractants

extractant saponification is as follows (Eqs. 1.1, 1.2). It was reported that the RE industry produced over 20 million tons of wastewater, and approximately over 9 million tons of high ammonia nitrogen wastewater was released in 2011 [10]. Nowadays, saponification by ammonia is gradually being replaced by sodium, which has also created unignorable salinity problems.

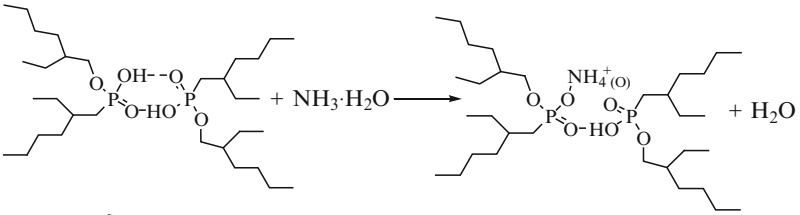

(1.1)

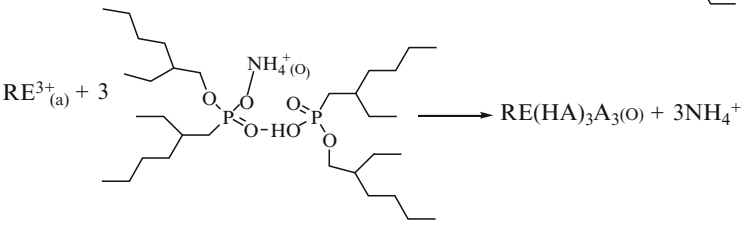

(1.2)

Low Separation Factor From the viewpoint of β values, the selectivity for heavy REs is generally lower than light REs in the P507 system, e.g., Tm/Er (3.34), Yb/Tm (3.56), and Lu/Yb (1.78) [11]. Another significant deficiency in P507 is that it is difficult to strip heavy REs completely, especially for Tm(III), Yb(III), and Lu (III), even at higher acidity.

Complicated Process The selection of extractant is not an easy process, owing to the complicated organic synthesis process, difficult impurity-removing process, and high preparation and evaluation cost. Some problems about P507 have been shown, but no suitable replacement has been found, even though lots of efforts have been made. Taking bis(2,4,4-trimethylpentyl) phosphinic acid (Cyanex 272), for example, the higher β for heavy REs is obtained, but the cost is high, and this system is difficult to control owing to low extraction capacity and easy emulsification phenomenon.

A challenging goal in RE separation is to develop an effective process to enhance separation and minimize environmental pollution. But what is the satisfied dilute and extractant? The desired dilute should be nonvolatile, nonflammable, and low toxicity, while high efficiency, high stability, low cost, and low acid and base consumption are required for the candidate extractant. In recent years, as a green solvent, ionic liquid gained extensive attention and showed tremendous potential to RE green separation.

1.4 Ionic Liquids in RE Separation

1.4.1 Introduction of Ionic Liquids

Room-temperature ionic liquids (RTILs) are defined as molten salts at or close to room temperature. Ionic media resulted from combinations of organic cations and various anions covering an extremely wide range of chemical compounds, although research about ILs in these years only involved a limited number of them. Some of the most typical cations and anions are listed in Fig. 1.2.

For ILs, their ionic nature imparts unique properties. Generally, they have low volatility, low combustibility, wide liquidus range, and high thermal stability. In view of these remarkable properties, RTILs have been used to replace traditional volatile organic solvents (VOC) in organic synthesis, solvent extraction, electrochemistry, polymerization, and synthesis of inorganic materials. But ILs' applications are far beyond these; they become tunable materials based upon the unique physical and chemical properties and now even can be used as functional materials by changing the cation or anion.

1.4.2 Why Choose ILs?

In recent years, considerable attention has been devoted to the application of ILs in RE separation, furthermore, as a replacement for VOC in liquid-liquid extraction system. Here is a simple comparison between ILs and VOC.

It is known that the number of ILs is far more than that of conventional organic solvents, which can be as high as 10^{18}. So, it is obvious that ILs provide us more choices.

The distinctive properties such as viscosity, conductivity, hydrophilicity, hydrophobicity, polarity, and hydrogen bond ability are extraordinarily tunable, relying

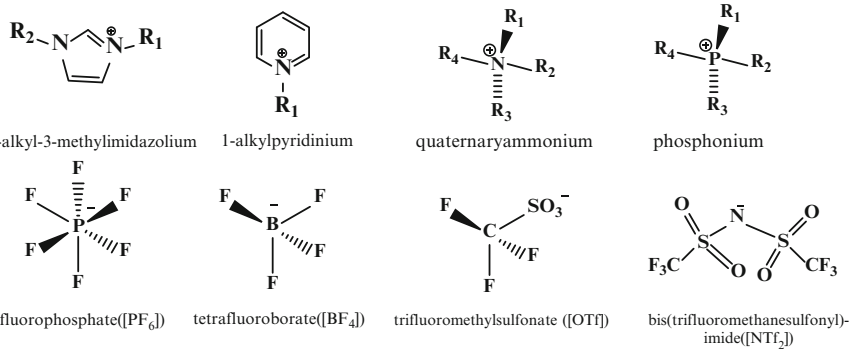

Fig. 1.2 Typical cations and anions of ionic liquids

on the selection of appropriate anion and cation. In other words, ILs can be tailored through rational design, and usually ILs can be obtained through a simple two-step ion exchange reaction.

1.4.3 Uniqueness of ILs for the Separation

Ionic liquids exhibit unique features in RE extraction and separation, both as solvent and extractant. Hardacre et al. found the clear charge ordering in ILs, and with increasing delocalization of the charge in anion, the ionic bonding becomes softer, which results in increasing overlap of the anion/cation coordination shells [12]. To understand the speciation of actinides and REs in ILs, Visser and Rogers investigated the coordination of U by extractants such as carbamoylphosphine oxide (CMPO) and TBP [13]. The extraction of UO_2^{2+} with hydrophobic amidoxime-functionalized ILs has been reported, and it was found that high selectivity is obtained via η^2 coordination [14].

1.4.3.1 ILs Used as Solvent

Huddleston and Rogers first applied $[C_4mim]PF_6$ as solvent to extract organic benzene derivatives, which created a precedent for extraction targets using ILs to replace VOC [15]. Dai et al. investigated the extraction of strontium (Sr) with IL as solvent and crown ether as extractant. Surprisingly, large distribution ratios were achieved attributing to the novel dual properties and a more favorable thermodynamics in these ILs [16]. Nakashima et al. studied the extraction of REs by using substituted octyl(phenyl)-n,n-diisobutyl (CMPO) as extractant and 1-butyl-3-methylimidazolium hexafluorophosphate ([Bmim][PF_6]) as dilute; the extraction ability was over 10^3 times than conventional organic solvents [17].

1.4.3.2 ILs Used as Extractant

Pure Extracting Phase A unique extraction behavior was found by investigating the separation of Ce(IV) from nitric acid solutions using pure $[C_8mim]PF_6$ as extracting phase [18]. This interesting phenomenon demonstrates that ILs have unique potential to behave as both solvent and extractant, while conventional solvent extraction method for separation of REs always consumes large amounts of organic dilute.

RE-F-P System ILs also exhibit excellent potential in complex systems. For dealing with light RE resources such as bastnasite and monazite, Ce (IV) separation chemistry and clean technique will open up new realms. Owing to the high β values of Ce(IV) to Th(IV) and RE(III), the removal of the high-

content Ce will dramatically reduce the solvent extraction capacity for the subsequent RE separation. In terms of conventional extractant, P204 or P507 is good to extract Ce(IV) but is difficult to extract coexisting F in sulfuric acid solution. Other extractants such as Cyanex 923 showed higher extraction ability for both Ce(IV) and F but were limited for their high price. Recently, bifunctional ionic liquid extractants (bif-ILEs), such as [A336][P507] ([trialkylmethylammonium] [di-(2-ethylhexyl) orthophosphinate]), were used to separate REs, and a satisfactory result was obtained. It was found that Ce(IV) could be extracted with F and/or P together in acidic solution, and the loaded organic phases could be used to prepare nano-size CeF_3 and $CePO_4$ through reductive stripping [1]. Other significant advantages of bif-ILEs are low acid and base consumption and no saponification process.

Individual RE(III) System In order to effectively separate RE(III), extensive researches have been carried out, and the promising results have been obtained on the use of ILs. Rout et al. investigated the $[A336]^+$-based ILs containing bis (2-ethylhexyl)phosphate ($[DEHP]^-$) and bis(2-ethylhexyl diglycolamate) ($[DGA]^-$) anions for the extraction of Eu(III) and Am(III) from aqueous solutions, which confirmed that the distribution ratio observed in the IL was always much higher than that obtained in the solution of the precursors [19]. Guo et al. investigated the extraction and separation of individual REs using [A336] [P204] [11]. In nitrate medium, the $\beta_{z+1/z}$ values of REs extracted by [A336] [P204] are higher than P204 and TBP, and the β values of adjacent heavy REs are high, Tm/Er (3.36), Yb/Tm (7.92), and Lu/Yb (8.55), which demonstrate that this system is suitable for heavy REs separation. Bif-ILEs are an important method to develop the new extractant by nonchemical bond preparation and a useful supplement to organic synthesis of extractants. Bif-ILEs showed high extraction efficiency in HNO_3, HCl, and H_2SO_4, and the high selectivity can be achieved without saponification; also the synthesis of bif-ILs is simple and economic. Another noteworthy method of RE recovery and purification is the electrodeposit with ILs taking advantages of their nonflammability, negligible vapor pressure, and high ionic conductivity [20].

To sum up, ILs provide a new platform with excellent separation performance. Although the ILs have some disadvantages, such as high viscosity and the possibility of loss along with ion exchange mechanism, a compromise can be found among these problems in the near future in order to achieve more advantageous separation.

1.5 Solid-Liquid Separation Systems

Although solvent extraction has been widely applied in the field of RE separation, there also exist some shortcomings. The main drawback of this process is the loss of the organic phase due to the dissolution of extractant into the aqueous solution. Another shortage is that when solvent extraction is used directly in low RE concentration extraction, more reagent and energy consumption would be needed. To overcome the drawbacks mentioned above, some studies have been focused on

solid-liquid separation systems. Using these systems, the minimal amount of extractant is consumed, and the extraction and stripping steps are combined into a single step. Unfortunately, the industrial use of solid-liquid separation systems is limited by their instability and short lifetime of solid adsorption materials. Recently, a variety of separation materials have been explored, especially for solvent-impregnated resins and supported liquid membrane system by ILs, which can not only achieve high efficiency and selectivity in low concentration of RE solutions but also reduce the amount of ILs and effectively avoid the loss.

Baba et al. studied the separation of Y^{3+} and Eu^{3+} from Zn^{2+} based on a supported liquid membrane system [21]. The system is prepared by immersing a hydrophobic porous polyvinylidene fluoride film in [C_nm im][Tf_2N] and n-dodecane, respectively. Using DODGAA as extractant, satisfied separation of Y^{3+} and Eu^{3+} from Zn^{2+} was observed, and the membrane showed better stability. IL-functionalized solvent-impregnated resins were also investigated. The resins impregnated with [A336] [CA-100] can be used to separate Sc(III) from REs, and a high separation factor was achieved [22]. Cui et al. prepared a series of ionic liquid levextrel resins, such as [D201][P204] and [A336][CMCTS], to recover various metal ions from dilute solution for the removal of many metal ions [23].

To conclude, based on the uniqueness of ionic liquids, appropriate ionic liquid immobilization strategies can be used to separate REs. The levextrel resin, supported liquid membranes, and sol-gel materials containing ILs and extractants have high stability, capacity, and selectivity for the RE separation, demonstrating the unique properties of ILs. It will be more useful in RE concentration from very dilute RE solutions and the purification of high-purity REs.

1.6 IL-Based RE Functional Materials

With the dual nature, thermal stability, and tunability, the application of ILs is not only in extraction and separation science. Nowadays, IL-involved new RE materials play an irreplaceable role in a wide range of areas, especially for RE-containing ILs, which combine the properties of ILs with additional intrinsic magnetic, spectroscopic, or catalytic properties depending on the enclosed REs.

Song et al. successfully synthesized RE material CaF_2:Ce^{3+}/Mn^{2+} sub-microcubes and nanospheres through an IL-assisted hydrothermal method, which can enhance the emission intensity of Mn^{2+} ions by co-doping with Ce^{3+} ions through an efficient resonance-type energy transfer process [24]. Yan et al. studied ILs as solvents to disperse RE fluorides with down-/up-conversion fluoride nanocrystals, which provide a strategy to prepare luminescent hydrogels, especially for up-conversion luminescent [25]. Li et al. showed an alternative way to obtain RE-containing ILs by directly co-dissolving Eu_2O_3 and organic ligands into a TSIL, 3-(5-carboxypropyl)-1-methylimidazolium bromide, without adding any extra solvent, which exhibit a fascinating prospect in designing RE-doping luminescent ILs [26].

1.7 Outlook

The extraordinary solvent powers of ILs provide RE chemists a potent tool to deal with some of the important challenges in RE green separation and utilization. Meanwhile, explosion risks and toxic effects for people, two obvious features associated with traditional VOC, are also diminished. The most meaningful thing is that ILs provide us a broad platform because of its diversity and unique tunable property. Facing with over 60 years of traditional RE separation technology, we need to change our concept and seek a breakthrough on a broader platform. While ILs do have some shortcomings that need to be overcome, there is still an enormous amount of hard work before the industrialization of RE separation and utilization processes.

References

1. Zou D, Chen J, Li DQ (2014) Separation chemistry and clean technique of Cerium (IV): a review. J Rare Earths 32(8):681–685
2. Xu GX (2005) Rare earths. Metallurgical Industry Press, Beijing, pp 360–361
3. Xu C, Taylor RN, Li WB et al (2012) Comparison of fluorite geochemistry from REE deposits in the Panxi region and Bayan Obo, China. J Asian Earth Sci 57:76–89
4. Jaireth S, Hoatson DM, Miezitis Y (2014) Geological setting and resources of the major rare-earth-element deposits in Australia. Ore Geol Rev 62:72–128
5. Wang GZ, Tan B (2014) Implement the rare earth environmental protection policy. World Nonferrous Metals 7:22–24
6. Gambogi J (2011) Rare earths. US Geological Survey, Minerals Yearbook 60, pp 1–12
7. Binnemans K, Jones PT, Blanpain B et al (2013) Recycling of rare earths: a critical review. J Clean Prod 51:1–22
8. Reuters (2007) Inner Mongolia Baotou Steel Rare-Earth announces fire in factory. http://www.reuters.com/finance/stocks/keyDevelopments?symbol=600111SS&pn=2
9. Peppard DF, Mason GW, Maier JL et al (1957) Fractional extraction of the lanthanides as their di-alkyl orthophosphates. J Inorg Nucl Chem 4(5–6):334–343
10. Sun XQ, Waters KE (2014) Development of industrial extractants into functional ionic liquids for environmentally friendly rare earth separation. ACS Sustainable Chem Eng 2:1910–1917
11. Guo L, Chen J, Shen L et al (2014) Highly selective extraction and separation of rare earths (III) using bifunctional ionic liquid extractant. ACS Sustainable Chem Eng 2:1968–1975
12. Hardacre C, Holbrey JD, Nieuwenhuyzen M et al (2007) Structure and solvation in ionic liquids. Acc Chem Res 40:1146–1155
13. Visser AE, Jensen MP, Laszak I et al (2003) Uranyl coordination environment in hydrophobic ionic liquids: an in situ investigation. Inorg Chem 42:2197–2199
14. Barber PS, Kelley SP, Rogers RD (2012) Highly selective extraction of the uranyl ion with hydrophobic amidoxime functionalized ionic liquids via η^2 coordination. RSC Adv 2:8526–8530
15. Huddleston JG, Willauer HD, Swatloski RP et al (1998) Room temperature ionic liquids as novel media for "clean" liquid-liquid extraction. Chem Commun 16:1765–1766
16. Dai S, Ju YH, Barnes CE (1999) Solvent extraction of strontium nitrate by a crown ether using room temperature ionic liquids. J Chem Soc Dalton Trans 8:1201–1202
17. Nakashima K, Kubota F, Maruyama T et al (2003) Ionic liquids as a novel solvent for lanthanide extraction. Anal Sci 19:1097–1098

18. Zuo Y, Liu Y, Chen J et al (2008) The separation of cerium (IV) from nitric acid solutions containing thorium (IV) and lanthanides (III) using pure $[C_8mim]PF_6$ as extracting phase. Ind Eng Chem Res 47:2349–2355
19. Rout A, Venkatesan KA, Srinivasan TG et al (2012) Ionic liquid extractants in molecular diluents: Extraction behavior of europium (III) in quarternary ammonium-based ionic liquids. Sep Purif Technol 95:26–31
20. Matsumiya M, Kondo H, Kurachi A et al (2011) Separation of iron group metal and recovery of neodymium metal by electrodeposition in ionic liquids. J Jpn Inst Metals 75(11):607–612
21. Baba Y, Kubota F, Kamiya N et al (2011) Recent advances in extraction and separation of rare-earth metals using ionic liquids. J Chem Eng Jpn 44(10):679–685
22. Sun XQ, Ji Y, Chen J et al (2009) Solvent impregnated resin prepared using task-specific ionic liquids for REs separation. J Rare Earths 27(6):932–936
23. Cui HM, Chen J, Yang HL et al (2013) Preparation and application of Aliquat 336 functionalized chitosan adsorbent for the removal of Pb(II). Chem Eng J 232:372–379
24. Song Y, Deng Y, Zhou H et al (2012) Ionic liquid-based hydrothermal synthesis and luminescent properties of $CaF_2:Ce^{3+}/Mn^{2+}$ nanocrystals. J Nanoparticle Res 14:1258–1266
25. Yan Z, Yan B, Jia L (2014) Hydrogels immobilized by doped rare earth fluoride nanocrystals: ionic liquid dispersion and down/up-conversion luminescence. Spectrochim Acta A 121:732–736
26. Li H, Shao H, Wang Y et al (2008) Soft material with intense photoluminescence obtained by dissolving Eu_2O_3 and organic ligand into a task-specific ionic liquid. Chem Commun 41:5209–5211

Part II
Chemistry of Ionic Liquids with Rare Earth

Chapter 2
Using Crystal Structures of Ionic Compounds to Explore Complexation and Extraction of Rare Earth Elements in Ionic Liquids

Steven P. Kelley, J. Seth Nuss, and Robin D. Rogers

Abstract Despite only being able to directly measure the solid state, single crystal X-ray diffraction is of use in understanding how the fully ionic environment of an ionic liquid (IL) affects complexation of rare earth element ions. Here we examine crystal structures of ionic lanthanide complexes as case studies in this context. The complexation of a dithiophosphate IL is compared to non-IL systems, where the crystal structure illustrates the formation of hydrophobic domains despite the presence of highly charged ions. The crystal structure of a lanthanum complex with 1,2-di(4-pyridyl)ethylene illustrates how a large, neutral ligand in a fully ionic system interrupts the ionic packing, leading to the inclusion of noncoordinating ligands in the outer coordination sphere. The crystal structure of a salt composed of discrete terbium and thorium complex ions illustrates how in two metal ions in a fully ionic environment need not be bridged directly with a ligand but can be linked entirely through noncovalent interactions. Because ILs are fully ionic systems, these effects can be interpreted in the context of rare earth element behavior in ILs.

Keywords Ionic liquids • X-ray crystallography • Lanthanide coordination chemistry • Liquid-liquid extraction • Crystalline hydrates

2.1 Introduction

The use of ILs in the production of rare earth elements (REEs) continues to develop at a rapid pace, particularly in the context of sustainability [1, 2]. REEs are critical materials in energy-saving applications such as magnets for renewable power generation and high-efficiency lighting, yet the solvent extractions used to produce

S.P. Kelley • J.S. Nuss
Department of Chemistry, The University of Alabama, Tuscaloosa, AL 35486-0336, USA

R.D. Rogers (✉)
Department of Chemistry, McGill University, 801 Sherbrooke St. West, Montreal H3A 0B8, QC, Canada
e-mail: robin.rogers@mcgill.ca

J. Chen (ed.), *Application of Ionic Liquids on Rare Earth Green Separation and Utilization*, Green Chemistry and Sustainable Technology,
DOI 10.1007/978-3-662-47510-2_2

them are chemical-intensive and generate large volumes of hazardous waste [3]. This puts REEs in the unusual position of simultaneously being both the source of and solution to a number of environmental problems. It also adds to the urgency of the search for more efficient means of REE production, which include IL-based approaches.

One of the first and largest areas of inquiry for ILs in REE separations has been solvent extraction with hydrophobic ILs [4]. Hydrophobic ILs, a class of salts which melt below the boiling point of water to give water-immiscible liquid phases, have been used as replacements for organic solvents based on their (often assumed) potential to be safer and more environmentally benign due to their low volatility and flammability [5, 6]. While this is still often posited as the motivation for their use in current research papers, ILs are now known to show toxicity [7], volatility [8], or flammability [9, 10] depending on the choice of ions, and the universal assumption that ILs are more "green" than organic solvents is no longer accepted. However, a rich chemistry based on the basic differences between ILs (composed of at least two dissociated ions) and organic solvents (composed of molecules) has emerged from this research. This has shifted the relevance of ILs in improving the sustainability of REE production from just their physical properties to the potential for unprecedented extraction efficiencies or totally new strategies for REE isolation.

Chemists now have access to a broad and chemically variable array of hydrophobic ILs for extracting REEs from aqueous phases. These range from largely noncoordinating ILs, such as dialkylimidazolium salts of perfluoroanions[11] or long-chain alkylammonium and phosphonium halides [12] and nitrates [13], to those which are designed to actively coordinate the metal ion [14–16]. On the other hand, ILs (and related systems such as deep eutectic solvents [17]) have also been designed which can dissolve highly insoluble metal phases (such as oxides) [18]. These solvents have primarily been investigated for nonaqueous electrodeposition of metals [19], but they could conceivably be used as alternatives to aqueous acids used in hydrometallurgical processing. ILs can also be designed with high enough redox stability to allow the electrodeposition of metallic REEs [20]. With ILs having the potential to act as replacements for both aqueous and hydrophobic phases in liquid-liquid extractions, selecting the appropriate strategy out of the many available will ultimately require a thorough understanding of REE speciation in these systems.

The differences in behavior of ILs as extraction solvents were noted early on, particularly the tendency for anionic metal complexes to be extracted through ion exchange mechanisms [21]. ILs are high ionic strength environments quite unlike those found in molecular solutions. Coulombic interactions are quite important in ILs [22], resulting in charge ordering and often nano-segregation of hydrophilic and hydrophobic domains [23]. Coulombic interactions in ILs can reduce the importance of specific, directional noncovalent interactions such as hydrogen bonding which dominate in molecular liquids such as water or alcohols [24]. The solvent affects all steps of the extraction process from complex formation to phase transfer, and even small energy changes can lead to meaningful differences in distribution

and separation factors. Still, studies on the use of ILs in REE extractions tend to investigate the performance more than the mechanism, and typically only the grossest differences between molecular- and IL-based extraction mechanisms are usually reported on, such as a change in the extracted species.

The differences between specific interactions of species in a system are often difficult to measure because many techniques (i.e., spectroscopy) show the aggregate effect of all interactions. Among the techniques which are capable of studying interactions, for instance, by measuring the correlation of two particular atoms in space, single crystal X-ray diffraction (SCXRD) is one of the most detailed and unambiguous. Crystal structures determined by SCXRD give unambiguous three-dimensional molecular structures and relative positions of molecules which greatly facilitate observing and quantifying specific interactions, especially noncovalent interactions. A commonly cited drawback to SCXRD is the fact that the crystal structure is not necessarily indicative of the actual system of interest, which for liquid-liquid extractions would be a solution. This is certainly a valid concern when one is comparing a crystal structure of a salt to its solution in a molecular solvent at low ionic strength, where the ions can easily be dissociated. However, a pure IL has a very similar ionic strength to its crystal. The structure of the liquid and the crystal will not be the same, but the nature of the interionic interactions in either will still likely be very similar. In this sense, the crystal structures of ILs and metal-IL complexes may have much to teach about the effects of high ionicity on metal ion behavior in IL solutions.

Borrowing from the tools of crystal engineering [25], here we use the crystal structures of lanthanide complexes to study interactions whose effects on solution chemistry, including extraction, may be important but are not easily measured. The examples discussed here will include crystal structures of a lanthanide cation complexed to an extractant-functionalized IL anion, a co-crystal of an ionic lanthanide complex with neutral ligands, and a salt composed of solvated metal complexes as both cations and anions. Each of these crystalline compounds is ultimately a pure salt, and in examining their crystal structures, we will pay particular attention to how high ionic strength affects both the inner- and outer-sphere interactions observed in these structures.

2.2 Inner-Sphere Interactions Between Metal Ions and Ionic Liquid Extractants: Bis(*O,O′*-ethyl) dithiophosphate

Extraction of a metal ion directly into an IL with no added extractant is the conceptually simplest case for illustrating the differences between neutral and fully ionic systems. In this case, the IL itself acts as the extractant, and its ions (usually the anion) coordinate to the metal ion to form the complex that is transferred into the IL phase. The coordination mode of an IL ion to a metal ion will likely be the same in the IL as in any other system because it is determined primarily by the chemical identities of the two species involved. However, the speciation of metal complexes, which

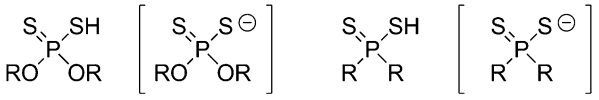

Fig. 2.1 (*Left*) General structure of dithiophosphoric acids and dithiophosphates. (*Right*) General structure of dithiophosphinic acids and dithiophosphinates

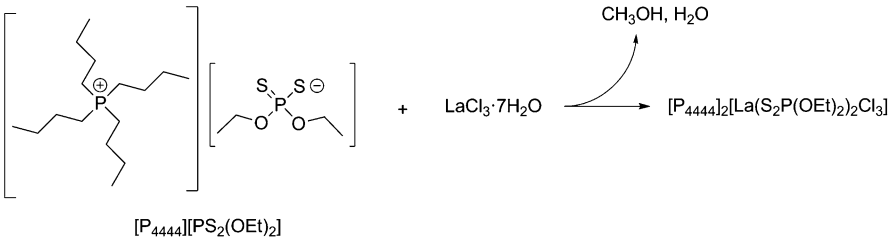

Fig. 2.2 Crystallization of $[P_{4444}]_2[La(S_2P(OEt)_2)_2Cl_3]$

depends on the competition between all potential donors in the system, will be affected by changing from a molecular solvent to an IL.

Crystallizing a metal complex from an IL based on an extractant would provide a convenient way for testing the aforementioned scenario. A number of ILs, commonly called task-specific ILs, are designed to coordinate to and extract metal ions by incorporating known extractant moieties [26–28]. One such system contains dithiophosphoric acids, which have been long studied as extractants for transition metals from aqueous acids [29]. These systems, along with the structurally related dithiophosphinic acids [30], are also studied as extractants in actinide/lanthanide separations, where the presence of sulfur donor atoms gives these ligands selectivity for actinides [31, 32]. The structures of both groups of extractants and their conjugate bases are shown in Fig. 2.1. ILs based on dithiophosphate anions are known [33] but have not been studied in extractions yet, likely because the most studied examples are water miscible.

We used a commercially available dithiophosphate room temperature IL, tetra-*n*-butylphosphonium bis(*O*,*O*'-ethyl)dithiophosphate ($[P_{4444}][PS_2(OEt)_2]$, using the common shorthand for tetraalkylphosphonium and ammonium ILs in the literature), and $LaCl_3 \cdot 7H_2O$ to study the inner-sphere interactions of a lanthanide ion with a dithiophosphate-containing IL. $LaCl_3 \cdot 7H_2O$ was found to be difficult to dissolve in $[P_{4444}][PS_2(OEt)_2]$, so methanol was used to dissolve both compounds. The use of a volatile solvent to co-dissolve a metal salt and an IL is one strategy for crystallizing compounds from ILs, as selective evaporation of the volatile solvent allows the system to become closer and closer to the neat IL until crystallization is achieved [34]. Slow evaporation of the methanol solution containing $LaCl_3 \cdot 7H_2O$ and $[P_{4444}][PS_2(OEt)_2]$ yielded crystals which were identified by SCXRD as $[P_{4444}]_2[La(S_2P(OEt)_2)_2Cl_3]$. This compound can be thought of as a 2:1 adduct of the IL with $LaCl_3$ which forms as the solvated/hydrated metal ion exchange coordinated solvent molecules for IL anions (Fig. 2.2).

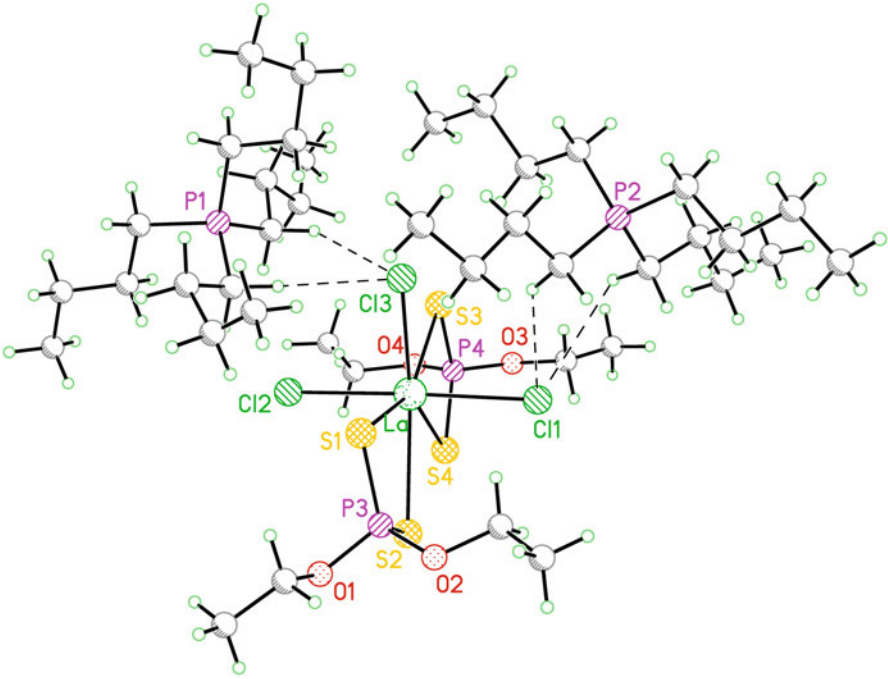

Fig. 2.3 Ball and stick plot of the asymmetric/formula unit for $[P_{4444}]_2[La(S_2P(OEt)_2)_2Cl_3]$. *Dashed lines* indicate the shortest contacts between molecules. Disorder and carbon atom labels omitted for clarity

$[P_{4444}]_2[La(S_2P(OEt)_2)_2Cl_3]$ crystallized in the monoclinic space group $P2_1/c$ with one unique formula unit ($Z = 4$) (Fig. 2.3). The lanthanum cation is coordinated by two bidentate dithiophosphonate anions and three chloride anions. The coordination geometry is pentagonal bipyramidal, and the complex has close to C_{2v} symmetry. The complex has a net charge of -2 and is counterbalanced by two $[P_{4444}]^+$ cations which have some structural differences with each other (Fig. 2.4, top). One cation has three chains oriented in an all-*anti* configuration, while the last two carbons on the fourth chain were found to be disordered over +/− *anti*-periplanar positions. The other cation has only one all-*anti* chain. Two chains are disordered at the ends, and the last has the terminal methyl group in a gauche conformation. This conformational flexibility is observed in many crystal structures of ILs with moderate length alkyl chains and is believed to be an important contributor to their low melting points [35].

The coordination mode of the dithiophosphate ligands and the overall geometry of the complex (shown in Fig. 2.4, bottom) match what is known in the literature. Several lanthanide dithiophosphate complexes are published in the Cambridge Structural Database (CSD) [36], and they fall in one of the three categories: anionic complexes with four dithiophosphate ligands [37, 38], neutral complexes with three dithiophosphate ligands and two neutral unidentate ligands [39–43], and cationic

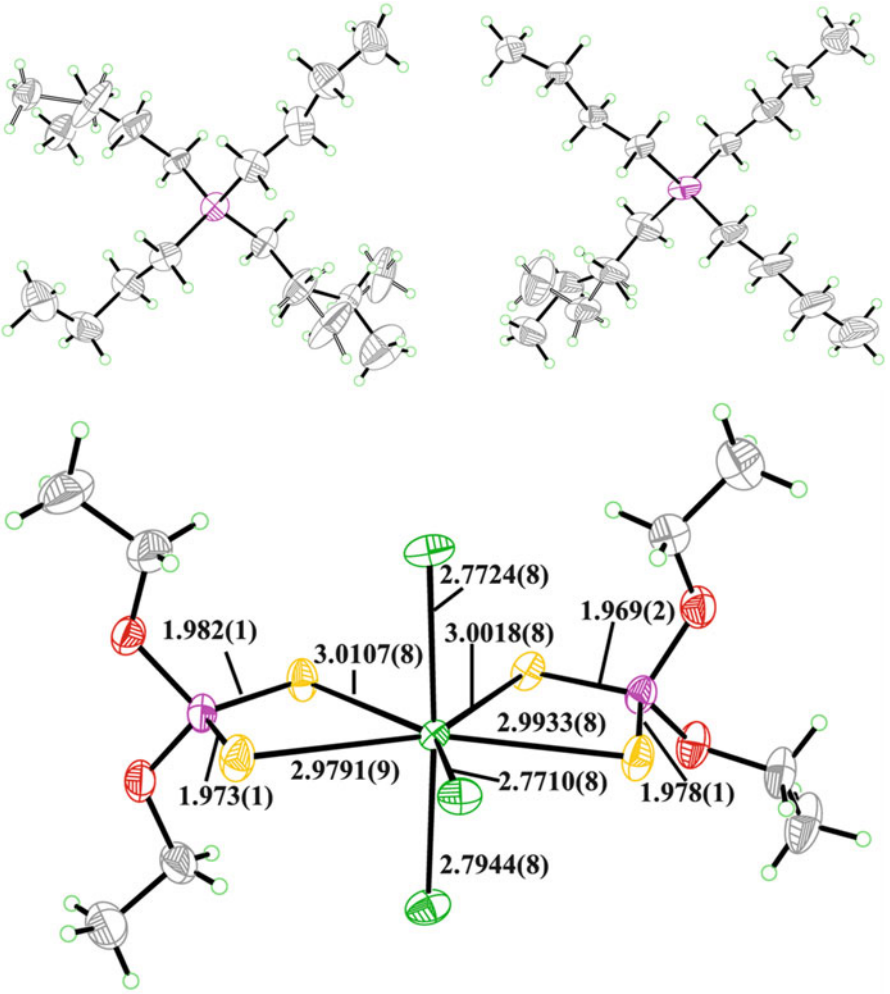

Fig. 2.4 50 % probability ellipsoid plots showing structural details of the individual ions. (*Top*) Both unique cations with all conformations for disordered alkyl chains shown. (*Bottom*) Anion with La-Cl, La-S, and P-S distances in Å

complexes with two dithiophosphate ligands and three neutral ligands (usually counterbalanced by a noncoordinating dithiophosphate ligand) [43, 44]. There are some cases where the cationic complex is counterbalanced by the anionic complex [42, 45]. $[La(S_2P(OEt)_2)_2Cl_3]^{2-}$ has the same geometry as the cationic complexes, with the chloride ions occupying the same sites that the neutral unidentate donor atoms would.

The presence of coordinated chloride ions, however, is unprecedented. Most lanthanide dithiophosphate complexes are synthesized from lanthanide chloride hydrates using methods derived from one published by Pinkerton et al. [45]. In

these methods, the lanthanide chloride hydrate is first dissolved along with the sodium salt of the dithiophosphate and either the neutral ligand or bulky counterion present in the crystal structure, evaporated to dryness, and extracted with an organic solvent. The organic washing step would separate insoluble NaCl from the more soluble dithiophosphinate complexes.

The complexes expected to form when lanthanide ions are extracted into an organic solvent by a dithiophosphate extractant match those in the reported crystal structures [46]. However, $[P_{4444}][La(S_2P(OEt)_2)_2Cl_3]$ was crystallized directly from a reaction of $LaCl_3 \cdot 7H_2O$ with the dithiophosphate salt and can be understood as the result of substitution of coordinated water molecules by IL ions. In this sense, the crystal structure should bear a closer relationship to the complexes formed when $LaCl_3$ is dissolved in this IL, which differ from those expected in an organic solvent.

From the point of view of an extraction, the most important effect of this speciation difference is the greater charge of the complex, which might make extraction from an aqueous solution more difficult. Examination of the short (less than the sum of the van der Waals radii) contacts around each ion reveals that the anion is surrounded by a hemispherical shell of cations which interact by donating hydrogen bonds from $–CH_2-$ groups α to the phosphorous atoms to the chloride and sulfur atoms. Only the ethyl groups of one of the dithiophosphonate ligands are not surrounded by a cation. The cations also make short contacts to other cations through their alkyl chains, indicating that hydrophobic interactions are possible in the crystal despite the presence of the highly charged complex ion. This results in reverse micelle-like structure with a charged core surrounded by alkyl groups from both the phosphonium cations and dithiophosphate anions (Fig. 2.5).

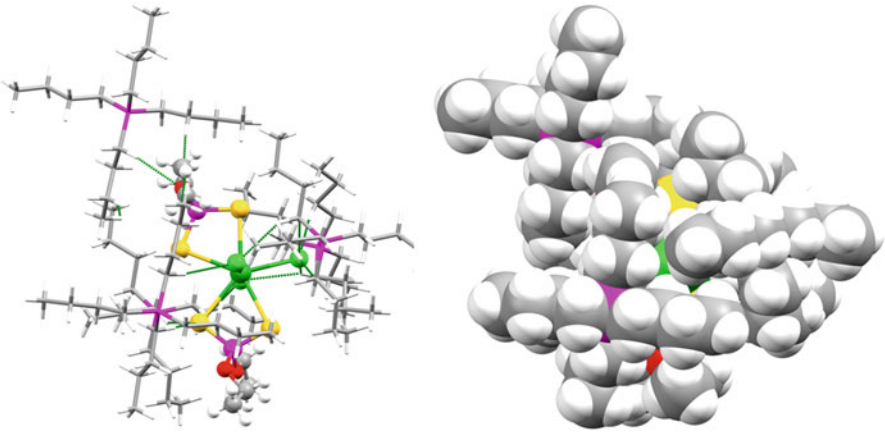

Fig. 2.5 (*Left*) Packing plot showing the short contact environment around the $[La(S_2P(OEt)_2Cl_3]^{2-}$ anion with short contacts indicated as *green lines*. (*Right*) Same plot with all atoms represented as space-filling spheres. Element colors are the same as Fig. 2.3

The crystal packing is dominated by charge ordering, but despite the short length of the alkyl chains compared to most surfactant-type molecules, segregation of hydrophobic and hydrophilic zones still manages to occur. The cation with more disorder and more chains deflected from the normally favored all-*anti* configuration (Fig. 2.4, top left) appears to be more closely interacting with the anion. The extra conformational complexity appears to be the result of the uncharged terminal alkyl groups being displaced by the close proximity of the anion to the charged phosphonium center. Hydrogen bonds between this cation and the anion result in infinite charge-ordered chains along the crystallographic *a* axis.

The other, more well-ordered cation (Fig. 2.4, top right) occupies positions next to the anion in the + and – *b* directions and interacts through apparently weaker hydrogen bonds (i.e., to weaker acceptors such as the uncharged phosphate oxygen atoms). This results in an infinite 2D sheet in the *ab* plane composed of chains of hydrogen-bonded cations and anions alternating with and bridged to each other by chains composed solely of cations. The sheets are then stacked antiparallel to each other along *c*, which allows the all-cation chains to be farther from each other (Fig. 2.6, top). The interface between any two of these sheets forms a thin, hydrophobic zone (about as thick as an ethyl group) and is composed of ethyl groups from the ends of the cation butyl chains and even dithiophosphate ligands (Fig. 2.6, bottom). The formation of hydrophobic zones from relatively short chains has been reported, for instance, in molecular dynamics simulations of imidazolium hexafluorophosphates [47] and the crystal structure of 1-ethyl-3-methylimidazolium hexafluorophosphate [48].

One of the major traits of ILs as extractants is their propensity to extract charged metal complexes through an ion exchange mechanism [49]. This has been perceived as a disadvantage as IL ions are lost to the aqueous phase although arguments have been made in favor of incorporating ion exchange as an extraction mechanism in applications [50]. Nevertheless, extraction studies in ILs are often conducted with the goal of promoting a neutral extraction mechanism over ion exchange. This is achieved by controlling the components of the IL, the extractant, and the aqueous phase (often empirically) so that the extracted metal species is neutral [51, 52].

Interestingly, although the metal complex in $[P_{4444}]_2[La(S_2P(OEt)_2)_2Cl_3]$ is charged, it is formed by the reaction of neutral $LaCl_3$ with the IL and gives a detailed model for how an IL can solubilize a metal-extractant complex in a hydrophobic environment. In this case, the formation of a charged metal complex through the addition of the IL anion to a neutral metal salt is important to the hydrophobicity, as the charge of the metal complex is what attracts the phosphonium cations which then build the hydrophobic environment around it. It was earlier mentioned that $LaCl_3 \cdot 7H_2O$ did not show appreciable solubility in $[P_{4444}][PS_2(OEt)_2]$. This likely stems from the fact that the abundance of alkyl groups in the IL makes it a poor solvent for hydrated metal cations such as the lanthanum cation in $LaCl_3 \cdot 7H_2O$ [53]. However, dissolving the two salts in methanol results in the dissociation of these separate hydrophobic and hydrophilic systems. The IL and $LaCl_3$ were subsequently free to assemble into crystalline $[P_{4444}]_2[La$

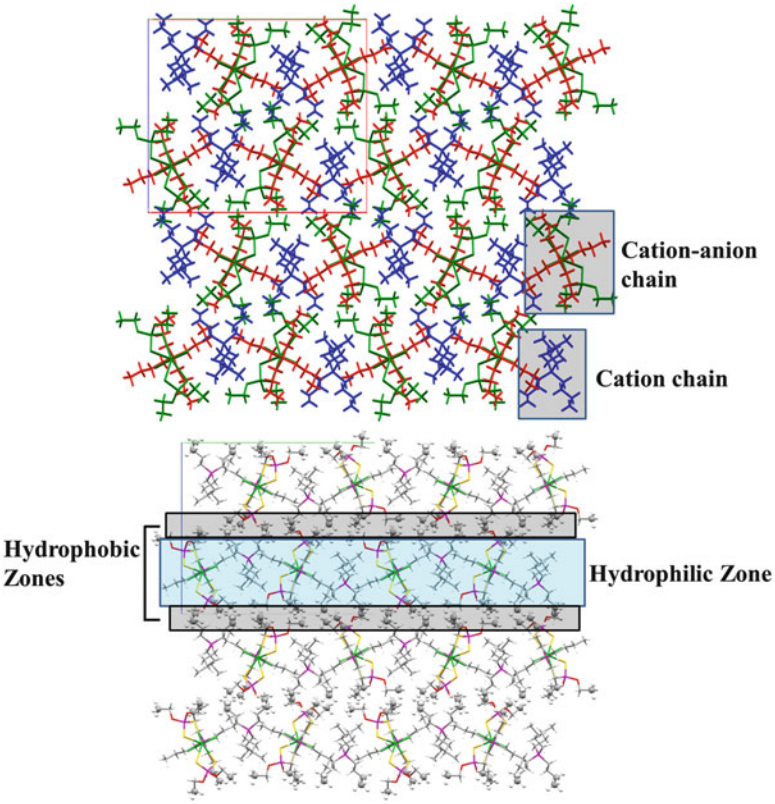

Fig. 2.6 Packing diagrams ($2 \times 2 \times 2$ unit cells) down *a*. with atoms colored by symmetry equivalence to emphasize separate roles of symmetry-independent cations (*top*) and atoms in hydrophobic zones rendered as balls and sticks to emphasize hydrophilic-hydrophobic ordering (*bottom*)

$(PS_2(OEt)_2)_2Cl_3]$, where charge ordering manages to exist within a hydrophobic microenvironment.

In this case, the crystal structure of a metal complex crystallized by reaction with an IL was compared to the structures of metal complexes with similar ligands grown through more conventional techniques to illustrate the effect of high ionic strength on the speciation of the metal complex. Here, the direct comparison served as the most powerful and straightforward way to show the difference. However, crystal structures of salts of ionic metal complexes can still be used to study the effects of ionicity regardless of whether they were crystallized from an IL or not. Indeed, the only difference between such compounds and ILs is an arbitrary melting point cutoff. In the next two cases, the compounds discussed were formed through the reactions of metal ions with neutral ligands to give ionic metal complexes.

2.3 Inner- and Outer-Sphere Interactions in a Fully Ionic Environment: 1,2-di(4-Pyridyl)ethylene

A number of outer-sphere processes are involved in extraction such as solvent reorganization upon formation of the metal complex and transfer into the receiving phase. These make small energetic contributions which are difficult to measure directly but can nonetheless significantly change distribution values and separation factors. ILs possess features which differ considerably from simple molecular solvents such as hydrocarbons, including nanoscale structuring [54, 55] and the ability to solvate several molar equivalents of water [56]. Differences like these are some of the most fundamental advantages of using ILs, but they are presently very difficult to understand and control. One of the strongest advantages of SCXRD is the ability to probe such noncovalent interactions. Thus, crystal structures of charged metal complexes with outer-sphere extractant and solvent molecules are one way in which highly detailed models can be constructed for their interactions at high ionic strength.

N-heterocyclic ligands have particularly complex behavior. In addition to coordinating to the metal, N-heterocycles can be protonated and act as counterions to anionic metal complexes. The polar, aromatic ring systems of these ligands can also give rise to a number of noncovalent interactions. As extractants, N-heterocycles such as bis(triazine) pincer ligands are an important class of extractants in actinide-lanthanide separations [57]. 1- and 2-methylimidazole have also been studied as extractants for lanthanides into ILs and show promise for intra-group separations [58].

We crystallized two isomorphous lanthanide (M = La, Gd) complexes with 1,2-di (4-pyridyl)ethylene (dipy, Fig. 2.7) in order to investigate the interplay between inner- and outer-sphere interactions in a high ionic strength environment. The dipy ligand is capable of bridging metal complexes through direct coordination or hydrogen bonding and has a rigid and extensive conjugated π-electron system. The reaction of $La(NO_3)_3 \cdot 6H_2O$ and $Gd(NO_3)_3 \cdot 6H_2O$ with dipy gave isomorphous crystals of the formula $[Ln(NO_3)_2(dipy)(OH_2)_4][NO_3] \cdot 2dipy$ [59]. The discussion here will focus on the lanthanum complex for which better SCXRD data could be obtained. $[La(NO_3)_2(dipy)(OH_2)_4][NO_3] \cdot 2dipy$ is a co-crystal of an ionic compound with a neutral molecule, and understanding the inclusion of the neutral ligand can reveal more about the outer-sphere metal complex-ligand interactions.

$[La(NO_3)_2(dipy)(OH_2)_4][NO_3] \cdot 2dipy$ is crystallized in $P2_1/c$ with one symmetry unique formula unit (Z = 4) (Fig. 2.8). The La^{3+} cation is coordinated by four water molecules, one unidentate dipyridyl ligand, and two bidentate nitrate ions in a tricapped trigonal prismatic arrangement (Fig. 2.9). This complex has a net charge

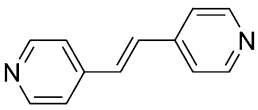

Fig. 2.7 Structure of 1, 2-di (4-pyridyl)ethylene

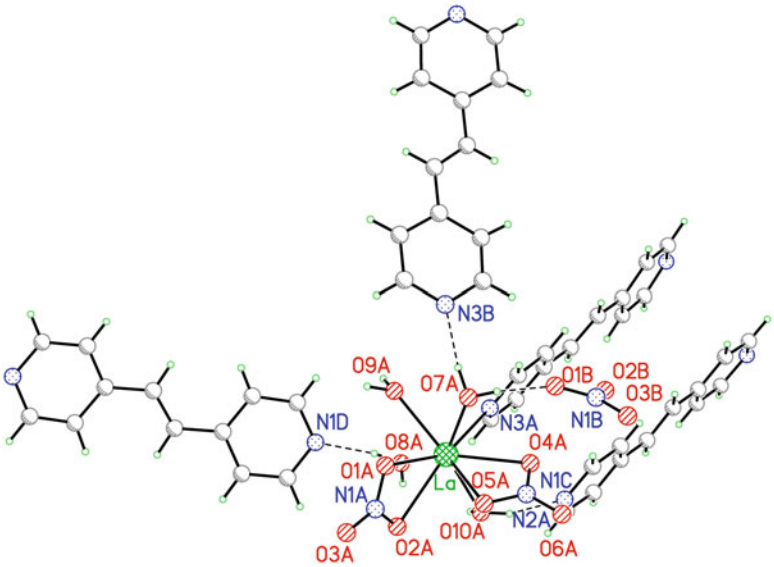

Fig. 2.8 Ball and stick plot of the asymmetric unit of $[La(NO_3)_2(dipy)(OH_2)_4][NO_3] \cdot 2dipy$ with half molecules expanded through symmetry. Labels on carbon atoms omitted for clarity

of +1 and is counterbalanced by a noncoordinating nitrate ion. All three nitrate ions have two long N-O bonds and one short one, but the difference is more pronounced in the coordinated nitrate ions. The two equivalents of noncoordinating dipy which co-crystallize with the salt are found as one symmetry unique molecule and two symmetry unique half molecules which reside on crystallographic inversion centers.

All dipy molecules were found to be neutral (as opposed to protonated and cationic) based on the position of difference map peaks near the oxygen atoms and a lack of appropriate peaks near the dipy nitrogen atoms. This assignment is further supported by the absence of short contacts between dipy nitrogen and nitrate oxygen atoms, which would be present due to $NH^{+}\cdots O^{-}$ charge-assisted hydrogen bonding, and by the presence of numerous contacts between dipy molecules which would be repulsive if the molecules were all cationic. The dipy molecules are close to but not perfectly flat, with the two rings being slightly out of plane with each other. Bonds around each aromatic ring vary; the C–N bonds are the shortest and the two C–C bonds to C1 (the carbon atom bound to the ethylene bridge) are the longest. The coordinated and full-occupancy free dipy ligands have more symmetric C–N bonds than the two crystallographically centrosymmetric dipy ligands. Coordination to the La^{3+} cation does not produce major changes in the structure of the ligand. Structures and bond distances are shown in Fig. 2.9 (top).

The presence of so many large dipy molecules means that over half the unit cell volume is occupied by nonionic organic functional groups. A view of the $2 \times 2 \times 2$ unit cell packing down the *a* axis reveals that the ionic groups are organized into

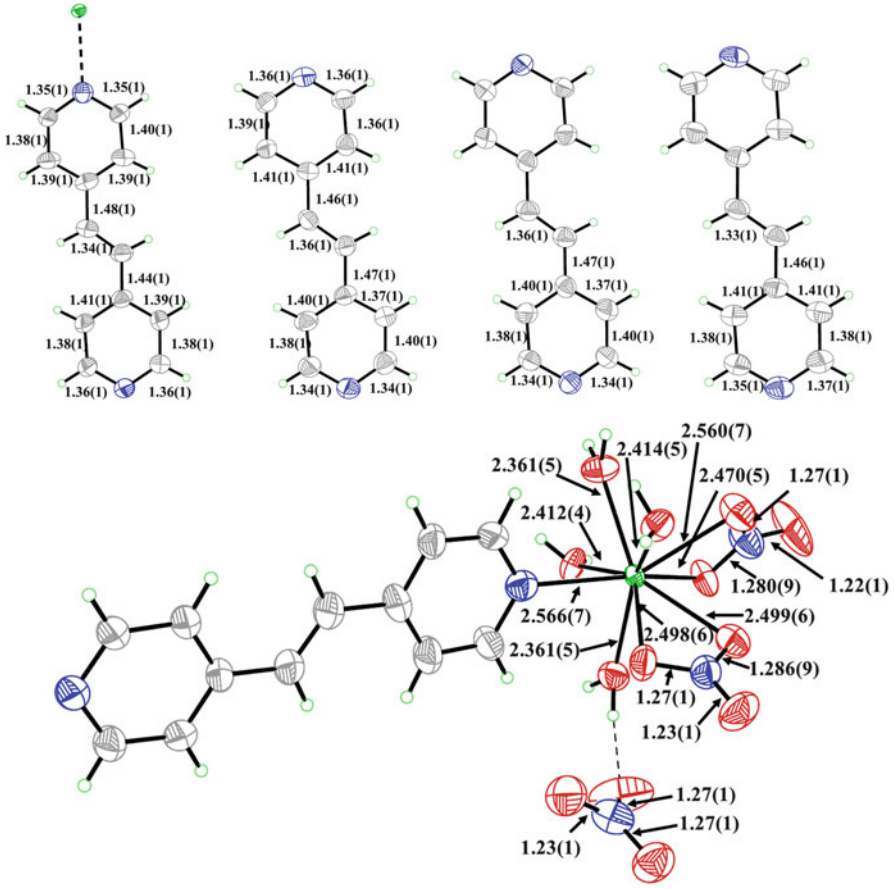

Fig. 2.9 Probability ellipsoid (50 %) plots showing detailed molecular structures and selected bond distances in Å. (*Top*) The four unique dipy molecules (A through D, from *left* to *right*). (*Bottom*) $[La(NO_3)_2(dipy)(OH_2)_4]^+$ cation and noncoordinating $[NO_3]^-$ anion

thin strips surrounded by a matrix of dipy molecules. The metal complex cations form centrosymmetric dimers in which the coordinated dipy ligand on one accepts a hydrogen bond from the other, and the two dipy ligands stack with a high degree of overlap (Fig. 2.10). Charge-assisted hydrogen bonds between the noncoordinating nitrate ions and coordinated water molecules on the cation form infinite chains along the *c* axis. These chains are bridged into sheets in the *bc* plane through dimerization of the cations, which changes direction along *c* (Fig. 2.11, top left). One of the noncoordinating dipy molecules stacks with the cation dimers, bridging them along *a*. The other two noncoordinating dipy molecule bridges form discrete stacks of three molecules which bridge the ionic chains diagonally along the *ab* plane (Fig. 2.11, bottom).

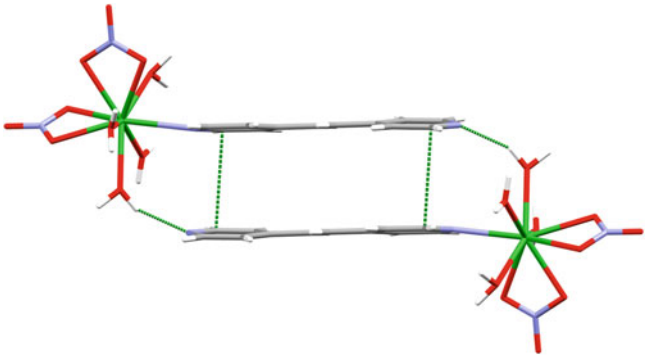

Fig. 2.10 Packing diagram showing hydrogen-bonded dimer between two $[La(NO_3)_2(dipy)(OH_2)_2]^+$ cations

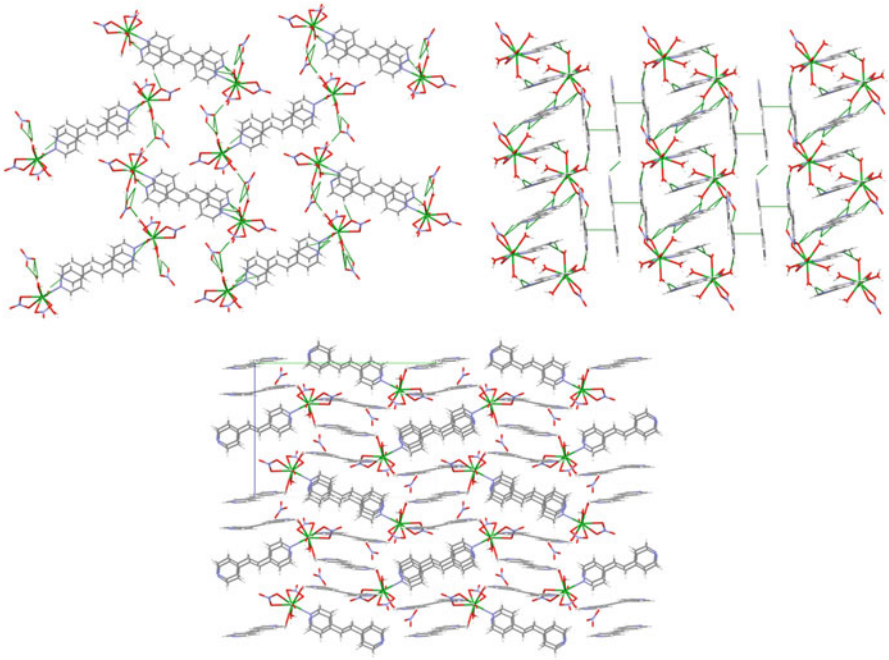

Fig. 2.11 Packing diagrams showing hydrogen bonding between metal complexes and nitrate ions forming chains (vertical) bridged by hydrogen bonding between cations (horizontal) (*top left*), neutral dipy molecules stacking with cation dimers (vertical) and forming discrete clusters which bridge the stacked cation chains (horizontal) (*top right*), and overall packing ($2 \times 2 \times 2$ unit cells) viewed down *a*

The packing of co-crystals of salts with neutral molecules can be complicated because it can show separate regions of salt-like packing (dominated by charge ordering) and molecular packing (dominated by directional interactions) [60]. This

manifests itself in the structure of $[La(NO_3)_2(dipy)(OH_2)_4][NO_3] \cdot 2dipy$ through the formation of a network which includes distinct, nonionic zones interacting through π···π stacking. This packing appears to be a way to offset the size difference between the cation and anion. The anion is only able to support the formation of one-dimensional charge-ordered structures, so the noncoordinating dipy ligands interact with both the cations and each other to further space out the cations along the other two axes. Interestingly, the size difference between the cation and anion is due largely to the size of the dipy ligand itself. The inclusion of dipy molecules in the outer sphere is therefore driven by the formation of the inner-sphere dipy complex.

This effect can be examined in more detail through comparison of the structures with a similar one from the literature, $[H(dipy)]_2[(La(NO_3)_4(OH_2)_2)_2] \cdot dipy$ [61]. This complex is a salt of a dimeric lanthanum complex anion in which the two metal centers are bridged by nitrate ions. It contains no La-dipy bonds, but a singly protonated $[H(dipy)]^+$ cation is present as a counterion. The neutral dipy molecule forms infinite stacks with the protonated $[H(dipy)]^+$ cation, forming a matrix which surrounds the anions. The absence of a metal-dipy bond may be due to the use of solvothermal synthesis in acetonitrile to prepare the compound. Acetonitrile has no hydrogen bond donors to stabilize dissociated nitrate, and protonation of dipy would make an ionic compound which would be less soluble in acetonitrile. However, despite not being directly coordinated to the metal ion, the dipy molecule is an integral part of the metal-containing compound as a counterion and is stabilized by the co-crystallization of additional neutral dipy molecules.

From these crystal structures it can be seen that the high ionic strength environment drives noncovalent interactions between nonionic parts of the extractant. Extractant molecules are virtually all designed to include large, hydrophobic groups to reduce the water solubility of the resulting complex, so interactions like these should not be considered uncommon in ILs. This effect could result in complicated relationships between extractant concentration and distribution value if the metal complex is extracted with nonstoichiometric amounts of noncoordinating extractant molecules. On the other hand, the IL itself can be designed to interact with and stabilize hydrophobic portions of the extractant as discussed earlier.

2.4 Ionic Interactions Between Charged Complexes of Different Metals: $[Tb(NO_3)_2(OH_2)_5][Th(NO_3)_5(OH_2)_2]$

There are three major ways by which elementally different metal ions can be incorporated into the same compound. First, a metal cation can coordinate directly to an anionic metal complex. This is especially common among metals which form stable oxyanions, and such compounds form the basis of many minerals such as aluminates, chromates, molybdates, etc. [62]. Next, two or more metal ions may be

tethered into a single complex by a bridging ligand, for instance, by reacting a metal salt with a pre-metallated molecule with remaining open coordination sites [63]. Third, two or more different metal ions can counterbalance a single anion, forming a double salt [64]. Double salts may involve the completely random substitution of metal ions throughout the crystal structure or may have a unique crystal structure which forms only at specific stoichiometries. All three of these phenomena are related in that the metal ions are joined by coordination to bridging ligands, i.e., an oxygen atom in the first case or a polyatomic anion in the third.

It is also quite common for cationic and anionic complexes of the same metal ion to crystallize as a salt. This happens especially often for metals that form stable polyatomic ions, such as tetrachlorocobaltate [65, 66] or tetrachlorozincate [67, 68]. Rare earths readily form both cationic and anionic complexes, and the CSD contains many examples of crystal structures showing this phenomenon in the rare earths such as the published dithiophosphate complexes discussed previously [33]. In this case the two metal ions are bridged only through outer-sphere interactions but are inseparable (without changing the speciation) since their complexes act as counterions to each other. It would seem reasonable that charged complexes containing two different metal ions could form a salt as well, but this approach is not as well documented. This is probably because it is difficult to control whether or not the two metals separate on crystallization if there is no covalent linkage between them.

It is quite easy, by contrast, to get multiple elements into a single phase by dissolving them. It is here that ILs deviate quite fundamentally from molecular solvents. Whereas dissolving ionic compounds in molecular solvents changes the ionic strength, an IL is a totally ionic system before and after dissolution of an ionic compound. We have proposed considering homogeneous liquid combinations of ionic compounds to be the liquid analogs of solid double salts to emphasize this property [69]. The dissolved ionic compound effectively becomes part of a new IL, and its ionic interactions with the other ions are part of the chemical bonding which holds the whole system together. The separation community has recognized combining ILs as a strategy for tuning their physicochemical properties [70], but there does not yet appear to be any consideration for how dissolution of charged metal complexes may change the interactions with the constituents of IL. Oppositely charged metal complexes may have an electrostatic interaction which prevents their effective separation.

To illustrate this phenomenon, we present the crystal structure of $[Tb(NO_3)_2(OH_2)_5][Th(NO_3)_5(OH_2)_2] \cdot H_2O$. This compound was prepared by evaporating a solution of $Tb(NO_3)_3 \cdot 5H_2O$ and $Th(NO_3)_4 \cdot 4H_2O$ in methanol. The separation of thorium(IV) from the lanthanides is one of the basic steps in the refinement of lanthanide-bearing minerals such as monazite [71]. Monazite itself is a double salt of thorium and several lanthanides with phosphate. Here, it is shown that thorium can also form a compound with the lanthanide terbium held together solely through outer-sphere interactions. The crystal structure of this compound provides a detailed look at how the ionic complexes which are favored in ILs can go on to interact with each other, possibly affecting separations.

$[Tb(NO_3)_2(OH_2)_5][Th(NO_3)_5(OH_2)_2] \cdot H_2O$ (Fig. 2.12) crystallized in the triclinic space group P-1 with one unique formula unit ($Z = 2$). Tb(III) and Th(IV) are in

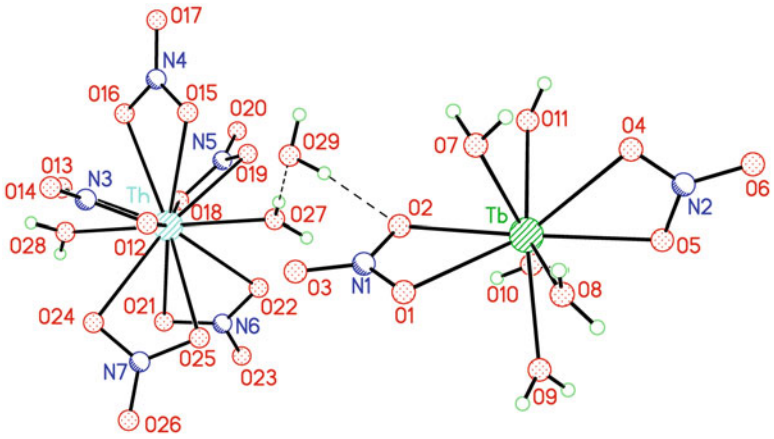

Fig. 2.12 Ball and stick plot of the asymmetric/formula unit of $[Tb(NO_3)_2(OH_2)_5][Th(NO_3)_5(OH_2)_2]$. *Dashed lines* indicate the shortest contacts between ions

discrete charged complexes. The cationic Tb(III) complex is coordinated to two bidentate nitrate ions and five water molecules in a tricapped trigonal prismatic geometry. The water molecules are arranged in a very rough pentagon with the two nitrate ions occupying positions that would be axial to this plane. The CSD contains examples of lanthanide nitrate complexes with this formula [72, 73], but none have this geometry.

The anionic Th(IV) complex is coordinated by five bidentate nitrate ions and two water molecules. The coordination geometry is icosahedral. The nitrate ions form a ring around the metal ion and are "tilted" to create two offset pentagons of oxygen atoms approaching the S_{10} symmetry of a true icosahedron. The remaining two vertices of the icosahedron are occupied by the water molecules, which are almost perfectly 180° to each other. The $[Th(NO_3)_5(OH_2)_2]^-$ anion has recently been reported by Sigmon and Burns as a potassium salt, where it coordinates directly to potassium counterions [74]. The geometry of the anion reported here matches the one reported by Sigmon and Burns. Structural details are shown in Fig. 2.13.

One striking feature of this crystal structure is the large amount of self-association between cations and anions. Each ion makes short contacts to six counterions and five ions of the same charge. The shapes of both complexes allow them to simultaneously donate and receive hydrogen bonds with neighboring complexes of the same charge. These mutual hydrogen bonds appear to be one of the major driving forces in the packing and organize the cations into chains and the anions into ribbons. The cation chains are bridged into sheets through more hydrogen bonding, and the anion chains are bridged into sheets through dipole-dipole interactions between nitrate groups as well as hydrogen bonds mediated by the lattice water molecules (Fig. 2.14, top). The resulting cationic and anionic layers form charge-ordered stacks along *c* and interacting with each other through a number of strong, charge-assisted hydrogen bonds and dipole-dipole interactions (Fig. 2.14, bottom).

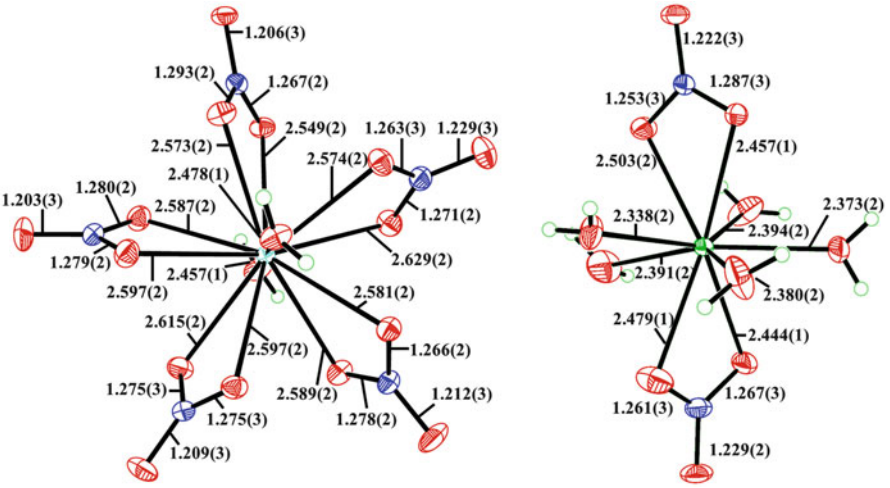

Fig. 2.13 Probability ellipsoid (50 %) plots showing the detailed structures and selected bond distances in Å for $[Th(NO_3)_4(OH_2)_2]^-$ (*left*) and $[Tb(NO_3)_2(OH_2)_5]^+$ (*right*)

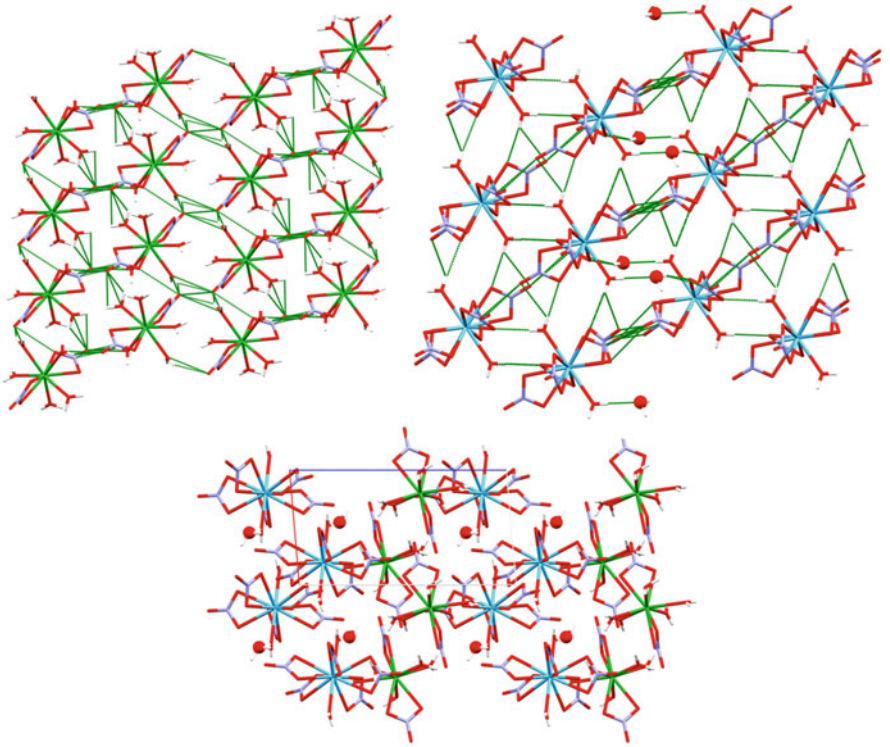

Fig. 2.14 Packing diagrams showing hydrogen-bonded layers of cation (*top left*), anions (*top right*), and overall packing ($2 \times 2 \times 2$ unit cells) down *b* (*bottom*). Element colors are the same as in Fig. 2.9; lattice water molecules are enlarged for visibility

2.5 Conclusions

It is important to recognize that crystal structures have their limits when dealing with the study of solution phenomena. However, it is also worth noting that crystallography has been one of the major tools leading to our modern understanding of ILs. Crystal structures have helped profoundly to develop models describing hydrogen bonding [75], hydrophilic-hydrophobic segregation [76], and ion structure and conformations in ILs [77]. Many crystal structures have been studied to find out why ILs crystallized and thus how to prevent it from happening [78]. This view helps to both intrinsically link the interactions observed in a liquid with those in the solid state yet maintains that the flexibility of the liquid state allows for more structural tunability.

The arrangement of ions is a major driving force in both solid and liquid salts, and crystallography is one of the only tools which can extract this information unambiguously. While emphasis is placed on molecular structure identification, packing phenomena relevant to metal speciation and distribution in ILs were observed in each of the structures examined here. This is especially important when considering that the majority of solution chemistry is still based on a foundation of molecular systems where neutral species dominate and ions, if present, are considered dissociated. The phenomena observed here such as the formation of ion pairs with hydrophobic exteriors, the effect of outer-sphere interactions on metal-extractant stoichiometry, and the formation of mixed metal ion pairs, which are all still relatively unexplored even IL-based separations, may not even be observed in neutral systems.

Today there is more appreciation than ever of the complexity of IL phases. What are needed now are experimentally validated models to explain these phenomena. We believe that the ionicity of ILs will continue to be revealed as the origin for many of their divergent properties. The contributions of crystallography to this area are by no means limited to the examples discussed here. A match between a crystal structure and its species in solution can only be obtained with luck, but the effects of charge ordering and ionicity manifest themselves inevitably in an ionic crystal structure. The examination of these effects should be a priority in further application of this technique toward understanding separations in ILs.

Acknowledgments The authors would like to thank the DOE Office of Nuclear Energy Nuclear Energy University Programs (Project DE-NE0000672 and DOE-NEUP Graduate Research Fellowship DE-NE0000366) for the support of this work.

References

1. Liu Y, Chen J, Li D (2012) Application and perspective of ionic liquids on rare earths green separation. Sep Sci Technol 47:223–232

2. Durga G, Goyal D, Mishra A (2013) Applications of ionic liquids in metal extraction. In: Mishra A, Clark JH (eds) Green materials for sustainable water treatment, vol 23, RSC green chemistry series. Royal Society of Chemistry, Cambridge, pp 155–180
3. Rare earth elements: A review of production, processing, recycling, and associated environmental issues (2012) U. S. Environmental Protection Agency National Service Center for Environmental Publications. http://nepis.epa.gov/Adobe/PDF/P100EUBC.pdf. Accessed 17 Feb 2015
4. Visser AE, Rogers RD (2003) Room-temperature ionic liquids: New solvents for *f*-element separations and associated solution chemistry. J Solid State Chem 171:109–113
5. Earle MJ, Seddon KR (2000) Ionic liquids. Green solvents for the future. Pure Appl Chem 72:1391–1398
6. Zhao H, Xia S, Ma P (2005) Use of ionic liquids as 'green' solvents for extractions. J Chem Technol Biotechnol 80:1089–1096
7. Pretti C, Chiappe C, Peiraccini D et al (2006) Acute toxicity of ionic liquids to the zebrafish (*Danio rerio*). Green Chem 8:238–240
8. Earle JM, Esperança JMSS, Gilea MA et al (2006) The distillation and volatility of ionic liquids. Nature 439:831–834
9. Singh RP, Verma RD, Meshri DT et al (2006) Energetic nitrogen-rich salts and ionic liquids. Angew Chem Int Ed 45:3584–3601
10. Smiglak M, Metlen A, Rogers RD (2007) The second evolution of ionic liquids: from solvents and separations to advanced materials – energetic examples from the ionic liquid cookbook. Acc Chem Res 40:1182–1192
11. Kozonoi N, Ikeda Y (2007) Extraction mechanism of metal ion from aqueous solution to the hydrophobic ionic liquid, 1-butyl-3-methylimidazolium nonafluorobutanesulfonate. Monatsh Chem 138:1145–1151
12. Hoogerstraete TV, Wellens S, Verachtert K et al (2013) Removal of transition metals from rare earths by solvent extraction with an undiluted phosphonium ionic liquid: separations relevant to rare-earth magnet recycling. Green Chem 15:919–927
13. Hoogerstraete TV, Binnemans K (2014) Highly efficient separation of rare earths from nickel and cobalt by solvent extraction with the ionic liquid trihexyl(tetradecyl)phosphonium nitrate: a process relevant to the recycling of rare earths from permanent magnets and nickel metal hydride batteries. Green Chem 16:1594–1606
14. Shimojo K, Kurahashi K, Naganawa H (2008) Extraction behavior of lanthanides using a diglycolamide derivative TODGA in ionic liquids. Dalton Trans:5083–5088
15. Odinets IL, Sharova EV, Artyshin OI et al (2010) Novel class of functionalized ionic liquids with grafted CMPO-moieties for actinides and rare-earth elements recovery. Dalton Trans 39:4170–4178
16. Mehdi H, Binnemans K, Van Hecke K et al (2010) Hydrophobic ionic liquids with strongly coordinating anions. Chem Commun 46:234–236
17. Abbott AP, Capper G, Davies DL et al (2006) Solubility of metal oxides in deep eutectic solvents based on choline chloride. J Chem Eng Data 51:1280–1282
18. Nockemann P, Thijs B, Pittois S et al (2006) Task-specific ionic liquids for solubilizing metal oxides. J Phys Chem B 110:20978–20992
19. Schubert T, El Abedin SZ, Abbott AP et al (2008) Electrodeposition of metals. In: Endres F, MacFarlane DR, Abbott AP (eds) Electrodeposition from ionic liquids. Wiley-VCH, Weinheim, pp 88–123
20. Rao CJ, Venkatesan KA, Nagarajan K et al (2010) Electrochemical and thermodynamic properties of europium(III), samarium(III), and cerium(III) in 1-butyl-3-methylimidazolium chloride ionic liquid. J Nucl Mater 399:81–86
21. Cocalia VA, Holbrey JD, Gutowski KE et al (2006) Separations of metal ions using ionic liquids: the challenges of multiple mechanisms. Tsinghua Sci Technol 11:188–193
22. Zhao W, Leroy F, Heggen B et al (2009) Are there stable ion pairs in ionic liquids? Molecular dynamics simulations of 1-*n*-butyl-3-methylimidazolium hexafluorophosphate. J Am Chem Soc 131:15825–15833

23. Shimizu K, Bernardes CES, Lopes JNC (2014) The complex structure of ionic liquids at an atomistic level: from "red-and-greens" to charge templates. Pure Appl Chem 86:119–133
24. Izgorodina EI, MacFarlane DR (2011) Nature of hydrogen bonding in charged hydrogen-bonded complexes and imidazolium-based ionic liquids. J Phys Chem B 49:14659–14667
25. Desiraju GR (2014) Chemical crystallography and crystal engineering. IUCrJ 1:380–381
26. Nockemann P, Thijs B, Lunstroot K et al (2009) Speciation of rare-earth metal complexes in ionic liquids: a multiple-technique approach. Chem Eur J 15:1449–1461
27. Mohapatra PK, Danwal P, Iqbal M et al (2013) A novel CMPO-functionalized task-specific ionic liquid: synthesis, extraction and spectroscopic investigations of actinide and lanthanide complexes. Dalton Trans 42:4343–4347
28. Barber PS, Kelley SP, Rogers RD (2012) Highly selective extraction of the uranyl ion with hydrophobic amidoxime-functionalized ionic liquids via η^2 coordination. RSC Adv 2:8526–8530
29. Handley TM, Dean JA (1962) O, O'-dialkyl phosphorodithioic acids as extractants for metals. Anal Chem 34:1312–1315
30. Zhu Y (1995) The separation of americium from light lanthanides by Cyanex 301 extraction. Radiochim Acta 68:95–98
31. Jensen MP, Bond AH (2002) Comparison of covalency in the complexes of trivalent actinide and lanthanide cations. J Am Chem Soc 124:9870–9877
32. Bhattacharyya A, Mohapatra PK, Manchanda VK (2011) Role of ligand softness and diluent on the separation behavior of Am(III) and Eu(III). J Radioanal Nucl Chem 288:709–716
33. Yoshii K, Yamaji K, Tsuda T et al (2013) Physicochemical properties of tri-*n*-butylalkylphosphonium cation-based room-temperature ionic liquids. J Phys Chem B 117:15051–15059
34. Reichert WM, Holbrey JD, Vigour KB et al (2006) Approaches to crystallization from ionic liquids: complex solvents-complex results, or, a strategy for controlled formation of new supramolecular architectures? Chem Commun:4767–4779
35. Krossing I, Slattery JM, Daguenet C et al (2006) Why are ionic liquids liquid? A simple explanation based on lattice and solvation energies. J Am Chem Soc 128:13427–13434
36. Allen FH (2002) The Cambridge Structural Database: a quarter of a million structures and rising. Acta Crystallogr B 58:380–388
37. Pinkerton AA, Schwarzenbach D (1981) Crystal and molecular structures of $[AsPh_4][Ln\{S_2P(OEt)_2\}_4]$ (Ln = La or Er) and their comparison with results obtained in solution from paramagnetic nuclear magnetic resonance data. J Chem Soc Dalton Trans:1470–1474
38. Spiliadis S, Pinkerton AA (1983) Dithiophosphinate complexes of the lanthanides. Preparation of the complexes $[Ln\{S_2PR_2\}_4][AsPh_4]$, R = OMe, OPr^i. Determination of the crystal structures for Ln = Ce, Er (R = OMe) and Ln = Nd, Ho ($R = OPr^i$). Inorg Chim Acta 75:115–123
39. Nagai K, Sato Y, Kondo S, Ouchi A (1983) The synthesis, properties, and structure of bis(N, N-dimethylacetamide)-tris(O, O'-diisopropyl dithiophosphato)lanthanum(III). Bull Chem Soc Jpn 56:2605–2609
40. Nakamura R, Nagai K, Shimoi M, Ouchi A (1984) The syntheses, properties, and crystal and molecular structures of bis(benzamide)tris(O, O'-diisopropyl dithiophosphato)neodymium (III), $[Nd\{(C_3H_7O)_2PS_2\}_3(C_6H_5CONH_2)_2]$, and its isomorphous complexes of La, Ce, Pr, Sm, Eu, and Gd. Bull Chem Soc Jpn 57:2919–2924
41. Imai T, Shimoi M, Ouchi A (1986) The structure of bis(dibenzyl sulfoxide)tris(O, O'-diethyl dithiophosphato)lanthanum(III), $La\{(C_2H_5O)_2PS_2\}_3\{(C_6H_5CH_2)_2SO\}_2$. Bull Chem Soc Jpn 59:669–670
42. Imai T, Nakamura M, Nagai K et al (1986) The syntheses, properties, and crystal and molecular structures of the lanthanoid mixed-complexes of O, O'-diisopropyl dithiophosphate and dimethyl sulfoxide: $[Ln\{(C_3H_7O)_2PS_2\}_3]$ (Ln = La or Nd), and $[Eu\{(C_3H_7O)_2PS_2\}_2\{(CH_3)_2SO\}_3][Eu\{(C_3H_7O)_2PS_2\}_4]$. Bull Chem Soc Jpn 59:2115–2122
43. Pinkerton AA, Schwarzenbach D (1976) Ligand displacement from tetrakis(OO'-diethyl phosphorodithioate)-lanthanoid(III) anions by triphenylphosphine oxide. X-Ray crystal

structure of $[La\{S_2P(OEt)_2\}_3(POPh_3)_2]$ and $[Sm\{S_2P(OEt)_2\}_2(POPh_3)_3][S_2POEt)_2]$. J Chem Soc Dalton Trans:2466–2471
44. Nagai K, Nakamura R, Shimoi M, Ouchi A (1984) Syntheses and crystal and molecular structures of tris(benzamide)(bis(O, O'-diisopropyl dithiophosphato)lanthanoid(III) O, O'--diisopropyl dithiophosphate (M = Gd, Tb, Dy, Er, and Yb). Bull Chem Soc Jpn 57:2725–2729
45. Pinkerton AA, Meseri Y, Rieder C (1978) Preparation and characterization of dithiophosphinato-complexes of yttrium and the lanthanoids. J Chem Soc Dalton Trans:85–90
46. Curtui M, Haiduc I (1992) Solvent extraction of lanthanum(III) and cerium(III) with dialkyldithiophosphoric acids. Separation from thorium(IV). J Radioanal Nucl Chem 164:91–101
47. Yan T, Burnham CJ, Del Pópolo MG et al (2004) Molecular dynamics simulation of ionic liquids: the effect of electronic polarizability. J Phys Chem B 108:11877–11881
48. Fuller J, Carlin RT, De Long HC, Haworth D (1994) Structure of 1-ethyl-3-methylimidazolium hexafluorophosphate: model for room temperature molten salts. J Chem Soc Chem Commun:299–300
49. Jensen MP, Neuefeind J, Beitz JV et al (2003) Mechanisms of metal ion transfer into room-temperature ionic liquids: the role of anion exchange. J Am Chem Soc 125:15466–15473
50. Billard I, Ouadi A, Gaillard C (2011) Liquid-liquid extraction of actinides, lanthanides, and fission products by use of ionic liquid: from discovery to understanding. Anal Bioanal Chem 400:1555–1566
51. Cocalia VA, Jensen MP, Holbrey JD et al (2005) Identical extraction behavior and coordination of trivalent or hexavalent f-element cations using ionic liquid and molecular solvents. Dalton Trans:1966–1971
52. Janssen CHC, Sánchez A, Witkamp G-J, Kobrak MN (2013) A novel mechanism for the extraction of metals from water to ionic liquids. ChemPhysChem 14:3806–3813
53. Habenschuss A, Spedding FH (1979) Di-μ-chloro-bis[heptaaqualanthanum(III)] tetrachloride $[(H_2O)_7LaCl_2La(H_2O)_7]Cl_4$. Cryst Struct Commun 8:511–516
54. Bhargava BL, Devane R, Klein ML, Balasubramanian S (2007) Nanoscale organization in room temperature ionic liquids: a coarse grained molecular dynamics simulation study. Soft Matter 3:1395–1400
55. Triolo A, Russina O, Fazio B et al (2008) Morphology of 1-alkyl-3-methylimidazolium hexafluorophosphate room temperature ionic liquids. Chem Phys Lett 457:362–365
56. Seddon KR, Stark A, Torres M-J (2000) Influence of chloride, water, and organic solvents on the physical properties of ionic liquids. Pure Appl Chem 72:2275–2287
57. Lewis FW, Harwood LM, Hudson MJ et al (2011) Highly efficient separation of actinides from lanthanides by a phenanthroline-derived bis-triazine ligand. J Am Chem Soc 133:13093–13102
58. Shen Y, Li W, Wu J, Li S, Luo H, Dai S, Wu W (2014) Solvent extraction of lanthanides and yttrium from aqueous solution with methylimidazole in an ionic liquid. Dalton Trans 43:10023–10032
59. Broker GA, Klingshirn MA, Rogers RD (2002) Green chemistry and lanthanide-based crystal engineering. J Alloys Compd 344:123–127
60. Kelley SP, Narita A, Holbrey JD et al (2013) Understanding the effects of ionicity in salts, solvates, co-crystals, ionic co-crystals, and ionic liquids, rather than nomenclature, is critical to understanding their behavior. Cryst Growth Des 13:965–975
61. Khanjani S, Morsali A (2009) Two metal-organic La(III) compounds as precursors for preparation of nano-sized LaO(OH) and $La(OH)_3$. J Coord Chem 62:3642–3650
62. Kraus EH (1911) Descriptive mineralogy with especial reference to the occurrences and uses of minerals. George Wahr, Ann Arbor, pp 131–164
63. Kumar G, Gupta R (2013) Molecularly designed architectures – the metalloligand way. Chem Soc Rev 42:9403–9453
64. Freund I (1907) Double Salts. In: Alcock NH, Freemen WG (eds) Science progress in the twentieth century, vol 2. John Murray, London, pp 135–139

65. Vance TB Jr, Holt EM (1980) Tetrahedral and octahedral cobalt(II) in hexaaquacobalt tetrachlorocobaltate-18-crown-6-acetone. Acta Crystallogr 36:150–153
66. Ciccarese A, Clemente DA, Marzotto A, Valle G (1993) Synthesis, structural, and spectroscopic characterization of hexakis (dimethyl sulfoxide)cobalt(II) tetrachlorocobaltate(II), [Co $(Me_2SO)_6][CoCl_4]$. J Crystallogr Spectrosc Res 23:223–229
67. Melegari M, Massera C, Ugozzoli F, Dalcanale E (2010) Tetraphosphonate cavitands: interplay between metal coordination and H-bonding in the formation of dimeric capsules. CrystEngComm 12:2057–2059
68. Xu R-B, Xu X-Y, Shi P-F, Wang D-Q, Gao J, Yang X-J, Lu L-D, Wang X, Xu G-X (2007) Synthesis and crystal structure of a new complex [Bis(dien)zinc(II)] zinc(II) tetrachloride (dien = diethylenetriamine). Chin J Struct Chem 26:1441–1444
69. Chatel G, Pereira JFB, Debbeti V, Wang H, Rogers RD (2014) Mixing ionic liquids – "simple mixtures" or "double salts"? Green Chem 16:2051–2083
70. Nidermeyer H, Hallett JP, Villar-Garcia IJ et al (2012) Mixtures of ionic liquids. Green Chem 41:7780–7802
71. Cotton S (2006) Lanthanide and actinide chemistry. Wiley, West Sussex, pp 1–7
72. Lipstman S, Goldberg I (2010) Coordination and hydrogen-bonding assemblies in hybrid reaction products between 5,10,15,20-tetra-4-pyridylporphyrin and dysprosium trinitrate hexahydrate. Acta Crystallogr C 66:m222–m226
73. Thuéry P (2012) Uranyl-lanthanide heterometallic assemblies with 1,2-ethanedisulfonate and cucurbit[6]uril ligands. CrystEngComm 14:3363–3366
74. Sigmon GE, Burns PC (2010) Crystal chemistry of thorium nitrates and chromates. J Solid State Chem 183:1604–1608
75. Kölle P, Dronskowski R (2004) Hydrogen bonding in the crystal structures of the ionic liquid compounds butyldimethylimidazolium hydrogen sulfate, chloride, and chloroferrate(II, III). Inorg Chem 43:2803–2809
76. Holbrey JD, Reichert WM, Nieuwenhuyzen M et al (2003) Crystal polymorphism in 1-butyl-3-methylimidazolium halides: supporting ionic liquid formation by inhibition of crystallization. Chem Commun 2003:1636–1637
77. Holbrey JD, Reichert WM, Rogers RD (2004) Crystal structures of imidazolium bis(trifluoromethanesulfonyl)imide 'ionic liquid' salts: the first organic salt with a *cs*-TFSI anion conformation. Dalton Trans 2267–2271
78. Dean PM, Turanjanin J, Yoshizawa-Fujita M et al (2009) Exploring an anti-crystal engineering approach to the preparation of pharmaceutically active ionic liquids. Cryst Growth Des 9:1137–1145

Part III
Ionic Liquids for the Extraction and Separation of Rare Earth

Chapter 3
Separating Rare-Earth Elements with Ionic Liquids

Nada Mehio, Huimin Luo, Chi-Linh Do-Thanh, Xiaoqi Sun, Yinglin Shen, Jason R. Bell, and Sheng Dai

Abstract The rare-earth elements (REEs) are a group of 17 chemically similar metallic elements; this group consists of scandium, yttrium, and 15 lanthanides. Due to their essential role in permanent magnets, lamp phosphors, catalysts, and rechargeable batteries, the REEs have become an essential component of the global transition to a green economy. Currently, with China producing over 90 % of the global REE output and its increasingly tightening export quota, the rest of the world is confronted with the potential risk of REE shortage. As such, many countries will have to rely on recycling REEs from pre-consumer scrap, industrial residues, and REE-containing end-of-life products. Over the course of the last two decades, ionic liquids have been increasingly used to separate REEs in the recycling process. Ionic liquids (ILs) are a class of molten salts that are liquid at temperatures below 100 °C. ILs are amenable to the recycling of REEs because the cation and anion components are readily tailored to a given process, and they offer numerous advantages over typical organic solvents, such as low volatility, low flammability, a broad temperature range of stability, the ability to dissolve both inorganic and organic compounds, high conductivity, and wide electrochemical windows. In this chapter, we discuss the performance of several IL-based extraction systems used to separate and recycle REEs.

N. Mehio • C.-L. Do-Thanh
Department of Chemistry, The University of Tennessee, Knoxville, TN 37996-1600, USA

H. Luo • J.R. Bell
Energy and Transportation Sciences Division, Oak Ridge National Laboratory, Oak Ridge, TN 37831-6201, USA

X. Sun • Y. Shen
Chemical Sciences Division, Oak Ridge National Laboratory, Oak Ridge, TN 37831-6201, USA

S. Dai (✉)
Department of Chemistry, The University of Tennessee, Knoxville, TN 37996-1600, USA

Chemical Sciences Division, Oak Ridge National Laboratory, Oak Ridge, TN 37831-6201, USA
e-mail: dais@ornl.gov

J. Chen (ed.), *Application of Ionic Liquids on Rare Earth Green Separation and Utilization*, Green Chemistry and Sustainable Technology,
DOI 10.1007/978-3-662-47510-2_3

Keywords Synthesis and purification of ionic liquids • Properties of ionic liquids • Rare-earth elements • Solvent extraction based on ionic liquids • TALSPEAK-like extraction for REEs

3.1 Introduction

The rare-earth elements (REEs) consist of scandium (Sc), yttrium (Y), and 15 lanthanides exhibiting similar chemical properties. The REEs have become increasingly important due to their essential role in a number of green, low-carbon applications, such as permanent magnets, lamp phosphors, rechargeable NiMH batteries, and catalysts [1]. Consequentially, as the global demand for hybrid and electric cars, wind turbines, and compact fluorescent lamps rises, so does the price of REEs [1]. As such, the European Commission labeled the REEs as the most critical raw materials group in its landmark report *Critical Raw Materials for the European Union* [2]. Likewise, the US Department of Energy (DOE) acknowledged the critical importance of REEs in their *Critical Materials Strategy* report by listing REEs in their medium term criticality matrix (Fig. 3.1) [3]. Furthermore, the US DOE labeled neodymium (Nd), europium (Eu), terbium (Tb), dysprosium (Dy), and yttrium (Y) as the five most critical REEs [3]. The demand for Nd and Dy is anticipated to increase by 700 % and 2600 % in the next 25 years, respectively [4].

Currently, China produces over 90 % of the global REE supply, although less than 40 % of the known REE supply is located in China [1]. This is largely due to

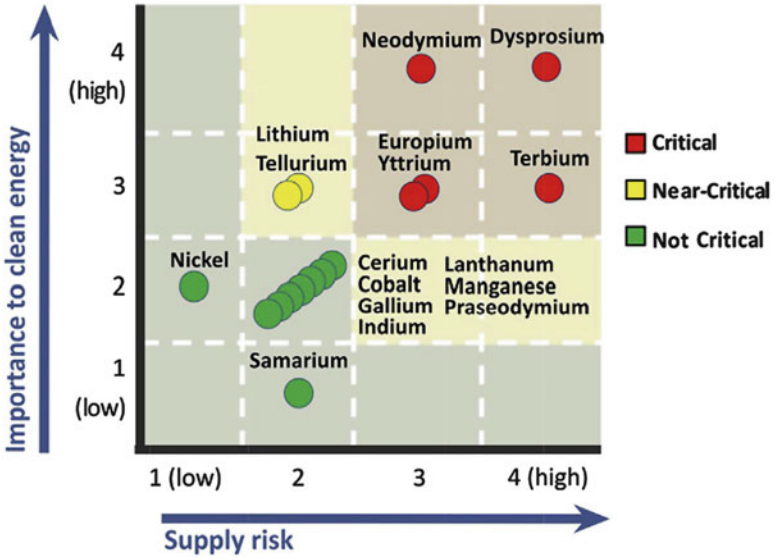

Fig. 3.1 DOE medium term criticality matrix depicting the five most critical REEs (Reprinted with permission from Ref. [3]. Copyright 2011 US Department of Energy)

the fact that China is specialized in extracting rare-earth oxides from their respective ores and in a variety of downstream activities, such as the separation of rare-earth oxides into individual elements, processing elements into rare-earth metals, and the production of rare-earth permanent magnets and lamp phosphors [1]. Moreover, in order to accommodate increased domestic demand, China decreased its export quota from 50,145 tons to 31,130 tons between 2009 and 2012 [1]. Thus, the decreased export quota may potentially inhibit REE usage and complicate the development of REE applications outside of China [1].

In light of these potential challenges, many countries will have to rely on recycling REEs from pre-consumer scrap, industrial residues, and REE-containing end-of-life products [1, 5]. Over the course of the last two decades, ionic liquids (ILs) have been increasingly used to separate REEs in the recycling process [6–12]. ILs are a class of molten salts that are liquid at temperatures below 100 °C [13]. ILs are amenable to the recycling of REEs because the cation and anion components are readily tailored to a given process, and they offer numerous advantages over typical organic solvents, such as low volatility, low flammability, a broad temperature range of stability, the ability to dissolve both inorganic and organic compounds, high conductivity, and wide electrochemical windows [14]. In this chapter, we discuss the performance of several IL-based extraction systems used to separate and recycle REEs.

3.2 Preparation of Ionic Liquids for Extraction

3.2.1 Synthesis Methods

Various synthetic methods for ILs have been reviewed in detail [14]. In order to provide a specialized capability for an IL, functional groups need to be present in the cation or anion. Such functionalized ILs are commonly termed "task-specific ionic liquids" (TSILs) [15]. Generally, the IL cation is the favored functionalization site because of the wide variety of available natural products that already contain the desired moieties. These compounds are usually transformed into cations via a quaternization reaction between a nucleophilic group such as an amine, *N*-heterocycle, phosphine, and an alkyl halide [16].

Recently, Mohapatra et al. developed diglycolamide-based TSILs to extract Eu^{3+} under acidic feed conditions [17]. The imidazolium-containing TSILs were synthesized by a quaternization reaction between *n*-butyl bromide and an imidazole attached to a diglycolamide, followed by anion metathesis to obtain the desired anion [17]. A modified diglycolamide derivative has also been used as a TSIL anion by Rout and Binnemans for extracting Nd^{3+} from acidic media [18]. The authors performed an anion exchange on a tetraalkylammonium chloride salt by NaOH to form the hydroxide and then reacted this intermediate with dioctyl diglycolamic acid (HDGA) for another metathesis to make the TSIL product [18].

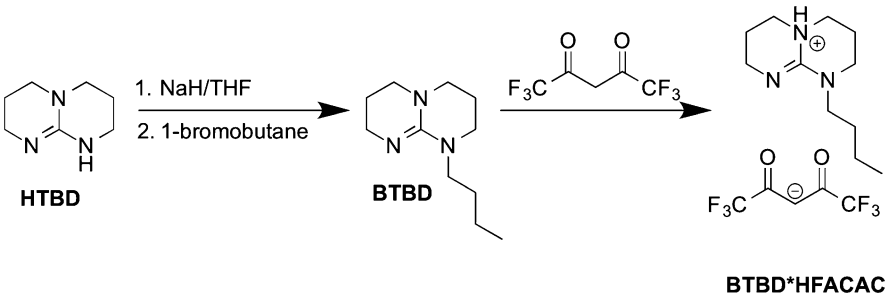

Fig. 3.2 Synthesis of new task-specific IL based on superbase and β-diketone

Protic ILs utilizing strong bases (i.e., organic "superbases" [19]) have been shown to have lower vapor pressures and superior thermal stabilities compared to typical protic ILs using amine bases. This is in accord with Angell et al. who found the vapor pressure of a protic IL varies inversely with the pK_a difference of the acid/base components [20]. Therefore, we recently synthesized task-specific protic ILs, utilizing organic superbases and fluorinated β-diketones as the cationic and anionic components, respectively [21]. This approach would allow for a facile synthesis of TSIL with high thermal stability [21]. The new protic TSILs were synthesized in high yield in a one-step neutralization process [21]. The superbase was cooled in an ice bath, and exactly one equivalent of fluorinated β-diketone was added dropwise with stirring [21]. No purification was necessary for these new protic TSILs [17]. One example of synthesis is illustrated in Fig. 3.2.

3.2.2 Purification Methods

Most ILs used for extraction are odorless and colorless [14]. Thus, multiple methods have been developed to remove color and odor impurities from ILs [14]. We will review some of these methods in this section. First, we will review literature methods for decolorizing ILs. For example, Earle and co-workers used a special column containing charcoal particles and silica gel to investigate the discoloration of ILs [22]. Earle et al. found that this special column worked particularly well with ILs that contained bistriflimide ($[NTf_2]^-$), tetrafluoroborate ($[BF_4]^-$), and hexafluorophosphate ($[PF_6]^-$) [22]. Moreover, Earle et al. found that this method worked better on the final IL than the corresponding halide salt [22]. Similarly, Burrell and co-workers reported a method for decolorizing large quantities of high-quality ILs [23]. Burrell et al. found that running IL precursors through decolorizing charcoal columns prior to synthesis yields high-quality ILs [23]. The final discoloration method is a synthetic method published by Nockemann and co-workers [24]. Nockemann and colleagues synthesized colorless ILs suitable for spectroscopic requirements by processing 1-methyl-3-alkylimidazolium precursors at low temperatures [24].

Next, we will discuss methods for removing odor impurities from ILs by reviewing methods for removing organic impurities and water impurities from ILs. One method that has been discussed in the literature is the use of supercritical CO_2 ($scCO_2$) [25]. For example, Baiker et al. have reported that $scCO_2$ is an efficient method for cleaning and drying [C_4mim][BF_4], [C_4mim][PF_6], and [C_4mim][TfO] [25]. Moreover, Baiker and colleagues reported that $scCO_2$ was efficient at drying hygroscopic and water-soluble ILs on reasonable time scales [25]. While Ren and co-workers used N_2 to remove volatile impurities, such as water, ethanol, methanol, acetonitrile, ethyl acetate, and acetone, from ILs [26], they observed that the process can be sped up by increasing the temperature and N_2 flow rates [26].

3.3 Properties of Ionic Liquids for Extraction

3.3.1 Volatility, Thermal Stability, and Flammability

The search for a safer alternative to volatile organic compounds (VOCs) is an overarching goal of the chemical and nuclear industries [27]. A safer, less volatile alternative to VOCs can minimize both solvent loss and the air pollution induced by solvent evaporation [14]. The key challenge in developing an IL capable of replacing VOCs is to develop a solvent system with enhanced thermal stability, reduced volatility and flammability, and less environmental impact [14]. As such, ILs are the ideal environmentally friendly replacement because they are characterized by low volatility, low combustibility, and high thermal stability [14].

ILs have long been regarded as nonvolatile liquids because the vapor pressure of an IL is generally immeasurable at room temperature [10]. Numerous experimental techniques have been used to measure the vapor pressures and vaporization enthalpies of ILs, such as ultraviolet absorption spectroscopy [28], mass spectrometry [29], the integral effusion Knudsen method [30], the thermogravimetric method [31], and the transpiration method [32]. It has been reported that some imidazolium ILs evaporate as ion pairs, and consequentially, the heats of vaporizations of these ILs depend primarily on Coulombic interactions within the liquid phase and the gas phase [33]. Thus, the evaporation of ion pairs indicates that ILs can be distilled without decomposition [14]. Furthermore, it has been demonstrated that the thermal decomposition products of ILs leads to an increase in pressure [20, 34]. Moreover, Wasserscheid recently reported that the vapor pressure of ILs remains negligible at near-ambient conditions and that most ILs investigated displayed no signs of distillation below their thermal decomposition temperature [35].

Thus, one of the greatest advantages of ILs as solvents is their exceptional thermal stability [14]. As such, multiple studies investigating the thermal stability of ILs have been reported in the literature, and we will discuss some of these studies

in greater detail in this section. It has been documented that the anionic species of the IL has a great bearing on the thermal stability of the IL [36–38]. Kulkarni and co-workers examined the thermal stability of a series of [1-benzyl-3-methylimidazolium][X] and ranked the thermal stability of the anions based on the thermal stability of the corresponding ILs [39]. In decreasing order, $[NTf_2]^- = [TfO]^- > [TSA]^- > [DCA]^- > [SAC]^- > [TFA]^- > [SCN]^-$ [39]. Similar studies were conducted on quaternary ammonium ILs, and likewise it was demonstrated that the anion species has a significant impact on the thermal stability of the IL [40]. In increasing order, $[CF_3BF_3]^- < [n\text{-}C_3F_7BF_3]^- \approx [n\text{-}C_4F_9BF_3]^- \approx [C_2F_5BF_3]^- < [BF_4]^- \approx [NTf_2]^-$ [40]. Likewise, a similar thermal stability investigation was carried out on a series of pyridinium ILs, and the following trend in thermal stability was observed: $I^- < [SCN]^- < [N(CN)_2]^- < [NTf_2]^- < [TfO]^- < [BF_4]^-$ [41]. Alternatively, Tokuda and co-workers investigated a series of ILs with the same $[NTf_2]^-$ anion: $[C_4mim]^+$, the 1-butylpyridinium cation ($[BuPy]^+$), $[C_4mpyrr]^+$, and the butyltrimethylammonium cation ($[BuMe_3N]^+$) [42]. By comparing the decomposition onset temperature of each IL, Tokuda et al. were able to rank the cationic thermal stability as follows: $[C_4mpyrr]^+ > [C_4mim]^+ > [BuMe_3N]^+ > [BuPy]^+$ [42].

While as Fox and co-workers studied the flammability of 1,2,3-trialkylimidazolium ILs in relation to their thermal stability, they observed that ILs with nucleophilic anionic species decomposed at temperatures about 150 °C lower than ILs with bulky fluoride-containing anions, thereby demonstrating that alkyl chain length does not substantially influence the thermal stability of ILs [43]. Moreover, Fox and co-workers demonstrated that while the onset decomposition temperature of trialkylimidazolium ILs is greater than the onset decomposition temperature of corresponding dialkylimidazolium ILs, the anionic species had a greater effect on the onset decomposition temperature overall than the cationic species [43]. Likewise, Anderson et al. investigated the thermal stabilities of germinal and monocationic imidazolium and pyridinium ILs and found that the thermal stability of germinal species was much greater than that of their corresponding monocationic species [44]. Our group also prepared a new family of low-volatility protic ionic liquids (PILs) that currently exhibit the highest thermal stability among known PILs to our knowledge [31]. The family of PILs that we recently synthesized is pairing superbasic organic proton acceptors with equally reactive superacid-based fluorous anions [31].

Alternatively, the thermal stability of ILs can be modulated by solute composition [45]. Smiglak and co-workers investigated the flammability of 20 imidazolium and phosphonium ILs and found that while ILs are not flammable themselves, they are not necessarily safe to use near fire and other sources of heat because solute impurities and the products of thermal decomposition are sensitive to composition [46, 47]. This is especially true when F, Cl, P, S, C, H, N, and O in ammonium, imidazolium, pyridinium, tetrazolium, and aminotetrazole cations are paired with anions such as $[NO_3]^-$, $[CH_3CO_2]^-$, $[N(CN)_2]^-$, $[C(CN)_3]^-$, $[PF_6]^-$, $[NTf_2]^-$, and $[N(NO_2)_2]^-$ [32, 48, 49]. Despite the vapor pressure and flammability issues associated with some of the ILs discussed, ILs are unquestionably classified as

green solvents when compared to the VOCs currently in use by the chemical and nuclear industries [14]. Specifically, ILs provide far superior volatility, thermal stability, and combustibility stability than VOCs under standard conditions [14]. However, the nonvolatile and noncombustible nature of ILs is also one of the main disadvantages of ILs as a solvent because it complicates the process of purifying, regenerating, and disposing spent IL-based systems [14]. Thus, before ILs can replace VOCs in industrial processes, methods for purifying, regenerating, and disposing spent IL-based systems need to be established [14]. This will require more investigations into the volatility, thermal stability, and flammability of ILs [14].

3.3.2 Viscosity

The viscosity of an IL is of great interest due to its effects on the mass transfer efficiency of IL-based extractions [14]. The van der Waals interactions between alkyl chains on cationic species can be used to modulate the viscosity of ILs [49–51]. For example, it has been reported that the viscosity of imidazolium ILs can be increased by increasing the length of the alkyl chain on the imidazolium cation due to the increased van der Waals interactions [49–51]. Likewise, the anionic species can be used to modulate the viscosity of an IL by altering their relative basicity and ability to participate in hydrogen bonding [52]. Holding alkyl chain length and anion species constant, the viscosity of cationic species increases as follows: $[Im]^+ < [Py]^+ < [Pyrr]^+$ [52]. Analogously, increasing the viscosity of the anionic species in the following order can increase the viscosity of imidazolium-based ILs: $[NTf_2]^- < [CF_3SO_3]^- < [BF_4]^- < [EtSO_4]^- < [MeSO_4]^- < [PF_6]^- < [CH_3COO]^-$ [52].

Alternatively, it has been demonstrated that increasing the alkoxy chain length of a cation species decreases the viscosity of an IL [39, 40, 53–62]. Kuhlmann and colleagues reported that increasing the chain length of a series of ethylene glycol-functionalized imidazolium cations decreased the viscosity of the corresponding ILs [56]. Moreover, Zhou and co-workers reported that the viscosity of quaternary ammonium ILs was reduced when alkyl chains were replaced with alkoxy chains [40]. While both alkyl and alkoxy chains on cationic species of ILs can aggregate into micelle-like structures, alkoxy chains are less prone to aggregation due to the higher ionic mobility of alkoxy species [56].

The viscosity of an IL is heavily influenced by temperature [14]. Specifically, an increase in temperature leads to an increase in the Brownian motion of the constituent molecules of an IL [39]. Okoturo et al. investigated the temperature dependence of IL viscosity and observed that ILs containing un-functionalized asymmetric cations typically obeyed the Arrhenius law [56]. On the other hand, the majority of ILs containing small, symmetric cations with low molar masses obeyed the Vogel-Tammann-Fulcher laws [56]. ILs that obeyed neither the Arrhenius law nor the Vogel-Tammann-Fulcher laws generally contained functionalized asymmetric cations with higher molar masses [56].

As would be expected, the presence of water [57–59] and organic solvents [60] decreases the viscosity of an IL. For example, it has been reported that the addition of water molecules decreased the viscosity of $[C_4mim][PF_6]$ by an order of magnitude [61]. Similarly, as the viscosity of $[C_2mim]^+$ ILs decreased, the mole fraction of solute water molecules increased [61]. This effect was most noticeable at low water concentrations where even slight increases led to dramatic variations in viscosity [62]. Moreover, nonpolar solutes have been reported to lower the concentration of $[C_2mim][NTf_2]$ ILs more than equal concentrations of water [63]. This is because the mixing of ILs and neutral solvents weakens the strong Coulombic interactions between ions, allowing for higher ion mobility [64]. Chloride impurities, on the other hand, dramatically increase the viscosity of imidazolium ILs because the hydrogen bonding between the chloride species and the protons on the imidazolium rings strongly enhances the cohesive forces in ILs [57].

The formation of eutectic mixtures is a key strategy to reduce the viscosity of ILs. In the literature, it is commonplace to form eutectic mixtures by adding molecular solvents to ILs. For example, Fox, Borodin, and co-workers examined the effects of adding three molecular solvents—propylene carbonate (PC), dimethyl carbonate (DMC), and acetonitrile (AN)—to an IL, *N*-methyl-*N*-pentylpyrrolidinium bis(trifluoromethanesulfonyl) imide ($PY_{15}TFSI$) via experimental measurements [65] and molecular dynamics simulation [66]. The Einstein relation was used to compute the viscosity of the experimentally and computationally characterized $PY_{15}TFSI$-solvent mixtures [66]. A plot of the simulated and experimental viscosity by solvent mole fraction can be observed in Fig. 3.3a [66]. As indicated in Fig. 3.3a, the viscosity of $PY_{15}TFSI$-PC mixtures is greater than the viscosity of $PY_{15}TFSI$-DMC and $PY_{15}TFSI$-AN mixtures [66]. Moreover, as would be anticipated, the increase in the viscosity of $PY_{15}TFSI$-solvent mixtures was correlated to the increase in the viscosity of the pure solvents [65].

Additionally, Fox, Borodin, and co-workers used a binary mixture viscosity (η_m) formula popularized by Grunberg and Nissan [67], to solve for the viscosity interaction parameter (G_{ij}) of each system. It is important to consider the variation

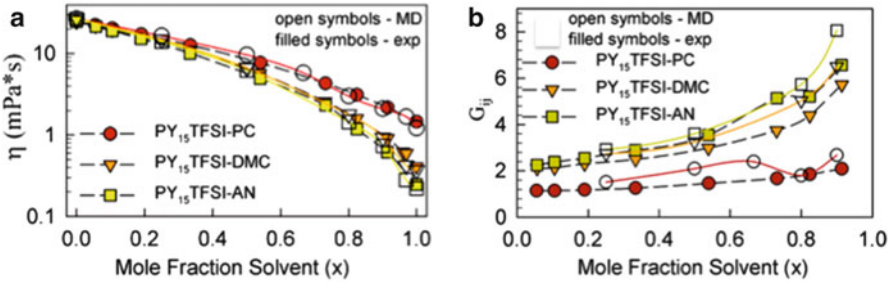

Fig. 3.3 (**a**) Variation of viscosity and (**b**) viscosity interaction parameter of $PY_{15}TFSI$-solvent mixtures by solvent mole fraction. Both MD simulation data and experimental data are represented (Reprinted with permission from Ref. [66]. Copyright 2013 American Chemical Society)

of G_{ij} by solvent mole fraction because it expresses the extent of the nonideality of the system [67] by quantifying the rise in interchange energy due to the increase in the lattice activation energy of solvent 2 due to the juxtaposition of solvent 1 molecules [68]. Moreover, with additional formula manipulation, $x_1x_2G_{ij}$ can be related to the molar Gibbs free energy of activation of the flow process by the Eyring absolute rate theory [69]. A plot of the relationship between the G_{ij} of each PY_{15}TFSI-solvent mixture and its respective solvent mole fraction can be found in Fig. 3.3b [66]. The smallest G_{ij} values were obtained for PY15TFSI-PC mixtures, and the greatest G_{ij} values were obtained for PY15TFSI-AN mixtures [66]. Moreover, as conveyed in Fig. 3.3b, the G_{ij} values of each PY_{15}TFSI-solvent mixture increased with increasing solvent mole fraction [66]. This behavior can be attributed to an increase in ion-solvent contacts due to the filling of the ion's first coordination shell [66].

3.3.3 Solubility and Degradation

Decreasing the solubility of ILs in water and organic solvents is an important aspect of designing IL-based extraction systems [14]. Industrial-scale liquid-liquid extractions will incur significant losses to waste water if the IL has any measureable solubility in water [70]. The miscibility of ILs in water is a consequence of the strength of the interaction between water molecules and ions; this is largely influenced by the size of the ion [71]. Interactions between water molecules and smaller ions are much stronger than interactions between water molecules and larger ions due to the localized ionic charge of small ions [71]. A second factor that influences the strength of water-ion interactions is the magnitude of the coordination between the charges on ionic surface atoms and surface water molecules [71]. As such, the activity coefficients of ILs in water can be split into contributions: the cationic contribution and the anionic contribution [72]. The miscibility of an IL in water is more heavily influenced by the associated anionic species [58]. In other words, the anionic species has the primary effect on water miscibility, and the cationic species has a secondary effect on water solubility [58]. In light of this information, a scale of hydrophobicity of common ionic species has been tabulated, in increasing order: Br^-, $Cl^- < [BF_4]^- < [PF_6]^- < [NTf_2]^- < [BETI]^-$ [70]. Likewise, the variation of water content in a number of imidazolium, pyrrolidinium, ammonium, and phosphonium ILs has been attributed to the identity of the anionic species; the following hydrophobic trend was observed: halides $< [OTf]^- < [BF_4]^- < [PF_6]^- < [NTf_2]^- < [FAP]^-$ [54]. Moreover, the acidity of a solution of water greatly impacts the solubility of an IL [73]. For example, when the solubility of $[A336][NO_3]$ in nitric acid systems was investigated by Sun et al. [73], it was noted that the solubility of the $[A336]^+$ species decreased noticeably as the acidity of the system increased due to the nitrate ion depressing the loss of $[A336]^+$ species [73]. Additionally, the alkyl chain length on cationic

species can influence the miscibility of ILs in water [70, 74]. Specifically, the solubility of an IL decreases the alkyl chain length as the cationic species increases due to the increased hydrophobicity of the IL [5, 74]. For example, it has been reported that the solubility of $[C_n\text{mim}][PF_6]$ ILs decreases monotonically as the 1-alkyl group on the cationic $[C_n\text{mim}]^+$ species was lengthened [70, 74, 75].

Alternatively, the miscibility of water and $[C_4\text{mim}][NTf_2]$ can be decreased by adding inorganic salts to either solvent [14]. Specifically, while at low concentrations an inorganic salt can lead to a salting-in of an IL, at increasing concentrations, inorganic salts can lead to the salting-out of an IL [76]. The salting-out of an IL by an inorganic salt at high concentrations is a consequence of the formation of hydration complexes and an increase in cavity surface tension, while the salting-in effect of an IL by an inorganic salt at low concentrations is a consequence of the direct ionic binding of low-charge-density ions to hydrophobic moieties of the solute [76]. As such, it was observed that the solubility of $[C_2\text{mim}][NTf_2]$ first increased and then decreased upon the addition of NaCl and KCl to solution [70]. The $[C_2\text{mim}][NTf_2]$ IL began to precipitate out of solution once a threshold salt concentration was reached [70]. This phenomenon is of great interest because it can facilitate the usage of ILs in high-ionic-strength applications [77]. Moreover, the salting-out effect can be used to enhance an IL during an aqueous-phase separation [77]. The influence of inorganic salts on the solubility of $[C_4\text{mim}]$ [tricyanomethane] in aqueous solutions has been widely documented and has been used to derive a salting-in and salting-out mechanism [78]. It has been noted that interactions between the anionic species of an inorganic salt not only influence the cationic species of an IL but the anionic species as well [78]. The observed solubility of an IL in an aqueous solution containing an inorganic salt is a direct consequence of a balance between these two kinds of interactions with the anionic species of the inorganic salt in aqueous solution [78].

As stated earlier, understanding the phase behavior of ILs and organic solvents is an essential aspect of designing IL-based extractions. It has been reported that the solubility of an IL in organic solvents can be decreased by increasing the alkyl chain length of an alcohol or an alkyl substituent of a benzene ring [79]. However, increasing the alkyl chain length of $[C_n\text{mim}][NTf_2]$ ILs increased the mutual solubility of $[C_n\text{mim}][NTf_2]$ ILs with benzene and toluene [72]. This is a consequence of the fact that the solubility of an IL is highly contingent upon its ability to form the conventional interactions with potential organic solvents, such as hydrogen bonds, dipole-dipole interactions, and van der Waals interactions [80]. However, ILs have strong ionic interactions, such as mutual electrostatic attraction or repulsion of charged cationic and anionic species [80]. These ionic interactions make ILs more prone to miscibility with polar substances [80]. For example, an increase in the alkyl chain length of aliphatic hydrocarbons decreases the solubility of trihexyl(tetradecyl)phosphonium (P_{66614}) chloride [81]. This effect is a consequence of the fact that shorter alkyl chain length of alkane solvents facilitates their accommodation in the hydrophobic region of the alkyl side chains of ILs [81].

The degradation of ILs is another essential safety aspect of ILs that needs to be considered. Biodegradation pathways for imidazolium [82, 83] and pyridinium [84]

ILs have been reported in the literature. Interestingly enough, it has been noted in the literature that the more eco-toxicologically sound cationic species containing shorter, functionalized alkyl side chains are more difficult to degrade [85]. Moreover, the IL biodegradation products are documented to be less toxic than their IL precursors in standard aquatic organism tests [86]. Furthermore, the biodegradability of an IL exhibits far less dependence on the anionic species than the cationic species [86]. For example, the degradation of *N*-ethylpyridinium IL by soil microorganisms was unaffected by the $[BF_4]^-$ and $[CF_3COO]^-$ anionic species [86]. In addition, a variety of chemical degradation methods have been reported. For example, the $[C_4mim]^+$ cation can be completely degraded via electrolysis [85]. Moreover, it has been reported that alkyl imidazolium and pyridinium ILs can be completely degraded with hydrogen peroxide [87]. However, substituting an alkyl-imidazolium IL at the 1-N position is more likely to increase the resistance of the IL to degradation by hydrogen peroxide [87]. Similarly, pyridinium analogs of imidazolium ILs are more resistant to degradation by hydrogen peroxide than their corresponding imidazolium IL [87]. The mechanism for the degradation of imidazolium ILs by hydrogen peroxide entails the attack of one of the three ring carbon atoms by OH• radicals [88]. Finally, a number of photodegradation methods for ILs have been reported as well, and we will discuss a few of them. Katoh et al. investigated the photodegradation of $[C_4mim][NTf_2]$ by UV-laser irradiation [89]. They observed that excited state cationic species $[C_4mim^+]^*$ degraded much more efficiently than the relatively stable neutral radical species $[C_4mim•]^*$ [89]. Moreover, H_2O_2/UV systems are far more effective at degrading imidazolium ILs than UV or UV/TiO_2 systems [90]. Furthermore, the H_2O_2-enhanced photodegradation of imidazolium ILs is highly dependent on the length of the alkyl chain; the following trend was observed: $[C_4mim]^+ < [C_6mim]^+ < [C_8mim]^+ < [Eeim]^+$ [90].

3.4 Recycling Rare-Earth Elements with Ionic Liquid-Based Extractants

3.4.1 Solvent Extraction Separation of La^{3+} and Ba^{2+}

As discussed in the introduction, there is a great interest in recycling REE such as La^{2+} due to their limited availability on the global market [1]. However, there is even greater interest in understanding the chemistry of separating La^{3+} from Ba^{2+} because they serve as cold surrogates for the radioactive Ac^{3+} and Ra^{2+}, respectively [91, 92]. Ac^{3+} and Ra^{2+} as two radioactive isotopes are the subject of great interest in the literature due to their potential application as short-range and site-specific treatment of cancers and micrometastatic disease [91, 92]. ILs are ideal for separating La^{3+} from Ba^{2+} and, consequentially, Ac^{3+} from Ra^{2+} because not only do ILs function as diluents but they are also intimately involved in the separation process via ion-exchange mechanisms and unique solvation interactions [93, 94]. In

this section, we will discuss two IL-based solvent extraction systems that have been applied to this separation process: superbase-β-diketone-derived PILs [91] and *N,N,N',N'*-tetra(*n*-octyl)diglycolamide (TODGA) [92].

β-Diketones have been widely utilized in the literature as ligands in metal ion extractions into conventional organic solvents, particularly in actinide and lanthanide separations [92]. Furthermore, an aprotic IL consisting of hexafluoroacetylacetone anions (hfacs) that is immiscible with water has been reported to be highly effective at extracting Nd^{3+}, Cu^{2+}, and Co^{2+} [95]. However, the synthesis of this IL is quite involved, entailing a multistep process including anion metathesis of an IL halide salt and ammonium hfca [95]. Alternatively, Gupta et al. [96, 97] and Li et al. [98] reported a method for synthesizing PILs utilizing β-diketones and tertiary amines, entailing a simple single pot neutralization reaction. Yet, none of the ILs synthesized by this method have been applied to extraction processes. However, Jensen and colleagues have reported a method for extracting lanthanide elements using β-diketones via imidazolium ILs [99]. Specifically, the authors employed 2-thenoyltrifluoroacetone (Htta) as an extractant in $[C_4mim][NTf_2]$ and demonstrated that Eu^{3+} forms a 1:4 complex with tta ligands, which, consequentially, facilitates the extraction of anionic complexes via an anion exchange process [99]. As such, we tested the β-diketones PILs by employing them as ion extractants for La^{3+} and Ba^{2+} extractions in common ionic liquids such as $[C_4mim][NTf_2]$ [91]. The common ionic liquids are utilized as diluents in these extraction processes [100]. The structures of the starting superbases and β-diketones of the PIL extractants and the common IL utilized as diluents are listed in Fig. 3.4 [91].

We performed our extraction experiments by contacting 0.5 mL of IL containing a certain concentration of PIL extractant with 5 mL of aqueous solution containing 0.65 mM each of $La(NO_3)_3$ and $Ba(NO_3)_2$ in a vibrating mixer for 60 min [91]. Afterward, the phases were disengaged by 10 min of centrifugation. Following centrifugation the upper aqueous phase was separated, and the metal ion concentrations were determined by ICP-AES [91].

In total, seven PILs based on five organic superbases and two β-diketones, illustrated in Fig. 3.4, were investigated as ionic extractants for La^{3+} and Ba^{2+} solvent extractions in the aprotic IL $[C_4mim][NTf_2]$ [91]. The La^{3+} and Ba^{2+}

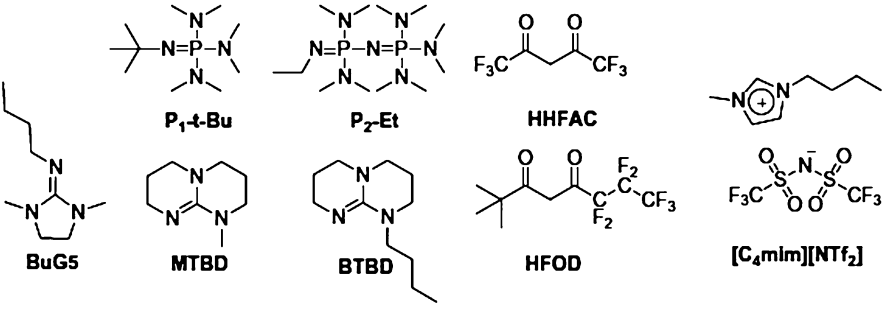

Fig. 3.4 Structures of superbase and β-diketone precursors for PIL extractants and IL diluent (Reprinted with permission from Ref. [91]. Copyright 2014 Elsevier Ltd)

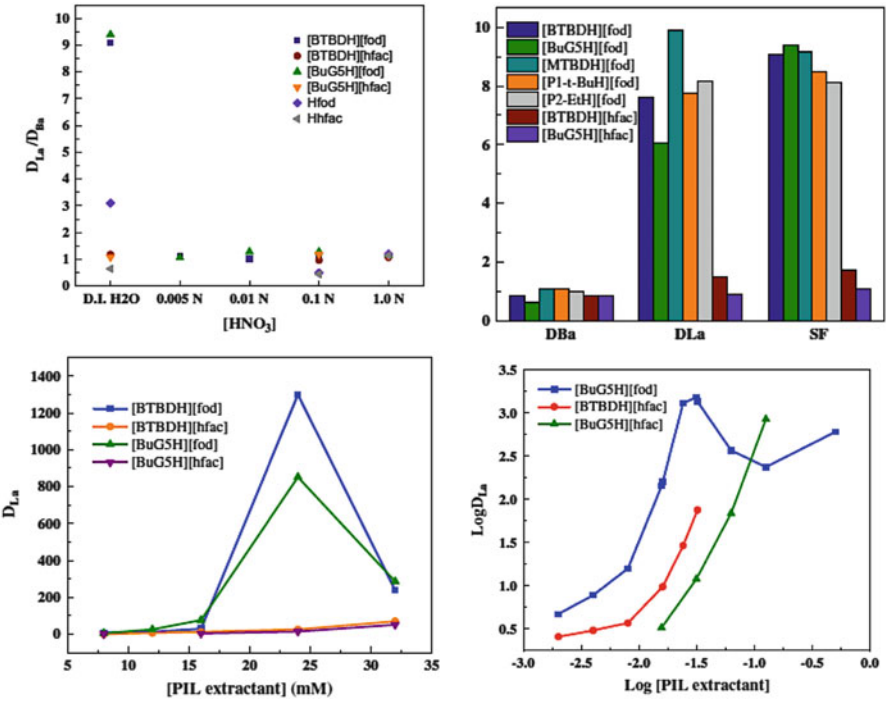

Fig. 3.5 (*Top left*) Dependence of the La^{3+}/Ba^{2+} separation factor of 8 mM extractants in [C_4mim][NTf_2] as a function of aqueous phase acidity (0.65 mM La^{3+}/Ba^{2+}). (*Top right*) Dependence of D_{Ba}, D_{La}, and *SF* of 8 mM extractants in [C_4mim][NTf_2] as a function of PIL extractant structure with D.I. H_2O solution (0.65 mM La^{3+}/Ba^{2+}). (*Bottom left*) Dependence of D_{La} on PIL extractant concentration in [C_4mim][NTf_2] with D.I. H_2O solution (0.65 mM La^{3+}/Ba^{2+}). (*Bottom right*) $LogD_{La}$ vs log [PIL extractant] in [C_4mim][NTf_2], with D.I. H_2O solution (0.43 mM La^{3+}/Ba^{2+}) (Reprinted with permission from Ref. [91]. Copyright 2014 Elsevier Ltd)

distribution ratios D_{La} and D_{Ba}, respectively, and the separation factor *SF* of each system measured by the extraction experiments are plotted in Fig. 3.5 [91]. *SF* is plotted as a function of the acidity of the aqueous phase in the top left plot in Fig. 3.5 [91]. As conveyed in the plot, as the acidity of the aqueous phase increased, the value of D_{La} significantly decreased; consequentially, so did *SF*. The dependence of D_{Ba}, D_{La}, and *SF* on PIL structure in 0.65 mM solution of La^{3+} and Ba^{2+} in D.I. water is revealed in the top right plot in Fig. 3.5 [91]. The extraction efficiency of La^{3+} was primarily impacted by the anionic component of the PIL; the cationic component, on the other hand, exerted very little influence [103]. Furthermore, as conveyed in the bottom plots in Fig. 3.5, [hfac]- and [fod]-based PIL extractants demonstrated different extraction efficiency trends [91]. Specifically, as the concentration of [hfac] PIL extractants increased, so did D_{La} and *SF*; this is conveyed in the bottom left plot in Fig. 3.5 [91]. However, as the concentration of [fod] increased, D_{La} and *SF* increased to reach a maximum value and then decreased as the concentration increased; this is illustrated in both bottom plots in Fig. 3.5 [91].

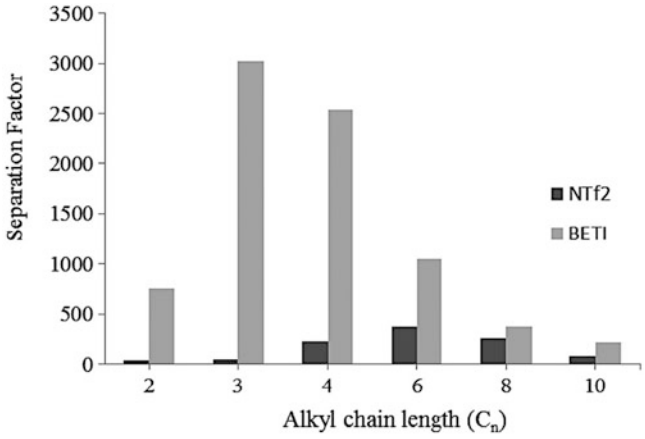

Fig. 3.6 Comparison of the SF of ILs containing NTf_2 and BETI anions in terms of the alkyl chain length of the cationic species (Reprinted with permission from Ref. [92]. Copyright 2012 Taylor & Francis)

As stated earlier, we have applied TODGA to the process of separating La^{3+} from Ba^{2+} [92]. Now we review the separation performance of TODGA in ILs in this section [92]. We investigated TODGA in ILs for separating La^{3+} from Ba^{2+} because it has been demonstrated in the literature that TODGA is an effective lanthanide and actinide extractant in liquid-liquid extraction systems [100–102]. As such, we applied it to the process of separating La^{3+} from Ba^{2+} by dissolving it in a series of $[C_n\text{mim}][NTf_2]$ or $[C_n\text{mim}][\text{BETI}]$ ILs ($n = 2, 4, 6, 8, 10$) [92]. The extraction experiments performed on the TODGA were identical to the extraction experiments carried out on the PILs in $[C_4\text{mim}][NTf_2]$ discussed earlier; however, 0.43 mM each of $La(NO_3)_3$ and $Ba(NO_3)_2$ was used instead [92]. A comparison of the *SF* of 14 mM TODGA in $[C_n\text{mim}][NTf_2]$ and that in $[C_n\text{mim}][\text{BETI}]$ as a function of alkyl chain length can be found in Fig. 3.6 [92]. In both cases the *SF* sharply increased with alkyl chain length until an optimal length was achieved and then began to sharply decrease as the length of the alkyl chain increased further [92]. For $[C_n\text{mim}][NTf_2]$, the optimal alkyl chain is six carbons long, while as for [BETI] ILs the optimal alkyl chain is three carbons long [92]. Moreover, as conveyed in Fig. 3.6, the best results were obtained with the 14 mM TODGA in $[C_3\text{mim}][\text{BETI}]$ systems [92].

3.4.2 TALSPEAK-Like Extraction of REEs with Task-Specific ILs

Originally developed in the 1960s at Oak Ridge National Laboratory, the trivalent actinide lanthanide separation by phosphorus-reagent extraction from aqueous

complexes (TALSPEAK) process has been used to separate minor actinides from rare-earth fission products [103–105]. The TALSPEAK method entails using diethylenetriamine-*N*,*N*,*N'*,*N''*,*N''*-pentaacetic acid (DTPA) as a complexing agent to selectively retain actinides, thus facilitating REE extraction into diisopropylbenzene (DIPB) solution containing di(2-ethylhexyl)phosphoric acid (HDEHP) [103–105]. While TALSPEAK has been widely utilized in actinide-REE separation processes, it has not been applied as frequently to processes separating REEs from among themselves [106]. We recently demonstrated that the selective extraction of some REEs by TALSPEAK was greatly improved when HDEHP was used as an extractant in ILs in place of DPIB [107]. However, the lower solubility of HDEHP in ILs was a challenge in IL-based TALSPEAK processes [107]. Therefore recently we synthesized three new TSILs containing di(2-ethylhexyl)phosphate (DEHP) as anion hoping better solubility in ILs [106]. While the majority of TSILs bear their functionality on their cationic species, we decided to investigate DEHP-based ILs in which the anionic species bear the functionality [106]. Three task-specific ionic liquids (TSILs), tetrabutylammonium di(2-ethylhexyl)phosphate ([TBA][DEHP]), trioctylmethylammonium di(2-ethylhexyl)phosphate ([TOMA][DEHP]), and trihexyl(tetra-decyl)phosphonium di(2-ethylhexyl)phosphate ([THTP][DEHP]), are investigated for REE separation in [C_6mim][NTf_2] and DIPB along with HDEHP [106]. The solubilities of the DEHP-based ionic extractants in [C_6mim][NTf_2] are much better than that of HDEHP in [C_6mim][NTf_2] [106]. The structures of the components used in this IL-based TALSPEAK process are illustrated in Fig. 3.7 [106].

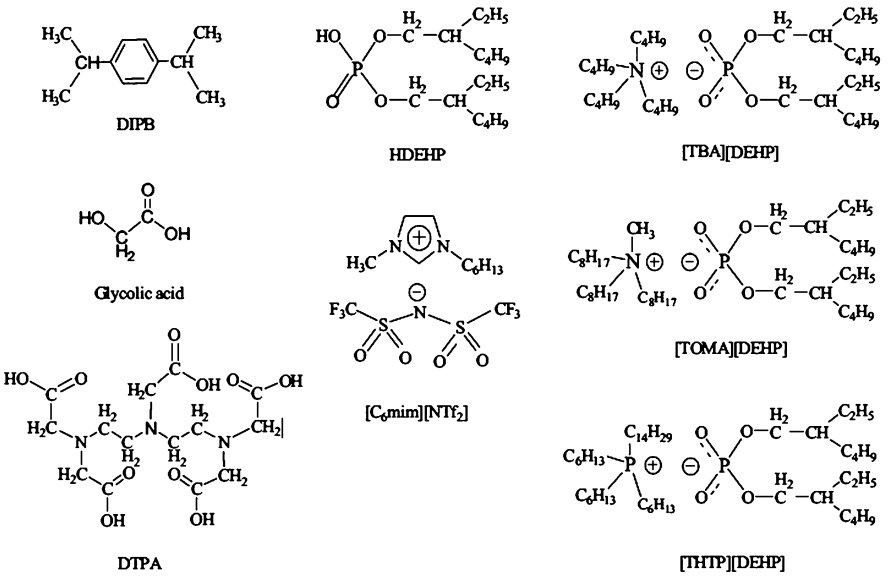

Fig. 3.7 Structures of the components used in the IL-based TALSPEAK processes for separations of REEs (Reprinted with permission from Ref. [106]. Copyright 2012 Elsevier Ltd)

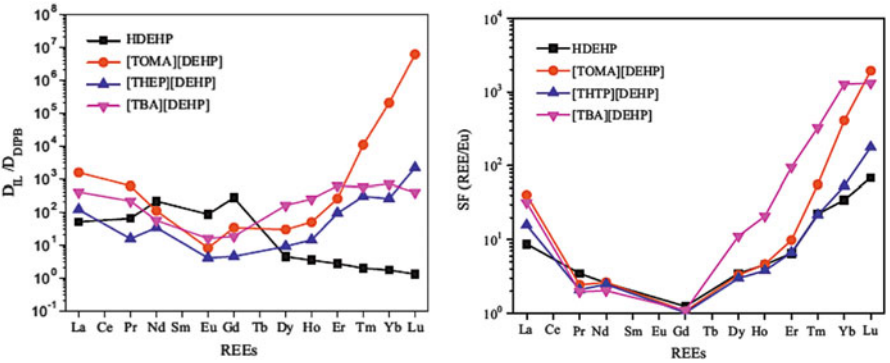

Fig. 3.8 (*Left*) Ratio of distribution of each REE by extractant in $[C_6mim][NTf_2]$ versus DIPB. (*Right*) Separation factor of each REE versus Eu^{3+} using HDEHP, [TBA][DEHP], [TOMA][DEHP], and [THTP][DEHP] in $[C_6mim][NTf_2]$. For both *left* and *right:* HDHEP = [TBA][DEHP] = [TOMA][DEHP] = [THTP][DEHP] = 0.8 M, REE^{3+} = 0.7 mM, DTPA = 0.1 M, glycolic acid = 1.0 M (Reprinted with permission from Ref. [106]. Copyright 2012 Elsevier Ltd)

The extraction experiments were carried out in a similar manor to the extraction experiments described in Sect. 3.4.1. We observed that the novel TSILs—[TBA][DEHP], [TOMA][DEHP], and [THTP][DEHP]—revealed much higher REE extractabilities in $[C_6mim][NTf_2]$ than in DIPP, as conveyed in Fig. 3.8 [106]. The left plot in Fig. 3.8 demonstrates the ratio of distribution of each REE by extractant in $[C_6mim][NTf_2]$ versus DIPB [106]. It is clear that the distribution ratios of REEs extracted by HDEHP, [TBA][DEHP], [TOMA][DEHP], and [THTP][DEHP] in $[C_6mim][NTf_2]$ are much higher than their respective distribution ratios in DIPB [106]. The high extraction efficiency of HDEHP, [TBA][DEHP], [TOMA][DEHP], and [THTP][DEHP] can be attributed to the "like-dissolves-like" principle; in other words, the ionic extracting complexes formed by REEs and ionic extractants have greater stability and solubility in ILs than in DPIB [107–110]. The right plot in Fig. 3.8 demonstrates the separation factor of each REE versus Eu^{3+} using HDEHP, [TBA][DEHP], [TOMA][DEHP], and [THTP][DEHP] in $[C_6mim][NTf_2]$ [106]. It is clear that the separation factors of [TBA][DEHP], [TOMA][DEHP], and [THTP][DEHP] are larger than those of HDEHP in$[C_6mim][NTf_2]$ [106]. The DEHP extractants exhibited better REE selectivity than HDEHP because of the larger steric hindrance in the cationic species [106].

3.4.3 *Mechanism Study of TALSPEAK-Like Extraction of REEs*

The extraction behavior of [TOMA][DEHP] for REEs in $[C_nmim][NTf_2]$/[BETI] (n = 4, 6, 8, 10) was further investigated here in order to understand which mechanism plays a major role in this IL-based extraction strategy [111]. As can

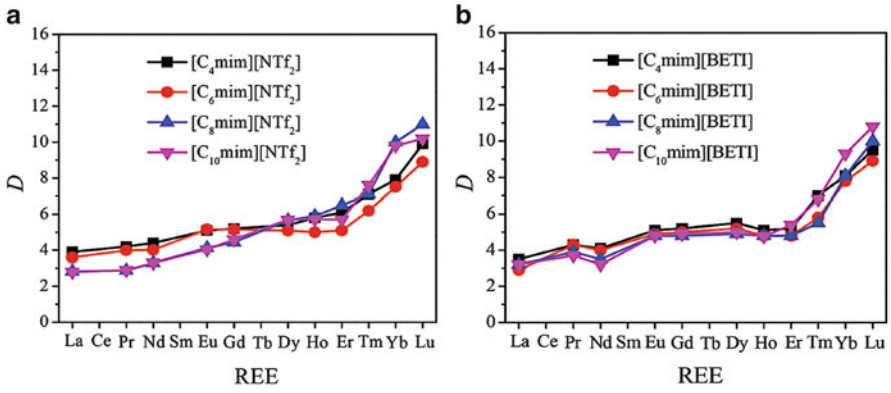

Fig. 3.9 The extraction behaviors of [TOMA][DEHP] in [$C_n$mim][NTf_2]/[BETI] ($n = 4, 6, 8, 10$) for REEs. [TOMA][DEHP] = 0.1 M, REE^{3+} = 0.84 mM for each rare-earth ion (Reprinted with permission from Ref. [111]. Copyright 2013 Royal Society of Chemistry)

be seen in Fig. 3.9, the extraction behaviors of [TOMA][DEHP] in all eight ILs for REEs are very similar, which is quite different from the ion exchange model [111]. It is worth pointing out that light REEs are better extracted in ILs with a shorter carbon chain length cation, and heavy REEs are better extracted in ILs with a longer carbon chain length cation [111]. However, the differences in extraction behaviors by this ionic extractant in all ILs are quite small [111]. The extraction behaviors of [TOMA][DEHP] for REEs are very similar in [$C_n$mim][NTf_2] (Fig. 3.9a) and [$C_n$mim][BETI] (Fig. 3.9b), suggesting that the anion of ILs seems to have minor effect on the extraction of REEs as well [111]. The similar extraction behavior of [TOMA][DEHP] for REEs in [$C_n$mim][NTf_2]/[BETI] indicates that both cation and anion exchanges do not appear to be involved in the mechanism of this IL-based extraction [111].

The additions of $[C_4mim]^+$ or $[NTf_2]^-$/$[BETI]^-$ to the aqueous phase have minor effect on the extraction as illustrated in Fig. 3.10 [111].

Interestingly, as can be seen in Fig. 3.11, the added $[C_{10}mim]^+$ enhanced the extractability of three heavy REEs in the [C_{10}mim][NTf_2]/[BETI]-based system, which can be attributed to the novel kind of salting-out effect [111].

The extraction mechanism of this IL-based extraction is more likely to be of solvation [111]. Even when the carbon chain length in [$C_n$mim][NTf_2]/[BETI] is as long as C_{10}, this IL-based TALSPEAK-like process can offer good separation performance for REEs [111]. The driving force of this IL-based system is mainly ion interaction rather than ion exchange [111]. The results of this study have shown this IL-based extraction to be a highly efficient and sustainable methodology [111].

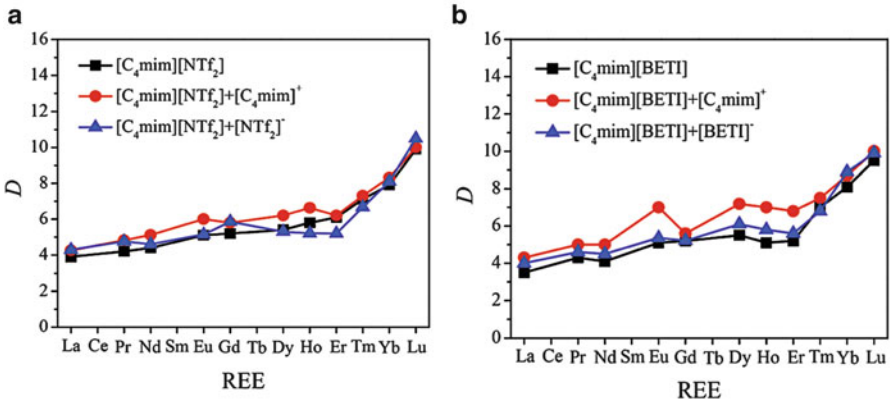

Fig. 3.10 The effect of the addition of $[C_4mim]^+$ and $[NTf_2]^-$/$[BETI]^-$ on $[C_4mim][NTf_2]$/[BETI]-based extraction for REEs. [TOMA][DEHP] = 0.1 M, REE^{3+} = 0.84 mM for each rare-earth ion. $[C_4mim]^+ = [NTf_2]^- = [BETI]^- = 0.05$ M (Reprinted with permission from Ref. [111]. Copyright 2013 Royal Society of Chemistry)

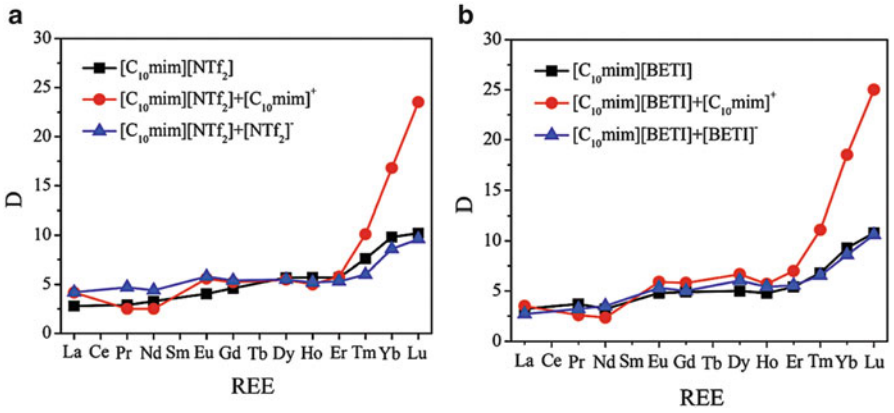

Fig. 3.11 The effect of the addition of $[C_{10}mim]^+$ and $[NTf_2]^-$/$[BETI]^-$ on $[C_{10}mim][NTf_2]$/[BETI]-based extraction for REEs. [TOMA][DEHP] = 0.1 M, REE^{3+} = 0.84 mM for each rare-earth ion.$[C_{10}mim]^+ = [NTf_2]^- = [BETI]^- = 0.05$ M (Reprinted with permission from Ref. [111]. Copyright 2013 Royal Society of Chemistry)

3.4.4 Extracting REEs from Aqueous Solution with Methylimidazole in Ionic Liquids

There are a number of advantageous attributes associated with imidazole, such as its miscibility in water and ILs, for example, imidazolium-based ILs [112–114]. Moreover, the imidazole structure, consisting of a five-membered heterocyclic ring with two N atoms, is amenable to selective coordinate to soft metal cations, such

as REEs and Y [112–116]. In light of these advantageous qualities, we employed imidazole and its derivatives, 1-methylimidazole (1-MIM) and 2-methylimidazole (2-MIM), in REEs and Y extraction from an aqueous phase into imidazolium-based ILs [115]. This was the first time the performance and mechanism of this extraction process have been reported [115]. This characterization entailed the investigation of several experimental parameters, such as (1) the nature of the IL, (2) the nature of the extractant, (3) contact time, (4) aqueous phase pH, and (5) effects of extractant concentration on the extraction behavior of metal ions [115]. Additionally, in order to compare the partitioning behavior of REEs in ILs, the extraction of La^{3+}, Eu^{3+}, and Lu^{3+} with methylimidazole was measured in *n*-pentanol as well [115]. Extraction experiments were carried out in a similar manner to the extraction experiments in Sect. 3.4.1 [115]. The room temperature ILs employed in the extraction of REEs and Y from aqueous solutions were in the absence of any extractant [115]. Shimojo and co-workers observed similar behavior when using an identical set of ILs in lanthanide extractions [116]. However, in the presence of MIM, the *D* values greatly increased [115]. The Lu^{3+} extraction capability in a series of imidazolium ILs as a function of 1-MIM concentration can be found at the top left of Fig. 3.12 [115]. In increasing order, the following trend in extraction capability was observed with increasing 1-MIM concentration: $[C_8mim][NTf_2] < [C_6mim][NTf_2] < [C_2mim][NTf_2]$ [115].

The extraction behavior of La^{3+}, Nd^{3+}, Eu^{3+}, Gd^{3+}, Tm^{3+}, Yb^{3+}, Lu^{3+}, and Y^{3+} was investigated as a function of 1-MIM concentration in order to assess the partitioning behavior of REEs and Y in $[C_4mim][NTf_2]$ [115]. As demonstrated in the top right of Fig. 3.12, the extractability of REEs and Y increases with increasing 1-MIM concentration [115]. This increase is indicative of 1-MIM participation in the extraction process as a component of the extracted species [115]. Moreover, the distribution ratios of the heavy and light REEs vary significantly under the same extraction conditions [115]. The light REEs and Y are poorly extracted at all concentrations of 1-MIM, while the heavy REEs are effectively extracted at increasing concentrations of 1-MIM [115]. Furthermore, the distribution ratios of the heavier REEs rapidly increase as the concentration of 1-MIM increases, while the lighter REEs and Y display slower distribution ratio growth [115], thus splitting the extraction behavior of the REEs into two categories [115]. Additionally, as the 1-MIM concentration increased up to a certain threshold, all metals in the aqueous phase were completely extracted [115].

Likewise, we investigated the partitioning behavior of three REEs, La^{3+}, Eu^{3+}, and Lu^{3+}, representing light, middle, and heavy, respectively, in $[C_4mim][NTf_2]$ as a function of the extractant concentration of either 1-MIM or 2-MIM [115]. These results are plotted in the bottom left plot in Fig. 3.12 [115]. The distribution ratios of Eu^{3+} and Lu^{3+} dramatically increased with increasing 2-MIM concentration. 2-MIM extractants displayed similar REE extraction trends to 1-MIM extractants [115]. However, when compared with the distribution ratios of La^{3+}, Eu^{3+}, and Lu^{3+} with 1-MIM, less 2-MIM was required to achieve the same degree of extraction [115]. Thus, the extraction capabilities of 2-MIM are superior to the extraction capabilities of 1-MIM in the same solvent, $[C_4mim][NTf_2]$ [115]. While 2-MIM

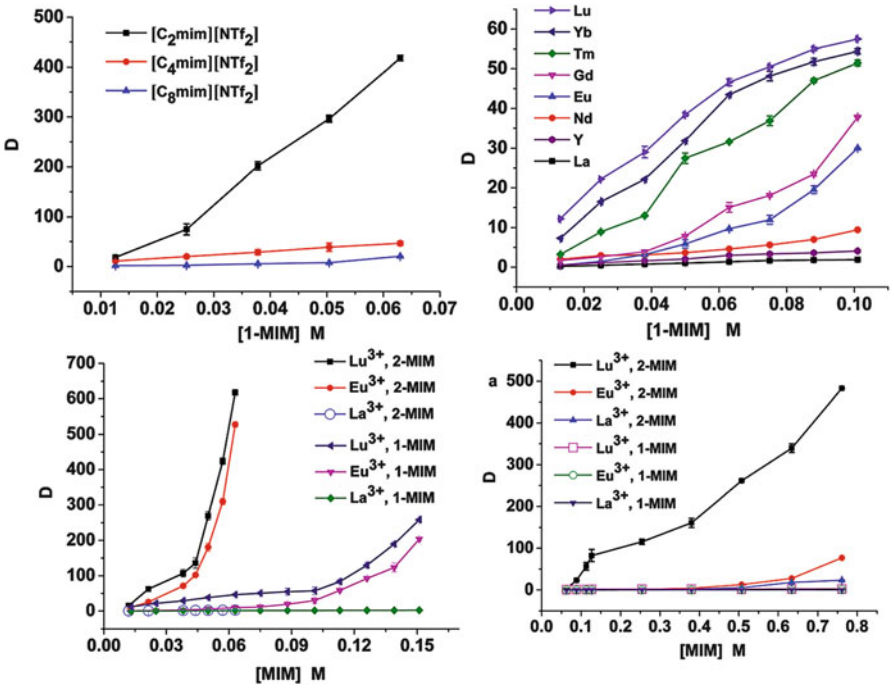

Fig. 3.12 (*Top left*) The distribution ratios of Lu^{3+} from the aqueous phase to the IL phase ($[C_n mim][NTf_2]$) as a function of 1-MIM concentration in the IL phase. (*Top right*) The distribution ratios of REE^{3+} from the aqueous phase to the IL phase ($[C_4mim][NTf_2]$) as a function of 1-MIM concentration in the IL phase. (*Bottom left*) The distribution ratios of Lu^{3+}, Eu^{3+}, and La^{3+} from the aqueous phase to the IL phase ($[C_4mim][NTf_2]$) as a function of the MIM concentration in the IL phase. (*Bottom right*) The distribution ratios of Lu^{3+}, Eu^{3+}, and La^{3+} from the aqueous phase to the *n*-pentanol phase as a function of the MIM concentration in the *n*-pentanol phase (Reprinted with permission from Ref. [115]. Copyright 2014 Royal Society of Chemistry)

and 1-MIM are isomers, 2-MIM is the superior extractant because there is an N-H bond in the imidazole ring of 2-MIM. There have been numerous reports demonstrating the stabilizing effect of ligand interactions, hydrogen bonding in particular, between ligands in the outer coordination spheres of metal cations [104, 117–119]. Consequentially, the observed strength and metal cation selectivity of these extractants have been attributed to these ligand interactions [115]. As such, the N-H bond in the imidazole rings of 2-MIM extractants is likely responsible for the high extraction efficiency observed in the bottom left plot in Fig. 3.12 [115].

In order to compare the partitioning behavior of REEs in ILs, the extraction of La^{3+}, Eu^{3+}, and Lu^{3+} with MIM were measured in *n*-pentanol as well [115]. These results are plotted in the bottom right plot in Fig. 3.12 [115]. The REE extraction ability in *n*-pentanol increased with increasing 2-MIM concentration; however, no REE extraction was observed with 1-MIM extractants in *n*-pentanol

[115]. Moreover, the extraction ability of 2-MIM in *n*-pentanol was lower than its extraction ability in ILs we tested [115]. Regardless, a similar extraction trend was observed, in that the lighter REEs were poorly extracted and the heavier REEs were extracted much more efficiently [115], thus demonstrating that 2-MIM provides better selectivity for heavy REEs [115].

3.5 Conclusions

Several ionic liquid-based extraction systems for the separation of and recycling rare-earth elements (REEs) have been reviewed in this chapter. There is a great interest in applying ILs to the REE recycling process [14]. However, before IL-based extractions of REEs can be carried out on an industrial scale, there are certain IL factors that need to be considered comprehensively, such as cost, purity, acidity stability, viscosity solubility, density, electrical conductivity, electrochemical windows, extraction efficiency, selectivity, extraction mechanism, stripping ratio, and methods of recycling [14]. The continuing studies in the above areas are warranted.

TSILs have been a major aspect of the advent of IL-based extractants [14]. Thus, as the IL-based extractant technology continues to develop, TSILs will become increasingly important [14]. In addition to enhancing the extractability and selectivity of ILs, the functional groups on the cationic and anionic species of TSILs provide excellent physiochemical properties for extraction as well [14]. While TSILs bearing cationic functionalities have been widely investigated in the literature, TSILs bearing anionic functionalities have not been extensively investigated [14]. However, TSILs with anionic functionalities can be an advantageous design strategy for extracting REEs because it facilitates design from a Coulombic interaction paradigm [14].

Additionally, the majority of IL-based extraction investigations have characterized the thermodynamic properties of extraction [14]. However, extraction kinetics and interfacial activity studies are essential to further develop IL-based extractants [14]. Extraction approaches based on the kinetics of extraction may allow for the separation of metal ions that cannot be separated at equilibrium [14]. Moreover, investigations of the interfacial activities of IL extractants can lead to the elucidation of essential parameters, such as parameters for controlling extraction reactions and mass transport kinetics that will improve our understanding of IL-based extractions [14].

Finally, small-scale industrial tests of IL-based extractants need to be implemented because these tests will reveal challenges that are not present on a smaller scale [14]. Consequentially, this will lead to a deeper understanding of the design paradigms that should be applied to the development of IL-based extractants for REE recycling [14].

References

1. Binnemeans K, Jones PT, Blanpain B, Van Gerven T, Yang YX, Walton A, Buchert M (2013) Recycling of rare earths: a critical review. J Clean Prod 51:1–22
2. European Commission (2010) Critical raw materials for the EU, Report of the Ad-hoc working group on defining critical raw materials
3. U.S. Department of Energy (2011) 2011 critical materials strategy
4. Alonso E, Sherman AM, Wallington TJ, Everson MP, Field FR, Roth R, Kirchain RE (2012) Evaluating rare earth element availability: a case with revolutionary demand from clean technologies. Environ Sci Technol 46:3406–3414
5. Jones PT, Van Gerven T, Van Ackert K, Geysen D, Binnemans K, Fransaer J, Blanpain B, Mishra B, Apelian D (2011) Characterization and modeling of heterogeneous deformation in commercial purity titanium. JOM 63:66–73
6. Wellens S, Goovaerts R, Möller C, Luyten J, Thijs B, Binnemans K (2013) A continuous ionic liquid extraction process for the separation of cobalt from nickel. Green Chem 15:3160–3164
7. Rout A, Karmark S, Venkatesan KA, Srinivasan TG, Vasudeva Rao PR (2011) Room temperature ionic liquid diluent for the mutual separation of europium(III) from americium (III). Sep Purif Technol 81:109–115
8. Bell TJ, Ikeda Y (2011) The application of novel hydrophobic ionic liquids to the extraction of uranium(VI) from nitric acid medium and a determination of the uranyl complexes formed. Dalton Trans 40:10125–10130
9. Papaiconomou N, Génand-Pinaz S, Leveque JM, Guittonneau S (2013) Selective extraction of gold and platinum in water using ionic liquids. A simple two-step extraction process. Dalton Trans 42:1979–1982
10. Han XX, Armstrong DW (2007) Ionic liquids in separations. Acc Chem Res 40:1079–1086
11. Reyna-González JM, Torriero AAJ, Siriwardana AI, Burgar IM, Bond AM (2011) Extraction of silver(I) from aqueous solutions in the absence and presence of copper(II) with a methimazole-based ionic liquid. Analyst 136:3314–3322
12. Heitzman H, Young B, Rausch D, Rickert P, Stepinski D, Dietz M (2006) Fluorous ionic liquids as solvents for the liquid–liquid extraction of metal ions by macrocyclic polyethers. Talanta 69:527–531
13. Hallett JP, Welton T (2011) Room-temperature ionic liquids: solvents for synthesis and catalysis. 2. Chem Rev 111:3508–3576
14. Sun XO, Luo HM, Dai S (2012) Ionic liquids-based extraction: a promising strategy for the advanced nuclear fuel cycle. Chem Rev 112:2100–2128
15. Visser AE, Swatloski RP, Reichert WM, Mayton R, Sheff S, Wierzbicki A, Davis JJH, Rogers RD (2001) Task-specific ionic liquids for the extraction of metal ions from aqueous solutions. Chem Commun 135–136
16. Chiappe C, Pomelli CS (2014) Point-functionalization of ionic liquids: an overview of synthesis and applications. Eur J Org Chem 6120–6139
17. Mohapatra PK, Sengupta A, Iqbal M, Huskens J, Verboom W (2013) Highly efficient diglycolamide-based task-specific ionic liquids: synthesis, unusual extraction behaviour, irradiation, and fluorescence studies. Chem Eur J 19:3230–3238
18. Rout A, Binnemans K (2014) Solvent extraction of neodymium(III) by functionalized ionic liquid trioctylmethylammonium dioctyl diglycolamate in fluorine-free ionic liquid diluent. Ind Eng Chem Res 53:6500–6508
19. Angell CA, Ansari Y, Zhao ZF (2012) Ionic liquids: past, present and future. Faraday Discuss 154:9–27
20. Yoshizawa M, Xu W, Angell CA (2003) Ionic liquids by proton transfer: vapor pressure, conductivity, and the relevance of ΔpKa from aqueous solutions. J Am Chem Soc 125:15411–15419
21. Bell JR, Luo HM, Dai S (2011) Superbase-derived protic ionic liquids with chelating fluorinated anions. Tetrahedron Lett 52:3723–3725

22. Earle MJ, Gordon CM, Plechkova NV, Seddon KR, Welton T (2007) Decolorization of ionic liquids for spectroscopy. Anal Chem 79:758–764
23. Burrell AK, Del Sesto RE, Baker SN, McCleaskey TM, Baker GA (2007) The large scale synthesis of pure imidazolium and pyrrolidinium ionic liquids. Green Chem 9:449–454
24. Nockermann P, Binnemans K, Driesen K (2005) Purification of imidazolium ionic liquids for spectroscopic applications. Chem Phys Lett 415:131–136
25. Baiker A, Anderson JM, Jutz F (2010) Purification of ionic liquids by supercritical CO_2 monitored by infrared spectroscopy. J Supercrit Fluids 55:395–400
26. Ren SH, Hou YC, Wu WZ, Liu WN (2010) Purification of ionic liquids: sweeping solvents by nitrogen. J Chem Eng Data 55:5074–5077
27. Gardas RL, Coutinho JAP (2009) Group contribution methods for the prediction of thermophysical and transport properties of ionic liquids. AIChE J 55:1274–1290
28. Wang CM, Luo HM, Li HR, Dai S (2010) Direct UV-spectroscopic measurement of selected ionic-liquid vapors. Phys Chem Chem Phys 12:7246–7250
29. Stark A, Behrend R, Braun O, Muller A, Ranke J, Ondruschka B, Jastorff B (2008) Purity specification methods for ionic liquids. Green Chem 10:1152–1161
30. Zaitsau DH, Kabo GJ, Strechan AA, Paulechka YU, Tschersich A, Verevkin SP, Heintz A (2006) Experimental vapor pressures of 1-alkyl-3-methylimidazolium Bis(trifluoromethylsulfonyl)imides and a correlation scheme for estimation of vaporization enthalpies of ionic liquids. J Phys Chem A 110:7303–7306
31. Luo HM, Barker GA, Lee SJ, Pagni RM, Dai S (2009) Ultrastable superbase-derived protic ionic liquids. J Phys Chem B 113:4181–4183
32. Emel'yanenko VN, Vervkin SP, Heintz A (2007) The gaseous enthalpy of formation of the ionic liquid 1-butyl-3-methylimidazolium dicyanamide from combustion calorimetry, vapor pressure measurements, and Ab initio calculations. J Am Chem Soc 129:3930–3937
33. Armstrong JP, Hurst C, Jones RG, Licence P, Lovelock KRJ, Satterley CJ, Villar-Garcia IJ (2007) Vapourisation of ionic liquids. Phys Chem Chem Phys 9:982–990
34. Kreher UP, Rosamilia AE, Raston CL, Scott JL, Strauss CR (2004) Self-associated, "distillable" ionic media. Molecules 9:387–393
35. Wasserchеid P (2006) Chemistry: volatile times for ionic liquids. Nature 439:797
36. Holbrey JD, Seddon KR (1999) The phase behaviour of 1-alkyl-3-methylimidazolium tetrafluoroborates; ionic liquids and ionic liquid crystals. J Chem Soc Dalton Trans 8:2133–2140
37. Baranyai KJ, Deacon GB, MacFarlane DR, Pringle JM, Scott JL (2004) Thermal degradation of ionic liquids at elevated temperatures. Aust J Chem 57:145–147
38. Pernak J, Smiglak M, Griffin ST, Hough WL, Wilson TB, Pernak A, Zabielska-Matejuk J, Fojutowski A, Kita K, Rogers RD (2006) Long alkyl chain quaternary ammonium-based ionic liquids and potential applications. Green Chem 8:798–806
39. Kulkarni PS, Branco LC, Crespo JG, Nunes MC, Raymundo A, Alfonso CAM (2007) Comparison of physicochemical properties of new ionic liquids based on imidazolium, quaternary ammonium, and guanidinium cations. Chem Eur J 13:8478–8488
40. Zhou ZB, Matsumoto H, Tatsumi K (2005) Low-melting, low-viscous, hydrophobic ionic liquids: aliphatic quaternary ammonium salts with perfluoroalkyltrifluoroborates. Chem Eur J 11:752–766
41. Papaiconomou N, Estager J, Traore Y, Bauduin P, Bas C, Legeai S, Viboud S, Draye M (2010) Synthesis, physicochemical properties, and toxicity data of new hydrophobic ionic liquids containing dimethylpyridinium and trimethylpyridinium cations. J Chem Eng Data 55:1971–1979
42. Tokuda H, Ishii K, Susan M, Tsuzuki S, Hayamizu K, Watanabe M (2006) Physicochemical properties and structures of room-temperature ionic liquids. 3. Variation of cationic structures. J Phys Chem B 110:2833–2839
43. Fox DM, Awad WH, Gilman JW, Maupin PH, DeLong HC, Trulove PC (2003) Flammability, thermal stability, and phase change characteristics of several trialkylimidazolium salts. Green Chem 5:724–727

44. Andersn JL, Ding RF, Ellern A, Armstrong DW (2005) Structure and properties of high stability geminal dicationic ionic liquids. J Am Chem Soc 127:593–604
45. Meine N, Benedito F, Rinaldi R (2010) Thermal stability of ionic liquids assessed by potentiometric titration. Green Chem 12:1711–1714
46. Smiglak M, Reichert WM, Holbrey JD, Wilkes JS, Sun LY, Thrasher JS, Kirichenko K, Singh S, Katritzky AR, Rogers RD (2006) Combustible ionic liquids by design: is laboratory safety another ionic liquid myth? Chem Commun 24:2554–2556
47. Jones CB, Haiges R, Schroer T, Christie KO (2006) Oxygen-balanced energetic ionic liquid. Angew Chem Int Ed 45:4981–4984
48. Tao GH, Guo Y, Joo YJ, Twamley B, Shreeve JM (2008) Energetic nitrogen-rich salts and ionic liquids: 5-aminotetrazole (AT) as a weak acid. J Mater Chem 18:5524–5530
49. Kagimoto J, Taguchi S, Fukomoto K, Ohno H (2010) Hydrophobic and low-density amino acid ionic liquids. J Mol Liq 153:133–138
50. Bonhote P, Dias P, Papageorgiou N, Kalyanasundaram K, Gratzel M (1996) Hydrophobic, highly conductive ambient-temperature molten salts. Inorg Chem 35:1168–1178
51. Fitchett BD, Knepp TN, Conboy JC (2004) 1-Alkyl-3-methylimidazolium Bis(perfluoroalkylsulfonyl)imide water-immiscible ionic liquids: the effect of water on electrochemical and physical properties. J Electrochem Soc 151:E219–E225
52. O'Mahony AM, Silvester DS, Aldous L, Hardacre C, Compton RG (2008) In vitro and in vivo photocytotoxicity of boron dipyrromethene derivatives for photodynamic therapy. J Chem Eng Data 53:2865–2874
53. Dzyuba SV, Bartsch RA (2002) Influence of structural variations in 1-alkyl(aralkyl)-3-methylimidazolium hexafluorophosphates and Bis(trifluoromethylsulfonyl)imides on physical properties of the ionic liquids. ChemPhysChem 3:161–166
54. Kuhlmann E, Himmler S, Giebelhaus H, Wasserscheid P (2007) Imidazolium dialkylphosphates—a class of versatile, halogen-free and hydrolytically stable ionic liquids. Green Chem 9:233–242
55. Siqueira LJ, Ribeiro MC (2009) Alkoxy chain effect on the viscosity of a quaternary ammonium ionic liquid: molecular dynamics simulations. J Phys Chem B 113:1074–1079
56. Okoturo OO, VanderNoot TJ (2004) Temperature dependence of viscosity for room temperature ionic liquids. J Electroanal Chem 568:167–181
57. Seddon KR, Stark A, Torres MJ (2000) Influence of chloride, water, and organic solvents on the physical properties of ionic liquids. Pure Appl Chem 72:2275–2287
58. Widegreen JA, Saurer EM, Marsh KN, Magee JW (2005) The effect of dissolved water on the viscosities of hydrophobic room-temperature ionic liquids. Chem Commun 12:1610–1612
59. Widegreen JA, Saurer EM, Marsh KN, Magee JW (2005) Electrolytic conductivity of four imidazolium-based room-temperature ionic liquids and the effect of a water impurity. J Chem Thermodyn 37:569–575
60. Zafarani-Mottar MT, Majdan-Cegincara R (2007) Viscosity, density, speed of sound, and refractive index of binary mixtures of organic solvent + ionic liquid, 1-butyl-3-methylimidazolium hexafluorophosphate at 298.15 K. J Chem Eng Data 52:2359
61. Carda-Broch S, Berthod A, Armstrong DW (2003) Solvent properties of the 1-butyl-3-methylimidazolium hexafluorophosphate ionic liquid. Anal Bioanal Chem 375:191–199
62. Rodriguez H, Bernnecke JF (2006) Solubility of β-carotene in near-critical mixtures of (ethane + propane). J Chem Eng Data 51:2445
63. Kellkar MS, Maginn EJ (2007) Effect of temperature and water content on the shear viscosity of the ionic liquid 1-ethyl-3-methylimidazolium Bis(trifluoromethanesulfonyl)imide as studied by atomistic simulations. J Phys Chem B 111:4867–4876
64. Kundu A, Kishore N (2002) Volumetric properties of nucleic acid bases and nucleosides in aqueous ethanol, 1,2-ethanediol, 2-propanol, and 2-methyl-2-propanol at 25°C. J Solut Chem 31:477–498
65. Fox ET, Paillard E, Borodin O, Henderson WA (2013) Physicochemical properties of binary ionic liquid–aprotic solvent electrolyte mixtures. J Phys Chem C 117:78–84

66. Borodin O, Henderson WA, Fox ET, Berman M, Gobet M, Greenbaum S (2013) Anchoring effect of exfoliated-montmorillonite-supported Pd catalyst for the oxygen reduction reaction. J Phys Chem B 117:10581–10588
67. Poling BE, Prausnitz JM, O'Connell JP (2001) Properties of gases and liquids, 5th edn. McGraw-Hill, New York
68. Anantaraman AV (1986) Thermodynamics of solvent mixtures. I. Density and viscosity of binary mixtures of *N*-methylpyrrolidinone – tetrahydrofuran and propylene carbonate – acetonitrile. Can J Chem 64:46–50
69. Martins RJ, Cardoso MJED, Barcia OE (2000) Excess Gibbs free energy model for calculating the viscosity of binary liquid mixtures. Ind Eng Chem Res 39:849–854
70. Toh SLL, McFarlane J, Tsourism C, DePaoli DW, Luo HM, Dai S (2006) Room-temperature ionic liquids in liquid-liquid extraction: effects of solubility in aqueous solutions on surface properties. Solvent Extr Ion Exch 24:33–56
71. Kalhn M, Stuber C, Sedurman A, Wu P (2010) What determines the miscibility of ionic liquids with water? Identification of the underlying factors to enable a straightforward prediction. J Phys Chem B 114:2856–2858
72. Makowsaka A, Siporska A, Szydlowski J (2009) Isotope effects on miscibility of 1-alkyl-3-methylimidazolium Bis(trifluoromethyl)sulfonyl imides with aromatic hydrocarbons. Fluid Phase Equilib 282:108–112
73. Sun XQ, Ji Y, Guo L, Chen J, Li DQ (2011) A novel ammonium ionic liquid based extraction strategy for separating scandium from yttrium and lanthanides. Sep Purif Technol 81:25–30
74. Huddleston JG, Visser AE, Reichert WM, Willauer HD, Broker GA, Rogers RD (2002) Characterization and comparison of hydrophilic and hydrophobic room temperature ionic liquids incorporating the imidazolium cation. Green Chem 3:156–164
75. Chun S, Dzyuba SV, Bartsch RA (2001) Influence of structural variation in room-temperature ionic liquids on the selectivity and efficiency of competitive alkali metal salt extraction by a crown ether. Anal Chem 73:3737–3741
76. Freire MG, Carvalho PJ, Silva AM, Santos L, Rebelo LPN, Marrucho IM, Coutinho JAP (2009) Ion specific effects on the mutual solubilities of water and hydrophobic ionic liquids. J Phys Chem B 113:202
77. Gutowski KE, Broker GA, Willauer HD, Huddleston G, Swatloski RP, Holbrey J, Rogers RD (2003) Controlling the aqueous miscibility of ionic liquids: aqueous biphasic systems of water-miscible ionic liquids and water-structuring salts for recycle, metathesis, and separations. J Am Chem Soc 125:6632–6633
78. Tome LIN, Varanda FR, Freire MG, Marrucho LM, Coutinho JA (2009) Towards an understanding of the mutual solubilities of water and hydrophobic ionic liquids in the presence of salts: the anion effect. J Phys Chem B 113:2815–2825
79. Domanska U, Marciniak A (2007) Phase behaviour of 1-hexyloxymethyl-3-methyl-imidazolium and 1,3-dihexyloxymethyl-imidazolium based ionic liquids with alcohols, water, ketones and hydrocarbons: the effect of cation and anion on solubility. Fluid Phase Equilib 260:9–18
80. Han D, Row KH (2010) Recent applications of ionic liquids in separation technology. Molecule 15:2405–2426
81. Makowska A, Siporska A, Oracz P, Sydlowski J (2010) Miscibility of trihexyl(tetradecyl) phosphonium chloride with alkanes. J Chem Eng Data 55:2829–2832
82. Docherty KM, Dixon JK, Kulpa CF (2007) Biodegradability of imidazolium and pyridinium ionic liquids by an activated sludge microbial community. Biodegredation 18:481–493
83. Jastorff B, Stormann R, Rnake J, Molter K, Stock F, Oberheitmann B, Hoffmann W, Nuchter M, Ondruschka B, Fisler J (2003) How hazardous are ionic liquids? Structure–activity relationships and biological testing as important elements for sustainability evaluation. Green Chem 5:136–142
84. Pham TPT, Cho CW, Jeon CO, Chung YJ, Lee MW, Yun YS (2009) Identification of metabolites involved in the biodegradation of the ionic liquid 1-butyl-3-methylpyridinium bromide by activated sludge microorganisms. Environ Sci Technol 43:516–521

85. Stolte S, Abdulkarim S, Arning J, Blomeyer-Nienstedt AK, Bottin-Webber U, Matzke M, Ranke J, Jastroff B, Thoming J (2008) Primary biodegradation of ionic liquid cations, identification of degradation products of 1-methyl-3-octylimidazolium chloride and electrochemical wastewater treatment of poorly biodegradable compounds. Green Chem 10:214–224
86. Zhang C, Wang H, Malhotra SV, Dodge CJ, Francis AJ (2010) Biodegradation of pyridinium-based ionic liquids by an axenic culture of soil *Corynebacteria*. Green Chem 12:851–858
87. Siedlecka EM, Stepnowski P (2009) The effect of alkyl chain length on the degradation of alkylimidazolium- and pyridinium-type ionic liquids in a Fenton-like system. Environ Sci Pollut Res 16:453–458
88. Siedlecka EM, Mrozik W, Kaczynski Z, Stepnowski P (2008) Degradation of 1-butyl-3-methylimidazolium chloride ionic liquid in a Fenton-like system. J Hazard Mater 154:893–900
89. Katoh R, Takahashi K (2009) Photo-degradation of imidazolium ionic liquids. Radiat Phys Chem 78:1126–1128
90. Stepnowski P, Zaleska A (2005) Comparison of different advanced oxidation processes for the degradation of room temperature ionic liquids. J Photochem Photobiol A Chem 170:45–50
91. Bell JR, Luo HM, Dai S (2014) Superbase-derived protic ionic liquid extractants for metal ion separation. Sep Purif Technol 130:147–150
92. Bell JR, Luo HM, Dai S (2012) Solvent extraction separation of La^{3+} and Ba^{2+} using imidazolium ionic liquids and TODGA extractant. Sep Sci Technol 47:2002–2006
93. Dietz ML, Dzielwa LA (2001) Ion-exchange as a mode of cation transfer into room-temperature ionic liquids containing crown ethers: implications for the 'greenness' of ionic liquids as diluents in liquid–liquid extraction. Chem Commun 20:2124–2125
94. Dai S, Ju YH, Barnes CE (1999) Solvent extraction of strontium nitrate by a crown ether using room-temperature ionic liquids. J Chem Soc Dalton Trans 8:1201–1202
95. Mehdi H, Binnermans K, Van Hecke K, Van Meervelt L, Nockemann P (2010) Hydrophobic ionic liquids with strongly coordinating anions. Chem Commun 46:234–236
96. Gupta OD, Twamley B, Shreeve JM (2004) Low melting and slightly viscous ionic liquids via protonation of trialkylamines by perfluoroalkyl β-diketones. Tetrahedron Lett 45:1733–1736
97. Gupta OD, Twamley B, Shreeve JM (2005) Acyclic tertiary diamines and 1,4,7,10-tetraazacyclododecane with fluorine-containing β-diketones: leading to low melting ionic adducts. J Fluor Chem 126:1222–1229
98. Li X, Zeng Z, Garg S, Twamley B, Shreeve JM (2008) Fluorine-containing ionic liquids from *N*-alkylpyrrolidine and *N*-methylpiperidine and fluorinated acetylacetones: low melting points and low viscosities. Eur J Inorg Chem 3353–3358
99. Jensen MP, Neufeind J, Beitz JV, Skanthakumar S, Soderholm L (2003) Mechanisms of metal ion transfer into room-temperature ionic liquids: the role of anion exchange. J Am Chem Soc 125:15466–15473
100. Sasaki Y, Sugo Y, Szuki S, Tachimorio S (2001) The novel extractants, diglycolamides, for the extraction of lanthanides and actinides in HNO_3–*N*-dodecane system. Solvent Extr Ion Exch 19:91–103
101. Ansari SA, Pathak PN, Macnchanda VK, Husain M, Prasad AK (2005) N, N, N', N'-tetraoctyl diglycolamide (TODGA): a promising extractant for actinide-partitioning from high-level waste (HLW). Solvent Extr Ion Exch 23:463–479
102. Ansari SA, Pathak PN, Mohapatra PK, Manchanda VK (2012) Chemistry of diglycolamides: promising extractants for actinide partitioning. Chem Rev 112:1751–1772
103. Weaver BS, Kappelma FA (1968) Preferential extraction of lanthanides over trivalent actinides by monoacidic organophosphates from carboxylic acids and from mixtures of carboxylic and aminopolyacetic acids. J Inorg Nucl Chem 30:263–272
104. Nilsson M, Nash KL (2007) Review article: a review of the development and operational characteristics of the TALSPEAK process. Solvent Extr Ion Exch 25:665–701

105. Leggett CJ, Liu GK, Jensen MP (2011) Do aqueous ternary complexes influence the TALSPEAK process? Solvent Extr Ion Exch 28:313–334
106. Sun XQ, Luo HM, Dai S (2012) Solvent extraction of rare-earth ions based on functionalized ionic liquids. Talanta 90:132–137
107. Sun XQ, Bell JR, Luo HM, Dai S (2011) Extraction separation of rare-earth ions *via* competitive ligand complexations between aqueous and ionic-liquid phases. Dalton Trans 40:8019–8023
108. Hovarth LT, Rabai J (1994) Facile catalyst separation without water: fluorous biphase hydroformylation of olefins. Science 266:72–75
109. Minoofar PN, Hernandez R, Chia S, Dunn B, Zink JI, Franville AC (2002) Placement and characterization of pairs of luminescent molecules in spatially separated regions of nano-structured thin films. J Am Chem Soc 124:14388–14396
110. Zahn S, Uhlig F, Thar J, Spickermann C, Krichner B (2008) Intermolecular forces in an ionic liquid ([Mmim][Cl]) versus those in a typical salt (NaCl). Angew Chem Int Ed 47:3639
111. Sun XQ, Luo HM, Dai S (2013) Mechanistic investigation of solvent extraction based on anion-functionalized ionic liquids for selective separation of rare-earth ions. Dalton Trans 42:8270–8275
112. Malachy McCann RC, Ben-Shoshan M, McKee V, Tahi AA, Devereux M, Kavanagh K, Creaven BS, Kellet A (2012) Silver(I) complexes of 9-anthracenecarboxylic acid and imidazoles: synthesis, structure and antimicrobial activity. Dalton Trans 41:6516–6527
113. Eilbeck WJ, Holmes F, Underhill AE (1967) Cobalt(II), nickel(II), and copper(II) complexes of imidazole and thiazole. J Chem Soc A 757–761
114. Lagutschenkov A, Lorenz UJ, Dopfer O (2011) IR spectroscopy of isolated metal-organic complexes of biocatalytic interest: evidence for coordination number four for Zn^{2+}(imidazole)^4. Int J Mass Spectrom 308:316–339
115. Shen YL, Li WK, Wu JR, Li S, Luo HM, Dai S, Wu WS (2014) Solvent extraction of lanthanides and yttrium from aqueous solution with methylimidazole in an ionic liquid. Dalton Trans 43:10023–10032
116. Shimojo K, Goto M (2004) Solvent extraction and stripping of silver ions in room-temperature ionic liquids containing calixarenes. Anal Chem 76:5039–5044
117. Barnard KR, Nealon GI, Ogden MI, Skelton BW (2010) Crystallographic determination of three Ni-α-hydroxyoxime-carboxylic acid synergist complexes. Solvent Extr Ion Exch 28:778–792
118. Mathur JN, Murali MS, Nash KL (2001) Actinide partitioning – a review. Solvent Extr Ion Exch 19:357–390
119. Turkington JR, Bailey PJ, Love JB, Wilson AM, Tasker PA (2013) Exploiting outer-sphere interactions to enhance metal recovery by solvent extraction. Chem Commun 49:1891–1899

Chapter 4
Ionic Liquid-Based Extraction and the Application to Liquid Membrane Separation of Rare Earth Metals

Fukiko Kubota, Jian Yang, and Masahiro Goto

Abstract Separation and recycling of rare-earth metals are attracting continuous attention worldwide. Liquid-liquid extraction is a conventionally employed technique for the separation of rare-earth metals. In recent years, growing attention has focused on room temperature ionic liquids as alternatives to conventional organic solvents.

The development of an efficient extraction system based on the ionic liquids (ILs) depends on the employment of an appropriate combination of the extractant and an ionic liquid. In the IL-based extraction system with neutral extractants such as CMPO and TOPO dissolved in the imidazolium ILs, the extraction efficiency and selectivity for rare-earth metals are greatly improved compared to that in an organic solvent system, and the stripping, however, is unfavorably difficult. The use of acidic extractants such as PC-88A is limited in the poor solubility in ILs, though the extraction is controllable by the acid concentration in the aqueous phase.

An extractant, recently developed *N,N*-dioctyldiglycol amic acid (DODGAA), seems to combine the advantages of a neutral and an acidic extractant. That is, DODGAA is soluble in the ILs and shows the high separation performance for rare-earth metals compared to that in n-dodecane. Furthermore, the stripping is possible by an acid solution. Due to the extremely high affinity of DODGAA for rare-earth metals, the extraction system is applicable in the recycling of rare-earth metals. Taking advantage of the feature of ILs, a supported liquid membrane system can be constructed using DODGAA as a carrier.

F. Kubota • J. Yang
Department of Applied Chemistry, Graduate School of Engineering, Kyushu University, 744 Motooka, Fukuoka 819-0395, Japan

M. Goto (✉)
Department of Applied Chemistry, Graduate School of Engineering, Kyushu University, 744 Motooka, Fukuoka 819-0395, Japan

Center for Future Chemistry, Kyushu University, 744 Motooka, Fukuoka 819-0395, Japan
e-mail: m-goto@mail.cstm.kyushu-u.ac.jp

J. Chen (ed.), *Application of Ionic Liquids on Rare Earth Green Separation and Utilization*, Green Chemistry and Sustainable Technology,
DOI 10.1007/978-3-662-47510-2_4

In this chapter, we summarize the IL-based extraction and separation of rare-earth metals and the application to the advanced technique, focusing on our research results.

Keywords Ionic liquids • Rare earth • Extraction • Separation • Metal recycling

4.1 Introduction

Rare-earth metals are of great importance in modern society because of their widespread applications in high-tech industries. Neodymium (Nd) and dysprosium (Dy), for instance, are especially indispensable in the manufacture of permanent magnets, which are essential to the generators and motors of wind turbines and electric vehicles. Other rare-earth metals such as yttrium (Y) and europium (Eu) are extensively used as fluorescent materials for lamps and TV displays [1]. In recent years, industrial wastes and scrap such as a spent TV display, fluorescent lamps, and permanent magnets have been recognized as valuable secondary resources of critical metals [2–4].

Liquid-liquid extraction is the most commonly applied technique for the separation of rare-earth metals, where large amounts of organic solvents are consumed as diluents. Ionic liquids (ILs), which are composed of only ions, have been attracting interest for their potential use in industrial and analytical fields due to their unique properties, such as low melting point, high thermal stability, and negligible vapor pressure. Therefore, ILs are considered to be greener and safer alternatives to the conventional molecular solvents [5]. The most attractive feature of ionic liquids is that their physicochemical properties, such as affinity with a solvent, density, viscosity, and conductivity, are highly tunable. Since the application of ILs to the separation of rare-earth metals was first reported [6], the research papers related to the separation of rare-earth metals have been increased year by year. In the IL systems, the combination of IL and extractant affects the success of the metal extraction; therefore, substantial efforts have been made to find the extractants suitable for the IL systems. Furthermore, IL-based extraction systems, utilizing their distinctive characteristics, were applied in supported liquid membranes (SLMs) for the first time [7].

In this chapter, we will overview the different extractants used in the IL-based extraction systems employing imidazolium-based ILs as illustrated in Fig. 4.1 and compare the extraction performance for rare-earth metal ions to that of conventional organic solvents. Attention is focused on the use of a novel extractant, a diglycolamide derivative, for rare-earth metals in the IL-based extraction system. We will introduce the practical use of the novel IL systems proposed for the recovery of rare-earth metals as a metal recycling technique and also an SLM system based on the ILs with the newly synthesized extractant.

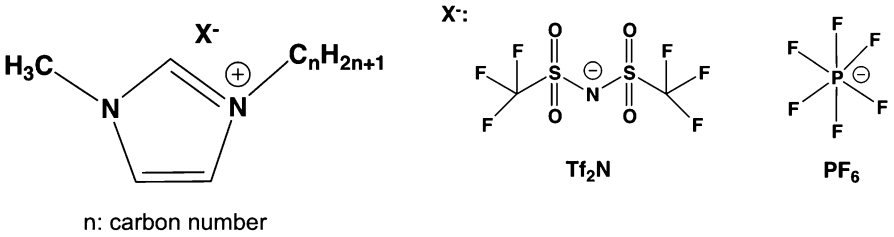

Fig. 4.1 Molecular structure of 1-alkyl-3-methylimidazolium-based ionic liquids, [$C_n$mim][Tf_2N] or [$C_n$mim][PF_6]

4.2 Extraction System for Rare-Earth Metals Using ILs

4.2.1 Extraction Using Industrial Extractants

Octyl(phenyl)-N,N-diisobutylcarbamoylmethylphosphine oxide (CMPO) is one of the representative extractants developed for the separation and recovery of actinides in the nuclear industry. Nakashima et al. investigated the extraction behavior of trivalent rare-earth metals with CMPO using ILs as an extracting phase and demonstrated that not only the extraction efficiency but also the mutual selectivity was remarkably enhanced, in comparison with that in n-dodecane [8]. Although such advantages were observed in the extraction step, the stripping of the metal ions from the extracting IL phase was difficult due to the unique extraction mechanism in the IL system as follows:

$$M^{3+}_{aq} + 3CMPO_{org} + 3C_4mim^{+}_{org} \leftrightarrows M^{3+} \times (CMPO)_{3,org} + 3C_4mim^{+}_{aq} \quad (4.1)$$

$$M^{3+}_{aq} + 3CMPO_{org} + 3NO^{-}_{3} \leftrightarrows M(NO_3)_3 \times 3CMPO_{org} \quad (4.2)$$

In the IL systems with a neutral extractant as CMPO, the extraction reaction was found to involve the component cations of ILs as expressed by Eq. (4.1), instead of the anion co-extraction from the aqueous phase such as NO^{-}_{3}, in the conventional organic systems as Eq. (4.2). It is known that the ILs having a shorter 1 substituted alkyl chain in the imidazolium cation give higher extraction ability in the neutral extractant systems because the imidazolium cation with a shorter alkyl chain is readily released to the aqueous phase compared to that with a longer one.

In addition, in the case using another neutral extractant tri-*n*-octylphosphine oxide (TOPO), the extraction ability was reported to depend on the number of extractants coordinated [9]. It was found that in the [C_4mim][Tf_2N], 6TOPO molecules coordinated to a rare-earth metal ion, whereas 4TOPO coordinated in the [C_8mim][Tf_2N]. In n-dodecane, extraction proceeded according to the same reaction as CMPO, described as Eq. (4.2).

The synergistic extraction behavior of a β-diketone and an organophosphine oxide for rare-earth metals was investigated [10]. A combination of 2-thenoyltrifluoroacetone (HTTA) and TOPO was found to be effective in synergistically extracting rare-earth metals into an IL, [C_4mim][Tf_2N].

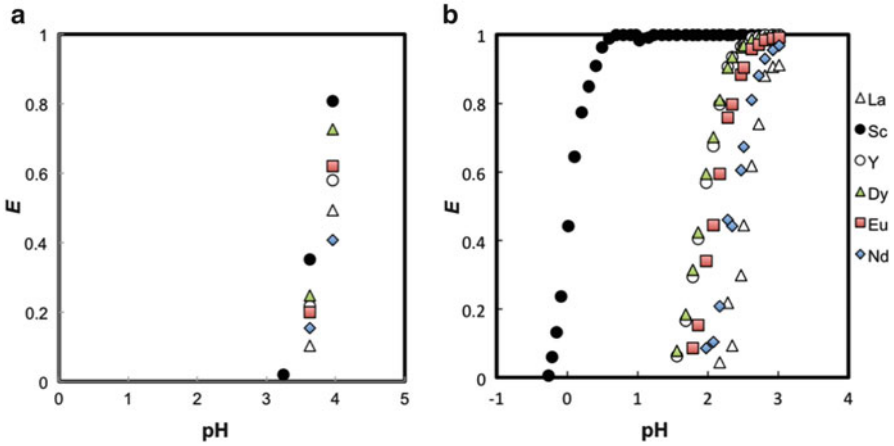

Fig. 4.2 Rare-earth metal extraction efficiencies using (**a**) only HTTA or (**b**) HTTA with TOPO in the IL system; aqueous phase, [M] = 0.1 mM; IL phase, (**a**) [HTTA] = 10 mM; (**b**) [HTTA] = [TOPO] = 10 mM (Reprinted with permission from Ref. [10]. Copyright 2014, The Society of Chemical Engineers, Japan)

When a conventional organic solvent (*n*-dodecane) was used as an extracting phase, extraction efficiencies for all the rare-earth metal ions were greatly enhanced by the synergistic effect. In contrast, in the IL system, the synergistic effect preferentially improved the Sc extraction, leading to higher selectivity for Sc toward other rare-earth metals, as shown in Fig. 4.2. Greater synergistic effect on Sc is attributable to the fact that the ionic radius and coordination number of Sc are much smaller than that of the other rare-earth metal ions. It was found that extraction mechanism of Sc was different from other rare-earth metal ions, and the smaller complex of Sc was more soluble in the IL than that of other rare-earth metals. Although the extraction reaction involves the release of the IL cations, stripping of Sc was possible because the proton dissociation of HTTA played the predominant role even in the IL-based extraction.

A proton dissociation-type organophosphorus extractant such as 2-ethylhexylphosphonic acid mono-2-ethylhexyl ester (PC-88A) in the ILs ($[C_n mim][Tf_2N]$, $n = 8 \sim 12$) showed the same extraction mechanism as in an organic solvent as follows [11]:

$$M_{aq}^{3+} + 3(HR)_{2,org} \leftrightarrows MR_3 \times 3HR_{org} + 3H^+ \tag{4.3}$$

Though the stripping of metal ions seemed to be feasible by an acid solution, the disadvantages in this case were the low solubility of PC-88A and the metal complexes in the ILs. This is also true with another organophosphorus extractant di(2-ethylhexyl)phosphoric acid (DEHPA) [12]. To develop a more practical IL-based extraction system, a new proton dissociation-type extractant, which is soluble in ILs like neutral extractants, was desired.

4.2.2 Extraction Using a Novel Extractant

N,*N*,*N*,*N*-Tetra(*n*-octyl)-diglycolamide (TODGA) (Fig. 4.3), a neutral tridentate extractant developed for the separation of actinides in spent nuclear fuel reprocessing [13], was reported to exhibit unprecedentedly higher extraction performance for rare-earth metals in [C_2mim][Tf_2N] [14].

A newly synthesized *N*,*N*-dioctyldiglycol amic acid (DODGAA) [15, 16], which is analogous to TODGA, as shown in Fig. 4.3, is ionizable by dissociation of the carboxy group and was readily soluble in all the ILs tested.

The extraction behavior of metal ions (Y^{3+}, Eu^{3+}, and Zn^{2+}) with DODGAA in both ILs and n-dodecane was examined [3]. As shown in Fig. 4.4, the extraction efficiency for Y^{3+} and Eu^{3+} in both ILs and n-dodecane systems increased, with

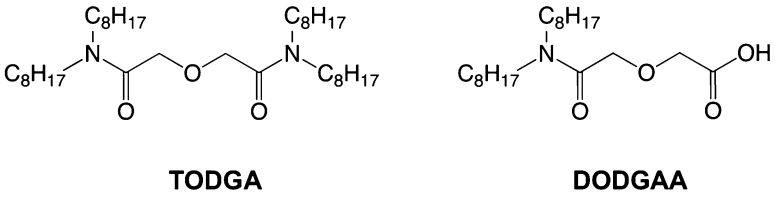

Fig. 4.3 Molecular structures of TODGA and DODGAA

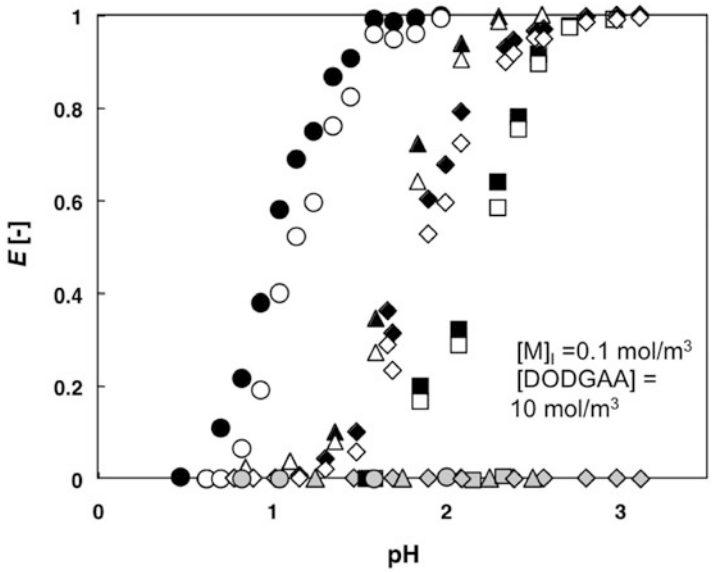

Fig. 4.4 Extraction behavior of metal ions with DODGAA in the IL and n-dodecane systems; Y^{3+} (*filled symbols*), Eu^{3+} (open symbols), Zn^{2+} (*gray symbols*); solvents, [C_4mim] (*circle*), [C_8mim] (*diamond*), [C_{12}mim] (*square*), n-dodecane (*triangle*) (Reprinted with permission from Ref. [3]. Copyright 2011, The Society of Chemical Engineers, Japan)

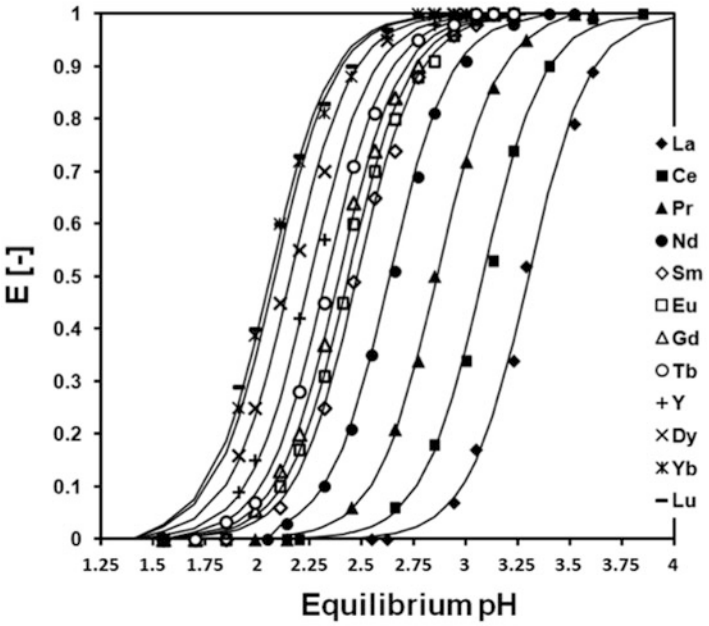

Fig. 4.5 Extraction behaviors of rare-earth metal ions. Aqueous phases: 0.1 mM rare-earth metal ions, 0.05 M H_2SO_4-$(NH_4)_2SO_4$; IL phases, 10 mM DODOAA in $[C_8mim][Tf_2N]$ (Reprinted with permission from Ref. [17]. Copyright 2012, Japan Association of Solvent Extraction)

increasing pH, suggesting that the metal extraction into ILs and n-dodecane proceeds in a similar manner, and the efficiency was greatly enhanced in the $[C_4mim][Tf_2N]$ compared to that in n-dodecane. The extraction behavior of rare-earth series with DODGAA shown in Fig. 4.5 was found to be similar to that with conventional PC-88A and D2EHPA [17].

Further slope analysis study revealed that both in IL and n-dodecane systems, the extraction reaction could be explained by a proton exchange mechanism, wherein one metal ion was extracted with three DODGAA molecules as follows:

$$M_{aq}^{3+} + 3HR_{org} \leftrightarrows MR_3 + 3H^+ \tag{4.4}$$

The metal ions were readily stripped with nitric acid, and quantitative recovery was realized at concentrations of nitric acid larger than 0.5 mol/dm^3.

4.2.3 Application of IL DODGAA System

The IL-based extraction system containing DODGAA as an extractant was then employed for the separation of rare-earth metal ions from real leaching solutions

[4]. The chemical composition of a sample of phosphor powder from spent fluorescent lamps was analyzed by XRF. Rare-earth elements such as Y, Eu, La, Ce, Pr, and Tb existed in concentrations of approximately 30 %, and other elements in the sample were found to be mainly Ca, Sr, and a variety of metals (Al, Ti, V, Fe, and Zn). The leach solutions were prepared by acid leaching of rare-earth metals from the waste phosphor powder with a two-stage leaching method, that is, Y and Eu, which exist as oxides, were leached in the first stage under relatively mild conditions, and the other rare-earth ions, existing as complex crystals of their phosphates, were leached in the second stage leaching from the residue on the first leaching.

In comparison to a conventional extraction system, where PC-88A was dissolved in n-dodecane as an extractant, the DODGAA IL system showed a better extraction selectivity for the rare-earth metal ions. PC-88A in n-dodecane system, the separation from impurity metal ions in the leach solution such as Fe, Zn, Al, Ti, etc., seemed to be difficult, whereas DODGAA dissolved in the $[C_4mim][Tf_2N]$ significantly enhanced the extraction efficiency even for light rare earths and the selectivity to other common metal ions. Only rare-earth metal ions could be successfully recovered from the first and second leaching solutions, the pH of which was adjusted for the extraction operation, as shown in Fig. 4.6.

As the quantitative stripping of the rare-earth metal ions from the IL extracting phase could be readily accomplished by acid solution greater than 0.5 or 1 M sulfuric or nitric acids for both stages, the reusability of the extraction system was studied. It was found that after five cycles of extraction and stripping processes, the extraction efficiency maintained almost unchanged, suggesting the extraction system could be reused. Figure 4.7 shows the conceptual diagram for the recovery of rare-earth metals from waste phosphor powder from spent fluorescent lamps.

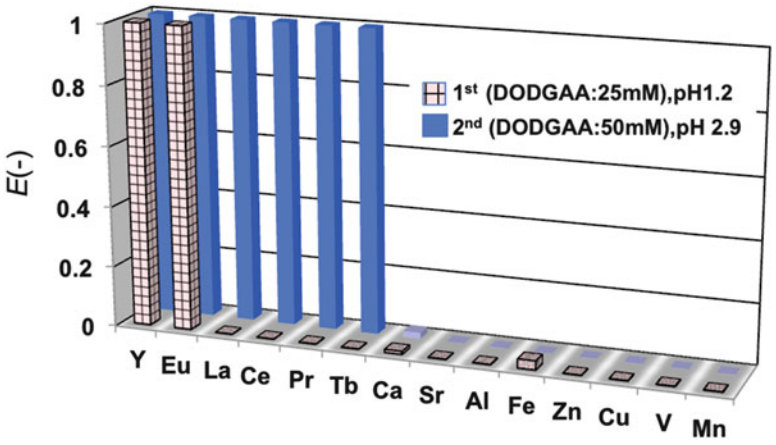

Fig. 4.6 Recovery of rare-earth metals from real leach dilutions using IL-based DODGAA system. Metal composition (ppm), from 1st leach dilution. Feed phase (ppm): Y, 100.3; Eu, 7.4; Ca, 36.1; Sr, 1; Al, 1.9; Ti, 3.9; Fe, 1; Zn, 0.8; Cu, 0.8; V, 0.03; Mn, 4. pH 1.2. From 2nd leach dilution. Feed phase (ppm): Eu 2.6, La 66.1, Ce 32.1, Pr 7.8, Tb 17.0, Ca 17.4, Sr 30.2, Al 2.6, Fe 0.1, Zn 0.7, V 0.24, Mn 2.5, pH 2.9; 30 °C

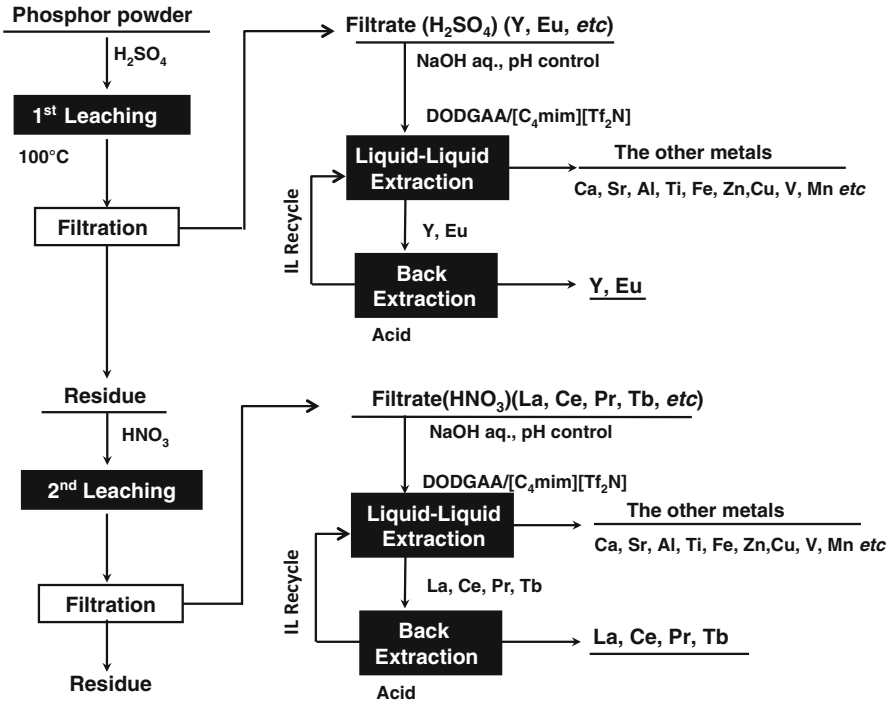

Fig. 4.7 Conceptual flow sheet for recovery of rare-earth metals from waste phosphor powder in spent fluorescent lamp

4.3 IL-Based Liquid Membrane System

As an advanced extraction system, an SLM using ILs was developed for the separation of rare-earth metals. In a liquid membrane system, as illustrated in Fig. 4.8, the feed and receiving phases are separated by an immiscible membrane phase, thus making the simultaneous extraction and stripping possible on both sides [18]. The liquid membrane phase containing a carrier to bind a target metal ion selectively is impregnated into pores of a microporous thin polymer film, and thus the obtained liquid membrane is sandwiched between the feed and receiving phases.

Quantitative transport of rare-earth metal ions such as Y^{3+}, Eu^{3+}, Dy^{3+}, and Nd^{3+} was achieved by using [C_8mim][Tf_2N] as the membrane phase, which contained DODGAA as the carrier [2, 7]. Figure 4.9 shows the time course of metal ion concentrations in the feed and receiving phases for three metal ions, Dy^{3+}, Nd^{3+}, and Fe^{3+}. It was demonstrated that Dy^{3+} and Nd^{3+} could be separated from the metal mixture, because a small amount of Fe could permeate the membrane. The key elements for the success of SLM separation include not only a good carrier, but also a liquid membrane that can withstand the long-term operation. The construction of stable membrane was difficult in the cases using n-dodecane or [C_4mim]

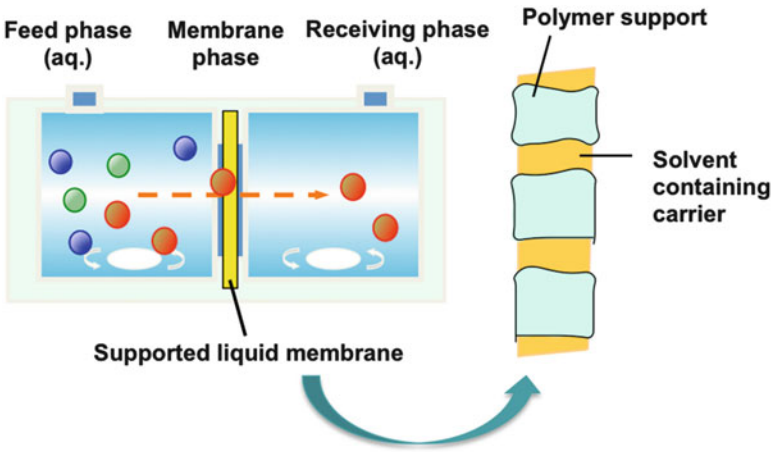

Fig. 4.8 Schematic of liquid membrane system

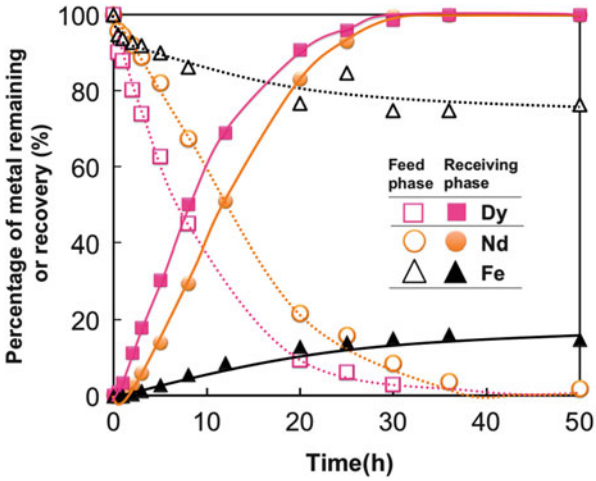

Fig. 4.9 Time courses of metal ion concentrations in the feed (*open symbols*) and receiving (*closed symbols*) phases during IL-based SLM operation. Feed phase, 0.1 mM metal ions, pH 2; receiving phase, 1 M H_2SO_4

[Tf_2N] as the membrane phase, because their viscosities are too low to be held in the membrane pores.

4.4 Conclusions

We reviewed the recent advances in IL-based extraction for rare-earth metal separation. When industrial extractants are employed, some advantages of using ILs are observed; however, there are several problems remaining for the practical use, such as solubility of extractant in ILs and difficulty in stripping. To make a

successful extraction and recovery of metal ions, the use of an extractant that is suitable for ILs is required. In this article, the extraction with a novel extractant DODGAA in ILs and the application to the rare-earth metal recycling from wastes were described as a successful example. The novel extraction system was applicable to construct a liquid membrane separation process. We expect that these findings will expand the application of ILs to the metal separation field.

References

1. Baba Y, Kubota F, Kamiya N, Goto M (2011) Recent advances in extraction and separation of rare-earth metals using ionic liquids. J Chem Eng Jpn 44:679–685
2. Baba Y, Kubota F, Kamiya N, Goto M (2011) Selective recovery of dysprosium and neodymium ions by a supported liquid membrane based on ionic liquids. Solvent Extr Res Dev 18:193–198
3. Kubota F, Shimobori Y, Baba Y, Koyanagi Y, Shimojo K, Kamiya N, Goto M (2011) Application of ionic liquids to extraction separation of rare earth metals with an effective diglycol amic acid extractant. J Chem Eng Jpn 44:307–312
4. Yang F, Kubota F, Baba Y, Kamiya N, Goto M (2013) Selective extraction and recovery of rare earth metals from phosphor powders in waste fluorescent lamps using an ionic liquid system. J Hazard Mater 254–255:79–88
5. Kubota F, Goto M (2006) Application of ionic liquids to solvent extraction. Solvent Extr Res Dev 13:23–36
6. Nakashima K, Kubota F, Maruyama T, Goto M (2003) Ionic liquids as a novel solvent for lanthanide extraction. Anal Sci 19:1097–1098
7. Kubota F, Shimobori Y, Koyanagi Y, Shimojo K, Kamiya N, Goto M (2010) Uphill transport of rare-earth metals through a highly stable supported liquid membrane based on an ionic liquid. Anal Sci 26:289–290
8. Nakashima K, Kubota F, Maruyama T, Goto M (2005) Feasibility of ionic liquids as alternative separation media for industrial solvent extraction processes. Ind Eng Chem Res 44:4368–4372
9. Yang F, Kubota F, Kamiya N, Goto M (2013) A comparative study of ionic liquids and a conventional organic solvent on the extraction of rare-earth ions with TOPO. Solvent Extr Res Dev 20:225–232
10. Zhao Z, Baba Y, Kubota F, Kamiya N, Goto M (2014) Synergistic extraction of rare-earth metals and separation of scandium using 2-thenoyltrifluoroacetone and tri-n-octylphosphine oxide in an ionic liquid system. J Chem Eng Jpn 47:656–662
11. Kubota F, Koyanagi Y, Nakashima K, Shimojo K, Kamiya N, Goto M (2008) Extraction of lanthanide ions with an organophosphorous extractant into ionic liquids. Solvent Extr Res Dev 15:81–87
12. Sun X, Luo H, Dai S (2012) Solvent extraction of rare-earth ions based on functionalized ionic liquids. Talanta 90:132–137
13. Sasaki Y, Sugo Y, Suzuki S, Tachimori S (2001) The novel extractants diglycolamides for the extraction of lanthanides and actinides in HNO3-n-dodecane system. Solvent Extr Ion Exch 19:91–103
14. Shimojo K, Kurahashi K, Naganawa H (2008) Extraction behavior of lanthanides using a diglycolamide derivative TODGA in ionic liquids. Dalton Trans 37:5083–5088
15. Naganawa H, Shimojo K, Mitamura H, Sugo Y, Noro J, Goto M (2007) A new “green” extractant of the diglycol amic acid type for lanthanides. Solvent Extr Res Dev 14:151–159

16. Shimojo K, Naganawa H, Noro J, Kubota F, Goto M (2007) Extraction behavior and separation of lanthanides with a diglycol amic acid derivative and a nitrogen-donor ligand. Anal Sci 23:1427–1430
17. Yang F, Baba Y, Kubota F, Kamiya N, Goto M (2012) Extraction and separation of rare earth metal ions with DODGAA in ionic liquids. Solvent Extr Res Dev 19:69–76
18. Kubota F, Goto M (2005) Recent advances in liquid membrane technology. Solvent Extr Res Dev 12:11–26

Chapter 5
Application of Ionic Liquid Extractants on Rare Earth Green Separation

Hualing Yang, Ji Chen, Hongmin Cui, Wei Wang, Li Chen, and Yu Liu

Abstract A green solvent extraction process for the separation of rare earth elements (REEs) in different media (such as hydrochloric acid media, nitric acid media, and sulfuric media) was developed using bifunctional ionic liquid extractants (Bif-ILEs) especially containing quaternary ammonium and phosphonium-based ILs. The characteristics of the Bif-ILEs are simple synthesis, high extraction ability and selectivity, low extraction acid and base consumption, and easy stripping. Bif-ILEs could be synthesized by acid/base neutralization, and this reaction process was under mild condition with easier purification. The extraction thermodynamics showed that the separation factor (β) values for REEs were changed with the different Bif-ILEs or reaction media. The inner synergistic effect between cations and anions in Bif-ILEs has greatly facilitated the β values of REEs and also avoided the production of ammonia nitrogen caused by the acidity extractant saponification. The kinetic experimental data on the separation of REEs by Bif-ILEs, with a constant interfacial area cell with laminar flow, showed that there exist real possibilities for increasing the efficiency of the separation by the use of kinetic factors. The kinetics model could be deduced from the rate-controlling step. Serving as extractants, additives, and templating materials, ILs were used in the preparation of separation materials, including silica-supported ionic liquids (S-SILs), membrane-supported ionic liquids (M-SILs), and polymer-supported ionic liquids (P-SILs). ILs were usually attached or doped into the solid support and offered high extraction efficiency and excellent stability for REEs separation. Using such separation materials may indeed enable us to substantially

H. Yang
State Key Laboratory of Rare Earth Resources Utilization, Changchun Institute of Applied Chemistry, Chinese Academy of Sciences, 5625 Renmin Street, Changchun 130022, China

School of Chemistry and Chemical Engineering, Nantong University, Nantong 226019, China

J. Chen (✉) • H. Cui • W. Wang • L. Chen • Y. Liu
State Key Laboratory of Rare Earth Resources Utilization, Changchun Institute of Applied Chemistry, Chinese Academy of Sciences, 5625 Renmin Street, Changchun 130022, China
e-mail: jchen@ciac.ac.cn

J. Chen (ed.), *Application of Ionic Liquids on Rare Earth Green Separation and Utilization*, Green Chemistry and Sustainable Technology,
DOI 10.1007/978-3-662-47510-2_5

reduce the steps for the separation of REEs and thus decrease both the separation time and waste production.

Keywords Rare earth • Bifunctional ionic liquid extractants • Extraction • Separation

5.1 General

Analytical and separation technologies for rare earth elements (REEs) are attracting more and more worldwide attentions because of their wide applications in many critical technological areas, such as luminescence, electronics, magnetism, catalysis, metallurgy, and the ceramic industry. However, REEs exist together in nature in some minerals, e.g., bastnasite, monazite, xenotime, oil shale, and others, and it is difficult to separate them from each other due to their similar chemical and physical properties. So the development of sustainable high-separating schemes for REEs is a technological challenge. An important technique for the separation of REEs is solvent extraction, because this technique allows the separation of REEs from other metals as well as the separation of mixtures of REEs into the individual elements. The choice of the extractants is a key factor for the extraction property and separation sequence of REEs in solvent extraction process. Up until now, there are many acidic organophosphorous, neutral organophosphorous, amine extractants used for REEs separation. Acidic organophosphorous 2-ethylhexyl phosphoric acid mono(2-ethylhexyl) ester (P507) is the main extractant for industrial separation of light REEs. However, the β values of heavy REEs are lower, e.g., the β values of Tm/Er, Yb/Tm, and Lu/Yb are 3.34, 3.56, and 1.78, respectively. The stripping acidity is high and the heavy REEs could not be completely stripped from loaded organic phase. Compared with P507, the β values of heavy REEs using bis(2,4,4-trimethylpentyl) phosphinic acid (CYANEX 272) are enhanced. But the high cost of CYANEX 272 and severe emulsifying phenomenon during the extraction and separation process limit its application. Li et al. investigated the REEs separation process using both P507 and alcohol as the extractant and additive to accelerate stripping and improve emulsification phenomenon [1]. Conventional acidity extractants, whether acidic organophosphorous or naphthenic acid used widely in REEs hydrometallurgy in China, always need to be saponified by $NH_3{\bullet}H_2O$, NaOH, or $Ca(OH)_2$ to facilitate the cation exchange of REEs, which will undoubtedly produce the corresponding ammonia nitrogen, Na^+, or Ca^{2+} wastewater into the environment. Especially, in recent years, the concept of "green chemistry" has been paid more and more attention, and more and more constraining environmental regulations have been adopted to limit the industrial pollution. Although the neutral extractants can alleviate the problem to some extent via formation of the neutral target metal complex, the selectivity will be lower than that of acidic extractants. On the other hand, P507 and other extractants including neutral extractants tri-n-butylphosphate (TBP), di(1-methylheptyl)methyl phosphate (P350), and quaternary amine trioctyl methyl ammonium chloride (Aliquat 336) for the REEs extraction at high acidity will do harm to the operator and equipment, and produce a large

amount of acidic wastewater. Moreover, it is hard to completely strip off heavy REEs, such as Tm^{3+}, Yb^{3+}, and Lu^{3+} from the loaded organic phase even at higher acidity by using P507. TBP or P350 has high solubility and low extractability for the REEs, while Aliquat 336 needs SCN- or DTPA-complexing agents to enhance the REEs separation selectivity. So, developing a new extraction system for the REEs extraction and separation is important.

Ionic liquids (ILs) are of particular interest for the development of environmentally friendly solvent extraction systems, especially for REEs separation in hydrometallurgy, just due to their favorable properties such as negligible vapor pressure, low flammability, and high thermal stability. ILs can be function not only as diluents in solvent extraction systems but also as extractants, and both functions can even be combined in one IL. ILs used as extractants are known as functionalized ionic liquids (FILs) or task-specific ionic liquids (TSILs). FILs combining the properties of ILs with those of conventional extracting reagents served as both solvents and extractants. Another simple approach for designing FILs containing functional groups is to use a well-known anionic complexing agent. The extraction of REEs can be achieved by using these FILs with specific REEs-coordinating groups anchored to the cation or anion. So FILs with the functional moiety as part of the cation or anion attracted strong interest as novel extractants for REEs extraction and separation. It is evident that ILs for use in solvent extraction systems should be immiscible with water by choosing a cation with long alkyl chains (e.g., CYPHOS® IL 101 or Aliquat® 336).

This chapter will review the recent developments of ILs in REEs separation, with a special emphasis on Bif-ILEs and IL-functionalized separation materials from our group. Besides the preparation of Bif-ILEs, we will discuss the extraction mechanisms and kinetics of Bif-ILEs, and the synergistic extraction from Bif-ILEs thus reveals highly efficient and environmentally friendly potential in REEs separation. In order to provide a supplement to liquid–liquid extraction, various IL-functionalized materials, demonstrating improved extraction efficiency toward REEs, are also commended.

5.2 Preparation and Classification of ILs for REEs Separation

5.2.1 General Terms and Signs for Extraction Procedure

5.2.1.1 Distribution Ratio (*D*)

Distribution ratio or distribution coefficient is the ratio of the concentration of the metal ion (REEs in this chapter) in the organic phase (IL phase) to the concentration of the metal ion in the aqueous phase at equilibrium, and is calculated by the following equation:

$$D = \frac{[\mathrm{RE}]_{\mathrm{IL}}}{[\mathrm{RE}]_{\mathrm{aq}}} \tag{5.1}$$

D shows the extractant extractability for RE ions in a certain condition. Actually, the distribution ratio also can be calculated most conveniently by measuring the concentration of RE ion in aqueous phase after extraction and initial concentration

$$D = \frac{[\mathrm{RE}]_{\mathrm{i}} - [\mathrm{RE}]_{\mathrm{f}}}{[\mathrm{RE}]_{\mathrm{f}}} \tag{5.2}$$

where $[\mathrm{RE}]_{\mathrm{i}}$ and $[\mathrm{RE}]_{\mathrm{f}}$ are the concentrations of the RE ions in the aqueous phase before (i = initial) and after extraction (f = final), respectively. The results show that the bigger the D value is, the stronger the extractability is; that means extracted REEs will easily be extracted into organic phase.

5.2.1.2 Extraction Efficiency ($E\%$)

$E\%$ is defined as the amount of metal extracted to the ionic liquid phase over the total amount of metal in both phases and is given by the following expression:

$$E\% = \frac{[\mathrm{RE}]_{\mathrm{IL}} \times \mathrm{V}_{\mathrm{IL}}}{[\mathrm{RE}]_{\mathrm{IL}} \times \mathrm{V}_{\mathrm{IL}} + [\mathrm{RE}]_{\mathrm{aq}} \times \mathrm{V}_{\mathrm{aq}}} \times 100\ \% \tag{5.3}$$

When $V_{\mathrm{aq}} = V_{\mathrm{IL}}$, the extraction efficiency is a function of the distribution ratio and can be evaluated:

$$E\% = \frac{D}{D + V_{\mathrm{aq}}/V_{\mathrm{IL}}} \times 100 = \frac{D}{D+1} \times 100\ \% \tag{5.4}$$

So the bigger the D value, the higher the $E\%$. So, in order to improve extraction efficiency, it's necessary to find new suitable extractants and search the optimal technological condition.

5.2.1.3 Separation Factor (β)

β is the distribution coefficient ratio between two isolated REEs:

$$\beta = \frac{D_{\mathrm{RE}_1}}{D_{\mathrm{RE}_2}} = \frac{[\mathrm{RE}_1]_{\mathrm{IL}}}{[\mathrm{RE}_1]_{\mathrm{aq}}} \times \frac{[\mathrm{RE}_2]_{\mathrm{aq}}}{[\mathrm{RE}_2]_{\mathrm{IL}}} \tag{5.5}$$

It can express separation capability of the extractants and provides a basis for REE separation. More importantly, the value of β can be used to evaluate the separation effect of two neighboring REEs. If $D_{\mathrm{RE}_1} = D_{\mathrm{RE}_2}$, $\beta = 1$ and it indicated that the extractant can't separate two REEs.

5.2.1.4 Stripping Ratio (*St*)

After the REEs have been extracted into the ILs, it is generally required to return to the aqueous phase. At this time, the loaded ILs are contacted with a stripping agent (usually an inorganic acid, base aqueous solution, or pure water), which makes the REEs transfer to water phase. This process is equivalent to the inverse process of extraction, hence called stripping or back extraction. The water phase from the back extraction is called the stripping solution, and the ILs from the back extraction are regarded as renewable ILs which could be returned to the extraction process. *St* is defined as the ratio of the equilibrium concentration of REEs in the stripping solution to the initial concentration of REEs in ILs:

$$St\% = \frac{[\mathrm{RE}]_{\mathrm{aq}}}{[\mathrm{RE}]_{\mathrm{IL}}} \times 100\ \% \tag{5.6}$$

5.2.2 Preparation of Bif-ILEs

In recent years, the quaternary ammonium-functionalized ILs have been investigated widely because of its cheap, low toxicity properties. A kind of ILs was designed and synthesized by tricaprylmethylammonium chloride (Aliquat 336 or A336) and traditional carboxylic acid and phosphoric acid extractant [2]. Because the cation and anion of this kind of ILs are all the functional group for the REEs extraction, we called them bifunctional ionic liquid extractants (Bif-ILEs). Bif-ILEs could be synthesized by acid/base neutralization, and this reaction process was under mild condition, with easier purification and good yield (about 70–80 %).

5.2.2.1 Acid/Base Neutralization Method

Acid/base neutralization using hydroxide-based IL and acid has been indicated to be an effective method for preparing halide-free ILs. The preparation of hydroxide-based IL could be achieved by ion exchange between halide IL precursor with silver hydroxide or solid potassium hydroxide, ion exchange resin, and electrodialysis membrane. Our lab studied a novel engineering-purpose acid/base neutralization strategy for preparing Bif-ILEs. Take [A336][P204] as an example. Figure 5.1 shows the synthetic route of Bif-ILEs by acid/base neutralization reaction. Figure 5.2 shows the structure of Bif-ILEs synthesized by acid/base neutralization reaction.

5.2.2.2 [A336][OH] ([Trialkylmethylammonium][Hydroxide])

Sodium alkoxide was prepared by combining 6.39 g (0.278 mol) sodium and 125 ml isopropanol for 3 h; 112.36 g (0.278 mol) Aliquat 336 was dissolved in 500 ml of isopropanol and added dropwise into the ethanol solution containing sodium alkoxide. The solutions were stirred for 4 h at 323 K. The mixture was centrifuged at

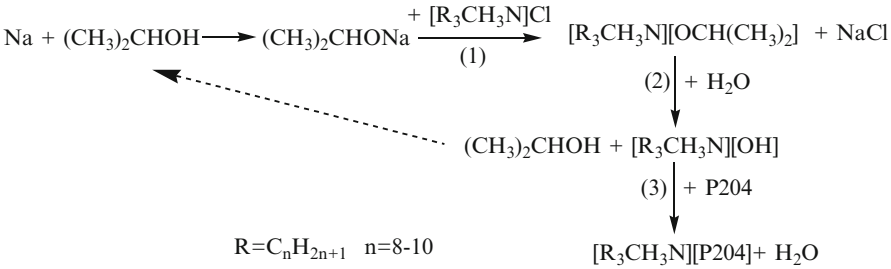

Fig. 5.1 Synthetic route of Bif-ILEs by acid/base neutralization reaction: (*1*) anion exchange, (*2*) hydrolysis, (*3*) acid/base neutralization

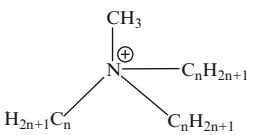

n=8~10

[A336]$^{+}$

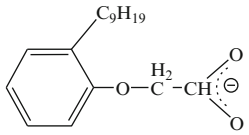

[CA-100]$^{-}$

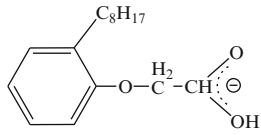

[CA-12]$^{-}$

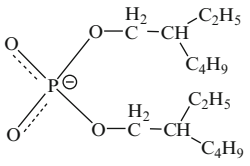

[P204]$^{-}$

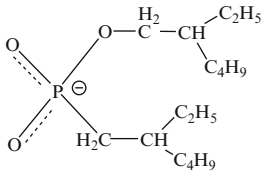

[P507]$^{-}$

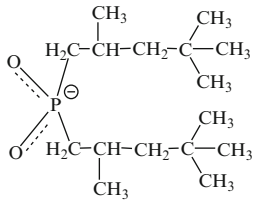

[Cyanex 272]$^{-}$

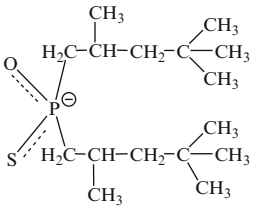

[Cyanex 302]$^{-}$

Fig. 5.2 The structure Bif-ILEs synthesized by acid/base neutralization reaction. ([A336]$^{+}$–tricaprylmethylammonium cation, [CA-100]$^{-}$–sec-nonylphenoxy acetic anion, [CA-12]$^{-}$–sec-octylphenoxy acetic anion, [P204]$^{-}$–di-2-ethylhexylphosphate anion, [P507]$^{-}$–di(2-ethylhexyl) orthophosphinate anion, [CYANEX 272]$^{-}$–bis(2,4,4-trimethylpentyl) phosphinic anion, [CYANEX 302]$^{-}$–bis(2,4,4-trimethylpentyl) monothiophosphinic anion)

8000 r/min for 10 min to remove the white precipitate of sodium chloride. Then, the filtrates were shaken with equal volume of DI water for half an hour to get [A336][OH] by the hydrolysis of [A336][OR]. The yield of [A336][OH] was 88.42 %.

5.2.2.3 [A336][CA-12] ([Trialkylmethylammonium][Sec-octylphenoxy acetate])

[A336][CA-12] was prepared by combining [A336][OH] and sec-octylphenoxy acetic acid (CA-12) (mole ratio is 1.1:1). The mixture was vigorously agitated for 12 h at 323 K under reflux and left to settle. After a while, an aqueous layer formed at the bottom. The upper phase was poured into a vacuum rotatory evaporator (353 K, 20 mbar, 60 min) to remove residual water and isopropanol. The final yield of [A336][CA-12] was 71.57 %.

5.2.2.4 [A336][CA-100] ([Trialkylmethylammonium][Sec-nonylphenoxy acetate])

[A336][CA-100] was prepared by the same procedure as [A366][CA-12], and sec-nonylphenoxy acetate acid (CA-100) was used instead of CA-12. The final yield of [A336][CA-100] was 78.69 %.

5.2.2.5 [A336][P204] ([Trialkylmethylammonium][Di-2-ethylhexylphosphate])

The synthesis of [A336][P204] followed the same procedure as [A366][CA-12], and di-2-ethylhexylphosphate acid (P204) was used instead of CA-12. The final yield of [A336][P204] was indicated to be 84.94 %. [A336][P507] ([trialkylmethylammonium][di-(2-ethylhexyl)orthophosphinate]), [A336][CYANEX 272] ([trialkylmethylammonium][bis(2,4,4-trimethylpentyl) phosphinate]), and [A336][CYANEX 302] ([trialkylmethylammonium][bis(2,4,4-trimethylpentyl) monothiophosphinate]) were prepared in an similar way, and the yield of Bif-ILEs was up to 70 %.

5.2.3 Bif-ILEs for REE Separation

A series of novel Bif-ILEs with ammonium-based cations and different anions have been applied in REEs extraction, for example, [A336][P204], [A336][P507], [A336][CA-12], [A336][CA-100], and [A336][CYANEX 272].

Extraction abilities of traditional organic phosphonic acids and organic carboxylic acids are restrained to a considerable extent since the intermolecular hydrogen bonds form dimers. In addition, the hydrogen ions released from acidic extractants in ion exchange mechanism (Equation (5.7)) affect negatively the metal ion extraction due to the increase of acidity in aqueous phase. To overcome the disadvantages, saponification of acidic extractant is a widely used method. Though ammonization of acidic extractants, the hydrogen bonds in dimers are partly broken (Equation (5.8)) and the extraction processes for REEs become more easier. Although saponification can enhance the extraction capacities of acidic extractants, the resulting loss of ammonium ion into the aqueous phase causes ammonia pollution (Equation (5.9)):

$$M^{n+}{}_{aq} + nH_2L_{2(o)} \rightleftharpoons M(HL_2)_{n(o)} + nH^+{}_{aq} \tag{5.7}$$

$$H_2L_{2(o)} + NH_3H_2O \rightleftharpoons NH_4{}^+(HL_2)^-{}_{(o)} + H_2O \tag{5.8}$$

$$M^{n+}{}_{aq} + nNH_4{}^+(HL_2)^-{}_{(o)} \rightleftharpoons M(HL_2)_{n(o)} + nNH_4{}^+{}_{aq} \tag{5.9}$$

The distribution coefficient (D) of Bif-ILEs for RE^{3+} is obviously higher than the corresponding mixtures of their precursors. For example, the ratio of distribution coefficients for Eu^{3+} extraction between [A336][P204] and their mixed precursors (A336 + P204) can reach 27.86 times in hydrochloric acid media. The highest ratio of distribution coefficients for Eu^{3+} extraction between [A336][P507] and their mixed precursors (A336 + P507) can be up to more than 70 times in nitric acid media. The phenomenon was attributed to the strong ion-pair interactions in Bif-ILs, such as electrostatic interaction, van der Waals force, and induction interaction. The inner synergistic effect and neutral complexing mechanism were proposed by investing the extraction of Eu^{3+} in nitric acid media using [A336][P204] [3]:

$$Eu^{3+}{}_{aq} + 3[A366][P204]_{IL} + 3NO_3{}^-{}_{aq} \rightleftharpoons Eu(NO_3)_3 3[A366][P204]_{IL} \tag{5.10}$$

The coordination ability and stability of $[A336]^+$ and $[P204]^-$ with Eu^{3+} are crucial for explaining the higher extraction ability and selectivity of [A336][P204]. On the other hand, H^+ was not involved in the extraction process, and these extractants could obtain higher extraction efficiency at lower acidity. The separation factor (β) values of heavy RE^{3+} extracted by [A336][P204] in HNO_3 are shown in Table 5.1 [4]. The β values of heavy RE^{3+} indicated that the heavy RE^{3+} could be separated from each other.

The average $\beta_{z+1/z}$ values of RE^{3+} from La^{3+} to Lu^{3+} by [A336][P204] and [A336][P507] in HNO_3 were 3.67 and 3.61 by calculation. The $\beta_{z+1/z}$ values of RE^{3+} by P204 and P507 in HNO_3 were 2.55 and 3.04. The $\beta_{z+1/z}$ values of TBP and P350 (di(1-methylheptyl)methyl phosphate) in HNO_3 were 1.56 and 1.16, respectively. Therefore, the $\beta_{z+1/z}$ value of [A336][P204] and [A336][P507] in HNO_3 was higher than those of P507, P204, TBP and P350; In addition, TBP and P350 extract RE^{3+} at high acid concentration in HNO_3. Therefore, [A336][P204] and [A336][P507] in nitric acid media would be suitable for heavy RE^{3+} separation at low acidity.

Table 5.1 Separation factor (β) of heavy RE^{3+} extracted by [A336][P204] in HNO_3[a]

RE(III)	Er	Tm	Yb	Lu
Ho	6.93	23.3	184	1577
Er		3.36	26.6	227
Tm			7.92	67.8
Yb				8.55

Reprinted with the permission from Ref. [4] Copyright © 2014, American Chemical Society
[a][[A336][P204]] = 0.05 $mol \cdot L^{-1}$, $[RE^{3+}]_{initial} = 7.5 \times 10^{-4}$ $mol \cdot L^{-1}$, $[NaNO_3]_{initial} = 1.0$ mol L^{-1}, $pH_e \approx 1.73$

Table 5.2 Separation factor (β) of Y^{3+} and heavy RE^{3+} in HNO_3[a]

	Y/Gd	Y/Tb	Y/Dy	Y/Ho	Y/Er	Tm/Y	Yb/Y	Lu/Y
[A336][P507]	138	8.58	4.61	11.2	1.98	1.62	7.01	7.49
[A336][P204]	111	15.4	8.19	10.7	1.55	2.17	17.2	147

[a][[A336][P204]] = 0.05 $mol \cdot L^{-1}$, $[RE^{3+}]_{initial} = 7.5 \times 10^{-4}$ $mol \cdot L^{-1}$, $[NaNO_3]_{initial} = 1.0$ $mol \cdot L^{-1}$, $pH_e \approx 1.79$

It is widely known that the separation and purification of Y^{3+} from heavy RE^{3+} by liquid–liquid extraction are difficult because of their similar chemical properties. The β values of Y^{3+} and heavy RE^{3+} by [A336][P507] or [A336][P204] in HNO_3 are shown in Table 5.2 [4]. So the distribution coefficient of Y^{3+} was between that of Er^{3+} and Tm^{3+} with [A336][P507] or [A336][P204] as an extractant. Liu et al. reported that in the $HNO_3 - CYPHOS$ IL 104 system, the β values were Y/Gd (6.17), Y/Tb (8.57), Y/Dy (40.81), Y/Ho (14.55), Er/Y (1.83), Tm/Y (2.06), Yb/Y (10.92), and Lu/Y (4.60), respectively [5]. Therefore, the β values indicated that Y^{3+} can be separated from other heavy RE^{3+}.

When using [A336][CA-12] or [A336][CA-100] as an extractant in HCl, the similar mechanism can be achieved [6]:

$$Ln^{3+}{}_{aq} + 4[A336][CA-12]/[A336][CA-100]_{(IL)} + 3Cl^{-}{}_{aq} \rightleftharpoons LnCl_3 \cdot 4[A336][CA-12]/[CA-100]_{(IL)} \quad (5.11)$$

The data obtained from RE^{3+} extraction are used to calculate the β of RE^{3+} pairs in both [A336][CA-12] and [A336][CA-100] extraction systems, the results are shown in Table 5.3 [6]. Comparing the two extraction systems, the β values of La^{3+} with other RE^{3+} in [A336][CA-12] extraction system are higher than those in [A336][CA-100] extraction system. The reason may be that [A336][CA-100] has higher extraction ability for RE^{3+} than [A336][CA-12], which results in less selectivity for RE^{3+} extraction in [A336][CA-100] system. When [A336][CA-12] was used to separate of RE^{3+}, the results show that the $\beta_{z+1/z}$ values of Ce/La, Nd/La, and Pr/La are 3.18, 2.89, and 3.56, respectively. It indicates that [A336][CA-12] in hydrochloric acid media has potential application for La^{3+} separation.

Table 5.3 Separation factors (β) of La/RE in HCl by [A336][CA-12] and [A336][CA-100][a]

	La/Ce	La/Pr	La/Nd	La/Sm	La/Eu	La/Gd	La/Tb
[A336][CA-12]	6.89	7.89	8.78	10.2	10.1	10.2	8.44
[A336][CA-100]	2.73	4.16	4.68	5.64	5.93	5.69	4.89
	La/Dy	La/Ho	La/Er	La/Tm	La/Yb	La/Lu	
[A336][CA-12]	10.9	6.56	9.44	8.56	5.67	11.8	
[A336][CA-100]	7.13	2.09	6.28	4.68	3.18	8.04	

[a][Extractant] = 0.05 mol · L^{-1}, $[RE^{3+}]_{initial} = 1.0 \times 10^{-3}$ mol · L^{-1}, $[NaCl]_{initial} = 1.0$ mol · L^{-1}, $pH_e \approx 4.8$

Table 5.4 Separation factor (β) of light RE^{3+} extracted by [A336][P507] in HCl[a]

β ([A336][P507])	Ce	Pr	Nd	Sm
La	2.03	2.62	24.9	117
Ce		1.29	12.3	57.7
Pr			9.52	44.7
Nd				4.70

[a][Extractant] = 0.05 mol · L^{-1}, $[RE^{3+}]_{initial} = 7.5 \times 10^{-4}$ mol · L^{-1}, $[NaCl]_{initial} = 1.0$ mol · L^{-1}, $pH_e \approx 2.96$

The β values of RE^{3+} by [A336][P507] in HCl were explored; these β values of light RE^{3+} are shown in Table 5.4 [4]. The β values of adjacent light RE^{3+} indicated that the light RE^{3+} could be separated from each other. Especially, when [A336][P507] was used as the extractant, the significantly large β values of Nd/Pr and Sm/Nd were obtained to be 9.52 and 4.70, respectively. Additionally in HCl, when P507 was utilized, both the corresponding β values were 1.17 and 2.00. Therefore, the [A336][P507] could enhance the separation ability. [A336][P507] was suitable for light RE^{3+} separation in HCl. The $\beta_{z+1/z}$ value of RE^{3+} form La^{3+} to Lu^{3+} by [A336][P507] was 2.75. While the corresponding $\beta_{z+1/z}$ value for P507 was 1.57.

With the increasing of atomic number of RE^{3+}, the variation of log D by [A336][P507] or [A336][P204] is shown in Fig. 5.3 [4]. In hydrochloric acid media, the variation trend of log D using [A336][P507] or [A336][P204] as extractant was similar to that with solitary P507 or P204 as the extractant. The position of Y^{3+} extracted by [A336][P204] was between Dy^{3+} and Ho^{3+}, and that extracted by [A336][P507] was between Er^{3+} and Tm^{3+}. In HNO_3 medium, the value of log D increased with the increasing of atomic number of RE^{3+} from Ho^{3+} to Lu^{3+}. At the same time, the D value of each RE^{3+} extracted by [A336][P204] was higher than that of [A336][P507] at the same condition. The position of Y^{3+} extracted by [A336][P507] or [A336][P204] was between Er^{3+} and Tm^{3+} in HNO_3. As shown in Fig. 5.3, in the circumstance of a different medium, the extraction sequence was different with the same extractant. The extraction sequence of RE^{3+} is closely related to the extractants and extraction medium. For example, in HCl, the selectivity of [A336][P507] and [A336][P204] on light RE^{3+} separation was higher.

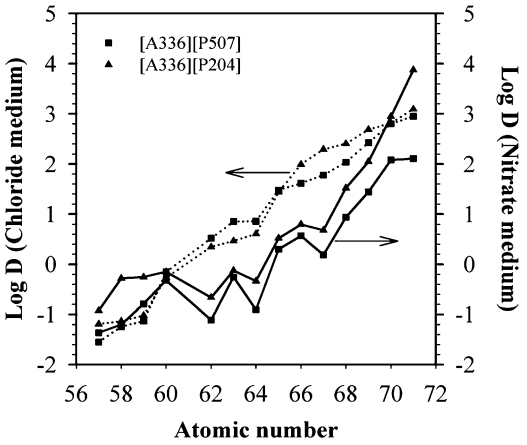

Fig. 5.3 The relationship between the distribution ratio (D) and atomic number of RE^{3+} (−−represent extraction in HNO_3, [extractant] = 0.05 mol · L^{-1}, $[RE^{3+}]_{initial} = 7.5 \times 10^{-4}$ mol · L^{-1}, $[NaNO_3]_{initial} = 1.0$ mol L^{-1}, $pH_e = 1.50$; . . .represent extraction in HCl, [extractant] = 0.05 mol L^{-1}, $[RE^{3+}]_{initial} = 7.5 \times 10^{-4}$ mol L^{-1}, $[NaCl]_{initial} = 1.0$ mol L^{-1}, $pH_e = 2.50$)

And in HNO_3 , the selectivity of [A336][P507] and [A336][P204] on heavy RE^{3+} separation was higher. When Bif-ILEs [A336][P507] and [A336][P204] were used in RE^{3+} separation, both the cation and anion of Bif-ILE combined with RE^{3+} and formed the bigger extracted complex as mentioned above. Then cation ($[A336]^+$) and anion ($[P507]^-$ or $[P204]^-$) all affect the RE^{3+}; this is the so-called inner synergistic effect. On the other hand, the extraction sequence of RE^{3+} was also attributed to the anion in aqueous phase. The variation of the extraction sequence in nitrate medium was different from that in chloride medium. The NO_3^- or Cl^- participated in forming the extracted complex. The property of NO_3^- or Cl^- could regulate the stability of the extracted complex and the selectivity of RE^{3+} extraction. On the other hand, the salting-out agent had beneficial effect on RE^{3+} extraction using neutral extractants. When the anion of the salting-out agent was the same as the anion of RE^{3+} in aqueous phase, adding the salting-out agent was equal to increasing the anion concentration of target metal ions. Then $E\%$ of RE^{3+} would be enhanced. So the neutral Bif-ILEs were found the same phenomenon on RE^{3+} extraction processes in hydrochloric acid or nitric acid media.

Cerium (Ce) is the highest REEs contents in the crust, which mainly comes from bastnaesite sources. The advanced technology for bastnaesite treatment is oxidation roasting, leaching with H_2SO_4, and then recovering REEs, fluorine (F), and thorium (Th) by solvent extraction. Cerium (III) (Ce^{3+}) is easily oxidized to Ce^{4+}, and it usually coexists with F^- in H_2SO_4 leaching solution. The extraction of Ce^{4+}, F^-, and Ce^{4+}–F^- mixture solution by [A336][P507] from H_2SO_4 is investigated, and the extraction mechanisms could be expressed as [7]

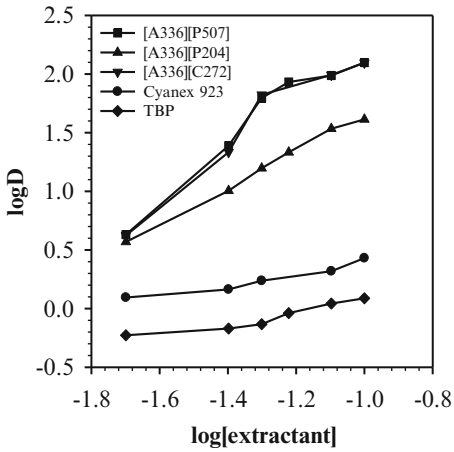

Fig. 5.4 Comparison of different extractants for the extraction of Ce^{4+} in Ce^{4+}–F^- mixture solution. Ce^{4+}–F^- mixed solution: $[Ce^{4+}] = 0.0107\ mol \cdot L^{-1}$, $[Ce_{(total)}] = 0.0138\ mol \cdot L^{-1}$, $[F^-] = 0.02\ mol \cdot L^{-1}$, $[H_2SO_4] = 0.06\ mol \cdot L^{-1}$ (Reprinted with the permission from Ref. [7]. Copyright © 2011 Elsevier B.V. All rights reserved)

$$Ce^{4+}{}_{aq} + 2HSO_4{}^-{}_{aq} + SO_4{}^{2-}{}_{aq} + [A336][P507]_{(IL)} \rightleftharpoons Ce(HSO_4)_2(SO_4) \cdot [A336][P507]_{(IL)} \quad (5.12)$$

$$CeF^{3+}{}_{aq} + HSO_4{}^-{}_{aq} + SO_4{}^{2-}{}_{aq} + 2[A336][P507]_{(IL)} \rightleftharpoons CeF(HSO_4)(SO_4) \cdot 2[A336][P507]_{(IL)} \quad (5.13)$$

The extraction of Ce^{4+}, F^-, and Ce^{4+}–F^- mixture solution with [A336][P507], CYANEX 923, and TBP under the same condition was compared, and the result was shown in Fig. 5.4 [7]. As seen in Fig. 5.4, log *D* increased with the increase of extractant concentration. The extraction ability of these extractants at the chosen acidity follows as [A336][P507] > CYANEX 923 > TBP. In fact, CYANEX 923 and TBP all have high extraction ability for Ce^{4+} or Ce^{4+}–F^- mixture solution under higher acidity condition. Compared with those extractants, [A336][P507] has almost the same even higher extraction ability, and the extraction acidity is lower, which reduces the consumption of acid.

The β value between Ce^{4+}, CeF^{3+}, and Ce^{3+} in the [A336][P507] extraction system was shown in Table 5.5 [7]. The largest β values of Ce^{4+}/Ce^{3+} and CeF^{3+}/Ce^{3+} were 3.32×10^3 and 6.94×10^2, which meant that Ce^{4+} and CeF^{3+} could be separated from Ce^{3+} and other RE^{3+} effectively. Figure 5.5 [7] showed the extraction of Ce^{3+}, Ce^{4+}, Ce^{4+} in Ce^{4+}–F^- mixture solution, and Th^{4+} with [A336][P507] in H_2SO_4. With increase of extractant concentration from 0.02 to 0.10 mol/L, the extraction efficiency of Ce^{4+}, Ce^{4+} in Ce^{4+}–F^- mixture solution, Th^{4+} and Ce(III) all increased. The extraction efficiency order followed as $Ce^{4+} > Th^{4+} > Ce^{3+}$. Therefore, it's possible to separate Ce^{4+} from Th^{4+} and Ce^{3+}. So the β values of REEs by Bif-ILEs in different media were predominantly affected by inner synergistic effect.

The stability and recycling of Bif-ILEs in different media were studied by a stripping process/repeated loading. Some RE^{3+} loaded by Bif-ILEs could be easily stripped by the low concentration H^+ (about $0.03\ mol \cdot L^{-1}$), and the value of *St* is

Table 5.5 The β values of Ce^{4+}/Ce^{3+} and CeF^{3+}/Ce^{3+} in [A336][P507] extraction system

$C_{extractant}$ (mol/L)	Ce^{4+}/Ce^{3+} [A336][P507]	CeF^{3+}/Ce^{3+} [A336][P507]
0.02	1.53×10^3	91.19
0.04	3.32×10^3	2.83×10^2
0.05	3.05×10^3	6.94×10^2
0.06	1.84×10^3	5.88×10^2
0.08	8.11×10^2	2.89×10^2
0.10	4.80×10^2	1.52×10^2

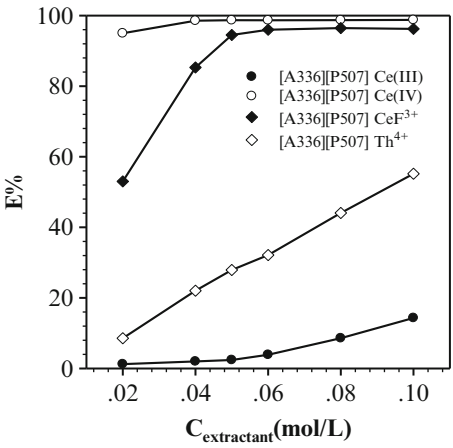

Fig. 5.5 Comparison of the extraction of Ce^{3+}, Ce^{4+}, Ce^{4+} in Ce^{4+}–F^- mixture solution, and Th^{4+}. $[Ce^{3+}] = 0.01\ mol \cdot L^{-1}$, $[Ce^{4+}] = 0.0100\ mol \cdot L^{-1}$, $[Ce_{(total)}] = 0.0105\ mol \cdot L^{-1}$, Ce^{4+}–F^- mixed solution: $[Ce^{4+}] = 0.0107\ mol \cdot L^{-1}$, $[Ce(total)] = 0.0138\ mol \cdot L^{-1}$, $[F^-] = 0.02\ mol \cdot L^{-1}$, $[Th^{4+}] = 2.0 \times 10^{-4}\ mol \cdot L^{-1}$, $[H_2SO_4] = 0.06\ mol \cdot L^{-1}$

more than 95 %, but part of RE^{3+} loaded by Bif-ILEs could not be stripped completely. Although the main extraction mechanisms by Bif-ILEs were proposed, it is still far away from the complete and detailed understanding of the extraction process. For example, Yb^{3+} can be partly stripped at $0.2\ mol \cdot L^{-1}$ H^+ in HCl, and this is possibly due to the forming of the new complex, $RE(Cl)_{3-n}[P204]_n \cdot (3\text{-}n)$ [A336][P204] ($n = 1$, 2, or 3), and the interaction of P – O···RE other than P = O···RE will greatly enhance the stability of the new complex, leading to the increased stripping acidity and low stripping ratio.

5.3 Kinetics of ILs for REE Separation

The extractions process using Bif-ILEs showed some advantages, such as no saponification wastewater, which is a remarkable advantage of the environmentally friendly extraction protocol, low acidy for extraction and good interfacial phenomena, and so on. The extraction results using [A336][CA-12] implied that the Bif-ILEs would have the prospects of potential applications for the La^{3+} separation in HCl. And in H_2SO_4 using [A336][P204], the results of the extraction and

recovery of Ce(IV) and F^- showed that the extraction systems exhibited strong separation ability [7]. So the Bif-ILEs may highlight considerable opportunities in such fields. In the extraction process, extraction thermodynamics of REEs with Bif-ILEs is closely related to the extraction kinetics. Extraction thermodynamics study the extraction mechanisms, and extraction kinetics characterizes the mass transfer velocity. That is, the extraction kinetics describes the process of two phases (the aqueous and ionic liquid phases) from the beginning to reach extraction equilibrium. And the kinetic parameters are signality to the design of industrial extractor. The faster the kinetics mass transfer, the shorter the residence time in the extractor and the smaller the volume of the extractor needed. Therefore, only when the speed of extraction is determined, the size of the extractor can be determined. In addition, the study of dynamics including the position of the extractive reaction and the key steps of influencing extraction rate can also help to further confirm the extraction mechanism. The internal factors influencing extraction rate are the extractive reaction rate and diffusion rate. The extractive reaction rate is mostly affected by the reaction type, the nature, and concentration of the extractants. The diffusion rate depends on diffusion product property and reactive medium.

In addition to extractive reaction, mass transfer is another important influence factor in the extraction process. When the mass transfer reached a stable state, the whole systems can keep a dynamic balance. The mass transfer happened between the aqueous phase and ILs, and the extraction kinetics interface of RE^{n+} ($n = 3$ or 4) in ILs was shown in Fig. 5.6. Because the mass transfer rate also affects the extraction rate, the rate of RE^{n+} extraction is determined both by the chemical reaction rate and the mass transfer rate. Which one is more important in the two main factors is up to the experimental conditions.

The two phases are separated from each other under severe mixing during the extraction process. There is an interface between them. Relatively slow movement exists between liquids on either side of the interface. It can be called the retention or interface layer. In this area, mass transfers through molecular diffusion. Mass transfer occurs through the interface; it is not only a longer path but also being more complex in this way. Far from the interface, due to the effect of stirring,

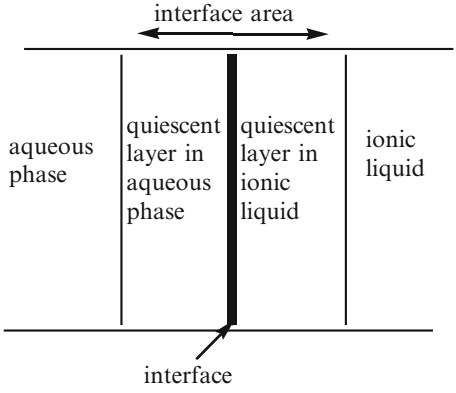

Fig. 5.6 The schematic view of interface area

two-phase fluids are respectively mixed strongly in the way of the turbulent flow of the fluid, so it is supposed to be a state of uniform. There are two main factors deciding the dynamics: one is the chemical reaction speed; the other is the diffusion effect. In this way, extraction kinetics can be divided into diffusion zone, dynamics zone, and mixed zone.

5.3.1 Dynamics Zone

When the transformation of interfacial material is much faster than the system's chemical reaction speed, the whole process of extraction can occur at the kinetics zone. That means there is a slow chemical reaction in the extraction system and also the thicknesses of two-phase diffusion films that are adjacent to the interface are almost zero, or we can say the mass goes through these membranes in a very fast way.

Experimental results show that when the extraction occurs in the dynamics zone, the controlled reaction mechanism would generally be described as follows: (1) coordination and substitution reaction in aqueous phase, (2) coordination on the interface, and (3) adsorption and stripping process on the interface.

These control steps in an extraction system may appear in any of these forms or more than one form at the same time.

5.3.2 Diffusion Zone

When the chemical reaction speed during solvent extraction is faster than the diffusion, the extraction is controlled by the diffusion speed only. In this case, the extraction process can be defined in the diffusion zone. When extraction reaction happened quickly in the interface area, assuming that the speed of every material entering and leaving the interface is equal, we can get a simplified model using mathematical processing. In short, in the real process of extraction, extractions are generally happening under strong mixing. So research in dynamics zone is of more practical significance, and the laws of the diffusion process focus on the theoretical knowledge. In the study of extraction kinetics, the diffusion effect cannot be completely ruled out.

5.3.3 Mixed Zone

When both the chemical reaction and diffusion rate have impact on the rate of extraction, the extraction process can be considered to happen in the mixed zone. Because of many factors influencing the extraction rate in the mixed zone, research is more difficult. At present, methods are all simplified as putting forward a simple approximate model and deducing the expressions of rate.

In order to study mass transfer rate, control step, and chemical reaction mechanism, same experimental equipments and techniques have been developed to investigate the extraction kinetics in traditional extractant systems, such as the single drop technique, rapid contact method, fully mixing method, the constant interfacial area stirred cell, the rotating membrane cell, etc. Diffusion membrane thickness will change with the fluid mechanics conditions inside the extraction equipment; only when the thickness is close to zero, the diffusion influence on extraction rate would disappear completely. Relatively, the constant interfacial area stirred cell is closer to the real extraction than the droplets, rapid contact method, and fully mixing method; it is more suitable for extraction kinetics research. In the constant interfacial area stirred cell, two phases are agitated independently without any mutual mixing; mass transfer happened at a constant interface. It was first designed by Louis and it is also called Lewis cell. A constant interfacial area cell with laminar flow developed by Zheng and Li is a new development of Lewis constant interface cell (Fig. 5.7) [8]. The experimental procedures are as follows:

Equal volume of the aqueous phase containing RE^{n+} and the organic phase containing Bif-ILE was introduced into the cell without much disturbing the interface. The motors, digital overhead stirrers (IKA® RW 20 digital), in aqueous phase and IL phase were employed for stirring. The rotation speed is adjusted with the rotary knob on the front plate and displayed on the LED display. The stirring speeds were controlled at the same value simultaneously in aqueous phase and organic phase to ensure these two phases can form laminar flow in reverse under the action of diversion board; then the mass transfer process occurred on the interfacial board. After each 3 min interval, 0.1 mL of the aqueous phase was taken through the sampling hole for analysis. The existing problem in using a constant interfacial cell

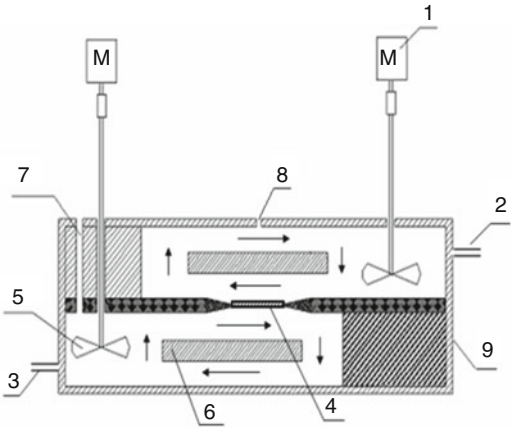

Fig. 5.7 Scheme of the constant interfacial area cell with laminar flow. (*1*, motor (LED display); *2*, outlet of the constant temperature water bath; *3*, inlet of the constant temperature water bath; *4*, interfacial board; *5*, stirrer; *6*, diversion board; *7*, sampling hole and injection hole for aqueous phase; *8*, injection hole for organic phase; *9*, wall of the constant interfacial area cell with laminar flow) (Reprinted with the permission from Ref. [8]. Copyright © 2014 The Nonferrous Metals Society of China. Published by Elsevier Ltd. All rights reserved)

Table 5.6 Study of systems and methods of the kinetics extraction of Ce^{4+}, Ce^{4+}–F^- and La^{3+} different extraction systems

System	Method	Ref.
Sc(III),Y(III), La(III), Gd(III)-HCl/CYANEX 302-*n*-heptane	Constant interfacial area cell with laminar flow	[9]
Ce(IV)-H_2SO_4/CYANEX 923-*n*-heptane	Constant interfacial area cell with laminar flow	[10]
Ce(IV)-F^--H_2SO_4/CYANEX 923-*n*-heptane	Constant interfacial area cell with laminar flow	[11]
Ce(IV), RE(III)-H_2SO_4/N1923-*n*-heptane	Hollow fiber membrane	[12]
Ce(IV)-H_2SO_4/N1923-*n*-heptane	Constant interfacial area cell with laminar flow	[13]
Ce(IV)-F^--HNO_3/DEHEHP-*n*-heptane	Constant interfacial area cell with laminar flow	[14]

with laminar flow for kinetics measurement is that the maximum error can reach up to ± 0.5 %.

Zheng and Li also put forward the use of liquid near the interface of the diagram of the linear velocity and extraction rate to determine the control mode. The cell is a rectangular cell, and impellers are respectively located at the ends of the cell. Fluid will reverse laminar flow in the guide plate. Because of the high mixing speed, the interface will maintain stability, and experiment is with good reproducibility.

Results performed by this instrument demonstrate that it is perfect to investigate extraction kinetics because of its stable interface and efficient forced convection. Table 5.6 showed the kinetics extraction study of La^{3+} or Ce^{4+} from different extraction systems.

The extraction kinetics of La^{3+} and Ce^{4+} using traditional extractants has been concerned widely. Therefore, the extraction kinetics of La^{3+} using [A336][CA-12] in HCl [15] and Ce^{4+} or Ce^{4+}–F^- mixture systems using [A336][P204] in H_2SO_4 [8] were also investigated by a constant interfacial cell with laminar flow, following the thermodynamic investigation.

The experimental data were calculated following the theoretical formulas deduced by Danesi [16]. Assuming that the mass transfer process could be formally treated as a pseudo-first-order reversible reaction with respect to the metal cation,

$$RE^{n+}{}_{aq} \rightleftharpoons RE^{n+}{}_{IL} \tag{5.14}$$

And the mass transfer rate equation for RE^{n+} can be expressed as

$$-\frac{d[RE_{IL}]}{dt} = \frac{\left(k_{ao} \cdot [RE]^{t}_{aq} - k_{oa} \cdot [RE]^{t}_{IL}\right) \cdot A}{V} \tag{5.15}$$

where k_{ao} and k_{oa} are forward pseudo-first-order rate constant and backward pseudo-first-order rate constants (cm/s), respectively. $[RE]^{t}_{aq}$ and $[RE]^{t}_{IL}$ are the

concentrations of RE^{n+} in the aqueous phase and IL at the time "t." A is the specific interfacial area (cm^2), and V is the volume of aqueous phase or IL (mL). By setting

$$[\mathrm{RE}]_{\mathrm{IL}}^{\mathrm{t}} = [\mathrm{RE}]_{\mathrm{aq}}^{\mathrm{ini}} - [\mathrm{RE}]_{\mathrm{aq}}^{\mathrm{t}} \tag{5.16}$$

And the mass transfer rate is zero at equilibrium, that is,

$$-\frac{d[RE_{IL}]}{dt} = 0 \tag{5.17}$$

It follows:

$$k_{\mathrm{ao}} \cdot [\mathrm{RE}]_{\mathrm{aq}}^{\mathrm{e}} - k_{\mathrm{oa}} \cdot \left([\mathrm{RE}]_{\mathrm{aq}}^{\mathrm{ini}} - [\mathrm{RE}]_{\mathrm{aq}}^{\mathrm{e}}\right) = 0 \tag{5.18}$$

That is,

$$(k_{\mathrm{ao}} + k_{\mathrm{oa}}) \cdot [\mathrm{RE}]_{\mathrm{aq}}^{\mathrm{e}} = k_{\mathrm{oa}} \cdot [\mathrm{RE}]_{\mathrm{aq}}^{\mathrm{ini}} \tag{5.19}$$

where (e) represents the equilibrium concentration of RE^{n+} and (ini) is the initial concentration of RE^{n+}. Thus, the relationship between k_{ao} and k_{oa} is as follows:

$$k_{\mathrm{oa}} = k_{\mathrm{ao}} \cdot \frac{[\mathrm{RE}]_{\mathrm{aq}}^{e}}{[\mathrm{RE}]_{\mathrm{aq}}^{\mathrm{ini}} - [\mathrm{RE}]_{\mathrm{aq}}^{e}} \tag{5.20}$$

By integrating mass transfer rate equation, we obtain

$$\frac{[\mathrm{RE}]_{\mathrm{aq}}^{\mathrm{ini}} - [\mathrm{RE}]_{\mathrm{aq}}^{e}}{[\mathrm{RE}]_{\mathrm{aq}}^{\mathrm{ini}}} \ln \frac{[\mathrm{RE}]_{\mathrm{aq}}^{\mathrm{ini}} - [\mathrm{RE}]_{\mathrm{aq}}^{e}}{[\mathrm{RE}]_{\mathrm{aq}}^{t} - [\mathrm{RE}]_{\mathrm{aq}}^{e}} = -\frac{A}{V} k_{\mathrm{ao}} \cdot t \tag{5.21}$$

or

$$\frac{[\mathrm{RE}]_{\mathrm{aq}}^{e}}{[\mathrm{RE}]_{\mathrm{aq}}^{\mathrm{ini}}} \ln \frac{[\mathrm{RE}]_{\mathrm{aq}}^{\mathrm{ini}} - [\mathrm{RE}]_{\mathrm{aq}}^{e}}{[\mathrm{RE}]_{\mathrm{aq}}^{t} - [\mathrm{RE}]_{\mathrm{aq}}^{e}} = -\frac{A}{V} k_{\mathrm{oa}} \cdot t \tag{5.22}$$

In the above expressions, the function $\left\{\left([\mathrm{RE}]_{\mathrm{aq}}^{\mathrm{ini}} - [\mathrm{RE}]_{\mathrm{aq}}^{e}\right) / [\mathrm{RE}]_{\mathrm{aq}}^{\mathrm{ini}}\right\} \cdot \ln\left([\mathrm{RE}]_{\mathrm{aq}}^{\mathrm{ini}} - [\mathrm{RE}]_{\mathrm{aq}}^{e}\right) / \left([\mathrm{RE}]_{\mathrm{aq}}^{t} - [\mathrm{RE}]_{\mathrm{aq}}^{e}\right)$ versus time t was plotted for each experiment. The slopes of the plots were used to calculate k_{ao} and k_{oa}. If all plots gave straight lines, the mass transfer process could be treated as a pseudo-first-order reversible reaction with respect to RE^{n+}.

The influences of stirring speed, specific interfacial area, and temperature on the extraction rate in both systems were discussed, suggesting that the extraction processes were slightly different in different Bif-ILE systems. Figure 5.8 [8, 15]

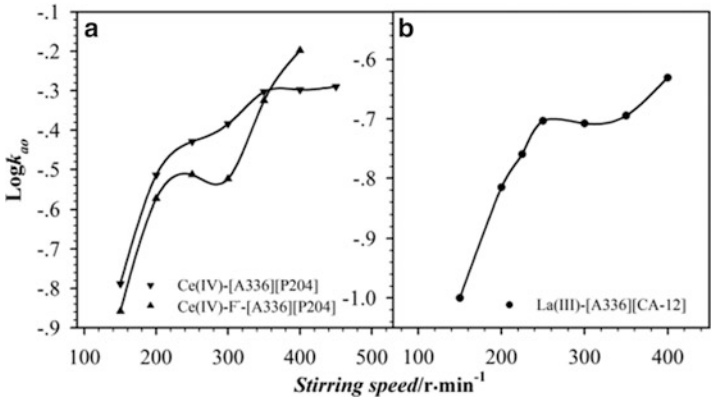

Fig. 5.8 Dependence of $\mathrm{Log}k_{ao}$ on stirring speed. Ce^{4+} extraction system: $[Ce^{4+}] = 0.01\ mol \cdot L^{-1}$, $[H_2SO_4] = 0.06\ mol \cdot L^{-1}$, $[[A336][P204]] = 0.10\ mol \cdot L^{-1}$, $A = 18.0\ cm^2$, $V = 90.0\ cm^3$, 298 K; Ce^{4+}–F^- mixture system: $[Ce^{4+}] = 0.01\ mol \cdot L^{-1}$, $[F^-] = 0.02\ mol \cdot L^{-1}$, $[H_2SO_4] = 0.06\ mol \cdot L^{-1}$, $[[A336][P204]] = 0.10\ mol \cdot L^{-1}$, $A = 18.0\ cm^2$, $V = 90.0\ cm^3$, 298 K; La^{3+} extraction system: $[La^{3+}] = 1.0 \times 10^{-3}\ mol \cdot L^{-1}$, $[NaCl] = 1.0\ mol \cdot L^{-1}$, $[[A336][CA\text{-}12] = 0.05\ mol \cdot L^{-1}$, $A = 18.0\ cm^2$, $V = 90.0\ cm^3$, 298 K

showed the effect of the stirring speed on the extraction rate constant k_{ao} of RE^{n+}(La^{3+}, Ce^{4+} and Ce^{4+}–F^-). The extraction rate exhibited a kinetics plateau when the stirring speed was in the range from 250 to 350 rpm in La^{3+}-[A336][CA-12] or Ce^{4+}–F^--[A336][P204] extraction system and 350–450 rpm in Ce^{4+}-[A336][P204] extraction system, respectively. The extraction rate increased in Ce^{4+}–F^--[A336][P204] or La(III)-[A336][CA-12] extraction system due to the waving observed at the interface. In a constant interfacial cell, the relationship of the extraction rate versus stirring speed was into a straight line in the early stage of the extraction reaction. The possible reason is that the stationary interfacial film is thicker at a lower stirring speed and diffusion limits the rate of an extraction with a relatively fast chemical reaction. With the increasing of the stirring speed, the interfacial film becomes thinner, and the diffusion resistance becomes smaller. Above a certain stirring speed, the increasing of stirring speed will not cause the increasing of extraction rate, that is, the "plateau region." The presence of the "plateau region" in the extraction rate versus stirring speed curve indicated that the extraction rate may be kinetics controlled. However, a "plateau region" can be also generated by other phenomena. And it is still possible that in spite of the experimentally determined independence of extraction rate on the stirring speed, the extraction rate is still diffusion controlled or at least not fully kinetics controlled. Therefore, the mass transfer in RE^{n+} extraction systems (Ce^{4+}-[A336][P204], Ce^{4+}–F^--[A336][P204], and La^{3+}-[A336][CA-12]) is a diffusion-controlled regime, and it is necessary with the help of other approaches to identify the extraction regime.

The effect of specific interfacial area on the extraction rate can also be used as one of the criteria for the rate-controlling step. If the reaction was controlled by diffusion control or mixed kinetic control regime, both stirring speed and specific

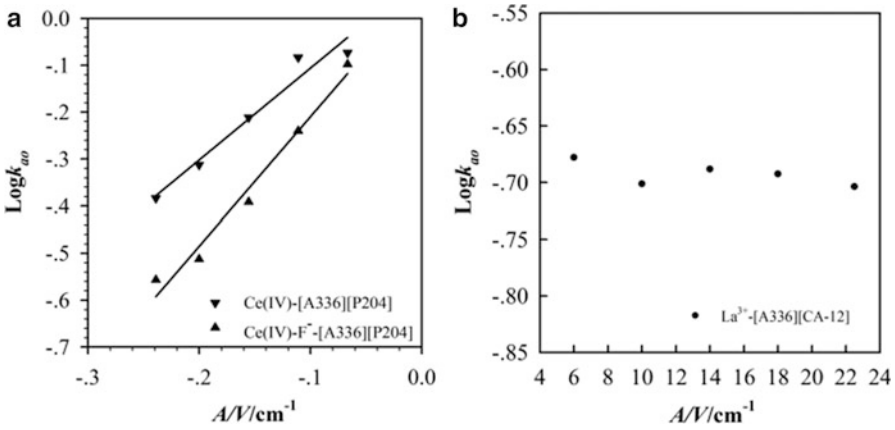

Fig. 5.9 Dependence of $Logk_{ao}$ on specific interfacial area. Ce^{4+} extraction system (**a**): $[Ce^{4+}] = 0.01\ mol \cdot L^{-1}$, $[H_2SO_4] = 0.06\ mol \cdot L^{-1}$, $[[A336][P204]] = 0.10\ mol \cdot L^{-1}$, rpm = 350 r/min, $V = 90.0\ cm^3$, 298 K; Ce^{4+}–F^- mixture system (a): $[Ce^{4+}] = 0.01\ mol \cdot L^{-1}$, $[F^-] = 0.02\ mol \cdot L^{-1}$, $[H_2SO_4] = 0.06\ mol \cdot L^{-1}$, $[[A336][P204]] = 0.10\ mol \cdot L^{-1}$, rpm = 250 r/min, $V = 90.0\ cm^3$, 298 K; La^{3+} extraction system (**b**): $[La^{3+}] = 1.0 \times 10^{-3}\ mol \cdot L^{-1}$, $[NaCl] = 1.0\ mol \cdot L^{-1}$, $[[A336][CA-12]] = 0.05\ mol \cdot L^{-1}$, rpm = 250 r/min, $V = 90.0\ cm^3$, 298 K

interfacial area will affect the extraction rate. If the reaction is chemical reaction control, according to the reaction position, it will be bulk phase reaction control, interfacial reaction control, or mixed bulk phase–interfacial reaction control. The reaction position can be deduced by studying how the initial rate of extraction varies with the specific interfacial area A/V (interfacial area/phase volume). If the initial rate will be independent on interfacial area, the chemical reactions occur in the bulk phases. On the contrary, the reaction will occur at the interface if the extraction rate and the interfacial area are in the direct proportionality relationship and the straight line goes through the origin. In addition, other linear relationships will be regarded as mixed bulk phases–interfacial area control process.

Figure 5.9 [8, 15] showed the linear relationship of $Logk_{ao}$ versus A/V in RE^{n+} extraction systems. The linear relationships in Ce^{4+}-[A336][P204] and Ce^{4+}–F^--[A336][P204] extraction systems were obtained (Fig. 5.9a). The results indicated that the reaction may be mixed bulk phases–interfacial area control processes. But in La^{3+}-[A336][CA-12] extraction system (Fig. 5.9b), the initial rate was independent on the interfacial area, and the chemical reaction possibly occurs in the aqueous homogeneous phases.

The apparent activation energy (Ea) of the extraction process is a further criterion to distinguish a diffusion-controlled process and a kinetics-controlled process by calculating Arrhenius equation. Generally, when Ea of an extraction is more than 42 KJ/mol, the extraction process is controlled by chemical reaction. When Ea is lower than 20 KJ/mol, species diffusion is the rate-limiting step. The extraction rate is determined by both chemical reaction and diffusion when Ea is in the range from 20 to 42 KJ/mol. However, Danesi reported that Ea is not sufficient

for the judgment of the kinetics process in the multicomponent chemical reaction system. Therefore, several comprehensive analysis ways are needed for the determination of the control procedures. In fact, if the rate is controlled by a chemical reaction, *E*a is usually higher than that of the diffusion control. However, *E*a value of many chemical solvent extraction processes is only a few kcal/mol, that is, the magnitude order is the same as *E*a of the diffusion process. So the apparent activation energy (*Ea*) judgment method is not very strict.

On the other hand, the concentrations of Bif-ILEs and salting-out agent also affect the extraction rate constant k_{ao} in RE^{n+} extraction systems. The kinetics models were deduced from the rate-controlling step, and the corresponding rate equations for RE^{n+} extraction systems can be obtained by the equimolar series method and the slope method.

Extraction kinetics not only provides useful information for optimizing processes but also is helpful in clarifying the mechanism of extraction. Hence, it is necessary to investigate the extraction kinetics of rare earths with Bif-ILEs and understand the extraction mechanism and mass transfer models. The solution of these problems associated with dynamic separation will undoubtedly facilitate the practical development of Bif-ILEs in REE separation.

5.4 IL-Functionalized Materials for REE Separation

Recently, separation and recovery of REEs from dilute solutions have received increasing attention in view of resource sustainable development and environmental improvement. However, solvent extraction processes are generally designed from concentrated solutions, and supplement processes should be used for the treatment of dilute solutions. In comparison, liquid-solid extraction is a simpler and greener alternative. Ion exchange resins and extraction resins have been used with respect to REE separation and purification. Based on the interesting extraction properties of ILs for REEs, IL-functionalized materials including silica-supported ionic liquids (S-SILs), membrane-supported ionic liquids (M-SILs), and polymer-supported ionic liquids (P-SILs) are thus developed for the separation of REEs.

5.4.1 Silica-Supported Ionic Liquids (S-SILs)

Direct bonding of chelating ligands to a matrix is still very difficult and time consuming due to relative inertness of matrix surface and, hence, requiring surface activation. But the impregnation technique is exceedingly easy to perform. In such a manner, silica materials doped with ILs have been extensively developed recently. Acting as solvent and template, ILs increase the diffusion rate of extractant in solid silica. Liu et al. prepared a macro-mesoporous silica material (IL923SG) doped with $[C_8mim][PF_6]$ and CYANEX 923 via a sol-gel method

[17]. The silica gel doped with CYANEX 923 and $[C_8mim][PF_6]$ was also compared with only CYANEX 923, and the former exhibited higher adsorption of Y^{3+} due to its excellent stability of $[C_8mim][PF_6]$ for complexing REEs. With the primary research of silica gel doped with a binary mixture of extractant and ILs, Liu attempted to replace the organic phase, in which trihexyl(tetradecyl)phosphonium bis-(2, 4, 4-trimethylpentyl) phosphinate (CYPHOS® IL 104) as extractant was dissolved, by an imidazolium IL which was entrapped into a silica solgel composite for the extraction of Y^{3+}. Surface areas of the silica hybrid materials (B104SGs and O104SGs) prepared by using ILs $[C_nmim][PF_6]$ ($n = 4$, 8) as template increased with the content of the ILs. High surface area was believed to facilitate rapid adsorption kinetics of porous materials. Moreover, the silica materials doped with CYPHOS IL 104 enhanced the selectivity for Y^{3+}; the separation factor values of Yb/Dy, Yb/Ho, Y/Dy, Y/Ho, and Er/Dy were large enough, which would help to achieve the separation of heavy RE^{3+}.

At present, some of the disadvantages of silica such as the high price and low coverage of the functional groups and the limited pH stability might limit its use. To circumvent this issue, polymers with high selectivity and a wide operating pH range are used as support matrices, and the properties of polymers can also be improved by modifying with ILs.

5.4.2 Membrane-Supported Ionic Liquids (M-SILs)

Membrane separation processes offer a number of advantages in terms of low energy use and capital investments, which has been recognized as a promising alternative to conventional techniques. As an economically and environmentally friendly technique, supported liquid membrane (SLM) for the selective separation and recovery of resources from dilute solutions has acquired increasing attention. During recent years, membranes with large permeabilities and high selectivities are becoming the focus to improve membrane performance. Polymer inclusion membranes (PIMs) composed of polymers, plasticizers, and ion carriers have gained considerable attention due to their excellent stability and versatility. Particularly, plasticizers can penetrate and increase the distance of molecules and decrease the polar groups of polymer, leading to the increased chemical and mechanical stability of membranes. $[C_nmim][PF_6]$ ($n = 4$, 6) as plasticizers have been attempted. A series of extractants including Aliquat 336 as carrier incorporated in PIM were summarized, and the metal ion complex or ion-pair would be formed and transported across the membrane. In the whole transport process, ILs hold prospects as alternative plasticizers in the rapidly growing plastic industry compared with different traditional plasticizers.

For this purpose, PIMs based on poly(vinylidene fluoride) (PVDF) as polymer, imidazolium ILs as plasticizer, and CYPHOS IL 104, [A336][C272], [A336][P204], or [A336][P507] as carrier were prepared. Using $[C_nmim][PF_6]$ or $[BF_4]$ ($n = 4$,8) as IL plasticizers (ILPs), their hydrophobic properties significantly

Table 5.7 Roughness and contact angle of PIMs and the hydrophobic property of ionic liquid plasticizers

	Plasticizer	Roughness (*Ra*) (nm)	Contact angle (°)	IL in water (wt.%)
a		6.61	90 ± 1	—
b	$[C_8mim][BF_4]$	49.8	94 ± 1	1.8 ± 0.5
c	$[C_8mim][PF_6]$	26.3	99 ± 2	0.7 ± 0.1
d	$[C_4mim][PF_6]$	25.1	91 ± 1	2.0 ± 0.3

influenced the contact angle of PIMs. Moreover, the contact angle was observed to increase in the hydrophobic region. Thus, the maximum contact angle ($99 \pm 2°$) was observed for PIM containing $[C_8mim][PF_6]$, while the minimum contact angle for PIM containing $[C_4mim][PF_6]$ ($91 \pm 1°$) was obtained (Table 5.7). By changing the amount of ILPs, the permeability coefficient (*P*) of metal ion in the extraction process could be influenced. Additionally, CYPHOS IL 104, [A336][C272], [A336][P204], and [A336][P507] were chosen as carrier to obtain the high *P* value. But Aliquat 336 as carrier exhibited the low *P* value, probably attributing to the anion exchange mechanism of Aliquat 336 towards metal ion.

Many research groups have studied the SLM-based processes for the various toxic metals separation, but only a few works about REEs separation by SLM have been published. At present, our research mainly focus on RE^{3+} separation using PIMs containing IL and neutral extractants, such as [A336][C272], [A336][P204], and [A336][P507]. The transport of $RECl_3$ and $RE(NO_3)_3$ was investigated under different experimental conditions, and the most appropriate stripping acidity was supposed as low as 1 mol L^{-1}. The initial flux J_i remained constant as nearly 4 μmol s^{-1} m^{-2} after eight cycles of transport experiments. Moreover, the transport of $Lu(NO_3)_3$ was proved faster than that of $Yb(NO_3)_3$, suggesting the possibility of separation between Yb and Lu. These initial results were obtained and demonstrated the possibility of easy recovery and regeneration of PIMs for many repeating cycles of RE^{3+} separation. Further studies are currently under investigation. We believe that the results presented here should pave the way for the use of PIMs containing IL and neutral extractants for the environmentally friendly separation of REEs.

5.4.3 Polymer-Supported Ionic Liquids (P-SILs)

Polymer-supported ILs offer many advantages, including easy handling and recoverability in the separation of REEs. Polystyrene-based resins, synthesized resins, and some abundant natural polymers have been the most common supports of P-SILs used in separation. But beyond that, the supporting methods for the

immobilization of ILs are also important, which greatly affect the properties and applications of P-SILs. According to the difference of supporting method, ILs can be immobilized by physical and chemical techniques. Solvent-impregnated resins (SIRs) prepared via physical method are alternative systems that combine the advantages of ion exchange and solvent extraction techniques. Consequently, SIRs offer possibilities for confining the extractant in a matrix, preventing the extractant loss, and reducing economical constraints and environmental issues.

By directly impregnating Amberlite XAD-7 resin with $[C_8mim][PF_6]$ and CYANEX 923, Sun et al. prepared and characterized a novel IL-functionalized SIR for RE^{3+} extraction [18]. Unlike the traditional SIR, there existed a homogeneous IL film containing extractant on the IL-functionalized SIR (Fig. 5.10), explained by the electrostatic interaction between IL and XAD-7. The IL film provided the extractant with a larger area to react with metal ions, which was helpful to restrain the loss of extractant, and also enhanced the rate of mass transfer. The equilibrium time of Sc^{3+} by solid-liquid extraction was 20 min, while 40 min was needed to attain the primary equilibrium by liquid–liquid extraction. Interestingly, the extraction efficiency increased from 29 to 80 %. To improve selectivity of the solid-liquid system, the complexing agent, EDTA, was added into the aqueous

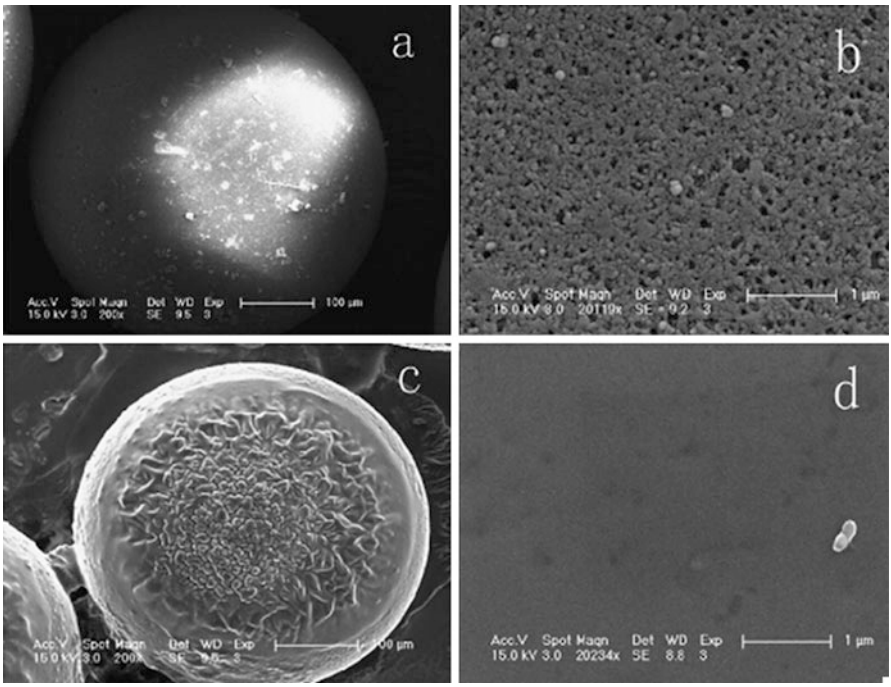

Fig. 5.10 SEM pictures of Amberlite XAD-7 resin (**a** and **b**) and the IL-SIR containing $[C_8mim][PF_6]$ and CYANEX 923 (**c** and **d**) (Reprinted with the permission from Ref. [18] Copyright © 2008 Elsevier B.V. All rights reserved)

phase. It appeared that the separation factors of Y^{3+} to the other REEs were large enough for effectively separating Y^{3+} from heavy REEs.

The new SIR functionalized with [A336][CA-100] attracts more attention because it could improve the mass transfer rate of Bif-ILEs and bring further selectivity in RE^{3+} separation in comparison with [A336][NO_3]. In this study, Sc^{3+} could be separated from RE^{3+} by adjusting the aqueous acidity, and the separation factors β of Sc^{3+} to Y^{3+}, Eu^{3+}, and Ce^{3+} were 16.49, 62.73, and 87.12, respectively. These favorable results gave an excellent estimation of the SIR with the presence of Bif-ILE in solid adsorbent. Surprisingly, Sc^{3+} were easily desorbed by HNO_3 at 0.1 mol $\cdot$ L^{-1}.

Although some reports have demonstrated the benefits of IL-functionalized SIRs in REEs separation, special emphasis in the studies showing the feasibility of IL-functionalized anion exchange resins has been placed on high thermal stability, fast mass transfer rate, and extraordinary selectivity for the target metal ions. Zhu et al. have summarized the study of preparing a new kind of anion exchange resins by covalent anchoring of N-alkylimidazolium onto polystyrene-based resin [19]. The new anion exchange resins with N-alkylimidazolium groups were similar with conventional St-DVB strong base I-type and II-type anion exchange resins only with different functional group structures (Fig. 5.11). The N--methylimidazolium functionalized anion exchange resins (MIm-AER), presented higher chemical stability than strong base I-type anion exchange resin Amberlite IRA-400 against oxidizing agents such as H_2O_2. The stability of MIm-AER was examined in 5 mol/L NaOH and 14 % NaOCl media. As shown in Table 5.8 [19, 20], less loss of anion exchange capacity was observed, revealing better chemical stability than that of strong base I-type anion exchange resin Amberlite IRA-400. These advantages contribute to the successful development of their applications.

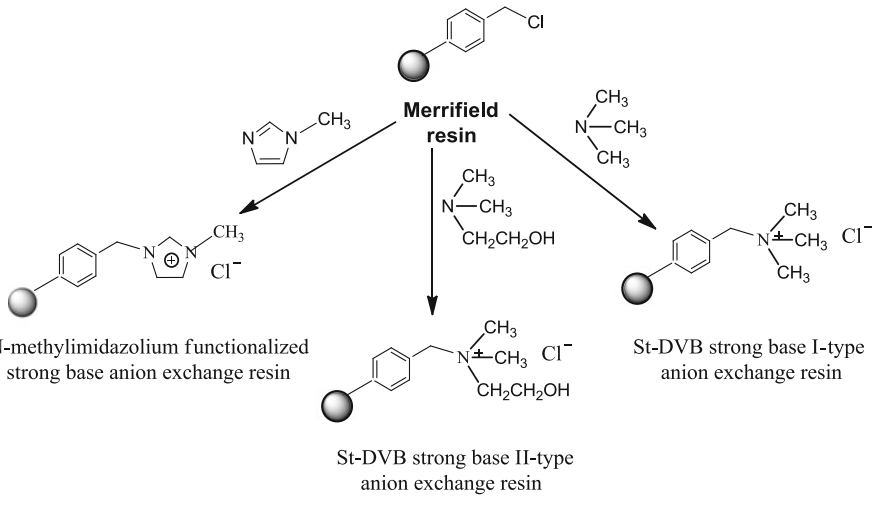

Fig. 5.11 The preparation of different strong base anion exchange resins

Table 5.8 Chemical stability of strong base anion exchange resins

Degradation agent	MIm-AER gel (porous)		St-DVB strong base I-type anion exchange resin Amberlite IRA-400	
	Exchange capacity (meq/g)	Loss of anion exchange capacity (%)	Exchange capacity (meq/g)	Loss of anion exchange capacity (%)
10 % H_2O_2	2.64(3.92)	0(0)	3.92	16.52
5 M NaOH	2.35(3.72)	10.98(5.1)	3.84	15.98
14 % NaOCl	2.35(3.72)	10.98(5.1)	3.65	20.14

Reprinted with the permission from Ref. [19]. Copyright © 2012, Science China Press and Springer-Verlag Berlin Heidelberg

The recovery of Ce(IV) from nitric acid medium using macroporous MIm-AER has been attempted. MIm-AER in NO_3^- forming RNO_3 was prepared and used for adsorption of Ce(IV). Anionic nitrate complexes of Ce(IV) such as $[Ce(NO_3)_5]^-$ and $[Ce(NO_3)_6]^{2-}$ were exchanged with NO_3^- in RNO_3, with the concentration of nitric acid higher than 1 $mol \cdot L^{-1}$. Ce^{4+} suffered the competitive adsorption with NO_3^-, while the concentration of $NaNO_3$ was added from 0 to 3 $mol \cdot L^{-1}$, which considerably decreased the adsorption of Ce(IV). The adsorption amount of Ce (IV) still increased with shaking time and then reached equilibrium. This result was different from the report that the adsorption amount of Ce(IV) on pyridine-based anion exchanger decreased with time. The performance of MIm-AER, in terms of stability, was clearly superior to that of commercial IRA-900 anion exchanger. In addition, Ce(IV) could be easily separated from RE^{3+} by RNO_3 due to its unique existence as anionic nitrate complexes.

It is also worth noting that MIm-AER can be used as the polymeric support to prepare SIR impregnated with CYANEX 923 [21], because the polymeric supports with imidazolium chloride group (RCl) and imidazolium hexafluorophosphate group (RPF_6) possess tunable hydrophilicity and hydrophobicity, different acid stabilities, and swelling behaviors in solvents. CYANEX 923 and $[C_8mim][PF_6]$ exhibited stronger affinity to RPF_6 than to RCl [22]. In the extraction process, Sc^{3+} was extracted in HNO_3 medium by CYANEX 923 onto RPF_6, and the neutral complex $Sc(NO_3)_3CYANEX\ 923_{3(org)}$ was formed (Eq. (5.23)). But the amount of NO_3^- extracted was far less than the amount of extracted Sc^{3+}; then it was insufficient to produce a neutral complex. In view of the fact that $[C_8mim]^+$ was detected in the aqueous solution, cation exchange mechanism was simultaneously proposed. The complex, $Sc(CYANEX\ 923)_3{}^{3+}$ formed by CYANEX 923 and Sc^{3+}, exchanged with $[C_8mim]^+$ of the attached IL, and $[C_8mim]^+$ was exchanged into the aqueous phase (Equation (5.24)). The combined effects may contribute to the high extraction efficiency for Sc^{3+} by RPF_6 containing CYANEX 923. By contrast, lower extraction efficiency for Tm^{3+}, Yb^{3+}, and Lu^{3+} was observed. The separation factors of Sc/Tm, Sc/Yb, and Sc/Lu were 4.50, 5.36, and 4.46, respectively,

so that Sc^{3+} could be selectively extracted from the Sc/Tm, Sc/Yb, and Sc/Lu mixtures:

$$Sc^{3+}aq + 3\,Cyanex\,923_{(IL)} + 3NO_3{}^-{}_{aq} \rightleftharpoons Sc(NO_3)_3 \cdot Cyanex\,923_{3,(IL)} \quad (5.23)$$

$$Sc^{3+}{}_{aq} + 3\,Cyanex\,923_{IL} + 3[C_8min]^+{}_{IL} \rightleftharpoons Sc \cdot Cyanex\,923^{3+}{}_{3,(IL)} + 3C_8min^+{}_{aq} \quad (5.24)$$

The results demonstrated using IL-functionalized SIRs or anion exchange resins as adsorbents for RE^{3+} separation were promising. However, the increasingly serious ore depletion of REEs resources and accelerated requirements for the high-purity REEs necessitate the development of highly efficient technologies to selectively adsorb RE^{3+} from dilute solutions. It should be noted that the flexibility of tailoring the desired metal-binding group in polymer is a unique property that could be easily exploited for improved affinity and specificity for the target metals.

Chitosan, a widely used natural biopolymer, has been studied for the adsorption of various metal ions from dilute solutions. Unfortunately, the inherent properties of chitosan, such as hydrophilicity and metal-binding capability, are often insufficient to meet the requirements of a number of applications. To improve these properties, both chemical and physical modifications of chitosan are required. Thus, Aliquat 336-functionalized chitosan as adsorbent was prepared. In fact, the new chitosan adsorbent can also be described as P-SIL containing quaternary ammonium ionic liquid [23]. Unlike the previous reported structure, the Aliquat 336-functionalized chitosan, which was prepared by acid/base neutralization reaction, consists largely of cations and anions (Fig. 5.12). The structure was so flexible that the adsorption ability could be controlled precisely. Moreover, incorporation of Aliquat 336 into the chitosan backbone could significantly enhance its metal ions extraction ability. It has been shown to have much improved affinity for Pb^{2+} than pure chitosan. This may be explained in that the new strategy doesn't reduce the original amino active sites; besides, the synergistic effect between cation and anion also contributes to the enhancement of adsorption capabilities. On the other hand, the effort to increase selectivity of the adsorbent for one metal ion over others is to make the adsorbent sterically efficient with that metal ion only. The new chitosan-

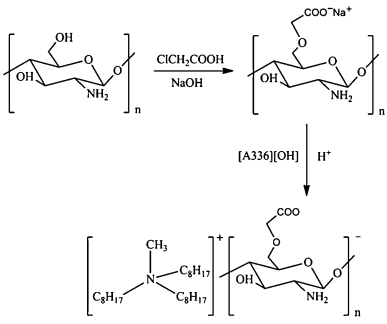

Fig. 5.12 Synthetic route for preparation of trioctylmethyl ammonium carboxymethylated chitosan ([A336][CMCTS])

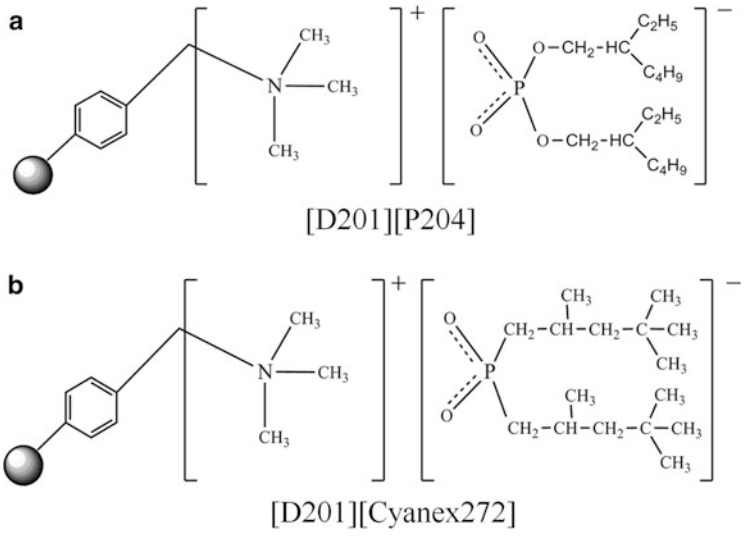

Fig. 5.13 Chemical structures of novel ionic liquid-functionalized resins, [D201][P204] (**a**) and [D201][CYANEX 272] (**b**) (D201: macroporous strong base anion exchange resin (also Amberlite IRA 900)); (**a**, [D201][P204]; **b**, [D201][CYANEX 272])

based adsorbent functionalized with Aliquat 336 used for the recovery of Y^{3+} has been reported. We investigated the possibility that the deprotonation for amine and carboxylic groups might create an effective adsorption for Y^{3+}. Indeed, the maximum adsorption capacity of 16.9 mg g^{-1} was obtained for Y^{3+} at pH 4.9. Based on resource sustainable development and environmental improvement, and the chitosan-based adsorbent functionalized with Aliquat 336 was thus used for the recovery of REEs from waste RE phosphor. Our work represents the first use of biopolymer as support and encourages its use in REEs separation. The recovery of Y^{3+} and Eu^{3+} was 71.2 % and 63.4 %, respectively. Further, this process avoided introducing the new impurity and environmentally reducing solid waste. We also anticipate that this may open avenue for future P-SIL development, including straightforward incorporation and surface functionalization using well-established chemistries to facilitate their use in REEs separation from ore processing.

The attractive method has also been extended to the preparation of a new kind of P-SIL, with the aim of controlling the selectivity of P-SIL for the target metals. For REEs separation, acidic organophosphorus compounds, such as P204 and CYANEX 272, were widely adopted as the impregnated extractants due to their chemical stabilities, low aqueous solubilities, and high distribution ratios and selectivities of metals. To improve the stability of impregnated extractants, similar method was used to prepare IL-functionalized resins by incorporating P204 and CYANEX 272 as anions into poly(styrene-divinylbenzene) copolymer (Fig. 5.13). The immobilization of P204 or CYANEX 272 by acid/base interaction with polymer matrix produced an interaction, which was far stronger than the usual physical adsorption of the extractants onto the inert polymeric support. Extraction of RE^{3+} in HCl medium using

IL-functionalized resins was evaluated in the presence of NaCl. Results of the batch extraction tests showed that the adsorption of REEs was significantly improved using the modified resins. Most importantly, [D201][P204] clearly expressed different selectivities towards REEs as a function of atomic radiuses, and the maximum K_d value ($K_d = 33\ L \cdot g^{-1}$) was obtained for Lu^{3+} at pH 1.65. In comparison, [D201][CYANEX 272] showed maximum K_d value ($K_d = 8.0\ L \cdot g^{-1}$) for Lu^{3+} at pH 5.16. Comparing the adsorption of Lu^{3+} and Yb^{3+} in single system, [D201][P204] and [D201][CYANEX 272] exhibit preferential adsorption for Lu^{3+} than Yb^{3+}. This affinity order holds for most pH values, and the difference of *D* favors the separation of Lu^{3+} and Yb^{3+}. The selective extraction trend observed for these two resins is due to a combination of steric effects and electrostatic interactions that may be more pronounced in the presence of the solid support than in liquid phase, which favors chelation of ions of a certain radius range only.

Using such resins may indeed enable us to reduce substantially the number of steps needed for the separation of REEs and thus decrease both the required time and waste production. Nevertheless, the distinct selectivity obtained for the two resins suggests that it is possible to further fine-tune the ligand environment on the surface in order to target each REE with high specificity. Further studies are needed to achieve a single REE-selective ligand design with optimized surface environment.

ILs, especially containing quaternary ammonium- and phosphonium-based Bif-ILEs, have been extensively used in the extraction and separation of REEs. Although the status of IL extractant as "green" solvent has been questioned, their designability, high selectivity, and low acid/base consumption make them full of potential. From the analysis of β by Bif-ILEs or separation materials in different media, the green and environmentally friendly separation systems could be achieved to meet the further challenge from the rare earth industry. So the fundamental study about the thermodynamics and kinetics mechanism for IL-based separation technology could push the development of REEs' clean and green metallurgy in the future.

References

1. Li DQ, Wang XL, Meng SL, Li W (2007) Process for adding improver to extract and separate the heavy Rare Earths. Chinese Patent CN 100352954C
2. Sun XQ, Ji Y, Liu Y et al (2010) An engineering purpose preparation strategy for ammonium-type ionic liquid with high purity. AIChE J 56(4):989–996
3. Sun XQ, Ji Y, Hu FC et al (2010) The inner synergistic effect of bifunctional ionic liquid extractant for solvent extraction. Talanta 81:1877–1883
4. Guo L, Chen J, Shen L, Zhang JP et al (2014) Highly selective extraction and separation of rare earths(III) using bifunctional ionic liquid extractant. ACS Sustainable Chem Eng 2 (8):1968–1975

5. Liu YH, Zhu LL, Sun XQ et al (2010) Toward greener separations of rare earths: bifunctional ionic liquid extractants in biodiesel. AIChE J 56(9):2338–2346
6. Wang W, Yang HL, Cui HM et al (2011) Application of bifunctional ionic liquid extractants [A336][CA-12] and [A336][CA-100] to the lanthanum extraction and separation from rare earths in the chloride medium. Ind Eng Chem Res 50:7534–7541
7. Zhang DL, Wang W, Deng YF et al (2012) Extraction and recovery of cerium(IV) and fluorine (I) from sulfuric solutions using bifunctional ionic liquid extractants. Chem Eng J 179:19–25
8. Yang HL, Chen J, Zhang DL (2014) Kinetics of cerium(IV) and fluoride extraction from sulfuric solutions using bifunctional ionic liquid extractant (Bif-ILE) [A336][P204].T Nonferr Metal Soc 24(6):1937–1945
9. Wu DB, Wang XL, Li DQ (2007) Extraction kinetics of Sc(III), Y(III), La(III) and Gd(III) from chloride medium by Cyanex 302 in heptane using the constant interfacial cell with laminar flow. Chem Eng Process 46(1):17–24
10. Yu GH, Yue ST, Li DQ (2001) Kinetic study of Ce^{4+} extraction with Cyanex 923. J Rare Earths 19:250–254
11. Liao WP, Yu GH, Yue ST et al (2002) Kinetics of cerium(IV) extraction from H_2SO_4-HF medium with Cyanex 923. Talanta 56:613–618
12. Wang YJ, Zhang SM, Li DQ (1998) Separation of Th^{4+} and RE^{3+} with hollow fiber membrane extraction. J Rare Earths 16:193–198
13. Liu JJ, Wang YL, Li DQ (2007) Extraction kinetics of cerium(IV) from sulfuric acid medium by the primary amine N1923 using a constant interfacial area cell with laminar flow. J Chem Technol Biotechnol 82:949–955
14. Zhao JM, Li W, Li DQ et al (2006) Kinetics of cerium(IV) extraction with DEHEHP from HNO_3-HF medium using a constant interfacial cell with laminar flow. Solvent Extr Ion Exch 24:165–176
15. Yang HL, Chen J, Wang W (2014) Extraction kinetics of lanthanum in chloride medium by bifunctional ionic liquid [A336][CA-12] using a constant interfacial cell with Laminar Flow. Chin J Chem Eng 22(10):1174–1177
16. Danesi PR, Vandegrift GF (1991) Kinetics and mechanism of the interfacial mass transfer of europium(3+) and americium(3+) in the system bis(2-ethylhexyl)-phosphate-n-dodecane-sodium chloride-hydrochloric acid-water. J Phys Chem 39:1425–1432
17. Liu YH, Zhu LL, Sun XQ et al (2009) Silica materials doped with bifunctional ionic liquid extractant for yttrium extraction. Ind Eng Chem Res 48(15):7308–7313
18. Sun XQ, Peng B, Ji Y et al (2008) The solid–liquid extraction of yttrium from rare earths by solvent (ionic liquid) impreganated resin coupled with complexing method. Sep Purif Technol 63(1):61–68
19. Zhu LL, Guo L, Zhang ZJ et al (2012) The preparation of supported ionic liquids (SILs) and their application in rare metals separation. Sci China Chem 55(8):1479–1487
20. (a) Neagu V, Avram E, Lisa G (2010) N-methylimidazolium functionalized strongly basic anion exchanger: synthesis, chemical and thermal stability. React Funct Polym 70(2): 88–97. (b) Neagu V, Bunia I, Plesca I (2000) Ionic polymers VI. Chemical stability of strong base anion exchangers in aggressive media. Polym Degrad Stabil 70(3): 463–468
21. Zhu LL, Liu YH, Chen J et al (2011) Extraction of scandium(III) using ionic liquids functionalized solvent impregnated resins. J Appl Polym Sci 120(6):3284–3290
22. Liu YH, Chen J, Li DQ (2012) Application and perspective of ionic liquids on rare earths green separation. Sep Sci Technol 47(2):223–232
23. Cui HM, Chen J, Yang HL et al (2013) Preparation and application of Aliquat 336 functionalized chitosan adsorbent for the removal of Pb(II). Chem Eng J 232:372–379

Part IV
Electrodeposition of Rare Earth Metal in Ionic Liquids

Chapter 6
Electrodeposition of Rare Earth Metal in Ionic Liquids

Masahiko Matsumiya

Abstract It is very important to develop the recovery process of Nd and Dy metals using ionic liquids from a standpoint of establishing an environmental harmonization system and a recycling-oriented society. For this purpose, the solubility, the solvation structures, the electrochemical behaviors, the diffusive properties, the nucleation, and the electrodeposition behaviors were investigated for Nd(III) and Dy(III) in ionic liquids on this study.

As for the solvation analysis of Nd(III) and Dy(III) by Raman spectroscopy, the solvation numbers of Nd(III), Dy(II), and Dy(III) in $[P_{2225}][TFSA]$ were 5.1, 3.8, and 5.0, respectively. These results also revealed that the solvation structures of Nd(III), Dy(II), and Dy(III) were $[Nd(TFSA)_5]^{2-}$, $[Dy(TFSA)_4]^{2-}$, and $[Dy(TFSA)_5]^{2-}$, respectively.

According to the electrochemical analyses with semi-integral and semi-differential methods, the reduction process of $[Nd(TFSA)_5]^{2-}$ or $[Dy(TFSA)_5]^{2-}$ proceeded in one step, $[Nd(TFSA)_5]^{2-} + 3e^- \rightarrow Nd(0) + 5[TFSA]^-$, or two steps, $[Dy(TFSA)_5]^{2-} + e^- \rightarrow [Dy(TFSA)_4]^{2-} + [TFSA]^-$ and $[Dy(TFSA)_4]^{2-} + 2e^- \rightarrow Dy(0) + 4[TFSA]^-$, respectively. The activation energies of the diffusion coefficients for $[Nd(TFSA)_5]^{2-}$ and $[Dy(TFSA)_5]^{2-}$ were 52.8 and 53.4 kJ mol^{-1}, respectively, and these behaviors were related to the similar solvation structures. The nucleation behaviors of $[Nd(TFSA)_5]^{2-}$ and $[Dy(TFSA)_5]^{2-}$ were altered from instantaneous to progressive nucleation by increasing the overpotential. The potentiostatic electrodepositions of Nd and Dy were also carried out and the recovered blackish electrodeposits were Nd and Dy metals evaluated by XPS. Finally, we demonstrated that the recovery process of Nd metal from spent Nd–Fe–B magnets by wet separation and electrodeposition using ionic liquids was effective.

Keywords Solubility of Nd(III) and Dy(III) in ionic liquids • Solvation structures of Nd(III) and Dy(III) in ionic liquids • Electrochemical behaviors of Nd(III) and Dy(III) in ionic liquids • Nucleation behaviors of Nd(III) and Dy(III) in ionic

M. Matsumiya (✉)
Graduate School of Environment and Information Sciences, Yokohama National University, 79-2 Tokiwadai, Hodogaya-ku, Yokohama 240-8501, Japan
e-mail: mmatsumi@ynu.ac.jp

J. Chen (ed.), *Application of Ionic Liquids on Rare Earth Green Separation and Utilization*, Green Chemistry and Sustainable Technology,
DOI 10.1007/978-3-662-47510-2_6

liquids • Electrodeposition of Nd and Dy metals in ionic liquids • Recovery process of Nd metal from spent Nd–Fe–B magnets

6.1 Introduction

Rare earth (RE) elements have become essential for high-tech industry, where they have been applied to many technical fields such as optical materials [1, 2], laser materials [3], and magnetic materials [4] due to their original properties. The demand of RE metals and oxides has drastically increased in recent years. However, the import situation of RE compounds has been influenced by the supply restrictions of the main exporting countries [5]. In addition, the supply of RE related compounds is occasionally unstable in certain parts of the world, where it is currently difficult to supply such RE elements locally, and thus Japan has been largely dependent on other countries for the supply of RE compounds. As one of RE elements, Nd has been incorporated into $Nd_2Fe_{14}B$ permanent magnets (Nd–Fe–B magnets) and Dy has also found similar application. Nd–Fe–B magnets are utilized in a variety of high technology products, e.g., voice coil motors (VCMs) for hard disk drives, magnetic field sources for magnetic resonance imaging (MRI), driving motors for hybrid-type electric vehicles, and so on [6]. The demand for Nd–Fe–B magnets has continued to elevate in recent years because these magnets play an important role in applications that require energy saving and efficiency. Hence, the recovery of Nd and Dy from the spent Nd–Fe–B magnets is necessary to secure a stable supply of these resources. Although the recovery process of Nd and Dy from spent Nd–Fe–B magnets has been actively studied [7–9], a practical recovery system has not been established to date. As one prospective means of recovering Nd and Dy metals, the electrodeposition using ionic liquids (ILs) is attractive from a standpoint of the environmental harmonization. The ILs have several attractive physicochemical properties, such as negligible vapor pressure, high ionic conductivity, and a wide electrochemical window [10, 11]. In particular, among the ILs consisting of bis(trifluoromethyl-sulfonyl) amide, $[TFSA]^-$ has a good hydrophobicity.

There are a few reports about the electrodeposition of RE metals from the TFSA-based IL bath, e.g., La [12] in 1-octyl-1-methyl-pyrrolidinium bis(trifluoromethyl-sulfonyl)amide, [OMP][TFSA]; Eu [13] in *N*,*N*,*N*-trimethyl-*n*-butylammonium bis (trifluoromethyl-sulfonyl)amide, $[N_{1114}]$[TFSA]; and Dy[14] in dimethylformamide/dimethylpyrrolidinium trifluoromethanesulfonate (DMF/DMPT). Recently, we demonstrated the electrodeposition of Nd [15–19] and Dy [20, 21] from the TFSA-based IL bath, e.g.,triethyl-pentyl-phosphonium bis(trifluoromethyl-sulfonyl)amide, $[P_{2225}]$ [TFSA]; 2-hydroxyethyl-trimethyl-ammonium bis(trifluoromethyl-sulfonyl)amide, $[N_{1112OH}]$[TFSA]; and *N*,*N*-diethyl-*N*-methyl-*N*-(2-methoxyethyl)ammonium bis (trifluoromethyl-sulfonyl)amide, [DEME][TFSA]. It is very important to electrodeposit Nd and Dy as a metallic state by elevating the bath temperature in order to decrease the overpotential of the electrodeposited metals. This elevation of the bath temperature is related to the important factors, e.g., the high solubility of RE amide

salts, high ionic conductivity, low viscosity of the ILs, and high diffusion coefficient of the RE complexes. The main results about the solubility, the solvation structure, the electrochemical behavior, the nucleation behavior, and the electrodeposition behavior are demonstrated in the following sections.

6.2 Solubility of Nd(III) and Dy(III)

The solubilities of $Nd(TFSA)_3$ and $Dy(TFSA)_3$ in $[P_{2225}][TFSA]$ neat solution were evaluated using an ultraviolet–visible (UV–Vis) spectroscopy spectrometer (ADC1000-USB, Ocean Optics Inc.) with a heating system. The UV–Vis measurement at elevated temperatures was required to investigate the temperature dependence of solubility for $RE(TFSA)_3$ salts. The heating system was composed of a spectrophotochemical thin-layer quartz microcell placed directly on the electrothermal equipment and covered with the ceramic fiber insulators (Kaowool Blanket, Aida Chemical Industries Co., Ltd.) in order to maintain the setting temperature of the measured samples. The temperature of the samples was measured using a K-type thermocouple ($\varphi = 1.6$ mm) inserted into the quartz microcell (light path length: 1.0 cm) and was recorded by a data logger (midi logger GL220, Graphtec Co., Inc.). The accuracy of the temperature control in this system was ± 0.1 K. The wavelength regions of deuterium and halogen lamps for the UV–Vis were within the range of 180–870 and 340–1020 nm, respectively. For the evaluation for the solubility of $RE(TFSA)_3$ in ILs, the volume molality m (mol dm^{-3}) in the range of 1.0–3.0 mol dm^{-3} was applied to each sample using two types of solutes: $Nd(TFSA)_3$ and $Dy(TFSA)_3$ in $[P_{2225}][TFSA]$ solvent.

The accurate solubility measurement of $RE(TFSA)_3$ as a function of temperature is particularly essential for understanding the dissolution behavior in the IL media. In addition, it was more effective to prepare IL samples beforehand by dissolving $Nd(TFSA)_3$ or $Dy(TFSA)_3$ salts with constant volume molarity. For example, the variation of the absorption spectra of 1.0 mol dm^{-3} Dy(III) in $[P_{2225}][TFSA]$ undergoing a temperature increase is shown in Fig. 6.1. At room temperature, no absorption spectrum for Dy(III) could be observed because this IL sample turned opaque owing to partial solidification of a large amount of $Dy(TFSA)_3$ salt. As the operating temperature subsequently increased, three peaks began to appear at approximately 760 nm ($^6H_{15/2} \rightarrow {}^6F_{5/2}$), 810 nm ($^6H_{15/2} \rightarrow {}^6F_{5/2}$), and 911 nm ($^6H_{15/2} \rightarrow {}^6F_{7/2}$), as shown in Fig. 6.1a. This spectroscopic behavior suggests that the IL dissolves the $Dy(TFSA)_3$ salt; therefore, the IL is altered from a semitransparent to a transparent state by increasing the temperature. The hypersensitive peak of Dy(III) appeared at 1290 nm ($^6H_{15/2} \rightarrow {}^6F_{11/2}$) and the observed peak at 911 nm for $^6H_{15/2} \rightarrow {}^6F_{7/2}$ had a secondary intensity when compared to the hypersensitive peak. Thus, the $^6H_{15/2} \rightarrow {}^6F_{7/2}$ peak with the secondary intensity is a good evaluator of the Dy(III) solubility state. As the temperature increased further, the peak intensity for $^6H_{15/2} \rightarrow {}^6F_{7/2}$ also increased gradually. When the temperature reached 336 K, the spectrum of Dy(III) indicated maximum absorbance. Moreover, there

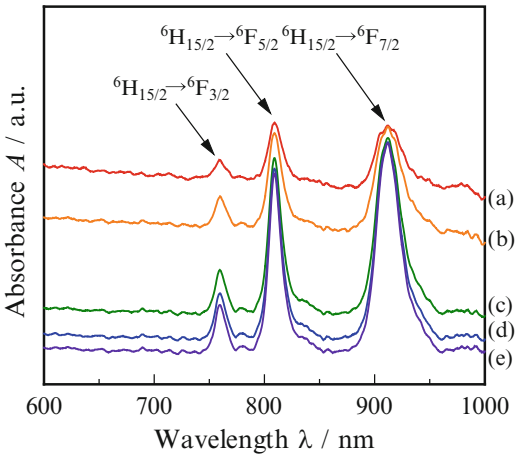

Fig. 6.1 The temperature dependence of the absorption spectrum of 1.0 mol dm^{-3} Dy(III) in [P_{2225}][TFSA]. (*a*) 323 K, (*b*) 333 K, (*c*)335 K, (*d*) 336 K, (*e*) above 338 K

was no further alternation on the Dy(III) spectrum above 338 K (Fig. 6.1e). Therefore, the sample was completely dissolved at 336 K and the volume molarity of 0.1 mol dm^{-3} Dy(III) is saturated at this temperature. The similar measurements for all prepared samples were performed and the temperature of each sample that reached the saturation point was recorded. For Nd(III) in ILs, the solubility was evaluated from the hypersensitive peak ($^4I_{9/2} \rightarrow {}^2G_{7/2}$) at 580 nm.

A series of experimental results on the volume molality for Nd(III) and Dy(III) is shown in Fig. 6.2. These results reveal that the solubility curves of Nd(III) and Dy (III) tend toward a nonlinear relationship. The temperature dependence of the mole fraction solubility of Nd(III) and Dy(III) was fitted using the modified Apelblat equation [22, 23]:

$$\ln x^{\mathrm{sol}} = A + \frac{B}{\tau} + \frac{C}{\tau^2} + \frac{D}{\tau^3} + E\ln\tau \tag{6.1}$$

where x^{sol} is the solubility of the solute in mole fraction; τ is equivalent to T/T_0, where the scaling temperature is $T_0 = 405.65$ K, which is the average empirical temperature for the solubility measurements and T is the absolute temperature; A, B, C, D, and E are the empirical parameters; and r^2 is the coefficient of determination as listed in Table 6.1. The logarithm of the mole fraction solubility, x^{sol} of Nd(III) and Dy(III) as a function of the inverse of the temperature, and the theoretical curves fitted by Eq. (6.1) are shown in Fig. 6.3.

The temperature dependence of the solubility curves of Nd(III) and Dy(III) displayed an analogous tendency. Free energy evaluation is the most reliable theoretical method for systematic studies of solvation properties [24, 25]. The thermodynamic properties characterizing the solvating process of the IL were derived from the temperature dependence of the solubility using Eq. (6.1):

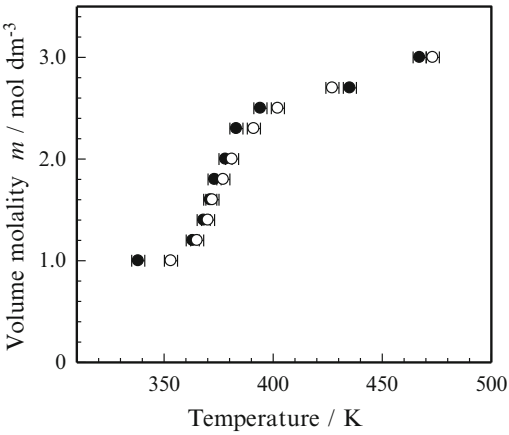

Fig. 6.2 The temperature dependence of the solubility curve for Nd(III) and Dy (III) in [P_{2225}][TFSA]. The error bar was evaluated from the temperature deviation. ○: Nd(III) and ●: Dy(III) (Reprinted with permission from Ref. [21] Copyright 2013, Elsevier Science)

Table 6.1 The correlated parameters used to fit the experimental results in the modified Apelblat equation and the coefficient of determination

	A	B	C	D	E	r^2
Nd(III)	−66.840	59.520	29.141	−22.568	51.665	0.970
Dy(III)	−63.178	55.183	25.713	−18.523	52.146	0.841

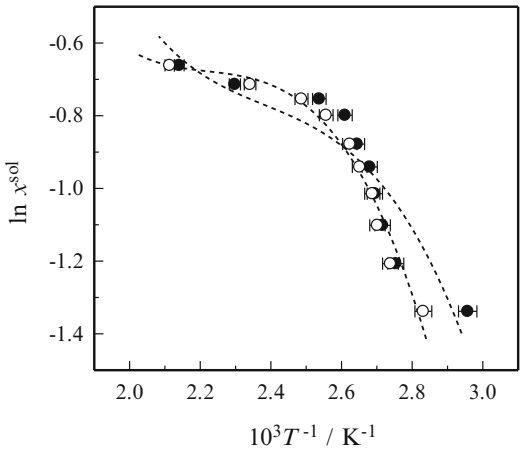

Fig. 6.3 Arrhenius plots for the molar fraction solubility x of Nd(III) and Dy(III) in [P_{2225}][TFSA] and the theoretical curves by modified Apelblat equation. ○: Nd(III) and ●: Dy(III) (Reprinted with permission from Ref. [21] Copyright 2013, Elsevier Science)

$$\Delta_{sol}G^{\infty} = -RT\ln x^{sol} = -RT\left(A + \frac{B}{\tau} + \frac{C}{\tau^2} + \frac{D}{\tau^3} + E\ln\tau\right) \tag{6.2}$$

$$\Delta_{sol}H^{\infty} = RT^2\frac{\partial \ln x^{sol}}{\partial T} = -RT\left(\frac{B}{\tau} + \frac{2C}{\tau^2} + \frac{3D}{\tau^3} - E\right) \tag{6.3}$$

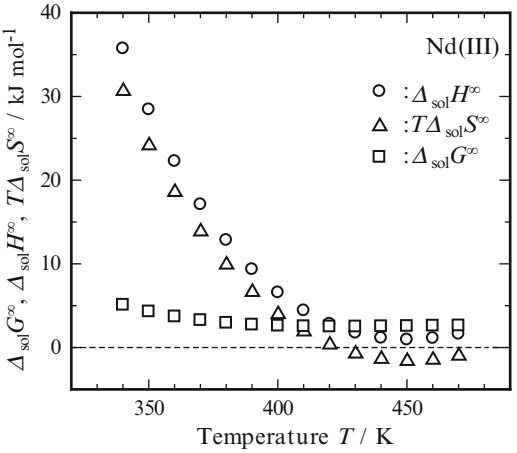

Fig. 6.4 Thermodynamic quantities of Nd(III) in $[P_{2225}][TFSA]$ estimated from temperature dependence of the solubility

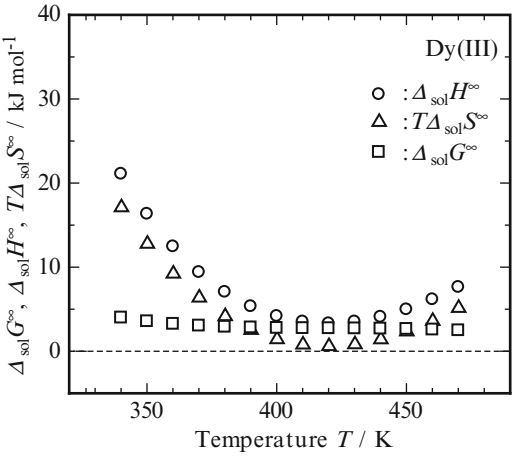

Fig. 6.5 Thermodynamic quantities of Dy(III) in $[P_{2225}][TFSA]$ estimated from temperature dependence of the solubility

$$\Delta_{sol}S^{\infty} = \frac{\Delta_{sol}H^{\infty} - \Delta_{sol}G^{\infty}}{T} = R\left(A - \frac{C}{\tau^2} - \frac{2D}{\tau^3} + E\ln\tau + E\right) \tag{6.4}$$

The calculated thermodynamic quantities of Nd(III) and Dy(III) with temperature dependence are shown in Figs. 6.4 and 6.5, respectively. The values of $\Delta_{sol}G^{\infty}$ regarding the interaction between the $RE(TFSA)_3$ salts and the IL solvent appeared to be reasonable, because the polar IL solvent exhibits positive values. The dissolution of $RE(TFSA)_3$ salts in ILs is enthalpy controlled. The values of $\Delta_{sol}H^{\infty}$ roughly followed those of $\Delta_{sol}G^{\infty}$ above 420 K, and entropy alternations for the dissolution process were close to zero. Assuming the small volume terms are ignored, the solvation free energy is equivalent to the interaction energy and is explained from the summation of the electrostatic interaction energy and the van der Waals interaction energy between the solute and solvent molecules [25]. For

this polar IL solvent, the van der Waals interaction would be weakened by the increase in the solvation energy. Concerning with the solubility evaluation of a solid solute into a polar IL solvent, there is a report on the dissolution of the elemental sulfur in the nonpolar toluene and polar imidazolium-based IL mixtures [23]. As for the dissolution of sulfur, the van der Waals interaction was weakened by the addition of polar imidazolium-based IL in the nonpolar toluene. This dissolution behavior was consistent with our results. The solubility curves are also important indicators of the applicability of electrodeposition in retrieving RE metals from phosphonium-based ILs.

6.3 Solvation Analysis of Nd(III) and Dy(III)

6.3.1 Solvation Structure of Nd(III)

Raman spectra of $[P_{2225}][TFSA]$ containing 0.2, 0.3, 0.4, and 0.5 mol dm^{-3} Nd $(TFSA)_3$ were investigated in this study. The water contents of all samples were confirmed to be less than 100 ppm. Raman spectra were measured at a temperature of 298 and 423 K using a 532 or 785 nm laser of Raman spectrometer (Renishaw inVia Reflex Raman Microscope). Spectral data were accumulated 512 times in order to obtain data of a sufficiently high S/N ratio. The free $[TFSA]^-$ anions had a characteristic intense band at 744 cm^{-1}, which was ascribed to the CF_3 bending vibration, $\delta_s(CF_3)$ coupled with the S-N stretching vibration ν_s(S-N-S) [26, 27]. In addition, there was an intense band at 750 cm^{-1}, which was ascribed to the $[TFSA]^-$ anions surrounding for the Nd(III). As the concentration of Nd(III) increased, the intensity positioned at 744 cm^{-1} decreased. On the other hand, as the concentration of Nd(III) in $[P_{2225}][TFSA]$ increased, the intensity assigned at 750 cm^{-1} increased. The obtained Raman spectra were deconvoluted to extract single Raman band for each assignment as shown in Fig. 6.6. A single Raman band was assumed to be represented as a pseudo-Voigt function, which consisted of the Lorentzian and Gaussian components. Moreover, based on Eq. (6.5) suggested in the reference [28], the solvation number of Nd(III) was analyzed from the following equation:

$$I_f/c_M = J_f(c_T/c_M - n) \tag{6.5}$$

where I_f is integral intensity, c_M is the concentration of Nd(III) in $[P_{2225}][TFSA]$, J_f is the molar Raman scattering coefficient, c_T is the total concentration of $[TFSA]^-$ anion, and n is the solvation number.

The integrated intensity of the deconvoluted Raman band of the free $[TFSA]^-$ in the bulk IL is represented as $I_f = J_f c_f$. The c_f is given as $c_f = c_T - c_b = c_T - nc_M$, which c_T and c_b denote the concentrations of total and bound $[TFSA]^-$ (solvated to the metal ion), respectively. The relationship between I_f/c_{Nd} and c_T/c_{Nd} is shown in

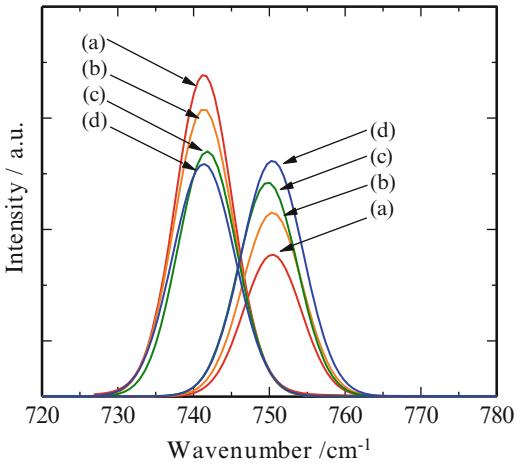

Fig. 6.6 The deconvoluted Raman spectra of $[P_{2225}]$ [TFSA] including (*a*) 0.3, (*b*) 0.4, (*c*) 0.5, and (*d*) 0.6 mol dm^{-3} $Nd(TFSA)_3$.

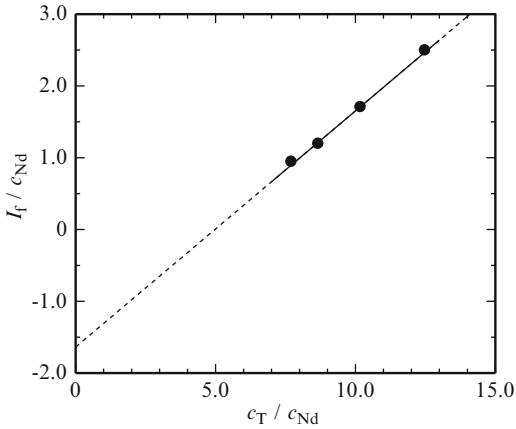

Fig. 6.7 The plot between I_f/c_{Nd} plots and R for Nd(III) in $[P_{2225}][TFSA]$

Fig. 6.7 and resulted in a straight line. Thus, the solvation number, n, is obtained as $n = \beta/\alpha$ from a slope $\alpha = J_f$ and an intercept $\beta = -J_f n$. In this study, the solvation number of Nd(III) in $[P_{2225}][TFSA]$ was calculated to be 5.1. The solvation structure between $[Nd^{3+}]$ cation and $[TFSA]^-$ anion was indicated as a complexation of $[Nd(TFSA)_5]^{2-}$.

6.3.2 Solvation Structure of Dy(III)

The deconvoluted Raman spectra with the concentration dependence in the frequency range 720–780 cm^{-1} for 0.23–0.45 mol kg^{-1} Dy(III) in $[P_{2225}][TFSA]$ were separated into two components at approximately 740 and 749 cm^{-1}, as shown in

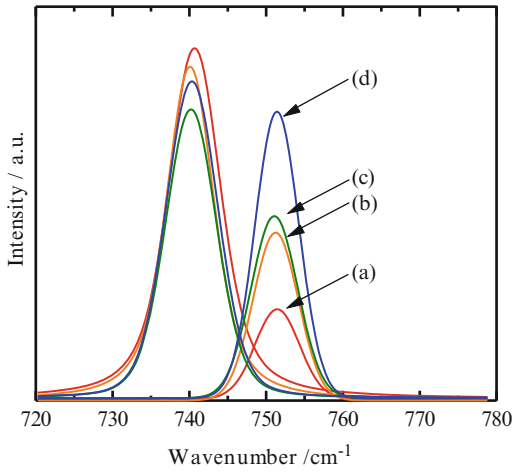

Fig. 6.8 The deconvoluted Raman spectrum of Dy(III) in $[P_{2225}][TFSA]$ with the concentration dependence, (*a*) 0.23 mol kg^{-1}, (*b*) 0.30 mol kg^{-1}, (*c*) 0.38 mol kg^{-1}, and (*d*) 0.45 mol kg^{-1}Dy(III) (Reprinted with permission from Ref. [21] Copyright 2013, Elsevier Science)

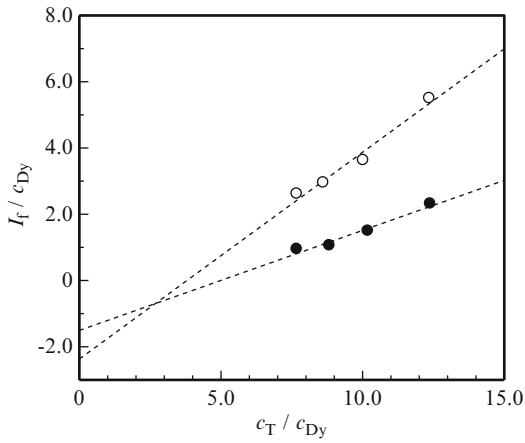

Fig. 6.9 Relationship between c_T/c_{Dy} and I_f/c_{Dy} for $[P_{2225}][TFSA]$ including Dy(II)/Dy(III) coexisted sample or Dy(III), ○: Dy (II)/Dy(III) coexisted sample and ●: Dy(III) (Reprinted with permission from Ref. [21] Copyright 2013, Elsevier Science)

Fig. 6.8. As shown in this figure, a new band was observed as a shoulder on the high frequency side (747 cm^{-1}) of the intense band (740 cm^{-1}); this new band was intensified by increasing the Dy(III) concentration. Therefore, the band at 747 cm^{-1} in the present system is also considered to be due to the $[TFSA]^-$ anion bound to the Dy(III), and the vibrational mode of the band at 740 cm^{-1} corresponds to that of the free $[TFSA]^-$ anion.

The number of $[TFSA]^-$ anion solvated to the Dy(III) can be evaluated from the plots of I_f/c_M vs. c_T/c_M, as shown in Fig. 6.9. This plot demonstrates a strong linear relationship with an estimated n value of 5.0. This result suggests that $[Dy^{3+}]$ in $[P_{2225}][TFSA]$ is solvated by five $[TFSA]^-$ anions and $[Dy(TFSA)_5]^{2-}$ complexation occurred in this system. The Raman spectrum of the Dy(II)/Dy(III) mixed sample also highlights the concentration dependence of the Dy(II)/Dy(III) ratio in the frequency range 720–780 cm^{-1}. A similar analysis of the solvent number was

performed on the deconvoluted data, and the obtained solvation number was 3.8, as shown in Fig. 6.9. This result suggests that the Dy(II) exists in this IL system and the solvation structure: $[Dy(TFSA)_4]^{2-}$ would be smaller than $[Dy(TFSA)_5]^{2-}$.

As for the fluorescence spectroscopy, an energy diagram reported for Dy(III) [29, 30] has indicated that the fluorescence emission of $[Dy(TFSA)_5]^{2-}$ is mainly due to the radiative transitions from the excited $^4F_{9/2}$ and $^4I_{13/2}$ to the ground multiplet of $^6H_{J/2}$ (J = 7–15). The fluorescence spectra of $[Dy(TFSA)_5]^{2-}$and the equimolar $[Dy(TFSA)_4]^{2-}$/$[Dy(TFSA)_5]^{2-}$ samples were also investigated in this study. The yellow-colored emission at 572 nm (due to the hypersensitive transition of $^4F_{9/2} \rightarrow {}^6H_{13/2}$) and the blue-colored emission at 479 nm (due to the $^4F_{9/2} \rightarrow {}^6H_{15/2}$ transition) [31, 32] were noticeably observed in the $[Dy(TFSA)_5]^{2-}$ samples. However, the normalized fluorescence intensity of the equimolar $[Dy(TFSA)_4]^{2-}$/$[Dy(TFSA)_5]^{2-}$ sample at 572 nm was drastically smaller than that of the $[Dy(TFSA)_5]^{2-}$ sample. This result suggests that the Dy(III) is reduced to the Dy(II), which is consistent with the above Raman investigation.

6.4 Physicochemical Properties of Nd(III)

The temperature dependence of the viscosity and the ionic conductivity for 0.5 mol dm^{-3} $[Nd(TFSA)_5]^{2-}$ in $[P_{2225}][TFSA]$ with various water contents was expressed in Figs. 6.10 and 6.11, respectively. The data for $[P_{2225}][TFSA]$ neat solution was also plotted in each figure.

In comparison with the $[P_{2225}][TFSA]$ neat solution, the viscosity of the $[P_{2225}][TFSA]$ including $[Nd(TFSA)_5]^{2-}$ increased in the whole temperature range. It was also observed that the ionic conductivity of this $[P_{2225}][TFSA]$ dissolving $[Nd(TFSA)_5]^{2-}$ decreased in the same temperature range. Thus, it was revealed that $[Nd(TFSA)_5]^{2-}$ complex was influenced by the transport property and the

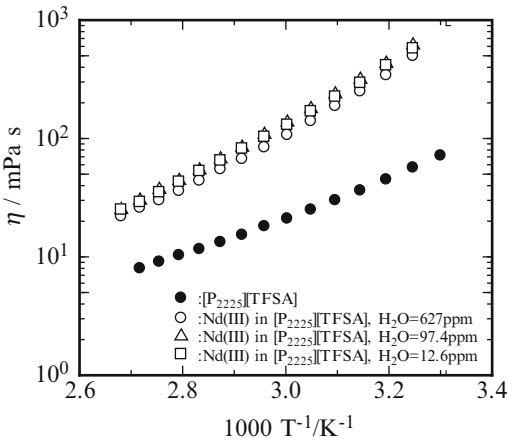

Fig. 6.10 Viscosity of $[P_{2225}][TFSA]$ and 0.5 mol dm^{-3} $[Nd(TFSA)_5]^{2-}$ in $[P_{2225}][TFSA]$ at different water contents

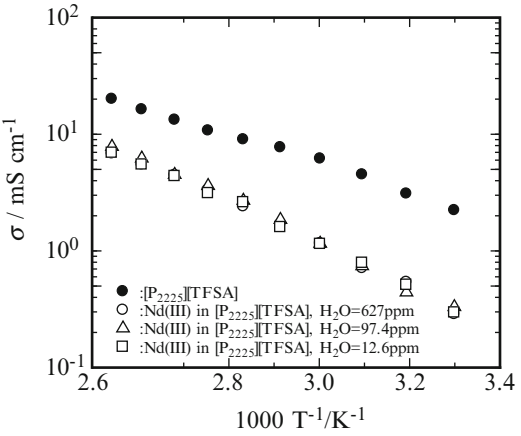

Fig. 6.11 Ionic conductivity of $[P_{2225}][TFSA]$ and 0.5 mol dm^{-3} $[Nd(TFSA)_5]^{2-}$ in $[P_{2225}][TFSA]$ at different water contents

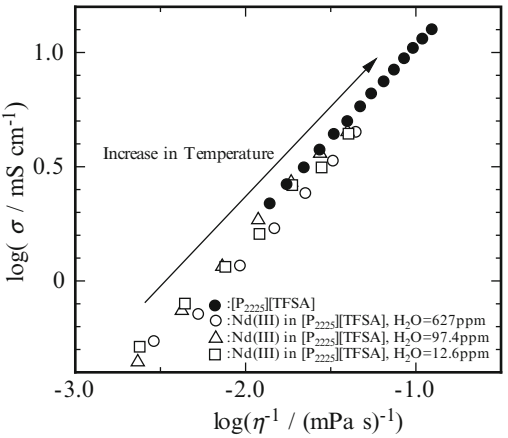

Fig. 6.12 Plots of the ionic conductivity against the inverse of the viscosity for $[P_{2225}][TFSA]$ and 0.5 mol dm^{-3} $[Nd(TFSA)_5]^{2-}$ in $[P_{2225}][TFSA]$ with different water contents based on Walden rule

conductive carrier. On the other hand, the viscosity decreased and the ionic conductivity increased by elevating the temperature. The trend of the viscosity and the ionic conductivity of $[N_{1116}][TFSA]$ containing various metallic amide salts indicated the similar tendency in the case of applying some kinds of metallic salts such as transition and RE elements [33]. In addition, these physicochemical properties were not severely influenced by the water content when it is less than 100 ppm in the electrolyte. Eventually, this result demonstrated that the ionic conduction of the IL was mainly caused by the transportation of metallic complexes and ions.

The ionic conductivity against the inverse viscosity based on Walden rule [34] is shown in Fig. 6.12. The relationship between these physicochemical properties under the same condition in log–log scale displayed clearly a straight line. This result also indicated that a kind of Walden rule ($\sigma\eta = \text{constant}$) was applicable for $[P_{2225}][TFSA]$ including $[Nd(TFSA)_5]^{2-}$ with and without trace amounts of water.

This linear relation was revealed that both the ionic species and metallic species in the bulk electrolyte were associated with each other and the mass transfer of the metallic species contributed to the ionic conductivity. The mass transfer of the metallic species was also correlated with the ionic mobility. In the case of electrodeposition from this kind of $[P_{2225}][TFSA]$ including $[Nd(TFSA)_5]^{2-}$, the mobility of metallic ions and related complexes would be influenced by the current efficiency of the cathodic process.

6.5 Electrochemical Behaviors of Nd(III) and Dy(III)

6.5.1 Electrochemical Behavior of Nd(III)

The reduction behavior of $[Nd(TFSA)_5]^{2-}$ in $[P_{2225}][TFSA]$ was investigated by CV. The cyclic voltammogram of 0.5 mol dm^{-3} $[Nd(TFSA)_5]^{2-}$ in $[P_{2225}][TFSA]$ using a Pt electrode at 353 K is shown in Fig. 6.13. This cyclic voltammogram was scanned cathodically from the initial potential of 0.0 V. A cathodic peak was observed around −3.30 V. The electrodeposits obtained from $[Nd(TFSA)_5]^{2-}$ in $[P_{2225}][TFSA]$ by potentiostatic electrodeposition at −3.40 V and −3.60 V consisted mainly of Nd metal, indicating that this cathodic peak was ascribed to the reduction reaction of $[Nd(TFSA)_5]^{2-}$ in $[P_{2225}][TFSA]$ according to the following reaction:

$$\left[Nd(TFSA)_5\right]^{2-} + 3e^- \rightarrow Nd(0) + 5[TFSA]^- \tag{6.6}$$

On the other hand, no anodic peaks corresponding to the oxidation of Nd(0) were apparent in this voltammogram, suggesting that the reduction of $[Nd(TFSA)_5]^{2-}$ is

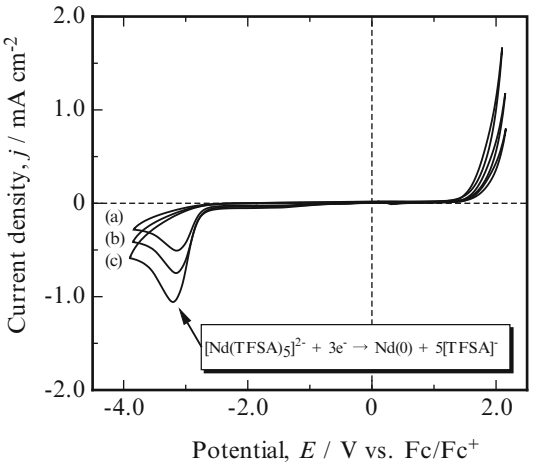

Fig. 6.13 Cyclic voltammogram of 0.5 mol dm^{-3} $[Nd(TFSA)_5]^{2-}$ in $[P_{2225}][TFSA]$ at 353 K on a Pt electrode with different scan rates: (*a*) 5 mV s^{-1}, (*b*) 10 mV s^{-1}, and (*c*) 20 mV s^{-1}

an irreversible reaction. A more detailed analysis of this irreversible reaction is presented below.

Elucidation of the reduction behavior of $[Nd(TFSA)_5]^{2-}$ in $[P_{2225}][TFSA]$ as well as the diffusion behavior is necessary in order to perform the electrodeposition of Nd metal in $[P_{2225}][TFSA]$; thus, we evaluated the diffusion coefficient of $[Nd(TFSA)_5]^{2-}$ in $[P_{2225}][TFSA]$. The diffusion coefficient of $[Nd(TFSA)_5]^{2-}$ in $[P_{2225}][TFSA]$ was calculated from semi-integral (SI) and semi-differential (SD) analyses. Initially, the SI curve was obtained from convolution analysis of the cyclic voltammogram for 0.5 mol dm^{-3} $[Nd(TFSA)_5]^{2-}$ in $[P_{2225}][TFSA]$ using a Pt electrode at 353 K, as shown in Fig. 6.14. An empirical graphical procedure [35] was applied for the determination of the limiting current, m^*, where the vertical lines AC and DF were traced and the mid-points B and E were located. The value of m^* is represented by GH at the potential $E_{1/2}$, which corresponds to the point where the dashed line BE intersects the SI curve. The diffusion coefficient of $[Nd(TFSA)_5]^{2-}$ was calculated from the value of the limiting current m^* according to the following equation [36]:

$$m^* = nFAD_O^{1/2}C_O^* \tag{6.7}$$

where n is the number of electrons involved in the charge transfer reaction, F is the Faraday constant, A is the electrode surface area, and C^* is the bulk concentration of the electroactive species. The diffusion coefficient of $[Nd(TFSA)_5]^{2-}$ in $[P_{2225}][TFSA]$ at 353 K was evaluated as 1.32×10^{-13} m^2 s^{-1} from SI analysis. Furthermore, the standard rate constant, k_s, can be obtained by using the following equation [36]:

$$E = E_s + \frac{RT}{\alpha nF}\ln\left(\frac{k_s}{D_O^{1/2}}\right) + \frac{RT}{\alpha nF}\ln\left(\frac{m^* - m(t)}{i(t)}\right) \tag{6.8}$$

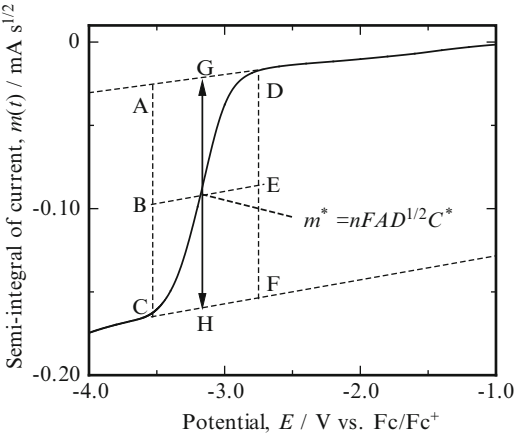

Fig. 6.14 Semi-integral curve obtained from the voltammogram of 0.5 mol dm^{-3} $[Nd(TFSA)_5]^{2-}$ in $[P_{2225}][TFSA]$ at 353 K on a Pt electrode with scan rate: 10 mV s^{-1}

where E is the electrode potential, E_s is the standard reversible potential of the reaction, R is the gas constant, T is the thermodynamic temperature, α is the transfer coefficient, m is the current semi-integral, and i is the faradaic current.

The value of αn was calculated from the slope of the E vs. $\log[m^*\text{-}m(t)]/i(t)$ plots, and that of k_s can be found from the intercept of the plots. Matsuda and Ayabe reported that in the case of the irreversible reaction, the following equation was satisfied [37]:

$$k_s/(DvnF/RT)^{1/2} < 10^{-2(1+\alpha)} \tag{6.9}$$

where v is the potential scan rate. Therefore, the following relation was obtained by deformation with substitution of the above equation:

$$k_s < 6.85 \times 10^{-6}\text{cm s}^{-1} \tag{6.10}$$

The k_s value calculated from the intercept of the E vs. $\log[m^*\text{-}m(t)]/i(t)$ plots was 1.77×10^{-8} cm s^{-1}. Accordingly, the reduction reaction of $[Nd(TFSA)_5]^{2-}$ in $[P_{2225}][TFSA]$ on the Pt electrode at 353 K was deduced to be an irreversible process.

SD analysis was applied to the cyclic voltammogram of 0.5 mol dm^{-3} $[Nd(TFSA)_5]^{2-}$ in $[P_{2225}][TFSA]$; the SD curve is shown in Fig. 6.15. The value of W_p, the width of a derivative neopolarographic peak at half its height, and e_p, the current semi-derivative at the peak of the derivative neopolarogram, were determined by SD analysis of the cyclic voltammogram. The diffusion coefficient of $[Nd(TFSA)_5]^{2-}$ was calculated using the following equations [38] that were established in the case of the irreversible reaction:

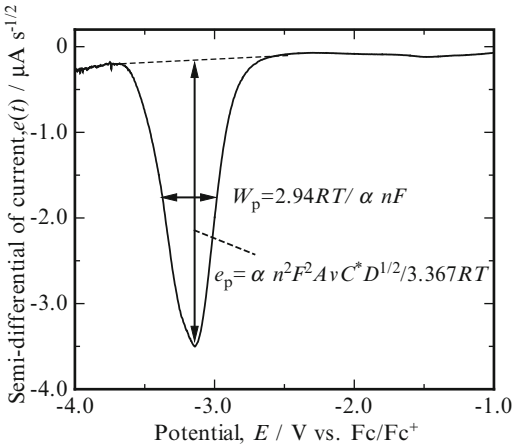

Fig. 6.15 Semi-differential curve obtained from the voltammogram of 0.5 mol dm^{-3} $[Nd(TFSA)_5]^{2-}$ in $[P_{2225}][TFSA]$ at 353 K on a Pt electrode with scan rate: 10 mV s^{-1}

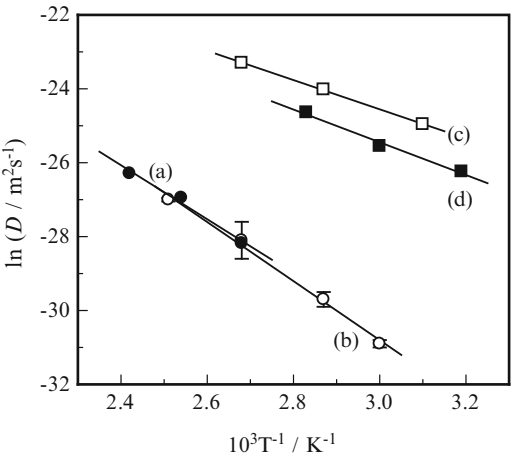

Fig. 6.16 Arrhenius plot of the diffusion coefficients for (*a*) $[Nd(TFSA)_5]^{2-}$, (*b*) $[Dy(TFSA)_5]^{2-}$, (*c*) $[Ni(TFSA)_3]^{-}$, and (*d*) $[Fe(TFSA)_3]^{-}$in $[P_{2225}][TFSA]$

Table 6.2 The activation energy of diffusion coefficient and the solvation number

	$E_{A,D}$/kJ mol^{-1}	Solvation number at 298 K	Solvation number at 423 K
$[Nd(TFSA)_5]^{2-}$	52.8	5.1	5.0
$[Dy(TFSA)_5]^{2-}$	53.4	5.0	5.1
$[Fe(TFSA)_3]^{2-}$	26.3	3.1	3.1
$[Ni(TFSA)_3]^{2-}$	26.0	2.6	3.3

For each metallic complex in $[P_{2225}][TFSA]$

$$W_p = 2.94RT/\alpha nF \tag{6.11}$$

$$e_p = \alpha n^2 F^2 A v C_O^* D_O^{1/2}/3.367RT \tag{6.12}$$

The diffusion coefficient of $[Nd(TFSA)_5]^{2-}$ in $[P_{2225}][TFSA]$ at 353 K was evaluated as 1.46×10^{-13} m^2 s^{-1} based on SD analysis, which is close to the value derived from SI analysis. This congruence suggests high reliability of the calculated diffusion coefficients of $[Nd(TFSA)_5]^{2-}$ in $[P_{2225}][TFSA]$ at 353 K derived from SI and SD analyses. The Arrhenius plot of the diffusion behavior for $[Nd(TFSA)_5]^{2-}$ in $[P_{2225}][TFSA]$ is presented in Fig. 6.16. The D values of $[Nd(TFSA)_5]^{2-}$ [16], $[Dy(TFSA)_5]^{2-}$ [20], $[Fe(TFSA)_3]^{2-}$, and $[Ni(TFSA)_3]^{2-}$ in $[P_{2225}][TFSA]$ from our previous investigations are also displayed in Fig. 6.16 for comparative purposes. The activation energy of the diffusion process was tabulated in Table 6.2 with the solvation number of each metallic complex. The activation energy of $[Nd(TFSA)_5]^{2-}$ or $[Dy(TFSA)_5]^{2-}$ was found to be larger than that of $[Fe(TFSA)_3]^{2-}$ or $[Ni(TFSA)_3]^{2-}$. The difference of $E_{A,D}$ value between the RE complex and iron group metallic complex is explained from the complexation between each centered metallic cation and the surrounding $[TFSA]^{-}$ anion ligand.

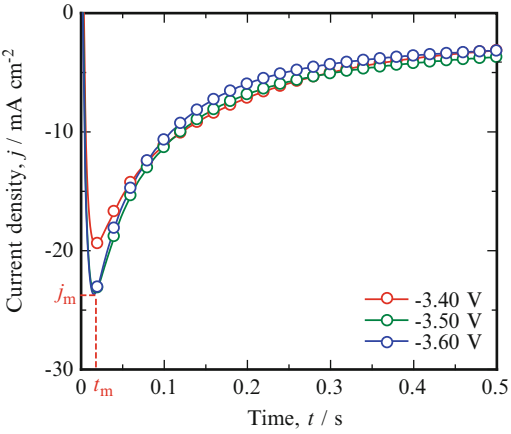

Fig. 6.17 Chronoamperogram on a Pt electrode for 0.5 mol dm^{-3} $[Nd(TFSA)_5]^{2-}$ in $[P_{2225}]$ [TFSA] at 353 K

6.5.2 Nucleation Behavior of Nd Nuclei

The initial nucleation and the growth behavior of Nd nuclei in $[P_{2225}]$[TFSA] were investigated by means of chronoamperometry. A characteristic peak of the nucleation process was observed just after the initial current decay corresponding to the charging of the electric double layer. This peak is indicative of the three-dimensional (3D) growth of the Nd nuclei; there was an initial increase in the faradaic current due to nucleation and the growth of the Nd nuclei that involves an increase of the electroactive area; eventually a current maximum, j_m, was achieved at time t_m; finally, this current quickly decayed to a diffusion limited current. Chronoamperograms were recorded at the Pt electrode as shown in Fig. 6.17.

For these chronoamperograms, the charging current of neat $[P_{2225}]$[TFSA] was deduced from the data for $[P_{2225}]$[TFSA] containing 0.5 mol dm^{-3} $[Nd(TFSA)_5]^{2-}$ in order to analyze the faradaic current only in the reduction reaction of $[Nd(TFSA)_5]^{2-}$. Several models have been developed to describe the *j*–*t* curves for metal deposition. It has been previously reported that the theoretical methodology developed by Scharifker and Hills [39] is applicable to the deposition of several metals from TFSA-based ILs [40–44]. Therefore, the initial stage of the nucleation and the crystal growth of Nd were analyzed by using the Hills–Scharifker method in this study. The previously mentioned study reported that 3D nucleation on an electrode surface can be classified into instantaneous and progressive nucleation. In the case of the instantaneous nucleation, the nuclei are deposited on the electrode surface and grow at a constant rate that is dependent on the applied potential. The resultant *j*–*t* curves are mathematically described by the following equation:

$$\left(\frac{j}{j_m}\right)^2 = \frac{1.2254}{t/t_m}\left\{1 - \exp\left[-2.3367\left(\frac{t}{t_m}\right)^2\right]\right\}^2 \tag{6.13}$$

where j is the current density at time t and j_m is the maximum current density at time t_m. In the case of the progressive nucleation, the initially deposited nuclei grow at varying rates dependent on the time of deposition. The j–t curves can be mathematically described by the following equation:

$$\left(\frac{j}{j_m}\right)^2 = \frac{1.9542}{t/t_m}\left\{1 - \exp\left[-1.2564\left(\frac{t}{t_m}\right)\right]\right\}^2 \tag{6.14}$$

The relationship between the squared dimensionless current density and the dimensionless time of $[Nd(TFSA)_5]^{2-}$ in $[P_{2225}][TFSA]$ is shown in Fig. 6.18, along with the theoretical curves derived from Eqs. (6.13) and (6.14). When the overpotential at −3.40 V was applied, the experimental data were consistent with the instantaneous nucleation model. On the other hand, when the applied potentials were −3.50 V and −3.60 V, the experimental data shifted from that of the instantaneous nucleation model to the progressive nucleation model. These results indicated that the nucleation mechanism changed depending on the applied potential. These nucleation behaviors would be related to the number density of active sites and the nucleation rates per site from the current transients [45] as will be discussed later. This alternation from instantaneous to progressive nucleation was consistent with the nucleation mechanism for Dy in 0.1 mol dm^{-3} $[Dy(TFSA)_5]^{2-}$ in $[P_{2225}][TFSA]$ [20]. The initial nucleation and the crystal growth processes would influence the formation of the electrodeposits in the initial stage of the electrodeposition. Accordingly, consideration of the applied potential is important for achieving electrodeposits with the desired morphology and quality from the electrodeposition process.

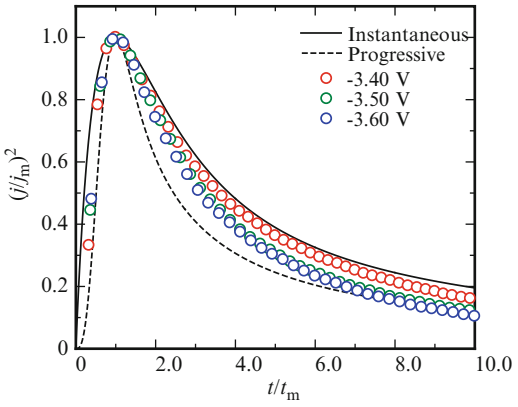

Fig. 6.18 $(j/j_m)^2$-t/t_m plots for 0.5 mol dm^{-3} $[Nd(TFSA)_5]^{2-}$ in $[P_{2225}][TFSA]$ evaluated from CA

Table 6.3 The nucleation number density of Nd nuclei from *j*–*t* curves at each applied potential in $[P_{2225}][TFSA]$ including 0.5 mol dm^{-3} $[Nd(TFSA)_5]^{2-}$

Applied potential (*E*)/V	−3.40	−3.50	−3.60
Nucleation number density ($10^{11}N_0$)/cm^{-2}	2.0	1.7	1.7

The number density of nuclei was also investigated as follows: the nucleation number density, N_0, can be calculated from the maximum current, j_{max}, and time, t_{max}, of the *j*–*t* curve based on the following equation [45]:

$$N_0 = 0.065\left(8\pi C_O^* M/\rho\right)^{-1/2}\left(nFC_O^*/j_{max}t_{max}\right)^2 \tag{6.15}$$

where M and ρ are the atomic mass and the density of the deposited metal, respectively. During the initial stages of deposition, well before the maxima in the *j*–*t* curves, the initial nucleation can be considered to be effectively instantaneous, i.e., all nuclei may be considered to have been formed at the same time [46]. Thus, in the analysis of the data from the very early portion of the current transient, Eq. (6.15) can be used to evaluate the value of N_0 for all systems studied. The number of Nd nuclei formed during the very early stages of nucleation was estimated using this methodology; the data are presented in Table 6.3. In general, the nucleation number density would increase with increasing overpotential on stable progressive nucleation, e.g., the nucleation of Sn nuclei in 1-ethyl-3-methylimidazolium chloride–tetrafluoroborate, $[C_2C_1Im][Cl,BF_4]$ [47]. However, contrary to our expectations, the number density of Nd nuclei at the initial stage of the nucleation decreased as the overpotential increased from −3.40 V to −3.50 V or −3.60 V in this study. These tendencies would be related with the alternation from instantaneous to progressive nucleation. It was reported that the rate of nucleation was changed by the overpotential for instantaneous or progressive nucleation [48]. Thus, the different nucleation rates on instantaneous or progressive nucleation would be affected for the nucleation number density. The nucleation mechanism of Nd and Dy [20] revealed that the number density of nuclei is dependent on the overpotential, suggesting that the applied potential for electrodeposition becomes an important factor from the perspective of the nucleation mechanism as well as the number of nuclei.

6.5.3 Electrochemical Behavior of Dy(II) and Dy(III)

The voltammetric analysis of 0.1 mol dm^{-3} $[Dy(TFSA)_5]^{2-}$ in $[P_{2225}][TFSA]$ was performed with various scan rates at different fractions of water content. The cyclic voltammogram of 0.1 mol dm^{-3} $[Dy(TFSA)_5]^{2-}$ in $[P_{2225}][TFSA]$ with 0.1 V s^{-1} at 363 K is shown in Fig. 6.19. The voltammograms shown in Fig. 6.19a, b contained 98 and 203 ppm water in the IL, respectively. No anodic peaks corresponding to the oxidation of Dy(0) were observed in any voltammogram. This result suggests that

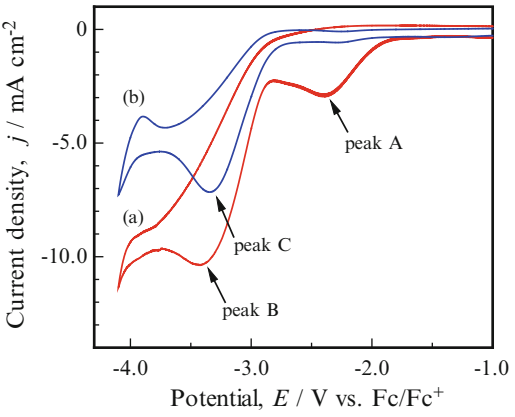

Fig. 6.19 The cyclic voltammogram of 0.1 mol dm^{-3} $[Dy(TFSA)_5]^{2-}$ in $[P_{2225}][TFSA]$ at 363 K with different water contents, (*a*) 98 ppm and (*b*) 203 ppm (Reprinted with permission from Ref. [21] Copyright 2013, Elsevier Science)

the reduction of $[Dy(TFSA)_5]^{2-}$ is an irreversible process. There was no oxidation peak of Dy(0) in DMF and DMPT bath, and this reduction process of Dy complex was an irreversible reaction [14]. Regarding the cathodic peaks, a remarkable difference in the reduction process appeared between two samples with different water contents, as shown in Fig. 6.19. In the case of a small amount of water (98 ppm) in IL (Fig. 6.19a), there were two reduction peaks around −2.4 and −3.5 V in the voltammogram. In contrast, there was only one reduction peak around −3.6 V for the sample with a relatively large amount of water content (203 ppm; Fig. 6.19b). This result suggests that water molecules in the electrolyte remarkably influenced the reduction process of $[Dy(TFSA)_5]^{2-}$ in $[P_{2225}][TFSA]$. For a small amount of water in the IL, the reduction peak A at approximately −2.4 V and the reduction peak B at approximately −3.5 V are expressed for the following two-step reactions:

$$\left[Dy(TFSA)_5\right]^{2-} + e^- \rightarrow \left[Dy(TFSA)_4\right]^{2-} + [TFSA]^- (\text{peak A}) \tag{6.16}$$

$$\left[Dy(TFSA)_4\right]^{2-} + 2e^- \rightarrow Dy(0) + 4[TFSA]^- (\text{peak B}) \tag{6.17}$$

On the other hand, for an increased amount of water in IL, the reduction reaction of $[Dy(TFSA)_5]^{2-}$ proceeds in one step by the following reaction:

$$\left[Dy(TFSA)_5\right]^{2-} + 3e^- \rightarrow Dy(0) + 5[TFSA]^- (\text{peak C}) \tag{6.18}$$

The latter one-step reduction reaction is consistent with our recent electrochemical investigation into $[Dy(TFSA)_5]^{2-}$ [20]. This result indicated that the presence of the water molecule and the solvation structure of ILs is related to the reduction behavior of $[Dy(TFSA)_4]^{2-}$ and $[Dy(TFSA)_5]^{2-}$. According to Raman spectroscopy [18], the solvation number of $[Nd(TFSA)_5]^{2-}$ in $[P_{2225}][TFSA]$ is 5.1. Raman spectroscopy has also revealed that five $[TFSA]^-$ anions act as a bidentate ligand as its two O atoms are centered around the $[Nd^{3+}]$ ion in the TFSA-based ILs. Similar

coordination structures with a multianion $[TFSA]^-$ bidentate ligand have already been demonstrated from DFT calculations in our recent study [49]. The coordination structure for $[Dy(TFSA)_5]^{2-}$ in $[P_{2225}][TFSA]$ was confirmed to have similar tendencies. However, if there were a relatively large amount of H_2O molecules in the TFSA-based ILs, the O atoms of H_2O molecules would preferentially coordinate with the centered $[Dy^{3+}]$ ion because, as per the spectrochemical series, the strength of O atoms in H_2O is greater than those of $[TFSA]^-$ anions. Thus, when an aqua complex such as $[Dy(H_2O)_9]^{3+}$ forms in ILs with a relatively large number of H_2O molecules, a larger overpotential is necessary for the reduction of the Dy–aqua complex when compared to the Dy–TFSA complex. Therefore, no intermediate reduction reaction from $[Dy(TFSA)_5]^{2-}$ to $[Dy(TFSA)_4]^{2-}$ occurs in ILs with 203 ppm water. In addition, a remarkable difference in the peak current density (j_p^{red}) at the electrodeposition potential of Dy(0) was observed in the voltammograms shown in Fig. 6.19. The values of j_p^{red} for samples containing 98 and 203 ppm water were -10.4 and -7.2 mA cm^{-2}, respectively. This increase in the current density contributes to the increase in the current efficiency of Dy electrodeposition. In conclusion, we revealed that $[Dy(TFSA)_5]^{2-}$ dissolved in $[P_{2225}][TFSA]$ was electrodeposited in a two-step reduction process by way of $[Dy(TFSA)_4]^{2-}$ in an IL system containing less than 100 ppm water.

Assuming each peak on CV is based on the cathodic reactions (6.16) and (6.17), we confirmed that the cathodic peak plot of the current density (j_p) vs. the square root of the potential scan rate ($v^{1/2}$) demonstrated a strong linear relationship. This result indicates that both the reduction reactions, (6.16) and (6.17), using a Pt electrode, were controlled by diffusion, i.e., mass transport under semi-infinite linear diffusion conditions. In addition, the slope of the j_p vs. $v^{1/2}$ plot is different between the two reactions, which suggests that there is a difference in the diffusion coefficient of each electrochemical species, $[Dy(TFSA)_4]^{2-}$ and $[Dy(TFSA)_5]^{2-}$. Therefore, the diffusion coefficients of $[Dy(TFSA)_4]^{2-}$ and $[Dy(TFSA)_5]^{2-}$ in $[P_{2225}][TFSA]$ were estimated from the SI analysis of the voltammogram. When discussing the rate of the electrode reaction, both mass transfer and charge transfer processes are very important. In particular, mass transfer by diffusion is a principal factor in deciding the aspects of the electrode reaction, particularly in IL solvents. Therefore, it is necessary to evaluate the diffusion coefficients of $[Dy(TFSA)_4]^{2-}$ and $[Dy(TFSA)_5]^{2-}$ in $[P_{2225}][TFSA]$ when considering the electrodeposition of the Dy metal. Analyzing the SI limiting current enabled us to more accurately evaluate the diffusion coefficients of $[Dy(TFSA)_4]^{2-}$ and $[Dy(TFSA)_5]^{2-}$ in an irreversible process. The SI curves obtained from the voltammogram of 0.1 mol dm^{-3} (water content: 98 ppm) $[Dy(TFSA)_5]^{2-}$ in $[P_{2225}][TFSA]$ at 363 K are shown in Fig. 6.20. The values of m_1^* and m_2^* were conventionally determined by subtracting the background current. The diffusion coefficients of $[Dy(TFSA)_4]^{2-}$ and $[Dy(TFSA)_5]^{2-}$ were, respectively, calculated from the values of m_1^* and m_2^* based on Eq. (6.7) [31]. The diffusion coefficients of $[Dy(TFSA)_5]^{2-}$ obtained for a 0.1 M in $[P_{2225}][TFSA]$ solution were in the same order as those of 7.5×10^{-2} and 0.5 mol dm^{-3} $[Dy(TFSA)_5]^{2-}$, as described in our recent electrochemical analyses [12]. In addition, we revealed that the diffusion coefficients of $[Dy(TFSA)_4]^{2-}$ were larger

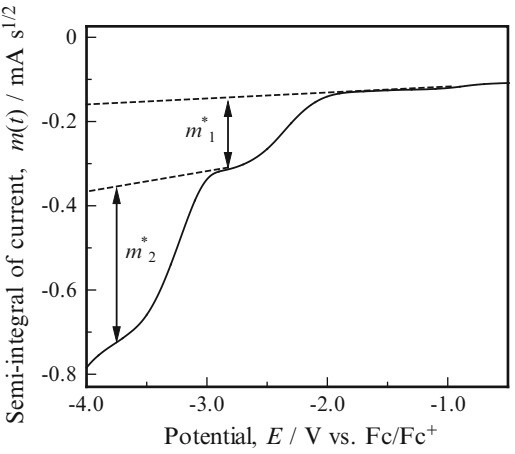

Fig. 6.20 The semi-integrated curves obtained from the voltammogram of 0.1 mol dm^{-3} $[Dy(TFSA)_5]^{2-}$ in $[P_{2225}][TFSA]$ (water content: 98 ppm) at 363 K (Reprinted with permission from Ref. [21] Copyright 2013, Elsevier Science)

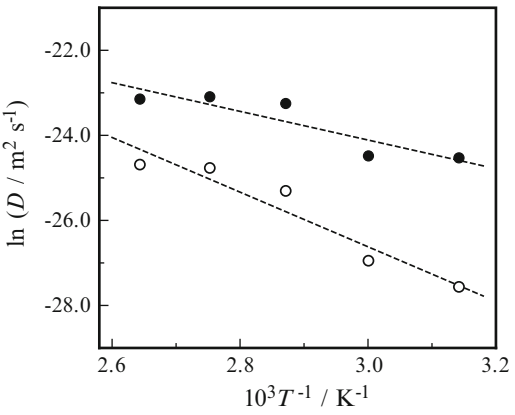

Fig. 6.21 Arrhenius plots for the diffusion coefficients of $[Dy(TFSA)_4]^{2-}$ and $[Dy(TFSA)_5]^{2-}$ in $[P_{2225}][TFSA]$, ●:$[Dy(TFSA)_4]^{2-}$ and ○: $[Dy(TFSA)_5]^{2-}$ (Reprinted with permission from Ref. [21] Copyright 2013, Elsevier Science)

than those of $[Dy(TFSA)_5]^{2-}$ in the entire range of temperatures measured, which indicates that the coordination number of TFSA anions around the centered Dy^{3+} ion for $[Dy(TFSA)_4]^{2-}$ is smaller than that of $[Dy(TFSA)_5]^{2-}$ because of the electrostatic interaction between the cation and the anion.

We then evaluated the activation energy for diffusion ($E_{A,D}$) using diffusion coefficient values with temperature dependence. The transfer of metallic cations in the electrolytic solution is generally affected by their electrostatic interaction with the ions constituting the metal complexes. Therefore, the diffusion of metallic cations in ILs needs more activation energy than the dissociation energy associated with the anions surrounding the metal complexes. The $E_{A,D}$ value is given by the Arrhenius rule:

$$D_O = A^* \exp(-E_{A,D}/RT) \tag{6.19}$$

where A^* is the frequency factor. The Arrhenius plot, a logarithmic plot of the diffusion coefficient for $[Dy(TFSA)_4]^{2-}$ and $[Dy(TFSA)_5]^{2-}$against the inverse of the temperature, is shown in Fig. 6.21. The $E_{A,D}$ values determined from Eq.(6.19) for $[Dy(TFSA)_4]^{2-}$ and $[Dy(TFSA)_5]^{2-}$in $[P_{2225}][TFSA]$ were 28.0 and 53.4 kJ mol^{-1}, respectively. The observation that the $E_{A,D}$ value of $[Dy(TFSA)_4]^{2-}$ is smaller than that of $[Dy(TFSA)_5]^{2-}$ is consistent with the tendency of the diffusion coefficient estimated from the slope of the j_p vs. $v^{1/2}$ plot. This result indicates that the electrostatic interaction of $[Dy(TFSA)_4]^{2-}$ with $[TFSA]^-$ anions is weaker than that of $[Dy(TFSA)_5]^{2-}$ because of smaller coulombic interactions and also that the total electrodeposition energy of the Dy metal would lead to smaller energy consumption.

6.5.4 Nucleation Behavior of Dy Nuclei

The CA responses at different overpotentials were measured to analyze the nucleation and nuclear growth mechanism. For these chronoamperograms, the charging current of neat $[P_{2225}][TFSA]$ was deducted from the data of $[P_{2225}][TFSA]$, along with that of $[Dy(TFSA)_5]^{2-}$, in order to analyze only the faradaic current in the reduction reaction of $[Dy(TFSA)_5]^{2-}$. The CA curves for the potential values close to E_p^{red} indicated that the faradaic current increased because of the nucleation and growth of the Dy nuclei; eventually, this increasing current reached a maximum, j_m, at time t_m, which was attributed to the 3D growth of the Dy metal over the nuclei, resulting in an increase in the surface area. Finally, this current decayed because of the increase in the thickness of the diffusion layer after reaching the maximum. Several models to describe the *j–t* curves for metal electrodeposition have also been developed. It has been previously reported that the theoretical methodology developed by Scharifker and Hills [39] is applicable to several metals dissolved in TFSA-based ILs [40–44]. Therefore, we analyzed the nucleation and crystal growth of Dy electrodeposition in $[P_{2225}][TFSA]$ by the Hills–Scharifker method. According to this report, the nucleation process is described by two limiting cases, instantaneous and progressive nucleation mechanisms. In the case of instantaneous nucleation, the nucleation particles are electrodeposited on the electrode surface and grown at a constant rate, which is dependent on the applied overpotential. In this nucleation process, the *j–t* curves can be mathematically described by Eqs. (6.13) and (6.14). In the case of the progressive nucleation, the electrodeposited nuclei proceed at various rates depending on the electrodeposition time. The resultant *j–t* curves are described by Eq.(6.13). The relationship between the squared dimensionless current density $(j/j_m)^2$ and the dimensionless time (t/t_m) for Dy nuclei in $[P_{2225}][TFSA]$ is shown in Fig. 6.22, with theoretical curves. When the overpotential of −3.6 V is applied, the nucleation behavior obeyed the instantaneous nucleation model. On the other hand, the nucleation curve at −3.8 V is followed by the progressive nucleation model. This result indicates that the nucleation mechanism of Dy changed, depending on the applied overpotential. At overpotential values close to the onset potential for Dy electrodeposition, instantaneous nucleation and growth occurs; however, as the overpotential becomes more negative than E_p^{red} on the

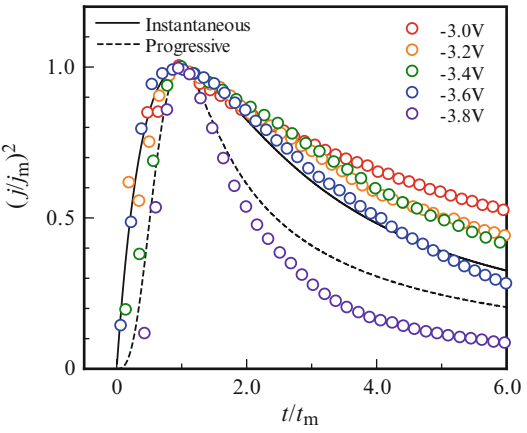

Fig. 6.22 $(j/j_m)^2$-t/t_m plots for 0.1 mol dm^{-3} [Dy(TFSA)$_5$]$^{2-}$ in [P_{2225}][TFSA] with different overpotentials evaluated from CA (Reprinted with permission from Ref. [21] Copyright 2013, Elsevier Science)

voltammogram, the process changes to progressive nucleation and growth. This alteration of nucleation behavior under different applied overpotential values was also reported for Ag electrodeposition in *N*-butyl-*N*-methyl-pyrrolidinium bis (trifluoromethyl-sulfonyl)amide, [C_4C_1Py][TFSA] [43]. Moreover, it has been reported that progressive nucleation occurred for both Pd [40] and Sn [41] in 1-*n*-butyl-1-methylpyrrolidinium bis(trifluoromethyl-sulfonyl)amide, [BMP][TFSA], when the induced overpotential values were more negative than the reduction peak potential (E_p^{red}) on the voltammogram, and that instantaneous nucleation proceeded for Ni [42] in [BMP][TFSA] when an overpotential more positive than E_p^{red} was applied. After all, the nucleation behavior in TFSA-based ILs is controlled by the applied overpotentials and is independent of the specific metallic species. This difference in the nucleation mechanism would also be greatly influenced by the formation of the electrodeposit in the initial stages of electrodeposition. Therefore, by applying an overpotential based on the desired nucleation mechanism, the morphology and quality of electrodeposits could be improved by the electrodeposition process. In the following section, we discuss the actual Dy electrodeposition under potentiostatic conditions at −3.8 V, which led to preferentially progressive nucleation.

6.6 Electrodeposition of Nd and Dy Metals

6.6.1 Electrodeposition of Nd Metal

Electrodeposition at −3.40 V produced blackish electrodeposits on the Cu substrate. The total transported charge was 178.4 C. The SEM image of the electrodeposits obtained by electrodeposition at −3.40 V was shown in Fig. 6.23. The morphology of both electrodeposits was granular with a nonuniform size

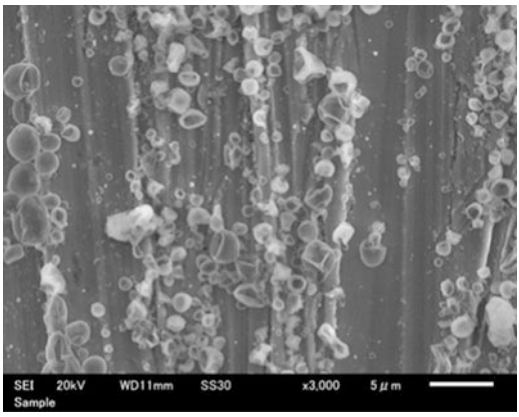

Fig. 6.23 The SEM images of deposits obtained by electrodeposition performed at −3.40 V

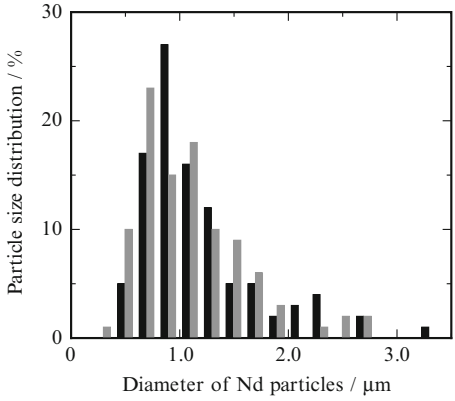

Fig. 6.24 The size distribution of the electrodeposited Nd particles. *Black*: Nd particle size distribution of −3.40 V. *Gray*: Nd particle size distribution of −3.60 V

distribution. This morphology is considered to be generated because the initial stage of nucleation and growth occurred according to the progressive nucleation model in which the nucleation rate was faster than the crystal growth rate. As shown in Fig. 6.22, at −3.40 V, the *j*–*t* curve could be fitted to the theoretical curve for instantaneous nucleation at the early stage, but the curve slowly shifted to conform to the progressive nucleation model as time elapsed. Furthermore, the initial nucleation data gradually approached the theoretical curve for the progressive nucleation model with time. Therefore, the results of the electrodeposition experiments are consistent with the data for initial nucleation and growth of Nd in $[P_{2225}]$ [TFSA] by CA discussed above. The particle size distribution of the Nd grains obtained at −3.40 V and −3.60 V is displayed in Fig. 6.24. With the use of applied potentials of −3.40 V and −3.60 V, the average diameters of the Nd particles were 1.17 μm and 1.08 μm, respectively. The particle size of the electrodeposits obtained by electrodeposition at −3.60 V was smaller than that achieved at −3.40 V. The number of particles deposited at −3.60 V was also larger than that at −3.40 V. These results were also consistent with the results obtained by CA, which

Table 6.4 The composition of electrodeposits on Cu substrate obtained by electrodeposition performed at −3.40 V and −3.60 V from 0.5 M $[Nd(TFSA)_5]^{2-}$ in $[P_{2225}][TFSA]$ at 353 K

Elements		C	N	O	F	S	Fe	Nd
wt.%	−3.40 V	1.78	1.02	18.26	4.24	2.74	0.00	71.96
	−3.60 V	1.92	1.47	23.34	6.72	3.92	0.00	62.63

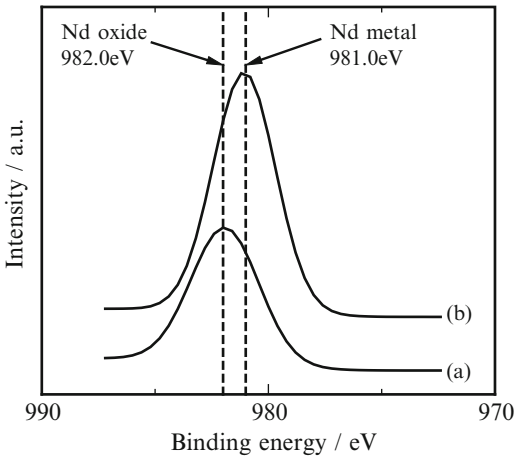

Fig. 6.25 The Nd $3d_{5/2}$ spectra of the electrodeposits by XPS analysis. (*a*) The surface layer at −0.15 μm of the electrodeposits. (*b*) The middle layer at −0.75 μm of the electrodeposit

indicated that the number density of Nd nuclei increased with increasing overpotential.

The quantitative analysis data for the electrodeposits obtained by electrodeposition at −3.40 V and −3.60 V using EDX are summarized in Table 6.4. The data demonstrate that the electrodeposits obtained on the Cu substrate at −3.40 V and −3.60 V both comprise mainly Nd. However, a relatively large amount of O was also detected in the electrodeposits, suggesting that Nd would be combined with O. Thus, the chemical bonding state of Nd in the electrodeposits was analyzed by using XPS. Elemental Fe that was dissolved from the anode was hardly detected in the electrodeposits generated at both potentials. Therefore, the separation of the anode from the main electrolyte using the Vycor glass filter was an effective strategy. Decomposition of the main electrolyte was prevented by this electrodeposition cell structure; thus, this cell structure enabled acquisition of Nd in the electrodeposits while preventing bonding with the light elements (C, F, and S) that constitute the ILs.

The Nd $3d_{5/2}$ XPS spectra of the electrodeposits deposited at −3.40 V and −3.60 V were shown in Fig. 6.25(a) and (b), respectively. The surfaces of both electrodeposits were sputtered using an Ar ion beam to facilitate in-depth analysis of the surface and the middle layer, that is, (a) −0.15 μm and (b) −0.75 μm, of the electrodeposits. Theoretically, the binding energy of Nd $3d_{5/2}$ for metallic Nd and oxides should be positioned at 980.5–981.0 eV and 981.7–982.3 eV, respectively, with the use of the monochromated Al Kα line [50]. The peak maxima in the Nd $3d_{5/2}$ spectra acquired for the layers (a) under 150 nm and (b) under 50 nm were

detected at 981.57 eV and 982.25 eV, respectively. Hence, the Nd species obtained by electrodeposition using $[P_{2225}][TFSA]$ were identified as Nd metal and oxide mixtures. It is thought that metallic Nd should initially be electrodeposited on the Cu substrate and subsequently oxidized by the O components in the electrolyte, that is, water or dissolved oxygen. It has been reported that the water content of the electrolyte did not significantly affect the oxidation state of the electrodeposits, but may influence the coordination number of the Nd complex and the diffusion behavior. Therefore, sufficient dehydration and control of the water content of the electrolyte are important points for achieving high-purity metallic Nd.

6.6.2 *Electrodeposition of Dy Metal*

In the electrodeposition experiments, a Cu substrate and a prismatic Nd–Fe–B rod were used as a cathode and an anode, respectively. A platinum QRE was used for this electrodeposition system because the applied overpotential was precisely induced on both electrodes. The electrodeposition of the Dy metal from 0.1 mol dm^{-3} $[Dy(TFSA)_5]^{2-}$ in $[P_{2225}][TFSA]$ at 393 K was conducted under an Ar atmosphere ($H_2O < 1.0$ ppm) in a glove box at 393 K. The applied overpotential on the cathode for the potentiostatic electrolysis was set at −3.8 V based on the above nucleation study. The potentiostatic electrolysis was carried out while stirring the electrolyte at 500 rpm in order to increase the current density of electrodeposition by continuously supplying the electroactive species $[Dy(TFSA)_5]^{2-}$ to the electrode surface.

The average current density and the total transported charge under these electrodeposition conditions were −32.9 mA cm^{-2} and 300 C for 43.6 h, respectively. We confirmed that the decomposition of IL did not occur under these electrodeposition conditions because there was little change in the color of the light-yellow electrolyte before and after electrodeposition. As for the cathode, we confirmed that the blackish-brown electrodeposits had a strong adhesion on the Cu substrate. The microscopic morphology and elemental analysis of the electrodeposited samples of Dy recovered at −3.8 V were examined by SEM/EDX. The SEM image and EDX mapping of the electrodeposits are represented in Fig. 6.26a, b, respectively. The round particles on the Cu substrate were confirmed to be Dy metals and other related compounds.

A quantitative analysis of the electrodeposits is listed in Table 6.5. We confirmed that the greater part of the electrodeposited Dy was composed of the metallic state, because very little oxygen was detected on the surface of the electrodeposited Dy metal using EDX mapping. The amounts of carbon and oxygen detected in EDX came from the Cu substrate. The particle size distribution indicated that metallic Dy particles with ca. 0.8–0.9 μm diameter showed a high distribution ratio. In summary, this electrodeposition experiment allowed us to demonstrate that electrodeposited Dy contains a large amount of the metallic state and a smaller amount of the oxide state on the top surface. An in-depth analysis of the

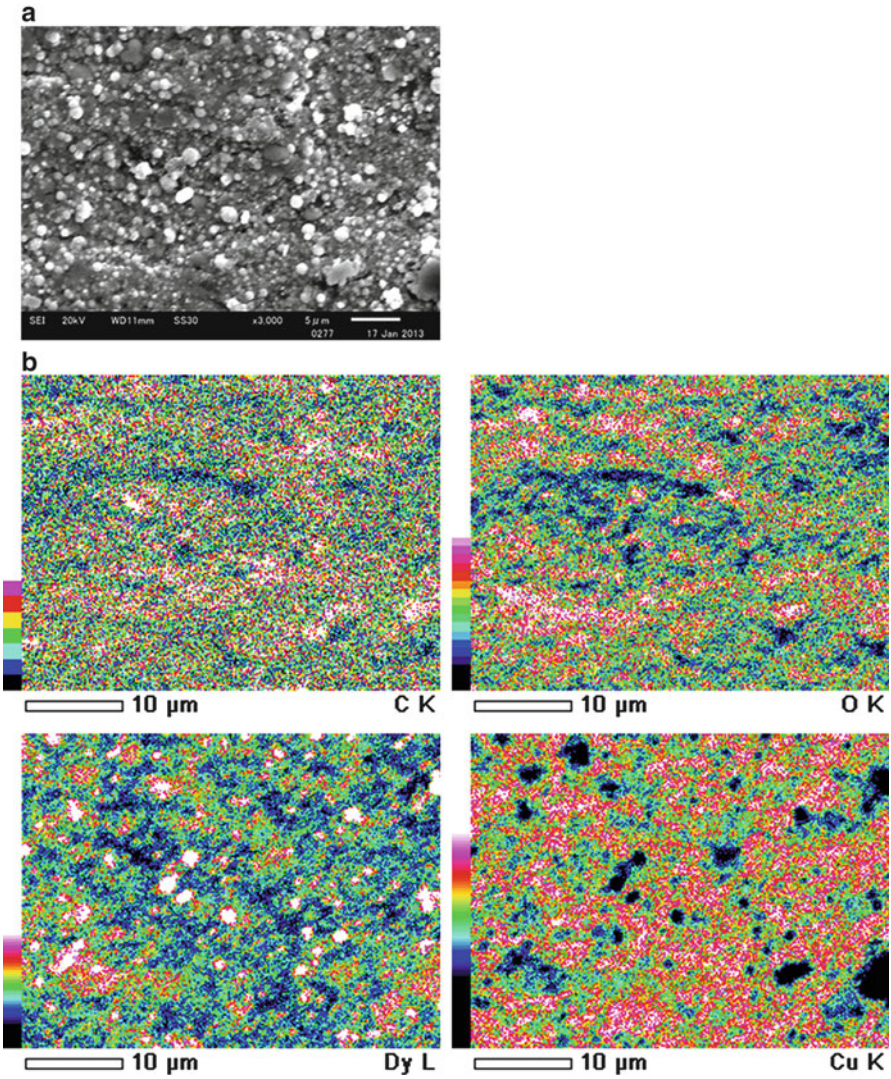

Fig. 6.26 (**a**) The SEM image and (**b**) the EDX mapping of the electrodeposited Dy sample on a Cu substrate at −3.8 V from 0.1 mol dm^{-3} $[Dy(TFSA)_5]^{2-}$ in $[P_{2225}][TFSA]$ at 393 K (Reprinted with permission from Ref. [21] Copyright 2013, Elsevier Science)

electrodeposited Dy was conducted with the Al-Kα radiation by XPS. The $Dy3d_{5/2}$ spectrum for the top surface and the middle layer (under 0.5 μm) of the electrodeposits is investigated, and the XPS analysis of the inner part of the electrodeposits was performed by Ar sputtering. The sputtering rate was 27.2 nm min^{-1} estimated from the sputtering rate of the Si standard. Theoretically, the $Dy3d_{5/2}$ peaks for the Dy metal and oxides should be positioned at 1295.8 and 1289.0 eV, respectively

Table 6.5 The quantitative analysis of the electrodeposits under the potentiostatic condition at −3.8 V by EDX

Elements	C	N	O	F	P	S	Dy	Cu
wt.%	10.83	1.15	11.82	3.87	0.86	1.87	9.27	60.33

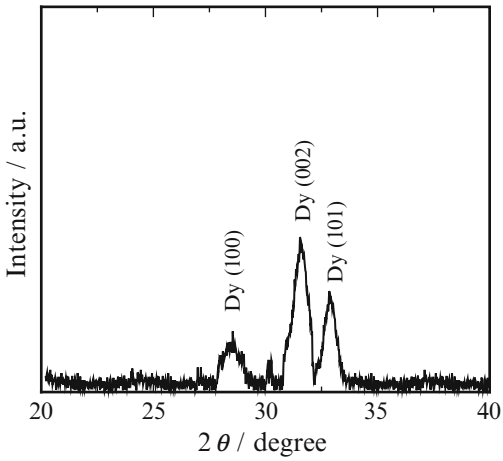

Fig. 6.27 XRD profile of the electrodeposits under potentiostatic electrodeposition at −3.8 V (Reprinted with permission from Ref. [21] Copyright 2013, Elsevier Science)

[50]. The $Dy3d_{5/2}$ peaks of the electrodeposits have a binding energy of 1297.2 eV, which hardly shifted before and after the Ar etching. The $Dy3d_{5/2}$ spectra of the top surface and the middle layer showed a relatively good agreement with the theory. The XRD pattern of the electrodeposits at a low angle is displayed in Fig. 6.27. As shown in this figure, the crystal plane indices of the Dy metallic phase are in good accordance with the JCPDS data. In this study, a series of analyses of Dy electrodeposits enabled us to conclude that most of the metallic state of Dy can be recovered from a phosphonium-based IL by electrodeposition.

6.7 Recovery Process of Nd Metal from Spent Nd–Fe–B Magnets

6.7.1 Pretreatment Process

The spent Nd–Fe–B magnet in voice coil motor (VCM) was applied as a starting material for the recovery process. The VCM in a 3.5 inch HDD was dismantled and separated from Al metals. The pretreatment process was constituted of the demagnetization, chemical etching, and roasting treatment. For the demagnetization process, Nd–Fe–B magnet was heated in an electric muffle furnace (FUW220PA, Advantec, Inc.,) at 90 K/h up to Curie temperature: 583 K. The iron yoke in contact with the VCM was dislocated from the RE-containing magnet. The magnetic flux

density of the Nd–Fe–B magnet was measured using a digital TESLA meter (TM-701, Kanetec Co. Ltd.,) before and after the demagnetizing treatment. The magnetic flux density before and after this treatment was 440 mT and less than 0.1 mT, respectively. Thus, the demagnetization ratio was performed at 99.9 %. After the demagnetization process, a base solution was prepared to exfoliate Ni layers by mixing ENSTRIP EN-79A, EN-79B (Meltex Inc.), and the NaOH (Wako Pure Chemical Industries, Ltd., >97.0 %) with the distilled water. The demagnetized Nd–Fe–B magnet components in VCM were immersed in the exfoliation solution at 363 K. In the case of Ni–Cu–Ni triple layers on the VCM coating, Cu layers were mechanically polished as necessary. Therefore, Ni–Cu–Ni layers were perfectly removed from the Nd–Fe–B magnet on this chemical etching process. Then, some pieces of Nd–Fe–B magnets were milled by using a grinder (IKA®-GMBH & Co. KG, A11) with a cutting tooth (IKA®-GMBH & Co. KG, A11.3). These fine particles which were classified less than 150 μm were heated to oxidize their components in a muffle furnace at 90 K/h up to 1133 K and were maintained for 2 h on the roasting process.

6.7.2 Wet Separation Process

The wet separation process was constituted of the leaching, deironization, and M $(TFSA)_n$ amide salts synthesis. For the leaching process, the fine particles of the oxidized VCM were immersed in 1.0 mol dm^{-3} 1,1,1-trifluoro-*N*-[(trifluoromethyl) sulfonyl]methanesulfonamide ($HN(SO_2CF_3)_2$, HTFSA, Kanto Kagaku, >99.0 %) aqueous solution at 343 K for >12 h. The leaching reactions of RE and Fe components were expressed as follows:

$$RE_2O_3 + 6HTFSA \rightarrow 2RE^{3+} + 6TFSA^- + 3H_2O \ (RE = Pr, Nd, Dy) \quad (6.20)$$

$$Fe_3O_4(\text{magnetite}) + 8HTFSA \rightarrow Fe^{2+} + 2Fe^{3+} + 8HTFSA^- + 4H_2O \quad (6.21)$$

In comparison with Nd–Fe–B magnet without roasting process, the leaching ratio of RE and Fe components in HTFSA solution increased and decreased, respectively. Considering from the total leaching quantity, 93.6 wt% of Nd and 18.1 wt% of Fe in Nd–Fe–B magnet components were found to be dissolved by one batch treatment. Thus, the leaching of Fe was prevented due to the formation of α-Fe_2O_3(hematite) layer on the roasting process. This leaching behavior was explained from the potential (*E*)-pH diagram of Fe–H_2O and Nd-H_2O systems as shown in Fig. 6.28, which showed the red circle determined from pH and ORP measurement of the actual leaching solution with different leaching times from 0 to 20 h. According to the *E*-pH diagram, under the condition of pH ~ 0.0 and *E* ~ 1.0, the most stable states of Fe and Nd are found to be α-Fe_2O_3(hematite) and Nd^{3+}.

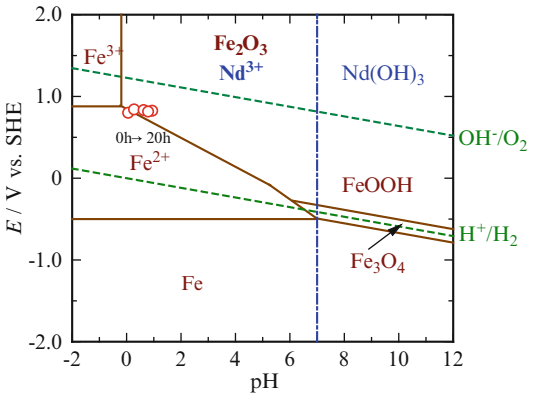

Fig. 6.28 *E*-pH diagram of Nd-H_2O (*chain line*) and Fe–H_2O (*dotted line*) systems

Therefore, the selective leaching of RE components proceeded in this condition. In the case of mineral acid, more than 99 % of RE components were leached, while the leaching of Fe was less than 0.5 %. On the contrary, more than 50 % of Fe was leached without roasting in mineral acid [51]. Then, Fe was selectively removed from HTFSA solution by the precipitation method after the oxidization treatment from Fe^{2+} to Fe^{3+} by O_2 bubbling. For the precipitation method, NaOH or KOH solution was applied as a kind of precipitant. The final precipitation formation of α-FeOOH was performed on the appropriate condition of pH ~ 4.5. The selective separation of α-FeOOH was explained from HSAB rule [52] and the related solubility products [53–56]. After the complete elimination of the precipitated α-FeOOH by centrifugation at 9840 G for 10 min (Model3740 Kubota Corp.), the HTFSA component including RE and alkali metal was evaporated in a draft chamber at 423 K. The obtained $M(TFSA)_n$ salts with fine powder were dried in a chamber under vacuum at 393 K for 24 h. The component of each metal in the $M(TFSA)_n$ salts was analyzed by ICP-AES analysis. Some compositions of the $M(TFSA)_n$ salts were tabulated in Table 6.6.

6.7.3 Electrodeposition Process

After the wet separation process, the obtained $M(TFSA)_n$ amide salts were dissolved in $[P_{2225}][TFSA]$ on the electrodeposition process. In the case of the three electrode systems as shown in Fig. 6.29, Cu cylindrical cathode was used for the electrodeposition. A prismatic Nd–Fe–B rod was employed as an anode and surrounded by a soda lime tube with a Vycor glass filter at the bottom in order to prevent the diffusion of dissolution components from the anode into the electrolyte. Then, Pt wire was applied as a quasi-reference electrode (QRE), because the

Table 6.6 Composition (wt %) of $M(TFSA)_n$ amide salts with different conditions

No.	Pr	Nd	Dy	Fe	Na	K	B	Trace metals	M $(TFSA)_n$	*n*
1-1[a]	13.40	38.86	10.73	N.D.[e]	5.23	30.23	1.55	N.D.[e]	547.87	1.73
1-2[a]	13.60	38.14	10.73	N.D.[e]	5.39	30.67	1.47	N.D.[e]	542.69	1.71
1-3[a]	11.20	32.99	9.38	N.D.[e]	6.03	37.83	1.35	1.23	484.51	1.53
2-1[b]	10.80	30.47	7.51	N.D.[e]	2.10	48.06	1.07	N.D.[e]	475.46	1.49
2-2[b]	11.04	30.10	7.56	N.D.[e]	2.16	48.10	1.04	N.D.[e]	474.48	1.49
3-1[c]	8.83	23.22	6.55	N.D.[e]	2.40	57.30	1.01	0.70	429.81	1.35
3-2[c]	9.52	20.77	6.89	N.D.[e]	2.52	59.50	1.02	0.71	421.97	1.33
3-3[c]	9.32	22.19	6.78	N.D.[e]	2.54	57.45	0.99	0.72	428.02	1.35
4-1[d]	19.84	49.90	1.65	N.D.[e]	N.D.[e]	26.20	1.94	0.47	627.38	1.98
4-2[d]	18.15	51.12	2.32	N.D.[e]	N.D.[e]	26.21	1.54	0.67	617.84	1.94

[a]The precipitant of NaOH and KOH in molar ratio of NaOH:KOH = 40:60
[b]The precipitant of NaOH and KOH in molar ratio of NaOH:KOH = 25:75
[c]The precipitant of NaOH and KOH in molar ratio of NaOH:KOH = 20:80
[d]The precipitant of NaOH and KOH in molar ratio of NaOH:KOH = 0:100
[e]N.D. = not detected

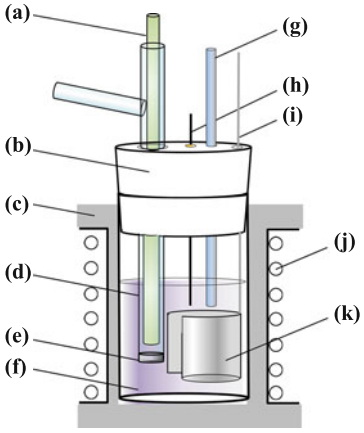

Fig. 6.29 The schematic illustration of the electrodeposition cell, (*a*) Nd–Fe–B rod (anode), (*b*) silicon cap, (*c*) heat insulator, (*d*) soda lime glass tube, (*e*) Vycor glass filter, (*f*) $[P_{2225}][TFSA]$ including $M(TFSA)_n$ amide salts, (*g*) K-type thermocouple, (*h*) Pt wire (QRE), (*i*) Cu wire, (*j*) mantle heater, and (*k*) Cu substrate (cathode)

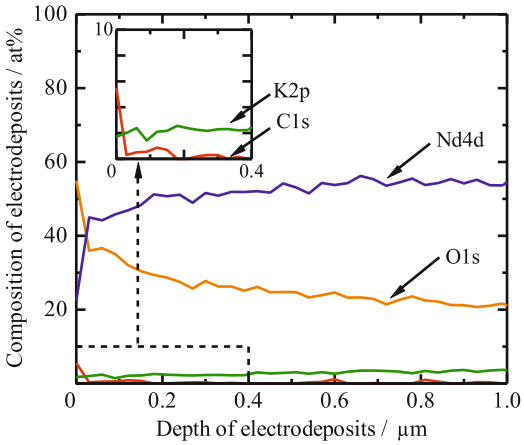

Fig. 6.30 The depth profile for each composition of the electrodeposits, ——: C1s, ——: O1s, ——: Nd4d, ——: K2p

potential of QRE was stabilized at elevated temperature. The electrodeposition was carried out at 373 K and the overpotential was controlled at −3.25 V vs. Pt QRE. After the electrodeposition, the electrodeposits were rinsed with a super dehydrated ethanol (Wako Pure Chemical Industries, Ltd., >99.5 %, the water content <50 ppm) in order to thoroughly remove the electrolyte adhered. The cathodic current density was estimated to be −0.18 mA cm^{-2} during electrodeposition, and the current density decreased gradually with electrodeposition time due to the limitation of the diffusion controlled. The cathodic and anodic current efficiencies were found to be 84.7 % and 92.3 %, respectively. These efficiencies were reasonably good in this electrodeposition, because the cathodic and the anodic reactions proceeded smoothly during electrodeposition.

After the electrodeposition process, some blackish electrodeposits were obtained on Cu substrate. The surface morphology of the electrodeposits was the different sizes of fine particle structures with some particles from SEM observations. Nd components were detected from EDX spectrum. In order to analyze chemical state of the electrodeposits, the energy spectra were measured before and after sputtering for 50 min on XPS analysis. The depth profile for each composition of the black electrodeposits is represented in Fig. 6.30. It was confirmed that Nd metal existing in electrodeposits eliminated the top surface and the oxygen content in the electrodeposits was gradually decreased with the increase of the depth of electrodeposits. This result revealed that a large amount of Nd metal was detected in the middle layer of electrodeposits and the oxygen content was also decreased with the increase of the depth. Moreover, it was confirmed that the content of K in the electrodeposit was less than 2.0 at.%. Although the practical Nd–Fe–B magnet rod

was used as an anode substrate, Fe was not detected in the electrodeposits. This result indicates that the Vycor glass filter can be prevented from the diffusion of the dissolution components such as Fe. In addition, the Nd $3d_{5/2}$ spectrum in the surface of the electrodeposits was detected at 982.0 eV. On the other hand, the $Nd3d_{5/2}$ spectrum in the middle layer of the electrodeposits after sputtering treatment was assigned at 981.2 eV. Each Nd metal and oxide has the binding energy of $Nd3d_{5/2}$ at 980.5–981.0 eV and 981.7–982.3 eV, respectively, in the case of monochromated Al Kα line [50]. According to the binding energy of $Nd3d_{5/2}$, the metallic state of Nd was ascertained on the middle layer of the electrodeposits, and the oxidation state of Nd appeared on the top surface of the electrodeposits.

6.7.4 Material Flow of Recovery Process

As described above, it is worthwhile for practical use to evaluate the material flow from all recovery processes such as pretreatment, wet separation, and electrodeposition using ILs. The material flow for all of recovery processes was displayed in Fig. 6.31, and the recovery target on this material flow was based on the oxidized Nd–Fe–B magnet wastes after roasting process.

As a first step of wet separation process, the selective leaching of RE components (93.5 % Nd and 66.7 % Dy) was performed on the leaching process. Then, the deironization treatment was executed by the precipitation method using the metallic hydroxide, and the residual Fe component was entirely removed on this process. After the iron removal treatment, the $M(TFSA)_n$ amide salts were obtained from the synthesis process, and the yield of RE components was achieved more than 90 % on this process. Thus, a series of wet separation process enabled us to reveal that the 86.1 % Nd and 66.7 % Dy can be recovered as a $M(TFSA)_n$ amide salt from the initial oxidized Nd–Fe–B magnet wastes. After the wet separation process, the $[P_{2225}][TFSA]$ including $M(TFSA)_n$ amide salts was available as an electrolytic bath on the electrodeposition process. As for the calculation of material flow, the induced potential, $E = -3.25$ V; the current density, $I_d = -0.18$ mA $cm^{-2;}$ and the current efficiency, $\varepsilon = 84.7$ %, were determined from the actual electrodeposition results described above. Assuming that total transported charge, $Q = 2960$ C, on a proper condition based on scaling up of the bath, the amount of 1.25 g Nd metal was recovered from this electrodeposition process, and the recovery yield calculated from the starting material (2.01 g Nd) was estimated to be 62.2 %. Therefore, this recovery process based on wet separation and electrodeposition processes using $M(TFSA)_n$ amide salts and $[P_{2225}][TFSA]$ was valid for the practical Nd–Fe–B magnet wastes. Further improvement of the recovery process for RE metals is now in progress.

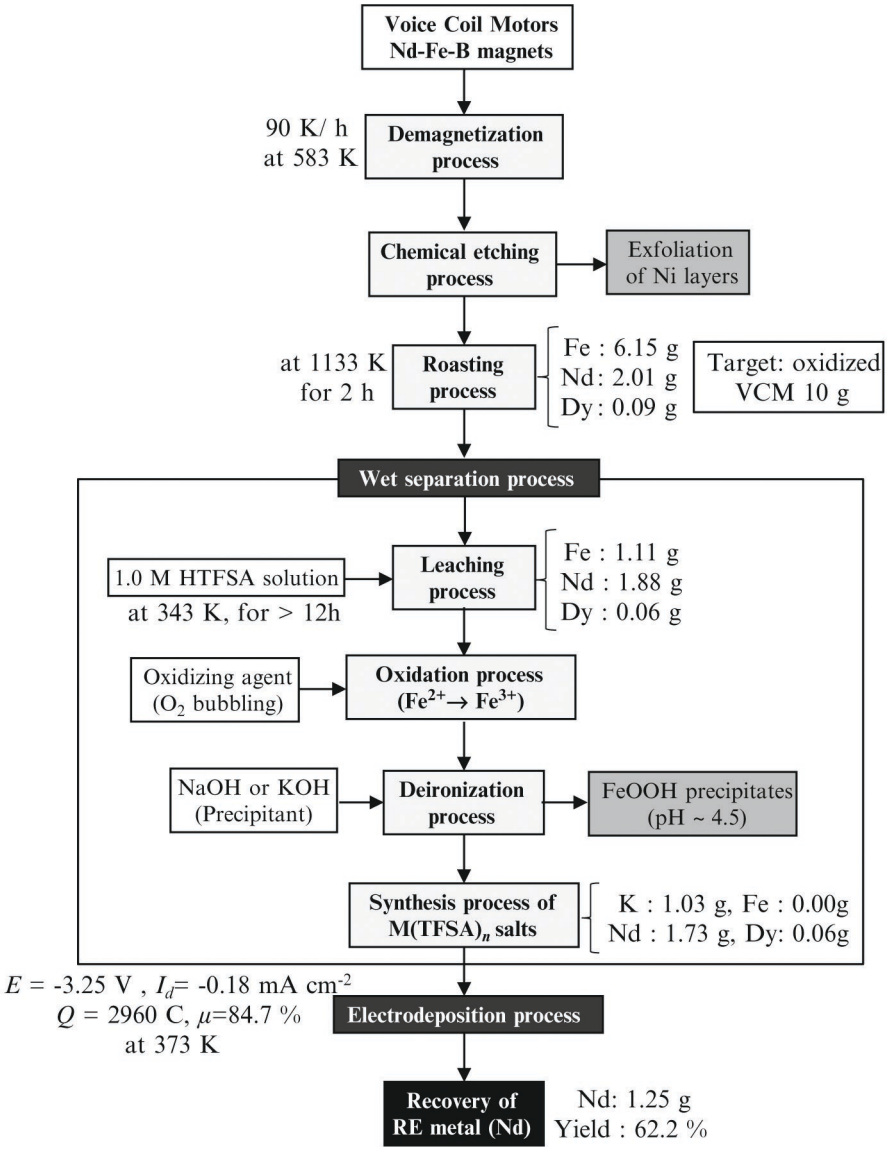

Fig. 6.31 Material flow of recovery process cooperated wet separation with electrodeposition using $M(TFSA)_n$ salts and $[P_{2225}][TFSA]$

Acknowledgments This research was supported by the Environment Research and Technology Development Fund (3K123018) of the Ministry of the Environment, Japan. This work was partially supported by the Grant-in-Aid for Scientific Research (No. 15H02848) from the Ministry of Education, Culture, Sports, Science and Technology, Japan.

References

1. Yang J, Li X, Lang J, Yang L, Wei M, Gao M, Liu X, Zhai H, Wang R, Liu Y, Cao J (2011) Structural, optical and magnetic properties of Eu-doped ZnO films. Mater Sci Semicond Process 14:247–252
2. Rao RP, Devine DJ (2000) RE-activated lanthanide phosphate phosphors for PDP applications. J Lumin 87–89:1260–1263
3. Thiel CW, Böttger T, Cone RL (2011) Rare-earth-doped materials for applications in quantum information storage and signal processing. J Lumin 131:353–361
4. Yuan D, Liu Y (2006) Electrochemical preparation La–Co magnetic alloy films from dimethylsulfoxide. Mater Chem Phys 96:79–83
5. Du X, Graedel TE (2011) Global in-use stocks of the rare Earth elements: a first estimate. Environ Sci Technol 45:4096–4101
6. Matsuura Y (2006) Recent development of Nd–Fe–B sintered magnets and their applications. J Magn Magn Mater 303:344–347
7. Kobayashi S, Kobayashi K, Nohira T, Hagiwara R, Oishi T, Konishi H (2011) Electrochemical formation of Nd-Ni alloys in molten LiF-CaF_2-NdF_3. J Electrochem Soc 158:E142–E146
8. Uda T (2002) Recovery of rare earths from magnet sludge by $FeCl_2$. Mater Trans 43(1):55–62
9. Takeda O, Okabe TH, Umetsu Y (2006) Recovery of neodymium from a mixture of magnet scrap and other scrap. J Alloys Compd 408–412:387–390
10. MacFarlane DR, Forsyth M, Howlett PC, Pringle JM, Sun J, Annat G, Neil W, Izgorodina EI (2007) Ionic liquids in electrochemical devices and processes: managing interfacial electrochemistry. Acc Chem Res 40:1165–1173
11. Simka W, Puszczyk D, Nawrat G (2009) Electrodeposition of metals from non-aqueous solutions. Electrochim Acta 54:5307–5319
12. Legeai S, Diliberto S, Stein N, Boulanger C, Estager J, Papaiconomou N, Draye M (2008) Room-temperature ionic liquid for lanthanum electrodeposition. Electrochem Commun 10:1661–1664
13. Bhatt AI, May I, Volkovich VA, Collison D, Helliwell M, Polovov IB, Lewin RG (2005) Structural characterization of a lanthanum bistriflimide complex, $La(N(SO_2CF_3)_2)_3(H_2O)_3$, and an investigation of La, Sm, and Eu electrochemistry in a room-temperature ionic liquid, $[Me_3NnBu][N(SO_2CF_3)_2]$. Inorg Chem 44:4934–4940
14. Londermeyer J, Multerer M, Zistler M, Jordan S, Gores HJ, Kipferl W, Dia-conu E, Sperl M, Bayreuther G (2006) Electroplating of dysprosium, electrochemical investigations, and study of magnetic properties. J Electrochem Soc 153(4):C242–C248
15. Ishii M, Matsumiya M, Kawakami S (2012) Development of recycling process for rare earth magnets by electrodeposition using ionic liquids media. ECS Trans 50(11):549–560
16. Kondo H, Matsumiya M, Tsunashima K, Kodama S (2012) Attempts to the electrodeposition of Nd from ionic liquids at elevated temperatures. Electrochim Acta 66:313–319
17. Kondo H, Matsumiya M, Tsunashima K, Kodama S (2012) Investigation of oxidation state of the electrodeposited neodymium metal related with the water contents of phosphonium ionic liquids. ECS Trans 50(11):529–538
18. Tsuda N, Matsumiya M, Tsunashima K, Kodama S (2012) Electrochemical behavior and solvation analysis of rare earth complexes in ionic liquids media investigated by SECM and Raman spectroscopy. ECS Trans 50(11):539–548
19. Matsumiya M, Ishii M, Kazama R, Kawakami S (2014) Electrochemical analyses of diffusion behaviors and nucleation mechanisms for neodymium complexes in [DEME][TFSA] ionic liquid. Electrochim Acta 146:371–377
20. Kurachi A, Matsumiya M, Tsunashima K, Kodama S (2012) Electrochemical behavior and electrodeposition of dysprosium in ionic liquids based on phosphonium cations. J Appl Electrochem 42:961–968

21. Kazama R, Matsumiya M, Tsuda N, Tsunashima K (2013) Electrochemical analysis of diffusion behavior and nucleation mechanism for Dy(II) and Dy(III) in phosphonium-based ionic liquids. Electrochim Acta 113:269–279
22. Apelblat A, Manzurola E (1999) Solubilities of o-acetylsalicylic, 4-aminosalicylic, 3,5-dinitrosalicylic, and p-toluic acid, and magnesium–aspartate in water from T = (278 to 348) K. J Chem Thermodyn 31:85–91
23. Ren Y, Shui H, Peng C, Liu H, Hu Y (2011) Solubility of elemental sulfur in pure organic solvents and organic solvent–ionic liquid mixtures from 293.15 to 353.15 K. Fluid Phase Equilib 312:31–36
24. Peter K (1993) Free energy calculations: applications to chemical and biochemical phenomena. Chem Rev 93:2395–2417
25. Gu W, Rahi SJ, Heim V (2004) Solvation free energies and transfer free energies for amino acids from hydrophobic solution to water solution from a very simple residue model. J Phys Chem B 108:5806–5814
26. Rey I, Johansson P, Lindgren J, Lassegues JC, Grondin J, Servant L (1998) Spectroscopic and theoretical study of $(CF_3SO_2)_2N^-$ ($TFSI^-$) and $(CF_3SO_2)_2NH$ (HTFSI). J Phys Chem A 102:3249–3258
27. Edman L (2000) Ion association and ion solvation effects at the crystalline–amorphous phase transition in PEO – LiTFSI. J Phys Chem B 104:7246–7254
28. Umebayashi Y, Mitsugi T, Fukuda S, Fujimori T, Fujii K, Kanzaki R, Takeuchi M, Ishiguro S (2007) Lithium ion solvation in room-temperature ionic liquids involving bis(trifluoromethanesulfonyl) imide anion studied by raman spectroscopy and DFT calculations. J Phys Chem B 111:13028–13032
29. Carnall WT, Fields PR, Rajnak K (1968) Electronic energy levels in the trivalent lanthanide aquo ions. I. Pr^{3+}, Nd^{3+}, Pm^{3+}, Sm^{3+}, Dy^{3+}, Ho^{3+}, Er^{3+}, and Tm^{3+}. J Chem Phys 49:4424–4442
30. Chambers MD, Clarke DR (2009) Doped oxides for high-temperature luminescence and lifetime thermometry. Annu Rev Mater Res 39:325–359
31. Su Q, Pei Z, Chi L, Zhang H, Zhang Z, Zou F (1993) The yellow-to-blue intensity ratio (Y/B) of Dy^{3+} emission. J Alloys Compd 192:25–27
32. Pei Z, Su Q, Li S (1991) Investigation on the luminescence properties of Dy^{3+} and Eu^{3+} in alkaline-earth borates. J Lumin 50:123–126
33. Katase T, Imashuku S, Murase K, Hirato T, Awakura Y (2006) Water content and related physical properties of aliphatic quaternary ammonium imide-type ionic liquid containing metal ions. Sci Technol Adv Mater 7:502–510
34. Yoshizawa M, Xu W, Angell CA (2003) Ionic liquids by proton transfer: vapor pressure, conductivity, and the relevance of ΔpKa from aqueous solutions. J Am Chem Soc 125:15411–15419
35. Goto M, Oldham KB (1973) Semiintegral electroanalysis. Shapes of neopolarograms. Anal Chem 45(12):2043–2050
36. Mahon PJ, Oldham KB (1998) Voltammetric modelling via extended semi-integrals. J Electroanal Chem 445:179–195
37. Matsuda H, Ayabe Y (1955) Zurtheorie der randles-sev.ikschenkathodenstrahl- polarographie. Z Elektrochem 59:494–503
38. Dalrymple-alford P, Goto M, Oldham KB (1977) Shapes of derivative neopolarograms. J Electroanal Chem 85:1–15
39. Scharifker B, Hills G (1983) Theoretical and experimental studies of multiple nucleation. Electrochim Acta 28:879–889
40. Bando Y, Katayama Y, Miura T (2007) Electrodeposition of palladium in a hydrophobic 1-*n*-butyl-1-methylpyrrolidinium bis(trifluoromethylsulfonyl)imide room-temperature ionic liquid. Electrochim Acta 53:87–91
41. Tachikawa N, Serizawa N, Katayama Y, Miura T (2008) Electrochemistry of Sn(II)/Sn in a hydrophobic room-temperature ionic liquid. Electrochim Acta 53:6530–6534

42. Zhu Y-L, Kozuma Y, Katayama Y, Miura T (2009) Electrochemical behavior of Ni(II)/Ni in a hydrophobic amide-type room-temperature ionic liquid. Electrochim Acta 54:7502–7506
43. Basile A, Bhatt AI, O'Mullane AP, Bhargava SK (2011) An investigation of silver electrodeposition from ionic liquids: influence of atmospheric water uptake on the silver electrodeposition mechanism and film morphology. Electrochim Acta 56:2895–2905
44. Fukui R, Katayama Y, Miura T (2011) The influence of potential on electrodeposition of silver and formation of silver nanoparticles in some ionic liquids. J Electrochem Soc 158(9):D567–D572
45. Mostany J, Mozota J, Scharifker BR (1984) Three-dimensional nucleation with diffusion controlled growth: Part II. The nucleation of lead on vitreous carbon. J Electroanal Chem 177:25–37
46. Gunawardena GA, Hills GJ, Montenegro I (1978) Potentiostatic studies of electrochemical nucleation. Electrochim Acta 23:693–697
47. Yang M-H, Sun I-W (2003) Electrodeposition of antimony in a water-stable 1-ethyl-3-methylimidazolium chloride tetrafluoroborate room temperature ionic liquid. J Appl Electrochem 33:1077–1084
48. Grujicic D, Pesic B (2005) Reaction and nucleation mechanisms of copper electrodeposition from ammoniacal solutions on vitreous carbon. Electrochim Acta 50:4426–4443
49. Matsumiya M, Kamo Y, Hata K, Tsunashima K (2013) Solvation structure of iron group metal ion in TFSA-based ionic liquids investigated by raman spectroscopy and DFT calculations. J Mol Struct 1048:59–63
50. Moulder JF, Stickle WF, Sobol PE, Bomben KD (1992) Handbook of X-ray photo-electron spectroscopy. Perkin-Elmer Corp., Eden Prairie
51. Tanaka M, Oki T, Koyama K, Narita H, Oishi T (2013) Recycling of rare earths from scrap. Handb Phys Chem Rare Earths 43:159–212
52. Pearson RG (1988) Absolute electronegativity and hardness: application to inorganic chemistry. Inorg Chem 27:734–740
53. Diakonov II, Ragnarsdottir KV, Tagirov BR (1998) Standard thermodynamic properties and heat capacity equations of rare earth hydroxides: − II. Ce(III)-, Pr-, Sm-, Eu(III)-, Gd-, Tb-, Dy-, Ho-, Er-, Tm-, Yb-, and Y-hydroxides. Comparison of thermochemical and solubility data. Chem Geol 151:327–347
54. Gnanaprakash G, PhilipJ RB (2007) Effect of divalent metal hydroxide solubility product on the size of ferrite nanoparticles. Mater Lett 61:4545–4548
55. Michelle M, Joseph M, Renee F (2008) Determining the solubility product of $Fe(OH)_3$: an equilibrium study with environmental significance. J Chem Educ 85(2):254–255
56. Diakonov I, Khodakovsky I, Schott J, Sergeeva E (1994) Thermodynamic properties of iron oxides and hydroxides. I. Surface and bulk thermodynamic properties of goethite (α-FeOOH) up to 500 K. Eur J Mineral 6:967–983

Part V
Utilization of Ionic Liquids on Rare Earth Materials

Chapter 7
Ionic Liquids and Rare Earth Soft Luminescent Materials

Huanrong Li, Yige Wang, Tianren Wang, and Zhiqiang Li

Abstract Soft luminescent materials resulting from the introduction of rare earth compounds to ionic liquids favorably combine the properties of ionic liquids with unique optical properties of rare earth compounds such as sharp emission band, long decay time of the excited state, and the tunable emission color over the entire spectral range of interest from UV to infrared spectral region. This chapter summarizes the progress ever made in such kind of soft luminescent materials, especially those that have been made in our research group. Our emphasis is put on the preparation strategies for the soft luminescent materials, the luminescent ionogels prepared from the immobilization of rare earth-containing ionic liquids by organosilica and polymers, and the unexpected luminescent enhancement of Eu^{3+}-β-diketonate complexes hosted in zeolite L nanocrystals and nanoclay upon addition of ionic liquid bearing bulky triethoxysilane groups in water.

Keywords Ionic liquid • Rare earth • Soft materials • Luminescence • Ionogels

7.1 Introduction

Over the past decades, ionic liquids have stimulated remarkable scientific interest owing to their special properties, functional versatility, and widely potential applications. Ionic liquids are organic salts totally composed of bulky organic cations and inorganic or organic anions with quite low-melting temperature below 100 °C or close to room temperature [1]. They have recently been proposed as green solvent to replace the conventional and harmful organic solvents owing to their obviously special and attractive properties. The main advantageous properties of ionic liquid over the conventional organic solvents are their negligible vapor pressure, non-flammability, wide liquid range, tunable solvation ability for various organic and inorganic substances, and the fine tunability of structure and properties through varying the cations and anions. Ionic liquids were also used as catalysts, reagents, or solvents in several

H. Li (✉) • Y. Wang • T. Wang • Z. Li
School of Chemical Engineering and Technology, Hebei University of Technology, Tianjin, China
e-mail: lihuanrong@hebut.edu.cn

J. Chen (ed.), *Application of Ionic Liquids on Rare Earth Green Separation and Utilization*, Green Chemistry and Sustainable Technology,
DOI 10.1007/978-3-662-47510-2_7

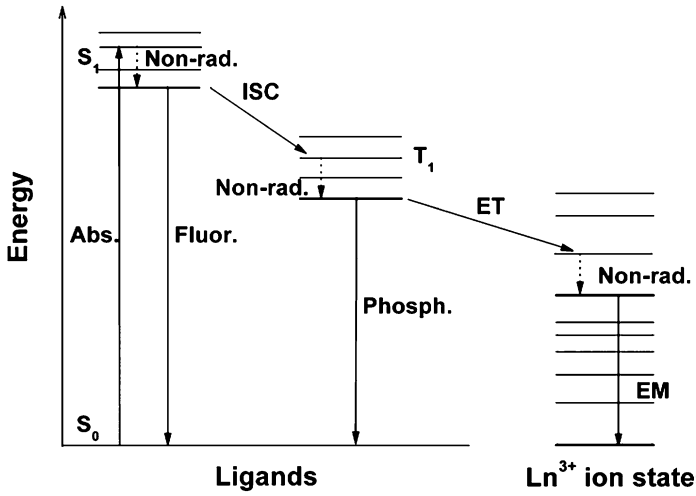

Fig. 7.1 Simplified energy diagram of the lanthanide organic complex system. *Abs.* absorption, *Fluor.* fluorescence, *Phosph.* phosphorescence, *EM* lanthanide (Ln^{3+}) ion emission, *ISC* intersystem crossing, *ET* energy transfer, *S* singlet, *T* triplet, *Non-rad.* nonradiative transitions (Reproduced from Ref. [18] by permission of the Royal Society of Chemistry)

chemical reactions [2, 3], and they can also be used in separation processes [4–9] and as functional materials, e.g., electrolytes for lithium cell and solar cells [3, 10–13]. Further applications of ionic liquids can be found as solvents and templates for materials science. Many excellent and comprehensive reviews have been published recently in this regard [14–17].

Metal-containing ionic liquids are proposed as promising new functional materials that combine the intriguing properties of ionic liquids with additional intrinsic magnetic, spectroscopic, and catalytic properties depending on the metal ions [19]. Among them, rare earth-containing ionic liquids (RE-ionic liquids) can be regarded as novel and promising soft luminescent materials for use in photochemistry and spectroscopy [20–23]. The motivation behind the utilization of ionic liquids to prepare RE-containing soft materials is that the resulting materials can favorably combine the properties of ionic liquids with unique optical properties of RE compounds such as sharp emission band, long decay time of the excited state, and the tunable emission color over the entire spectral range of interest from UV to infrared spectral region. Furthermore, many ionic liquids are colorless or only show slight color and are transparent through the whole visible and near-infrared spectral regions [20]. In addition, good solubility of ionic liquids for various compounds makes it easy to prepare RE-ionic liquids. Initial studies on RE-ionic liquids are mostly involved with RE salts [24]; however, most of the RE^{3+} ions have extremely low molar extinction coefficients since their f-f electronic transitions are forbidden by parity and spin rules, which results in the very limited luminescence intensity upon direct excitation in 4f levels [25]. Fortunately, this problem can be overcome by the so-called antenna effect (or sensitization) from certain organic ligand. The commonly accepted mechanism for the sensitization has been believed to be the energy transfer from ligand to central RE^{3+} ions (Fig. 7.1), a process that is comprised of

light absorption into the singlet state of the ligand, followed by the energy transfer to the ligand triplet state through intersystem crossing, intramolecular energy transfer from the ligand triplet states to the RE^{3+} emissive state(s), and finally the characteristic emission of RE^{3+} [18, 26, 27]. Therefore, the introduction of RE complexes with organic ligand into ionic liquids was recently found to be an alternative method to prepare highly luminescent soft materials [23, 28], and soft luminescent material with bettered luminescence behavior and improved stability can be obtained using this method [23, 29]. Most of them can be regarded as luminescent soft materials, which show obvious advantages in fabricating soft optical devices. Furthermore, soft luminescent materials consisting of RE complexes and ionogels have appeared recently. The so-called ionogels were prepared by immobilizing ionic liquids with silica, polymer, and etc. [30, 31]. One of the advantages of ionogels over the corresponding ionic liquids is that the former can retain most of the attractive properties of ionic liquids except their liquid state. The liquid characteristic of ionic liquids is commonly believed to be a big hamper for them to be used as advanced functional materials [32]. The aim of this chapter is to give an overview of the progress ever made in RE-ionic liquids soft luminescent materials. The emphasis herein will be mainly put on the work that carried out in our group. Rare earth-based ionic liquid crystals and rare earth nanoparticles in ionic liquids are not included in this chapter.

7.2 Methods for the Preparation of RE-Ionic Liquids

Up to now, several methods have been developed to prepare RE-ionic liquids in the literatures: (1) simple doping method, (2) incorporating RE compounds in anions of ionic liquids, and (3) grafting RE compounds to the organic cations of ionic liquids.

7.2.1 Doping RE Compounds in Ionic Liquids

One of the most simple and easily handled methods to prepare RE-ionic liquids was to simply dissolve RE salts or RE complexes in the ionic liquids, which initially aimed to test the catalytic performances of RE compounds in ionic liquids [12, 33]. Recently, more attention has been paid to the investigation on the photoluminescence properties of RE compounds in ionic liquids, which demonstrate that the dissolution of RE compounds in ionic liquids can be used as ideal and promising soft luminescent materials. Bünzli and co-workers [22] studied the luminescence of RE^{3+} salts dissolved in 1-alkyl-3-methylimidazolium chloride (or $[C_n\text{-mim}]X$, where $n = 12–18$, $X = NO_3^-$ or Cl^-). Luminescence properties of Eu^{3+} salts are significantly improved by energy transfer from ionic liquids to the metal center (71). Of high importance is the facile tuning of the luminescence characteristic of the resulting RE-ionic liquids from blue to red through choosing either the excitation wavelength or the counterion (Fig. 7.2b). In addition to visible

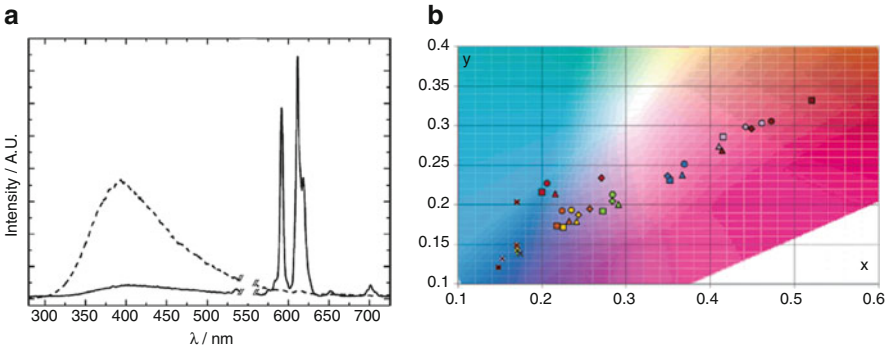

Fig. 7.2 (**a**) The emission spectra obtained at room temperature under broad band excitation at 274 nm; (**b**) trichromatic diagram displaying the position of the studied samples in function of their composition and the excitation wavelength (*gray*, 274 nm; *violet*, 285 nm; *blue*, 334 nm; *green*, 344 nm; *yellow*, 353 nm; *orange*, 361 nm; *red*, 393 nm) (Reprinted with the permission from Ref. [22]. Copyright 2004 American Chemical Society)

luminescence, strong emissions in infrared spectral region were also observed in ionic liquids. The Nd(III) complexes can be doped at the highest concentration of 3.0 % (w/w) in 1-alkyl-3-methylimidazolium ionic liquids. Intense NIR luminescence has been observed upon ligand excitation for Nd(III) complexes with 1,10-phenanthroline or β-diketonate ligands (4,4,4-trifluoro-1-(2-naphthyl)-1,3-butanedionate ligands). The obtained soft materials show great potentials in liquid chelate lasers [20]. The NIR luminescence of other Er^{3+} complexes dissolved in ionic liquids was also investigated [21]. However, drawbacks of this simple method such as low concentration of RE compounds in ionic liquids have frequently been observed due to the weakly coordinating properties of the constituting anions and cations [34]. Ionic liquids containing high concentrations of RE are highly desirable in electrodeposition, catalysis, or photophysics.

7.2.2 *Incorporating RE Compounds in Anions of Ionic Liquids*

An alternative way to directly dissolve RE compounds is using RE compounds as the anions when preparing RE-containing ionic liquids. Nockeman and co-workers synthesized a series of low-melting RE-containing ionic liquids based on the 1-butyl-3-methylimidazolium (BMIM) cation and RE thiocyanate anions of general formula $[Ln(NCS)_x(H_2O)_y]^{3-x}$ ($x = 6$–8; $y = 0$–2, Ln = Y, La, Pr, Nd, Sm, Eu, Gd, Tb, Ho, Er, and Yb). The new RE-containing ionic liquids show good solubility in apolar solvent and good miscibility with other ionic liquid, which makes them interesting candidates for catalytic and spectroscopic applications [35]. Liquid crystalline phases might be obtained if one extends the alkyl chain length of the

imidazolium cation [36]. Other striking examples of such types of RE-containing ionic liquids were reported by Mudring and co-workers [37, 38]. They reported an unprecedented series of Eu-containing ionic liquids with low-melting point by metathesis reactions from stoichiometric amounts of europium(III)bis(trifluoromethanesulfonyl)amide salts and the imidazolium-based ionic liquids. The resulting ionic liquids were believed to be the first f-element ionic liquids that do not need the stabilization of their liquid state by neutral coligands such as water molecules. Characteristic emissions of Eu^{3+} can be observed for all the samples under UV illumination. Of high importance is that the lifetimes of the samples in the liquid state are quite high (up to 2.2 ms) under such high europium concentration (100 % Eu doped). Typically, radiationless decay caused by concentration quenching becomes pronounced at such concentrations in traditional solid luminescent materials. Dy-containing ionic liquids of low-melting point exhibiting both magnetism and luminescence were also synthesized according to similar strategy by the same group [39].

The aforementioned luminescence of the RE-containing ionic liquids with RE compounds as their anions was observed by direct excitation into their 4f absorption lines. Low absorption is one of the biggest problems for them since luminescence intensity is proportional to both the luminescence quantum yield and to the amount of light absorbed [27]. RE complexes with organic ligand that can sensitize the luminescence of RE via the so-called antenna effect have also been used as the anions for preparing RE-containing ionic liquid. Binnemans and co-workers synthesized an RE-containing ionic liquid, the anions of which are europium(III) b-diketonate complexes, 1-hexyl-3-methylimidazolium tetrakis(2-thenoyltrifluoroacetonato)europate(III) complex, and [HMIM][Eu(tta)$_4$] (Fig. 7.3) [23]. The solubility of the compound in the corresponding ionic liquid [HMIM][Tf_2N] (Tf_2N=bis(trifluoromethanesulfonyl)imide) is quite high, and dissolving [HMIM][Eu(tta)$_4$] in the ionic liquid [HMIM][Tf_2N] leads to soft luminescent materials emitting bright light with remarkably improved photostability under UV illumination [23].

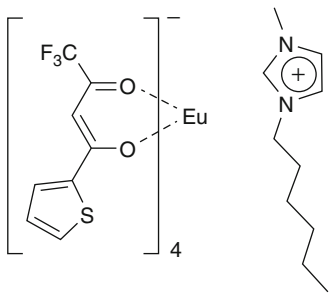

Fig. 7.3 1-Hexyl-3-methylimidazolium tetrakis (2-thenoyltrifluoroacetonato) europate(III) complex (Reproduced from Ref. [23] by permission of the Royal Society of Chemistry)

7.2.3 Grafting RE Compounds to the Organic Cations of Ionic Liquids

Grafting of RE complexes with organic ligand to the organic cations is another effective way to increase the doping concentration of RE in ionic liquid. This method principally involves (1) the synthesis of task-specific ionic liquid (TSIL) in which organic moieties capable of coordinating to and sensitizing RE^{3+} ions are covalently linked to the organic cations and (2) the coordination reaction of the TSIL with RE^{3+} ions under optimal conditions. Up to now, TSILs functionalized with organic ligands such as terpyridine [40, 41], β-diketone [9], aromatic carboxylic acid [39], and phosphine oxides [42] have been successfully synthesized. Wen et al. synthesized a new TSIL functionalized with aromatic carboxylic acid group in one simple step by reacting the commercially available 1-methylimidazole and (4-bromomethyl)benzoic acid in EtOH. Interestingly, heating the mixture of $EuCl_3.6H_2O$ (or $TbCl_3.6H_2O$, or the mixture of both RE salts) in EtOH, MeOH, or DMF solution at 80 °C for several hours leads to the formation of transparent and luminescent gels upon the evaporation of solvents. The achievement of RE^{3+} characteristic emission under UV illuminations is due to the energy transfer from the TSIL to RE^{3+} ions. The emission color of the transparent gels can be fine-tuned by changing RE salts (Fig. 7.4). Both the coordination of RE^{3+} to TSIL and the presence of hydrogen bonding within the RE-coordinated organic salts are believed to be responsible for the formation of the ionogels [39].

Although TSILs consisting of terpyridine moieties have been reported previously [40], the study of such family of ionic liquids in developing novel soft luminescent materials appeared in 2013 [41]. Wang et al. reported terpyridine-functionalized ionic liquids, which were donated as [Cnterpyim]X ($n = 1$, 4, 16, X = Br and NTf_2). All [Cnterpyim]Br were pale yellow solid at room temperature, while substituting Br with NTf_2 leads to yellow brown oils. Both [Cnterpyim]Br and [Cnterpyim]NTf_2 can effectively sensitize europium(III); bright red-emitting soft luminescent materials can therefore be obtained through coordination of Eu^{3+}-coordinated carboxyl-functionalized ionic liquids with terpyridine-functionalized ionic liquids (Fig. 7.5). The obtained materials are either paste-like substances or viscous fluids, depending on the anions of the carboxyl-functionalized ionic liquids. The merits of these soft materials like a high content of ionic liquids, easy coating on surfaces, and excellent luminescence properties (e.g., long lifetime, high color purity) might render them extremely valuable for various optical applications of such flexible displays.

7.2.4 Dissolution of RE Oxides in Carboxyl-Functionalized Ionic Liquid

It has been well documented that normal ionic liquids have quite a low solubility for metal salts. The use of TSILs that contain a functional group covalently tethered to

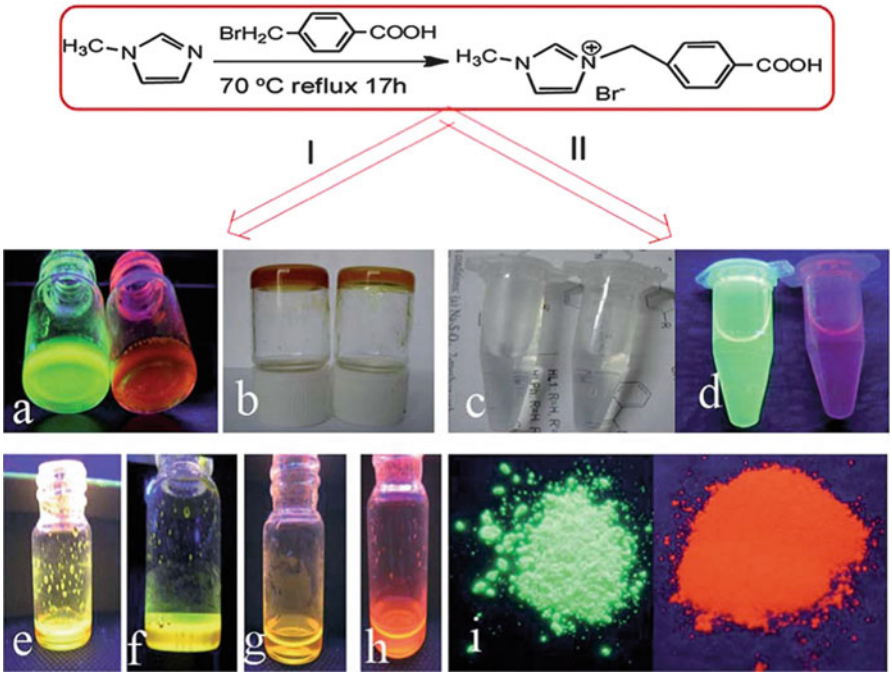

Fig. 7.4 Synthesis of IL-ACC and digital photos of the samples. Gel-Eu and Gel-Tb under UV light (**a**) and daylight (**b**), precipitate dissolved in water under daylight (**c**) and UV light (**d**), gel with increased molar ratio of Tb^{3+}/Eu^{3+} (**e–h**) under UV light and the precipitate under UV light (**i**). (*I*) Without NaOH and (*II*) with NaOH. The UV light used in this study is 254 nm (Reproduced from Ref. [39] by permission of the Royal Society of Chemistry)

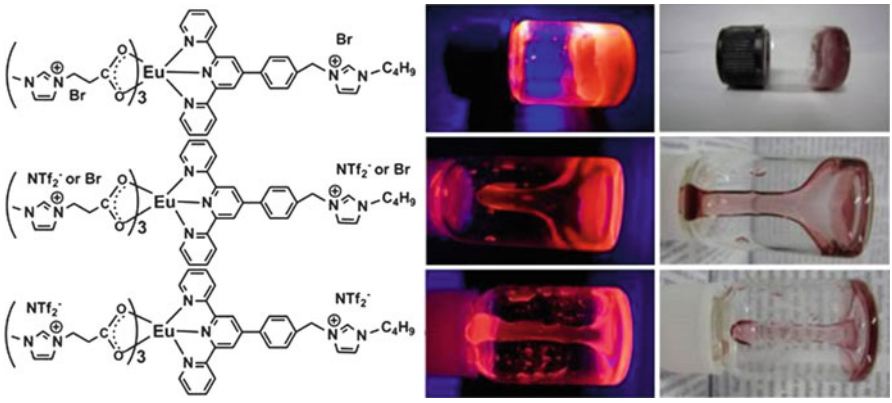

Fig. 7.5 Digital photos of the soft materials taken under UV light (Reprinted with the permission from Ref. [40]. Copyright 2013 American Chemical Society)

the cationic or anionic part can substantially increase the solubility of metal salts in the ionic liquids. However, these TSILs usually are obtained through a multistep synthetic procedure, limiting their use in large-scale industrial applications. Nockemann et al. synthesized a carboxyl-functionalized ionic liquid, [Hbet][Tf_2N], by reacting an aqueous solution of cheap and commercially available betaine hydrochloride with lithium bis(trifluoromethylsulfonyl)imide. The ionic liquid shows ability to dissolve large quantities of metal oxides, including trivalent RE oxides, because the ionic liquids can form stoichiometric compounds with the metal [43]. The presence of water can facilitate the dissolution of the metal oxide in the ionic liquids because water molecules can help to wet the metal oxides. Inspired by this report, we developed a novel and facile method to prepare soft luminescent materials by directly dissolving both rare earth oxide and organic ligands in carboxyl-functionalized ionic liquids, 3-(5-carboxypropyl)-1-methylimidazolium bromide, and 3-(5-carboxypropyl)-1-butylimidazolium bromide that is obtained through the reaction of commercially available 3-bromopropanoic acid and 1-methylimidazole or 1-butylimidazole, respectively (Fig. 7.6) [28, 29].

Like [Hbet][Tf_2N] previously reported by Nockemann et al. [43], both 3-(5-carboxypropyl)-1-methylimidazolium bromide and 3-(5-carboxypropyl)-1-butylimidazolium bromide can react with RE oxides to form carboxylate complexes and water. Upon dissolution of rare earth oxides assisted with an appropriate amount

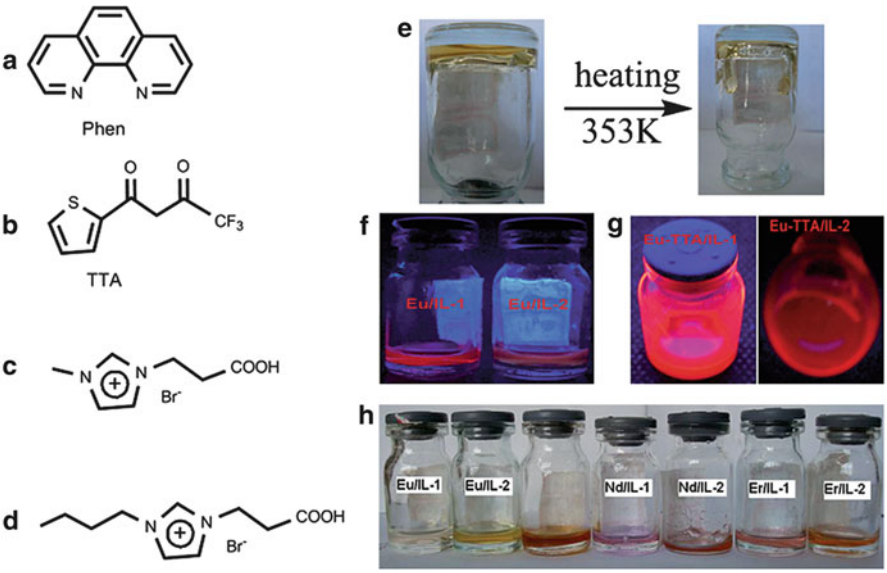

Fig. 7.6 Chemical formula of organic ligand (**a, b**) and ionic liquid (**c, d**) and digital photographs of the soft luminescent materials (**e–h**) (Reproduced from Ref. [29] by permission of the Royal Society of Chemistry)

of water, the carboxyl-functionalized ionic liquids show a slight color (Fig. 7.6h) and become highly viscous at room temperature. Heating at 80 °C renders them fluid (Fig. 7.6e). Interestingly, the ionic liquids have a selective solubilizing ability for RE oxides under heating at 100 °C for 12 h. Eu_2O_3, Nd_2O_3, Er_2O_3, and Dy_2O_3 were found to be soluble, whereas Tb_4O_7 and Pr_6O_{11} were insoluble or very poorly soluble in the ionic liquids. However, both Tb_4O_7 and Pr_6O_{11} can be dissolved when they were contained in a Teflon-lined stainless steel autoclaved and then subjected to heating at temperature of 120 °C for 1 week [44]. Eu-containing and Tb-containing ionic liquids show weak bright red and green emission illuminated by UV light due to the presence of Eu^{3+} and Tb^{3+}, respectively. For 3-(5-carboxypropyl)-1-butylimidazolium bromide, besides the Eu^{3+} intra-$4f^6$ yellow-red sharp lines ascribing to the transitions between $^5D_0$ and $^7F_{0-4}$ levels, a strong broad band in the blue spectral region was observed. The broad band might arise from 3-(5-carboxypropyl)-1-butylimidazolium bromide. Furthermore, the relative intensity between the broad band and the Eu^{3+} cation lines strongly depends on the Eu^{3+} concentration. Increasing the Eu^{3+} concentration induces a decrease in the intensity of the broad band associated with the Eu^{3+} cation lines. This means that fine-tuning of the emission characteristics is easily achieved through adjustment of the Eu^{3+} concentration.

Luminescent RE complexes can be formed if organic ligand such as TTA was further dissolved in the RE-containing carboxyl-functionalized ionic liquid. Concentration as high as 25 mole% (with respect to ionic liquid) of RE can be obtained by this method. Strong bright red-emitting light was observed for Eu-containing ionic liquids (Fig. 7.6g). Interestingly, emissions in the infrared spectral region can be observed for Nd- and Er-containing ionic liquids upon further dissolving the TTA ligands. It is worthy to note that under identical measurement conditions, the pure $Er(TTA)_3.2H_2O$ complex cannot display any emission and $Nd(TTA)_3.2H_2O$ only presents very weak emissions under the same measuring conditions [29]. Wang et al. prepared red-emitting soft materials according to the same strategy by dissolving 4,4′,4″-trifluoro-1-(2-naphthyl)-1,3-butanedione (NTA) and Phen or Bpy in Eu-containing 3-(5-carboxypropyl)-1-butylimidazolium bromide with molar ratio of Eu^{3+}:ionic liquid: NTA (Bpy or Phen) = 1:3:1. FTIR spectra reveal that at least parts of the ionic liquids (carboxylic acid) are replaced with β-diketone ligand rather than the formation of europium complex with the molar ratio of Eu^{3+}:ionic liquid: ligand being 1:3:1, while no ionic liquids could be replaced by the heterocyclic ligand such as Bpy and Phen [45].

7.3 Luminescent Ionogels

Ionic liquids show great potential applications in various fields owing to their unique properties. However, for material applications, there is a challenging need for immobilizing ILs in solid matrices while keeping their specific properties except outflow [31]. Ionogels are therefore claimed as a new class of hybrid materials resulting from the immobilization of ionic liquids within organic (low molecular

weight gelator, biopolymer), inorganic (silica, carbon nanotubes, etc.), or organic–organic hybrid components [31]. Ionogels have found applications such as catalysts [47], electrolytes for lithium batteries [48] and solar cells [49, 50], and drug release [51]. Recently, RE complex-doped ionogels have appeared as a new type of organic–inorganic hybrid luminescent materials.

7.3.1 Organosilica-Based Luminescent Ionogels

The europium(III) tetrakis β-diketonate complex was doped into an ionogel via a three-step procedure: (1) a monolith ionogel was firstly prepared by confining $[C_6mim][Tf_2N]$ ionic liquid in a silica network through a non-hydrolytic sol–gel processing, (2) the ionic liquid was replaced in the ionogel by acetonitrile, and (3) finally, the acetonitrile contained in the porous network was replaced by the europium(III)-doped ionic liquid. The resulting luminescent ionogel was crack-free, fully transparent, and colorless. It is noteworthy that this solid contained 80 % vol. of ionic liquid. The results showed that the complex was still dissolved in the ionic liquid and the photophysical properties of the complex were barely changed by the silica network. The luminescent ionogels emit bright red light of a high monochromatic purity with a $I(^5D_0 \rightarrow {}^7F_2)/I(^5D_0 \rightarrow {}^7F_1)$ intensity ratio of 21.6, as revealed by the luminescence spectrum of the ionogel shown in Fig. 7.7.

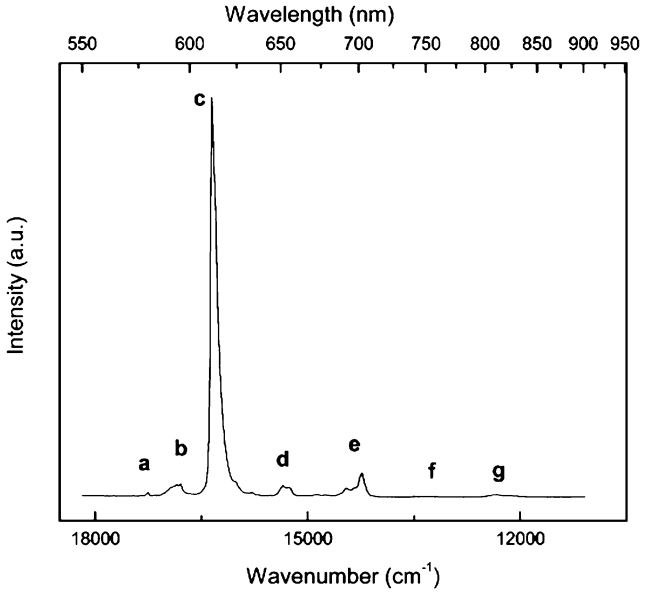

Fig. 7.7 Room temperature emission spectrum of the ionogel (Reprinted with the permission from Ref. [46]. Copyright 2006 American Chemical Society)

Fig. 7.8 Illustration of the procedure used to obtain the transparent and luminescent ionogel (Reproduced from Ref. [53] by permission of the Royal Society of Chemistry)

Luminescent ionogels doped with the complexes $[C_6mim][Ln(tta)_4]$ (tta = 2-thenoyltrifluoroacetonate and Ln = Nd, Sm, Eu, Ho, Er, Yb) and $[choline]_3[Tb(dpa)_3]$ (dpa = dipicolinate) were also reported [52].

Feng and co-workers recently reported a simple way for preparing luminescent ionogel monoliths (Eu@IL-Bipy-SiO_2) by doping carboxyl-functionalized ionic liquid solubilizing Eu_2O_3 to a organosilica derived from a silylated bipyridine, which has dual roles, i.e., the bipyridine moieties can sensitize the luminescence of Eu^{3+} ions, and the alkoxysilane substituent can be hydrolyzed and condensed through a sol–gel process (Fig. 7.8) [53]. In the luminescent ionogels, Eu^{3+} ions are coordinated to the ionic liquid via oxygen atoms and to the covalently bonded bipyridine moieties via nitrogen atoms as shown in Fig. 7.8.

Excitation into the absorption band at 320 nm leads to the characteristic emission of Eu^{3+} ions $^5D_0 \rightarrow {}^7F_J$ (J = 0–4), with the hypersensitive transition $^5D_0 \rightarrow {}^7F_2$ as the most prominent line, indicative of energy transfer from bipyridine moieties to Eu^{3+}. Interestingly, the emission color of the ionogel can be tuned by varying the excitation wavelength. Excitation into the Eu^{3+} absorption band of 395 nm resulted in the emission spectrum composed of sharp line of Eu^{3+} and a broad emission band in the blue region peaking at 458 nm. The possible origin of the latter band is due to an intracomplex metal-to-ligand energy transfer. It is worthy to note that the presence of the carboxyl-functionalized ionic liquids in Eu@IL-Bipy-SiO_2 affords a longer lifetime and a higher quantum efficiency of Eu^{3+} excited state with respect to Eu@ Bipy-SiO_2 in which no ionic liquids are present (Table 7.1).

The organosilica-based ionogels discussed aforementioned is that the ionic liquid was either simply doped to the organosilica networks [46] or linked to the

Table 7.1 Experimental $^5D_0$ lifetime, calculated radiative and nonradiative $^5D_0$ decay rate, $^5D_0$ quantum efficiency value, and the number of water coordinated to Eu^{3+} ion

Sample	τ (ms)	k_r (ms^{-1})	k_{nr} (ms^{-1})	q (%)	n_w
Eu@IL-Bpipy-SiO_2	0.72	0.469	0.911	33.99	0.66
Eu@ Bpipy-SiO_2	0.46	0.375	1.79	17.28	1.60

Reproduced from Ref. [53] by permission of the Royal Society of Chemistry

organosilica component via coordination bond [53]. Ru and co-workers recently reported a family of thermally reversible, flexible, and transparent RE complexes doping ionogels in which the ionic liquid component was covalently bonded to organosilica [54]. The ionogels were prepared by the hydrolysis and condensation of an ionic liquid that bears hydrolysable alkoxysilane groups and urea moieties in the presence of RE^{3+} species under acidic conditions. The luminescence color of the resulting ionogels can be fine-tuned by changing the RE^{3+} ions (Eu^{3+}, Tb^{3+}, or a mixture of Eu^{3+} and Tb^{3+}) and by changing the excitation wavelength (Fig. 7.9). More interestingly, the organosilicas show thermal reversibility and flexibility, which are uncommon in organosilicas that contain Ln^{3+} species (Fig. 7.9). The thermal reversibility of the organosilicas makes them attractive for the development of flexible optical devices and flexible luminescent devices such as organic light-emitting diodes (OLEDs).

Fan and co-workers also reported the preparation, characterization, and luminescent properties of transparent and luminescent thin film of ionogels [55]. The red-emitting thin films were obtained by hydrolysis and condensation of silylated ionic liquid (**1**) and silylated 2-thienyhrifluoroacetonate (TTA–Si) under acidic conditions. **1** acts both as the ionic liquid and as one of the sol–gel precursors, and TTA–Si can be used both as the sol–gel precursor and as the ligand for coordinating to and sensitizing Eu^{3+} ions. As a consequence, both the ionic liquid and the luminescent RE complexes are covalently bonded to the silica matrix via Si–C bond in the red-emitting thin films. Substitution of Eu^{3+} and TTA–Si with Tb^{3+} and **2** which is an organic salt consisting of aromatic carboxylic acid group and is an effective sensitizer for Tb^{3+} yielded the green-emitting films. The molecular structure of silylated ionic liquid (**1**), TTA–Si, and the organic salt (**2**) is displayed in Fig. 7.10. The resulting films are transparent and show bright emission under UV light.

7.3.2 Polymer-Based Luminescent Ionogels

In addition to organosilica, polymer is also frequently used to immobilize ionic liquid to prepare luminescent ionogels. Flexible luminescent polymers were prepared by doping europium(III) complexes to matrices composed of poly(methyl methacrylate) (PMMA) and ionic liquids. The liquids were reported to act as a plasticizer for PMMA. The films doped with $[choline]_3[Eu(dpa)_3]$ show a very long lifetime (1.8 ms) of the $^5D_0$ excited state. These materials can find great potential

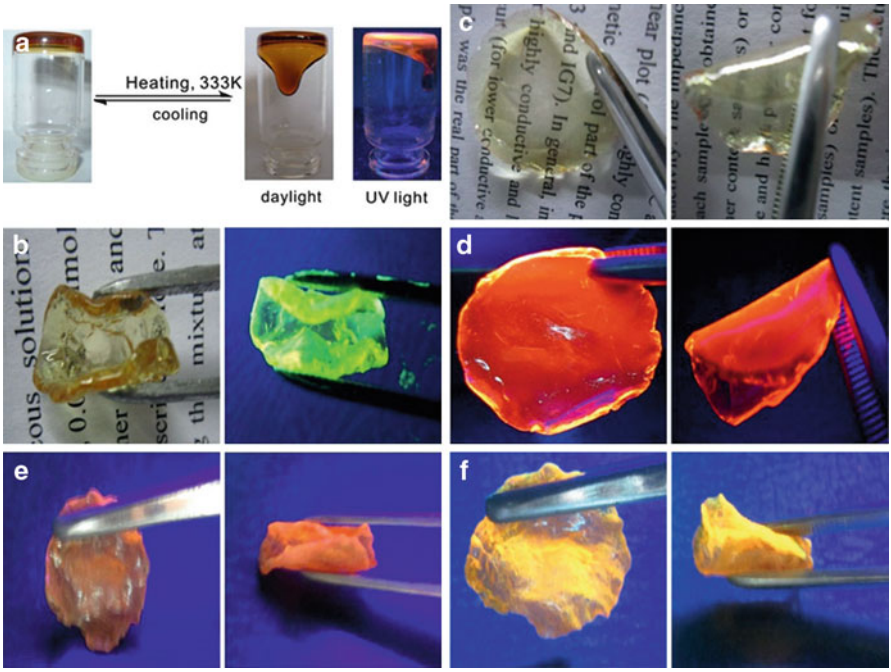

Fig. 7.9 Digital photos of the organosilicas. (**a**) $EuCl_3$-containing organosilica, it can be thermal reversible; (**b**) Tb(SA)-containing organosilica under daylight and UV light; (**c**) $Eu(tta)_3$-containing organosilica under daylight. (**d**) $Eu(tta)_3$-containing organosilica under UV light, (**e**) $Eu(tta)_3$/Tb(SA)-containing organosilica irradiated under 365 nm, and (**f**) $Eu(tta)_3$/Tb(SA)-containing organosilica irradiated under 254 nm. The photos also exhibit the flexibility of the transparent and luminescent organosilicas (Reproduced from Ref. [54] by permission of John Wiley & Sons Ltd)

applications in various fields, such as in optical devices including OLEDs and luminescent solar concentrators [56]. However, the environmentally hazardous solvents like dichloromethane were used in preparing these luminescent films. Wang et al. developed a simple and environmentally friendly method to prepare transparent and luminescent ionogels [57]. Firstly, RE-containing ionic liquids were prepared by dissolving rare earth oxides and organic ligands in a carboxyl-functionalized ionic liquid; secondly, the ionic liquids were dissolved in MMA monomers; and finally, the luminescent ionogels were formed by polymerizing the MMA monomers. The obtained luminescent materials are composed of ionic liquids, PMMA, and RE complexes.

Up to now, most of the polymer-based luminescent ionogels were obtained by immobilizing ionic liquid with PMMA [56, 57, 59] although ionogels obtained by immobilizing ionic liquid with biopolymer such as gelatin have been reported frequently [60–62]. Gelatin is a widely available, inexpensive, and biodegradable gelling agent with good physical and chemical properties. Li and co-workers reported a novel luminescent ionogels, which was obtained by doping water soluble

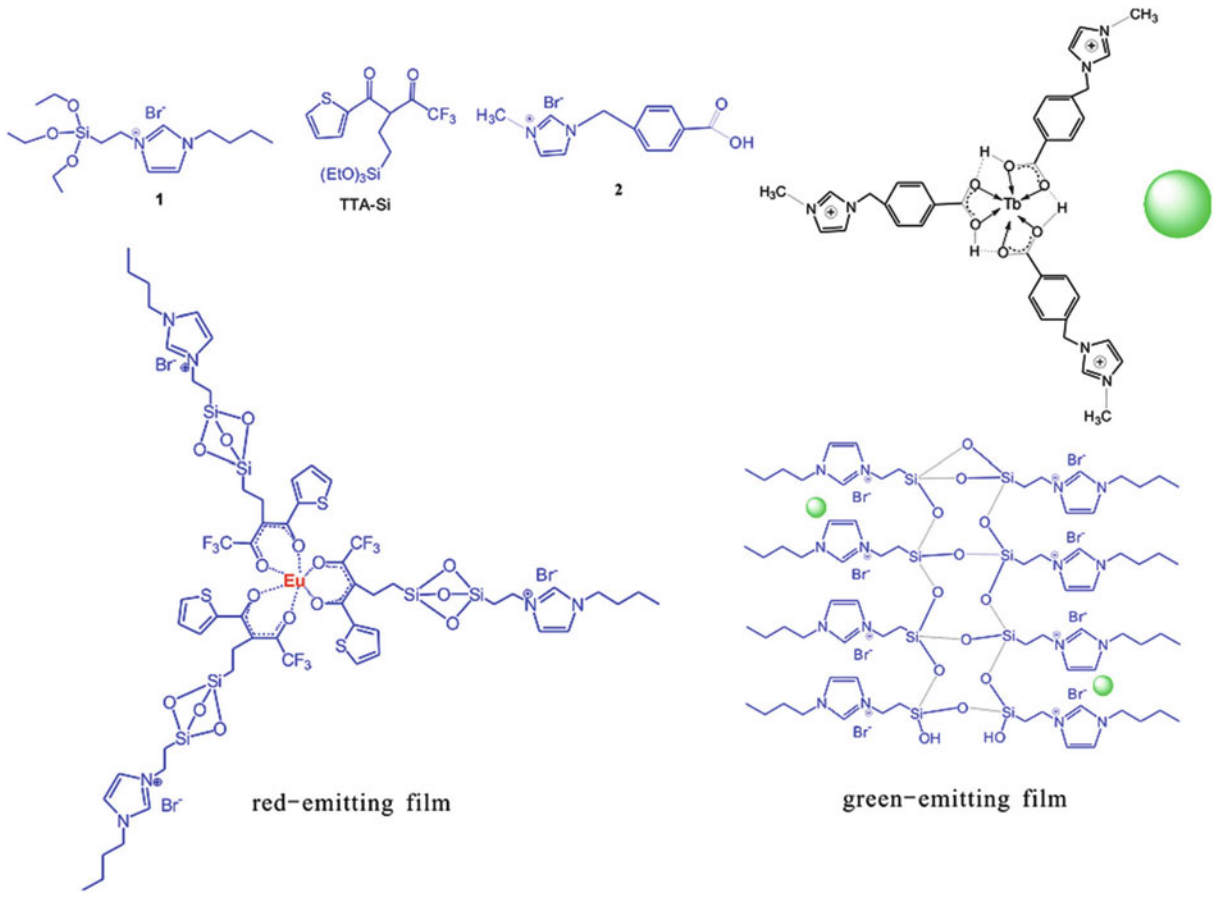

Fig. 7.10 The molecular structure of silylated ionic liquid (**1**), TTA–Si, the organic salt (**2**), and the complexes between Tb^{3+} and **2** formed in situ and the predicted structure of the films (Reprinted from Ref. [55], with kind permission from Springer Science + Business Media)

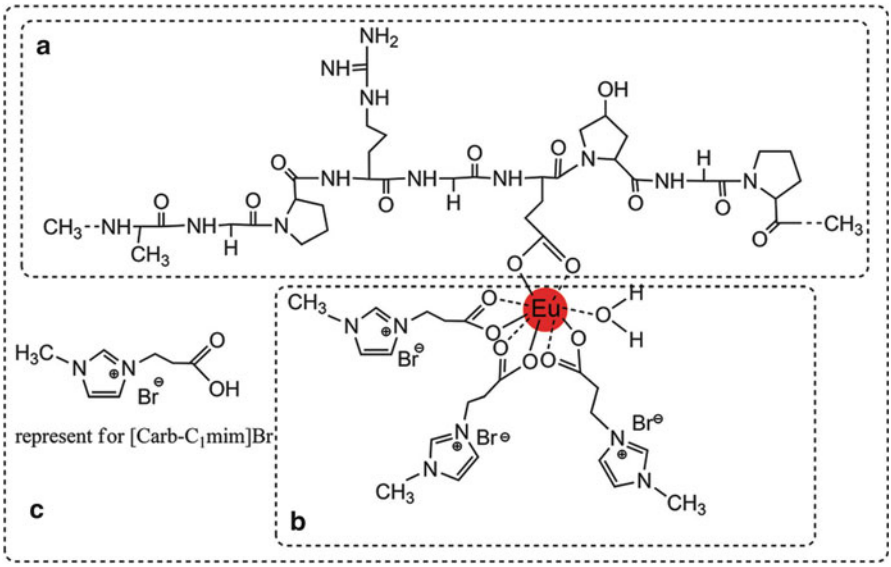

Fig. 7.11 Possible chemical structure of (**a**) gelatin, (**b**) the luminescent ionogel, and (**c**) the ionic liquid (Reproduced from Ref. [58] by permission of the Royal Society of Chemistry)

europium(III)-coordinated ionic liquids to the biodegradable gelatins (Fig. 7.11) [58]. All the Eu^{3+} ions are coordinated to oxygen atoms of the carboxyl groups from the ionic liquids. The decay time of the Eu^{3+} excited state is longer than that of Eu^{3+} ions without gelatins. The prolonged lifetime implies the repulsion of water molecules from the coordination sphere of Eu^{3+} through the extra coordination of C═O groups of gelatin. The authors claim that Eu^{3+} ions from the quenching of H_2O are well protected by the ionic liquid and gelatin from deleterious quenching interactions with water molecules. As a consequence, a long decay time of 0.81 ms for Eu^{3+} can be observed even in aqueous environment.

7.3.3 Poly(Ionic Liquid)-Based Luminescent Ionogels

We have discussed luminescent ionogels prepared from the immobilization of ionic liquids by PMMA polymer and gelatin biopolymer. Among the polymers, poly (ionic liquid)s have attracted considerable attention in the field of polymer chemistry and materials science, because they combine the unique properties of ILs with a macromolecular architecture. Poly(ionic liquid)s are a special kind of electrolytes synthesized by polymerization of monomeric ionic liquids, which combine the functionality of ionic liquid with the spatial control of the ionic liquid moieties. They show obvious advantages, such as enhanced mechanical stability, improved processability, durability, etc., which make them suitable for various applications

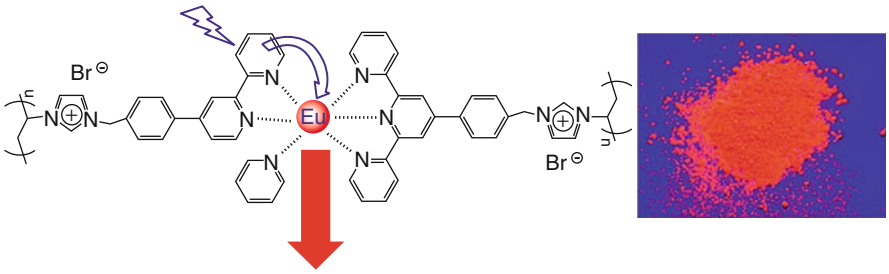

Fig. 7.12 Possible structure of the luminescent material, which shows the coordination of the terpyridine moieties to Eu^{3+} ions and the energy transfer as well as a digital photo taken under UV light (λmax = 365 nm) (Reproduced from Ref. [63] by permission of John Wiley & Sons Ltd)

[64, 65]. We recently reported a novel luminescent ionogel based on poly(ionic liquid). A new poly(ionic liquid) with terpyridine moieties incorporated in the polymer chain was prepared by polymerizing monomeric terpyridine-functionalized ionic liquid [63]. One of the obvious advantages of the new poly (ionic liquid) over the previously reported ones is the availability of terpyridine groups in the repeating units of the polymer as shown in Fig. 7.12. Terpyridine can bind various metal ions, which impart many properties like luminescence and electrochemical, photochemical, or catalytic activity. For instance, luminescent materials were obtained by coordinating europium(III) to the new poly(ionic liquid), displaying a bright red emission when it is irradiated by UV light (Fig. 7.12), which makes them suitable for combinations with UV light-emitting LEDs, because they can be excited in the near-UV region. Furthermore, the lifetime of Eu^{3+} is significantly prolonged after the polymerization, which might be due to the confinement of the terpyridine–europium(III) complexes within the rigid chains of the polymer architecture.

7.4 Luminescence Enhancement of Eu(III)-β-Diketonate Complexes by Ionic Liquid

We have summarized luminescent materials obtained by the introduction of inorganic RE salts and complexes with organic ligands to ionic liquid and ionogels. The ionic liquids utilized in those studies play an important role in improving the photostability and thermal stability [23]. Furthermore, ionic liquids with special functional moieties like carboxyl groups [39] and terpyridine groups [40, 63] can protect the RE^{3+} ions from luminescence quenching caused by water molecules via coordinating the metal ions to oxygen atoms and nitrogen atoms, respectively. They can also act as the sensitizer for RE^{3+} luminescence due to the energy transfer from ionic liquids to the metal ions. Interestingly, Li et al. recently observed a remarkable luminescence enhancement when attaching an ionic liquid consisting of bulky triethoxysilane (**1**) to zeolite L nanocrystals (NZL), the channels of which contained

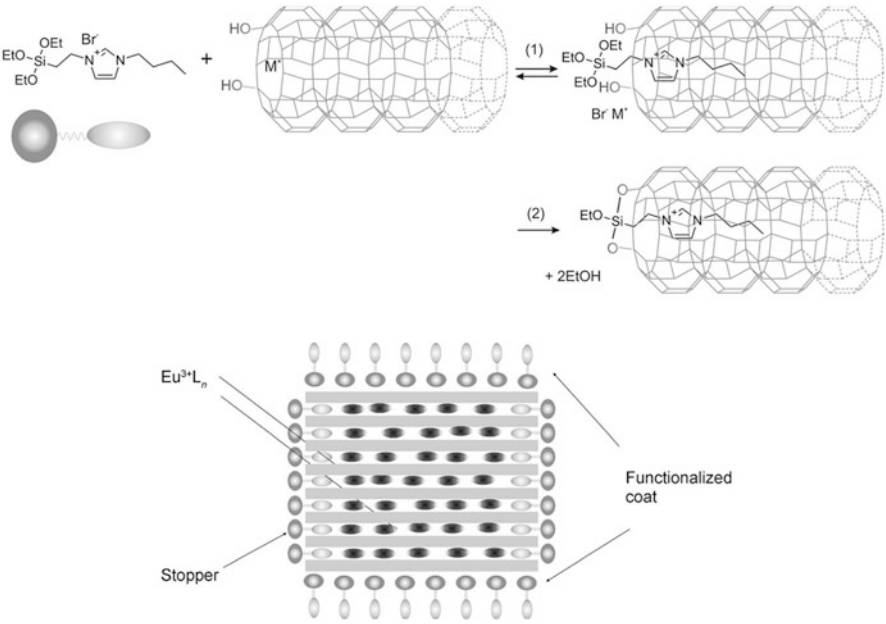

Fig. 7.13 Ionic liquid-functionalized NZL crystal containing inside Eu^{3+} complexes as guests (Reproduced from Ref. [66] by permission of John Wiley & Sons Ltd)

Eu(III)- bzeolite L n ($Eu^{3+}(TTA_n)$-NZL) [66]. This was surprising because **1** completely lacks the ability to sensitize Eu^{3+} ions. The chosen ionic liquid bears a positively charged part which easily enters the negatively charged NZL channel upon exchanging a nearby cation, and the bulky triethoxysilane moiety can react with the OH groups present at the channel entrances and in lower amount also at the coat. The reaction was shown in Fig. 7.13. The authors revealed the mechanism responsible for the unexpected luminescence enhancement. The result is that the presence of the imidazolium-based stopper is favorable to the sustainable formation of Eu^{3+}-β-diketonate complexes with high coordination by decreasing the proton strength inside the channels of NZL.

Similar luminescence enhancement was also observed by Yang et al. when ionic liquid **1** was added to the luminescence nanohybrid ($Eu^{3+}(TTA_n)$@Lap) composed of Eu(III)-β-diketonate complexes and the synthesized clay, Laponite, dispersed in water (Fig. 7.14) [67]. The addition of **1** to the nanohybrid in water leads to a pronounced increase in luminescence efficiency, and the absolute quantum yield of the modified nanohybrid is of ~0.7, a high value that is rarely seen for luminescent nanohybrid in water. The mechanism is that the removal of the abundant protons on the Laponite platelets through a mechanism of synergic effect of ion exchange and neutralization drives the formation of Eu^{3+}-β-diketonate complexes with high coordination number (Fig. 7.14). Abundant acidic sites exist on the surface of the

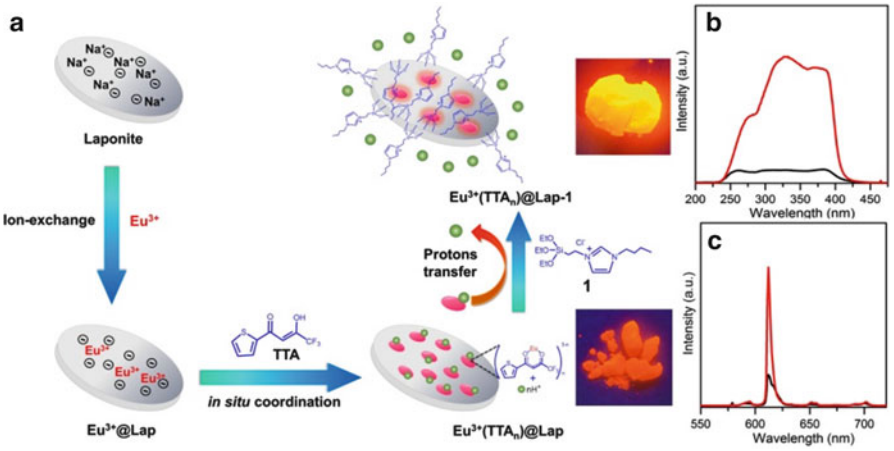

Fig. 7.14 (**a**) Fabrication process of the luminescent nano-LnOIH with photographs under near-UV light illumination. For $Eu^{3+}(TTA_n)$@Lap-**1**, the amount of **1** actually used per unit cell is 6.3. (**b**) Excitation spectra monitored at 612 nm and (**c**) emission spectra excited at 340 nm of Eu^{3+}(TTAn) @Lap (*black line*) and $Eu^{3+}(TTA_n)$@Lap-**1** (*red line*) (Reprinted with the permission from Ref. [67]. Copyright 2015 American Chemical Society)

individually delaminated platelets of Laponite in water, which exert negative influence on the luminescence efficiency of lanthanide complexes on the Laponite platelets [68].

7.5 Conclusions

In summary, we have reviewed the main research carried out in our group in the field of soft luminescent materials resulting from the integration of RE compounds to the ionic liquids. Interesting results reported by other groups are also frequently involved when it is necessary in this chapter. Most of the resulting luminescent materials simultaneously exhibit the attractive properties of both components, which makes them highly potential for opening up new potential applications for these materials, e.g., as laser dyes or as materials for emissive displays, and for the development of flexible optical devices and flexible luminescent devices such as organic light-emitting diodes (OLEDs). Although the study on such kind of soft luminescent materials is still in its infancy, the exciting results obtained have already highlighted the important role played by the ionic liquid in developing new RE-based luminescent materials, typical examples include that the ionic liquids can significantly improve the photo- and thermal stability of RE complexes, can improve the processability of RE earth complexes, and can increase the luminescence efficiency of RE complexes by repulsion of the water molecules

from the coordination sphere of RE^{3+} ions and through the so-called antenna effect as well as by improving the microenvironment where RE complexes are located.

References

1. Chen Z-J, Xi H-W, Lim KH, Lee J-M (2013) Distillable ionic liquids: reversible amide O alkylation. Angew Chem Int Ed 52(50):13392–13396
2. Miao W, Chan TH (2006) Ionic-liquid-supported synthesis: a novel liquid-phase strategy for organic synthesis. Acc Chem Res 39(12):897–908
3. Welton T (1999) Room-temperature ionic liquids. Solvents for synthesis and catalysis. Chem Rev 99(8):2071–2084
4. Han X, Armstrong DW (2007) Ionic liquids in separations. Acc Chem Res 40(11):1079–1086
5. Sun X, Wu D, Chen J, Li D (2007) Separation of scandium(III) from lanthanides(III) with room temperature ionic liquid based extraction containing Cyanex 925. J Chem Technol Biotechnol 82(3):267–272
6. Gruner B, Kvicalova M, Plesek J, Sicha V, Cisarova I, Lucanikova M, Selucky P (2009) Cobalt bis(dicarbollide) ions functionalized by CMPO-like groups attached to boron by short bonds; efficient extraction agents for separation of trivalent f-block elements from highly acidic nuclear waste. J Organomet Chem 694(11):1678–1689
7. Zhu LL, Guo L, Zhang ZJ, Chen J, Zhang SM (2012) The preparation of supported ionic liquids (SILs) and their application in rare metals separation. Sci China Chem 55 (8):1479–1487
8. Liu YH, Chen J, Li DQ (2012) Application and perspective of ionic liquids on rare earths green separation. Sep Sci Technol 47(2):223–232
9. Olivier JH, Camerel F, Ziessel R (2011) Lanthanide ion extraction by trifluoromethyl-1,3-diketonate-functionalised ionic liquids adsorbed on silica. Chem Eur J 17(33):9113–9122
10. Dubreuil JF, Bazureau JP (2000) Rate accelerations of 1, 3-dipolar cycloaddition reactions in ionic liquids. Tetrahedron Lett 41(38):7351–7355
11. Binnemans K (2007) Lanthanides and actinides in ionic liquids. Chem Rev 107(6):2592–2614
12. Mudring AV, Tang S (2010) Ionic liquids for lanthanide and actinide chemistry. Eur J Inorg Chem 2010(18):2569–2581
13. Erdmenger T, Guerrero-Sanchez C, Vitz J, Hoogenboom R, Schubert US (2010) Recent developments in the utilization of green solvents in polymer chemistry. Chem Soc Rev 39 (8):3317–3333
14. Ma Z, Yu J, Dai S (2010) Preparation of inorganic materials using ionic liquids. Adv Mater 22 (2):261–285
15. Zhang P, Wu T, Han B (2014) Preparation of catalytic materials using ionic liquids as the media and functional components. Adv Mater 26(40):6810–6827
16. Giernoth R (2010) Task-specific ionic liquids. Angew Chem Int Ed 49(16):2834–2839
17. Freudenmann D, Wolf S, Wolff M, Feldmann C (2011) Ionic liquids: new perspectives for inorganic synthesis? Angew Chem Int Ed 50(47):11050–11060
18. Feng J, Zhang HJ (2013) Hybrid materials based on lanthanide organic complexes: a review. Chem Soc Rev 42(1):387–410
19. Wu W, Lu Y, Ding H, Peng C, Liu H (2015) The acidity/basicity of metal-containing ionic liquids: insights from surface analysis and the Fukui function. Phys Chem Chem Phys 17 (2):1339–1346
20. Driesen K, Nockemann P, Binnemans K (2004) Ionic liquids as solvents for near-infrared emitting lanthanide complexes. Chem Phys Lett 395(4):306–310

21. Arenz S, Babai A, Binnemans K, Driesen K, Giernoth R, Mudring A-V, Nockemann P (2005) Intense near-infrared luminescence of anhydrous lanthanide(III) iodides in an imidazolium ionic liquid. Chem Phys Lett 402(1–3):75–79
22. Guillet E, Imbert D, Scopelliti R, Bünzli J-CG (2004) Tuning the emission color of europium-containing ionic liquid-crystalline phases. Chem Mater 16(21):4063–4070
23. Nockemann P, Beurer E, Driesen K, Van Deun R, Van Hecke K, Van Meervelt L, Binnemans K (2005) Photostability of a highly luminescent europium [small beta]-diketonate complex in imidazolium ionic liquids. Chem Commun 34:4354–4356
24. Getsis A, Tang S, Mudring A-V (2010) A luminescent ionic liquid crystal: [C12mim]4[EuBr6] Br. Eur J Inorg Chem 2010(14):2172–02177
25. Eliseeva SV, Bunzli JCG (2010) Lanthanide luminescence for functional materials and bio-sciences. Chem Soc Rev 39(1):189–227
26. Martin-Ramos P, Silva MR, Coya C, Zaldo C, Alvarez AL, Alvarez-Garcia S, Matos Beja AM, Martin-Gil J (2013) Novel erbium(iii) fluorinated [small beta]-diketonate complexes with N, N-donors for optoelectronics: from synthesis to solution-processed devices. J Mater Chem C 1 (15):2725–2734
27. Binnemans K (2009) Lanthanide-based luminescent hybrid materials. Chem Rev 109:4283–4374
28. Li H, Shao H, Wang Y, Qin D, Liu B, Zhang W, Yan W (2008) Soft material with intense photoluminescence obtained by dissolving Eu(2)O(3) and organic ligand into a task-specific ionic liquid. Chem Commun 41:5209–5211
29. Li H, Liu P, Shao H, Wang Y, Zheng Y, Sun Z, Chen Y (2009) Green synthesis of luminescent soft materials derived from task-specific ionic liquid for solubilizing lanthanide oxides and organic ligand. J Mater Chem 19(31):5533–5540
30. Li Y, Tian Y, Hua Y, Xu S (2013) Europium(III)-doped ionogels with improved luminescent properties. J Non Cryst Solids 376:38–42
31. Le Bideau J, Viau L, Vioux A (2011) Ionogels, ionic liquid based hybrid materials. Chem Soc Rev 40(2):907–925
32. Néouze M-A, Bideau JL, Gaveau P, Bellayer S, Vioux A (2006) Ionogels, new materials arising from the confinement of ionic liquids within silica-derived networks. Chem Mater 18 (17):3931–3936
33. Song CE, Shim WH, Roh EJ, Choi JH (2000) Scandium(III) triflate immobilised in ionic liquids: a novel and recyclable catalytic system for Friedel-Crafts alkylation of aromatic compounds with alkenes. Chem Commun 17:1695–1696
34. Nockemann P, Thijs B, Parac-Vogt TN, Van Hecke K, Van Meervelt L, Tinant B, Hartenbach I, Schleid T, Ngan VT, Nguyen MT, Binnemans K (2008) Carboxyl-functionalized task-specific ionic liquids for solubilizing metal oxides. Inorg Chem 47 (21):9987–9999
35. Nockemann P, Thijs B, Postelmans N, Van Hecke K, Van Meervelt L, Binnemans K (2006) Anionic rare-earth thiocyanate complexes as building blocks for low-melting metal-containing ionic liquids. J Am Chem Soc 128(42):13658–13659
36. Binnemans K (2005) Ionic liquid crystals. Chem Rev 105(11):4148–4204
37. Mallick B, Balke B, Felser C, Mudring AV (2008) Dysprosium room-temperature ionic liquids with strong luminescence and response to magnetic fields. Angew Chem Int Ed 47 (40):7635–7638
38. Tang S, Babai A, Mudring AV (2008) Europium-based ionic liquids as luminescent soft materials. Angew Chem Int Ed 47(40):7631–7634
39. Wen T, Li H, Wang Y, Wang L, Zhang W, Zhang L (2013) Ln(3+)-mediated formation of luminescent ionogels. J Mater Chem C 1(8):1607–1612
40. Wang D, Wang H, Li H (2013) Novel luminescent soft materials of terpyridine-containing ionic liquids and europium(III). ACS Appl Mater Interfaces 5(13):6268–6275
41. Olivier J-H, Camerel F, Selb J, Retailleau P, Ziessel R (2009) Terpyridine-functionalized imidazolium ionic liquids. Chem Commun 9:1133–1135

42. Vicente JA, Mlonka A, Gunaratne HQN, Swadzba-Kwasny M, Nockemann P (2012) Phosphine oxide functionalised imidazolium ionic liquids as tuneable ligands for lanthanide complexation. Chem Commun 48(49):6115–6117
43. Nockemann P, Thijs B, Pittois S, Thoen J, Glorieux C, Van Hecke K, Van Meervelt L, Kirchner B, Binnemans K (2006) Task-specific ionic liquid for solubilizing metal oxides. J Phys Chem B 110(42):20978–20992
44. Li H, Li D, Wang Y, Ru Q (2011) A series of carboxylic-functionalized ionic liquids and their solubility for lanthanide oxides. Chem Asian J 6(6):1443–1449
45. Huifang Shao YW, Li D (2011) The soft material obtained from an europium (III)-containing ionic liquid. Bull Kor Chem Soc 32:973–976
46. Lunstroot K, Driesen K, Nockemann P, Görller-Walrand C, Binnemans K, Bellayer S, Le Bideau J, Vioux A (2006) Luminescent ionogels based on europium-doped ionic liquids confined within silica-derived networks. Chem Mater 18(24):5711–5715
47. Shi F, Zhang Q, Li D, Deng Y (2005) Silica-gel-confined ionic liquids: a new attempt for the development of supported nanoliquid catalysis. Chem Eur J 11(18):5279–5288
48. Armand M, Endres F, MacFarlane DR, Ohno H, Scrosati B (2009) Ionic-liquid materials for the electrochemical challenges of the future. Nat Mater 8(8):621–629
49. Ito S, Zakeeruddin SM, Comte P, Liska P, Kuang D, Gratzel M (2008) Bifacial dye-sensitized solar cells based on an ionic liquid electrolyte. Nat Photonics 2(11):693–698
50. Bai Y, Cao Y, Zhang J, Wang M, Li R, Wang P, Zakeeruddin SM, Gratzel M (2008) High-performance dye-sensitized solar cells based on solvent-free electrolytes produced from eutectic melts. Nat Mater 7(8):626–630
51. Liu Y, Wang M, Li J, Li Z, He P, Liu H, Li J (2005) Highly active horseradish peroxidase immobilized in 1-butyl-3-methylimidazolium tetrafluoroborate room-temperature ionic liquid based sol-gel host materials. Chem Commun 13:1778–1780
52. Lunstroot K, Driesen K, Nockemann P, Van Hecke K, Van Meervelt L, Görller-Walrand C, Binnemans K, Bellayer S, Viau L, Le Bideau J (2009) Lanthanide-doped luminescent ionogels. Dalton Trans 2:298–306
53. Feng Y, Li H, Gan Q, Wang Y, Liu B, Zhang H (2010) A transparent and luminescent ionogel based on organosilica and ionic liquid coordinating to Eu3+ ions. J Mater Chem 20 (5):972–975
54. Ru Q, Wang Y, Zhang W, Yu X, Li H (2013) Thermally reversible, flexible, transparent, and luminescent ionic organosilica gels. Eur J Inorg Chem 2013(13):2342–2349
55. Fan Z, Wang Y, Xue Z, Zhang L, Chen Y, Zhang S (2014) Preparation, characterization and luminescence of transparent thin film of ionogels. J Sol–gel Sci Technol 72(2):328–333
56. Lunstroot K, Driesen K, Nockemann P, Viau L, Mutin PH, Vioux A, Binnemans K (2010) Ionic liquid as plasticizer for europium(iii)-doped luminescent poly(methyl methacrylate) films. Phys Chem Chem Phys 12(8):1879–1885
57. Wang H, Wang Y, Zhang L, Li H (2013) Transparent and luminescent ionogels based on lanthanide-containing ionic liquids and poly(methyl methacrylate) prepared through an environmentally friendly method. RSC Adv 3(22):8535–8540
58. Li M, Wang Y, Chen Y, Zhang S (2014) A luminescent ionogel based on an europium(iii)-coordinated carboxyl-functionalized ionic liquid and gelatin. Photochem Photobiol Sci 13 (7):1025–1030
59. Xie Z-L, Ge XH-B, Kumke MU, Priebe M, Fromm KM, Taubert A (2012) A transparent, flexible, ion conductive, and luminescent PMMA ionogel based on a Pt/Eu bimetallic complex and the ionic liquid [Bmim][N(Tf)2]. J Mater Chem 22(16):8110–8116
60. Vidinha P, Lourenco NMT, Pinheiro C, Bras AR, Carvalho T, Santos-Silva T, Mukhopadhyay A, Romao MJ, Parola J, Dionisio M, Cabral JMS, Afonso CAM, Barreiros S (2008) Ion jelly: a tailor-made conducting material for smart electrochemical devices. Chem Commun 44:5842–5844
61. Qiao C, Li T, Zhang L, Yang X, Xu J (2014) Rheology and viscosity scaling of gelatin/1-allyl-3-methylimidazolium chloride solution. Kor-Aust Rheol J 26(2):169–175

62. Leones R, Sentanin F, Rodrigues LC, Ferreira RAS, Marrucho IM, Esperança JMSS, Pawlicka A, Carlos LD, Manuela Silva M (2012) Novel polymer electrolytes based on gelatin and ionic liquids. Opt Mater 35(2):187–195
63. Ru Q, Xue Z, Wang Y, Liu Y, Li H (2014) Luminescent materials of europium(III) coordinated by a terpyridine-functionalized poly(ionic liquid). Eur J Inorg Chem 2014(3):469–474
64. Mecerreyes D (2011) Polymeric ionic liquids: broadening the properties and applications of polyelectrolytes. Prog Polym Sci 36(12):1629–1648
65. Yuan J, Wunder S, Warmuth F, Lu Y (2012) Spherical polymer brushes with vinylimidazolium-type poly(ionic liquid) chains as support for metallic nanoparticles. Polymer 53(1):43–49
66. Li P, Wang Y, Li H, Calzaferri G (2014) Luminescence enhancement after adding stoppers to europium(III) nanozeolite L. Angew Chem Int Ed 53(11):2904–2909
67. Yang D, Wang Y, Wang Y, Li Z, Li H (2015) Luminescence enhancement after adding organic salts to nanohybrid under aqueous condition. ACS Appl Mater Interfaces 7(3):2097–2103
68. Lezhnina MM, Bentlage M, Kynast UH (2011) Nanoclays: two-dimensional shuttles for rare earth complexes in aqueous solution. Opt Mater 33(10):1471–1475

Chapter 8
Photofunctional Rare Earth Materials Based on Ionic Liquids

Bing Yan

Abstract This chapter mainly focuses on recent research progress in photofunctional rare earth materials based on ionic liquids, with an emphasis on the photofunctional rare earth hybrid materials using ionic liquid compounds as both double functional linkers and matrices. It covers photofunctional rare earth compounds with ionic liquids, photofunctional rare earth compounds dispersed in ionic liquids, and photofunctional rare earth hybrid materials based on ionic liquid with special groups (organically modified siloxanes, carboxyl groups, and thiol groups). Herein we focus on the work of our group in the recent years.

Keywords Rare earth • Photofunctional materials • Ionic liquids • Photophysical properties • Luminescence

8.1 Introduction

Ionic liquids (ILs) are organic salts with low melting point, by convention, below 100 °C, which consist of only ions and show properties different from molecular liquids [1–3]. Ionic liquids have attracted considerable attention within the past decades, owing to their potential applications as environmentally benign solvents for chemical synthesis, separation, catalysis, electrochemistry, etc. [4–6]. The prominent properties of ionic liquids such as negligible vapor pressure, thermal stability, as well as widely tunable cations or anions have aroused wide public interest in material chemistry. Ionic liquids offer the possibility to synthesize and crystallize quite uncommon rare earth compounds. Ionic liquids can also be designed in such a way that they become excellent media to study the optical properties of rare earth compounds. And even ionic liquids based on rare earth elements can be made. Many rare earth compounds have interesting photophysical properties. It is well known that rare earth ions possess luminescent features such as generally narrow emission bands, long decay times, and a large Stokes shift. Rare

B. Yan (✉)
Department of Chemistry, Tongji University, Siping Road 1239, Shanghai 200092, China
e-mail: byan@tongji.edu.cn

J. Chen (ed.), *Application of Ionic Liquids on Rare Earth Green Separation and Utilization*, Green Chemistry and Sustainable Technology,
DOI 10.1007/978-3-662-47510-2_8

earth compounds have gained enormous attention for their potential use as materials in light-emitting diodes and medical and biological applications. Many of the ILs are colorless (or slightly yellowish) and transparent through almost the whole visible and near-infrared spectral region. This typical property makes them very suitable as optical solvents. As a favorable medium, ionic liquid compounds can be used to prepare some photofunctional rare earth solid state compounds or phosphors [7–10]. Among the main advantages of using ILs as solvents or additives in inorganic synthesis is their superior capability for the dissolution and stabilization of metal cations, which endows them with the possibility of acting as capping agents or surfactants [11]. Besides, ionic liquids behave as the ideal media for photoactive rare earth ions to replace the common solvents such as water, which can be expected to enhance the luminescence of rare earth ions and decrease the quenching effect of hydroxyl groups [12]. Further, photoactive rare earth species can be dispersed into ionic liquid media to form corresponding soft materials [13]. Moreover, the introduction of rare earth complex anion can lead to a functional ionic liquid which can combine the properties of ionic liquid and metal ion [14]. On the other hand, some ionic liquid compounds can be coordinated to rare earth ions to form the small molecule complexes, which possess the photofunctional behavior of rare earth ions [15]. Considering some derived ionic compounds with special functional groups, they can be used as chemical linker to construct the photofunctional rare earth hybrid materials [16]. Several approaches have been developed to prepare ionic liquid-based hybrid materials including in situ or post polymerization of monomers, sol-gel processing in the ionic liquid, physical gelation, or impregnation into an as-prepared matrices [17]. Among which, the method that anchors the ionic liquid to specific supporting matrices followed by anion metathesis has been proven to be an effective way to construct functional materials [18].

In this context, our focus is on the photofunctional rare earth materials involving ionic liquid compounds. The topic consists of three parts: photofunctional rare earth compounds of ionic liquids, photofunctional rare earth compounds dispersed in ionic liquids, and photofunctional rare earth hybrid materials based on ionic liquids with special groups (organically modified siloxane, carboxyls, and thiol groups). The main emphasis is on the work of our group in photofunctional hybrid materials.

8.2 Photofunctional Rare Earth Compounds with Ionic Liquids

In fact, photofunctional rare earth compounds with ionic liquids are derived from rare earth compounds (mainly rare earth salts) dissolved into or dispersed in ionic liquids as solvents. Sometimes, it is impossible to distinguish the photofunctional rare earth compounds with ionic liquid and the photofunctional rare earth compounds dispersed in ionic liquids. In such solution systems, ion exchange occurs

between rare earth salts and ionic liquid compounds, forming some rare earth compounds consisting ionic fragment of ionic liquids, and even the exact crystal structure of some can be analyzed. It is worth pointing out that Mudring's group did a lot of work in this field and wrote a micro review on luminescent rare earth compound with ionic liquids [19].

Jensen' group studied the anion exchange mechanism of rare earth ion transfer into room-temperature ionic liquids [20]. The structure and stoichiometry of the RE^{3+} complexes with 2-thenoyl-trifluoroacetonate (TTA) are studied, which form in a biphasic aqueous room-temperature ionic liquid (1-butyl-3-methylimidazolium bis[(trifluoromethyl)sulfonyl]imide, $C_4mimTf_2N^-$) system. The presence of anionic rare earth complexes in C_4mimTf_2N is made possible by the exchange of the ionic liquid anions into the aqueous phase for the rare earth complexes, which should be considered as weak $[C_4mim^+][RE(TTA)_4^-]$ ion pairs. The required charge balance is maintained by the exchange of $RE(TTA)_4^-$ (RE = Nd, Eu) anions with Tf_2N^- anions from the ionic liquid, and $RE(TTA)_4^-$(RE = Nd, Eu) becomes part of the ionic liquid without greatly altering the general structure of the RTIL phase. This research is important to understand the exchange reaction between RTILs and rare earth complex anion in RTIL media.

Bünzli's group reported the emission color tuning of Eu^{3+} ionic liquid-crystalline phases produced by introducing EuY_3 (Y = Cl, NO_3, ClO_4, CF_3SO_3) in four room-temperature ionic liquids (RTIL) derived from 1-alkyl-3-methylimidazolium, $[C_nmim]X$ (X = Cl, NO_3; $n = 12-18$) [21]. The RTIL displays a blue fluorescence and its intensity decreases substantially upon the introduction of Eu^{3+} salts for the energy transfer from RTIL to Eu^{3+}. A high-resolution luminescent study demonstrates the existence of a single solvated Eu^{3+} species. For Cl^-, ClO_4^-, or $CF_3SO_3^-$, it appears to be a polychloro complex with a low symmetry derived from an idealized cubic symmetry, while it is contrary to NO_3^- with a stronger anion–Eu^{3+} interaction for dominant hypersensitive red transition ($^5D_0 \rightarrow {}^7F_2$). Therefore, controlling the excitation wavelength and the counter ion Y, the emission color of the liquid-crystalline phases can be easily tuned from blue to red.

Binnemans's group found that a high quantum yield and an enhanced photostability are achieved for a Eu^{3+} tetrakis(2-thenoyltrifluoroacetonate) complex dissolved in a weakly coordinating 1-hexyl-3-methylimidazolium ionic liquid [22]. To decrease the high non-radiative decay rates from efficient vibronic coupling of the coordinated water to oxophilic Eu^{3+}, hydrophobic ionic liquids ($[C_6mim][Tf_2N]$) and strongly coordinating ligands ($Eu(TTA)_4^-$) are used to improve the quantum yield and photostability. The tunable properties of the systems can open up new potential applications such as laser dyes for emissive displays, whose research can be also extended to other rare earth tetrakis (b-diketonate) complex system in ionic liquids.

Mudring's group obtained the anhydrous praseodymium salts (PrI_3 and $Pr(Tf_2N)_3$) in the ionic liquid 1,1-n-butyl-methylpyrrolidinium bis(trifluoromethanesulfonyl) amide, $[bmpyr][Tf_2N]$, formulated as $[bmpyr]_4[PrI_6][Tf_2N]$ and $[bmyr]_2[Pr(Tf_2N)_5]$ [23]. Compound $[bmpyr]_4[PrI_6][Tf_2N]$ crystallizes in the space group $P4_32_12$ with a = b = 14.648(2) Å and c = 28.469(5) Å at 298(2) K and a = b = 14.5452(7) Å and c = 28.524(2) Å at 170(2) K, respectively. Compound $[bmyr]_2[Pr(Tf_2N)_5]$ crystallizes in

a triclinic space group $P1$, with a = 12.3217(13) Å, b = 12.4275(14)Å, c = 22.6422 (24) Å, α = 94.440(9) °, β = 102.630(8) °, and γ = 105.791(9)°. As expected for the solid compounds, the intensities for the $^3P_0 \rightarrow {}^3H_4$ are enhanced compared to the $^1D_2 \rightarrow {}^3H_4$ transition. So the ionic liquids are promising media to study the luminescent properties of Pr^{3+} in the liquid state for that they generally quench to a far lesser extent the optical transition than conventional solvent.

Mudring, Binnemans, and Giernoth further collaborated to study the other two near-infrared luminescent anhydrous rare earth (Nd^{3+}, Er^{3+}) iodides in ionic liquid 1-dodecyl-3-methylimidazolium bis(trifluoromethylsulfonyl)imide, $[C_{12}mim][Tf_2N]$ [24]. Both of the two systems show the intense near-infrared emission for Nd^{3+} and Er^{3+}. For Nd^{3+} system, three transitions can be observed between 750 and 1450 nm: $^4F_{3/2} \rightarrow {}^4I_{9/2}$(877 nm), $^4F_{3/2} \rightarrow {}^4I_{11/2}$ (1054 nm), and $^4F_{3/2} \rightarrow {}^4I_{13/2}$(1330 nm). The most intense transition is the $^4F_{3/2} \rightarrow {}^4I_{11/2}$ transition. Its experimental luminescent lifetime is 15.3 μs and its luminescent quantum yield is 1.5 ± 0.2 %, which is high for a Nd^{3+} compound dissolved in an organic solvent and even higher than the values obtained for many Nd^{3+} complexes in deuterated solvents. Er^{3+} system exhibits one emission band centered at 1540 nm that corresponds to the $^4I_{13/2} \rightarrow {}^4I_{15/2}$ transition, and its luminescent intensity is weaker than that of the Nd^{3+} system. The presence of a small energy gap between the excited state and the ground state in Er^{3+} leads to its quenching by nonradiative processes and so its experimental luminescent lifetime is 10.4 μs. Besides, exposure of the hygroscopic samples to atmospheric moisture conditions produces a rapid decrease of the luminescent intensities.

In addition, REI_3 (RE = Nd, Dy, and Tb) in the ionic liquid 1-dodecyl-3-methylimidazolium bis(trifluoromethanesulfonyl)imide are studied, and the emission lifetimes for DyI_3 in $[C_{12}mim][Tf_2N]$ are discussed [25]. Traces of water dramatically reduce the otherwise long lifetimes and comparatively high quantum yields, which indicates that the ionic liquid $[C_{12}mim][Tf_2N]$ is an excellent medium to study luminescent properties of trivalent RE^{3+} in solution. The lifetimes of excited states seem to be generally higher in this medium compared to those observed unconventional solvents. These results seem to be due to the absence of any C–H, N–H, and O–H bonds in the immediate neighborhood of RE^{3+}, so that non-radiative decay becomes less likely compared to typical solvents.

May's group discussed the luminescent properties and water coordination of Eu^{3+} in the binary solvent mixture water/1-butyl-3-methylimidazolium chloride ([BMI]Cl) and confirmed that coordinating chloride ligands increase the energy of the LMCT (ligand to metal charge transfer) state [26]. They found that the Eu^{3+} species present are $[EuCl_x]_{3-x}$, $[EuCl_y(H_2O)_{3-4}]_{3-y}$, $[EuCl_z(H_2O)_6]_{3-z}$, and $[Eu(H_2O)_{8-9}]^{3+}$(x > y > z). So [BMI]Cl is a promising medium for Eu^{3+} compounds due to the low-energy phonon environment of $[EuCl_x]_{3-x}$ complex. Besides, moderate water contamination does not result in direct binding of water to Eu^{3+} to produce luminescent quenching. They have also studied an unprecedented series of low-melting europium-containing ionic liquids, formulated as $[R]x[Eu(Tf_2N)_{3+x}]$

(Tf_2N = bis-(trifluoromethanesulfonyl)amide, x = 1 for R = 1-propyl-3-methylimidazolium (C_3mim) and 1-butyl-3-methylimidazolium(C_4mim), and x = 2 for R = 1-butyl-1-methylpyrrolidinium(C_4mpyr)) [27]. This avoids the use of any neutral coligand and can be regarded as the first true f-element-based ionic liquids. All compounds possess excellent photophysical properties such as high lifetimes at high Eu^{3+} concentration, small line-width, and high color purity, which might render them extremely valuable for various optical applications.

Mudring's group checked a kind of dysprosium RTILs ($[C_6mim]_{5-x}[Dy(SCN)_{8-x}(H_2O)_x]$($x$ = 0–2), C_4mim = 1-butyl-1-methylimidazolium) with strong luminescence and response to magnetic fields [28]. They show a bright yellow luminescence and their luminescent lifetimes depend on the number of water molecules in the coordination sphere of Dy^{3+}, 23.8 μs for x = 2, 40.34 μs for x = 1, and 48.4 μs for x = 0, respectively. On the other hand, they show a strong response to externally applied magnetic fields to become the first examples of RTILs that combine magnetic and luminescent properties. More interestingly, Mudring's group studied dysprosium-based ionic liquid crystal $[C_{12}mim]_3[DyBr_6]$ (C_{12}mim = 1-dodecyl-3-methylimidazolium), which presents interesting photo- and magnetophysical properties [29]. The emission color of $[C_{12}mim]_3[DyBr_6]$ can be tuned from white to orange–yellow by the selective excitation, presenting blue–whitish luminescence from the imidazolium cation itself with λ_{ex} = 366 nm and Dy^{3+} emission to the $^4F_{9/2} \rightarrow {}^6H_{13/2}$ transition with λ_{ex} = 254 nm, respectively. Besides, the crystal structure of the corresponding acetonitrile solvate $[C_{12}mim]_3[DyBr_6]_3 \square CH_3CN$ is determined (orthorhombic, *Pbca*, No.62, Z = 8, a = 14.888(4)Å, b = 18.240(7)Å, c = 49.411(13)Å, 5596 unique reflections with $I_o > 2\sigma(Io)$, R_1 = 0.1047, wR_2 = 0.2442, GOF = 1.167, T = 298(2) K). It is characterized by alternating double layers of $[C_{12}mim]$ cations of opposite orientation and nearly ideal $[DyBr_6]^{3-}$ octahedra with hydrogen-bonded acetonitrile.

Besides, Mudring's group studied two new Eu-based ionic liquid systems, $[C_4mim][DTSA]:[Eu(DTSA)_3]$ and $2[C_4mim][DTSA]:[Eu(DTSA)_3]$, under inert conditions from 1-butyl-1-methylimidazoliumditoluenesulfonylamide ($[C_4mim][DTSA]$) [30]. However, no crystallization could be observed – only glass formation. These materials exhibit a strong red luminescence of high color purity.

Tang and Mudring also synthesized the single crystals $[C_4mim][Tb(HFA)_4]$ and $[C_4mpyr][Tb(HFA)_4]$ (C_4mim = 1-butyl-3-methylimidazolium, C_4mpyr = *N*-butyl-*N*-methylpyrrolidinium) with (hexafluoroacetyl)acetone (HFA) and Tb^{3+} chloride in a basic ethanol/water solution [31]. Both compounds show strong enhancement of green luminescence upon cooling. They also synthesized europium compounds $[C_{12}mim]_4[EuBr_6]Br$ ($[C_{12}mim]_3$-$[EuBr_6] \square [C_{12}mim]Br$) and $[C_{12}mim]_4[EuBr_6]Br \square CH_3CN$ by reacting $EuBr_3$ with $[C_{12}mim]Br$ (1-dodecyl-3-methylimidazolium bromide) in acetonitrile [32]. $[C_{12}mim]_4[EuBr_6]Br \square CH_3CN$ crystallizes in the triclinic space group with two formula units in the unit cell. The structure is characterized by double layers of $[C_{12}mim]$ cations with interdigitated alkyl chains

which are separated by anion layers formed by [$EuBr_6$] octahedral and Br···CH_3CN units. Upon warming to room temperature, it can be grasped as the acetonitrile solvate of the double salt [C_{12}mim]$_4$[$EuBr_6$]Br, whose crystallization of similar double salts contains the "free" halide and a [$EuBr_6$] unit. At 77 K, [C_{12}mim]$_4$[$EuBr_6$]Br ([C_{12}mim]$_3$-[$EuBr_6$]·[C_{12}mim]Br) shows a strong red emission with an appreciable lifetime of 2.6 ms. Furthermore, they investigate the switchable green and white luminescence in Tb^{3+}-based ionic liquid crystals [C_{12}mim]Br (C_{12}mim = 1-dodecyl-3-methyl) and [C_{12}mpyr]Br(C_{12}mpyr = N-dodecyl-N-methylpyrrolidinium) [33]. The crystal structure of the acetonitrile solvate of the imidazolium compound, [C_{12}mim]$_3$[$TbBr_6$]·2CH_3CN, is determined by single X-ray diffraction, which forms liquid crystal double layers of [C_{12}mim]$^+$ cations and [$TbBr_6$]$^{3-}$ octahedral with hydrogen-bonded acetonitrile. All materials show strong green luminescence from the $^5D_4$ level of Tb^{3+} after excitation into the $4f^8 \rightarrow 4f^7 5d^1$ transition. In case of the imidazolium compounds, the color of this emission can be switched between green and blue–white color depending on the excitation energy.

Binnemans's group studied the visible and near-infrared emission by Sm^{3+}-diketonate and dipicolinate complexes dissolved in imidazolium ionic liquid 1-hexyl-3-methylimidazolium bis(trifluoromethylsulfonyl)imide, [C_6mim][Tf_2N]: [C_6mim][Sm(TTA)$_4$] (TTA = 2-thenoyltrifluoroacetonate); [C_6mim][Sm(NTA)$_4$], (NTA = 2-naphthoyltrifluoroacetonate); [C_6mim][Sm(HFA)$_4$] (HFA = hexafluoroacetylacetonate); and [choline]$_3$-[Sm(dpa)$_3$] (dpa = pyridine-2,6-dicarboxylate (dipicolinate), [choline]$^+$ = (2-hydroxyethyl)trimethyl ammonium), respectively [34]. The crystal structures of the tetrakis samarium(III)-diketonate complexes belong to a distorted square antiprismatic coordination for Sm^{3+} in all three cases. High-luminescent quantum yields are obtained for the Sm^{3+}-diketonate complexes in solution. They find the existence of the strong hydrogen bonding between the imidazolium cations and the β-diketonate ligands in the solid state.

Baker's group investigated the ionic liquids containing fluorinated β-diketonate anions [35]. The inherent binding capability of the β-diketonate moiety made possible a task-specific IL amenable to rare earth ion recognition. The coordination with Eu^{3+} produces a striking three-order-of-magnitude intensification of luminescence. Interestingly, these RTILs display prominent acidochromism performance, whose intense visible color can be modulated in the presence of an acid source. Therefore, it can be expected to have the potential application visual transduction of local pH changes.

More recently, Li's group reported novel luminescent soft materials of terpyridine-containing ionic liquids (Terpy-TSIL) and Eu^{3+} [36]. They show bright red emission irradiated with UV light for the energy transfer from terpyridine-functionalized imidazolium salts to the Eu^{3+} ions. Depending on the anions used in the ILs, the lifetime of Eu^{3+} in the soft materials is in the range of 0.8–1.1 ms, the absolute quantum yield is determined to be ranging from 8.8 to 14.7 %, and the energy transfer efficiency from Terpy-TSIL to Eu^{3+} is calculated to be in the range of 36.7–42.9 %.

8.3 Photofunctional Rare Earth Compounds Dispersed in Ionic Liquids

Rare earth ions (salts) dissolved or dispersed in ionic liquids may form the rare earth compounds with ionic liquids, as mentioned above, which is an important and common form of photofunctional rare earth compounds dispersed in ionic liquids. Besides, some other rare earth species also can be dispersed or dissolved into ionic liquid media. This can develop series of hybrid soft materials based on ionic liquids through the simple dispersion or doping method.

Binnemans's group used 1-alkyl-3-methylimidazolium ionic liquids as solvents to produce near-infrared emitting Nd^{3+} tosylate, bromide, triflate, and sulfonylimide complexes [37]. These ionic liquids are polar non-coordinating solvents to solubilize rare earth complexes, which are beneficial for near-infrared emitting rare earth complexes. Near-infrared luminescence of these Nd^{3+} is observed by direct excitation of Nd^{3+} upon ligand excitation for Nd^{3+} complexes with 1,10-phenanthrolineor β-diketonate ligands, which suggests that ionic liquids are very stable and transparent and are able to dissolve Nd^{3+} complexes in order to operate in a similar way as dye lasers do.

May's group discussed the luminescent properties and quenching mechanisms of $RE(Tf_2N)_3$ complexes in the ionic liquid bmpyr Tf_2N(RE = Eu, Tm, Dy, Sm, Pr, Nd, Er; Tf_2N = bis-(tri fluoromethanesulfonyl)amide; bmpyr = 1-n-butyl-1-methylpyrrolidinium) [38]. The luminescent quantum efficiencies and radiative lifetimes are determined for $Eu^{3+}(^5D_0)$, $Tm^{3+}(^1D_2)$, $Dy^{3+}(^4F_{9/2})$, $Sm^{3+}(^4G_{5/2})$, and $Pr^{3+}(^3P_0)$ emission. The 1.5 μm emission corresponding to the Er^{3+} ($^4I_{13/2} \rightarrow {}^4I_{15/2}$) transition exhibits a lifetime of 77 μs. The multiphonon relaxation rate constants are determined for 10 different RE^{3+} emitting states, and the trend in multiphonon relaxation is analyzed in terms of the energy gap law. It is demonstrated that $Eu(Tf_2N)_3$ can be used as a reasonable internal standard, both for monitoring the dryness of the solutions and for estimating the quantum efficiencies and radiative lifetimes for visible-emitting $[RE(Tf_2N)_x]$ complexes in bmpyrTf_2N.

Hopkins and Goldey study the luminescence of rare earth halides ($EuBr_3$, $TbCl_3$) and rare earth complexes ($Eu(dpa)_3^{3-}$, where dpa = 2,6 pyridine dicarboxylate dianion) dissolved in a 1-butyl-3-methylimidazolium bromide(BMIBr)/water mixture [39]. The observed spectroscopic properties of Tb^{3+} or Eu^{3+} salts are expectedly impacted by the high water content, but unexpectedly impacted by the BMIBr ionic liquid, contrary to $Eu(dpa)_3^{3-}$. BMIBr ionic liquid does sensitize Eu^{3+} and Tb^{3+} luminescence, but the Eu^{3+} and Tb^{3+} luminescent spectra are quenched by the ionic liquid, as evidenced by the large decay constants in Eu^{3+} (relative to aqueous and BMICl samples). However, the spectroscopic properties of $Eu(dpa)_3^{3-}$ complexes were insensitive to the presence of BMIBr, which indicates that they are plausible as intermolecular interaction probes even in binary solvent systems (BMIBr/water).

Getsis and Mudring discovered that doping the ionic liquid crystal C_{12}mimBr with various rare earth halides ($EuBr_2$, $SmBr_3$, $TbBr_3$, and $DyBr_3$) yields interesting

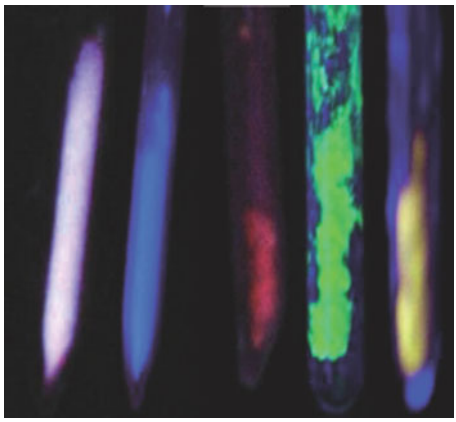

Fig. 8.1 Neat C_{12}mimBr (*left*) doped with various rare earth bromides under UV light (Reproduced from Ref. [40] with permission from John Wiley and Sons)

novel liquid-crystalline and luminescent materials [40]. C_{12}mimBr itself is an ionic liquid crystal that shows bluish–white emission upon excitation with UV light due to transitions in the imidazolium π-system. $EuBr_2$ in C_{12}mimBr yields a material, which shows a blue emission originating from 4f–5d transitions. $SmBr_3$- and $TbBr_3$-doped samples show a red and a green luminescence, respectively. Upon doping C_{12}mimBr with $DyBr_3$, an orange luminescent liquid-crystalline material is obtained. Most interestingly, the emission color for the $TbBr_3$- and $DyBr_3$-containing materials can be tuned from bluish–white (mainly C_{12}mimBr emission) to green (for $TbBr_3$) and orange–yellow (for $DyBr_3$) depending on the wavelength of the excitation light used. These rare earth halide systems turn out to be promising new soft optical materials (see Fig. 8.1).

Viswanathan's group designed a novel RTIL, 1-butyl-3-methylimidazolium benzoate ([bmim][BA]), and observed the fluorescence enhancement of Eu^{3+} and Tb^{3+} [41], which results from a sensitization of the rare earth fluorescence by the benzoate anion of the ionic liquid, [bmim][BA], and a reduction in the nonradiative channels in the nonaqueous environment provided by the ionic liquid. Unfortunately, the fluorescence enhancement of Eu^{3+} and Tb^{3+} in the ionic liquid is limited due to the operation of the inner filter effect. The inner filter effect is minimized by observing the Eu^{3+} fluorescence using a front face geometry and also by diluting the RE^{3+}-[bmim][BA] system, using another ionic liquid, 1-butyl-3-ethylimidazolium bis(trifluoromethylsulfonyl)imide ([bmim][Tf_2N]), as a solvent. Their work provides a possibility of suitably tailoring the ionic liquids to be fluorescence-enhancing agents for pushing limits of detection.

Ionic liquid anion nature also has an influence on the properties of Eu-containing luminescent materials [42]. The 1-methyl-3-tetradecyl imidazolium ionic liquid with $N(CN)_2$, CF_3SO_3, and $N(CF_3SO_2)_2$ anions doped with 1 % of $[EuCl_2Phen_2(H_2O)_2]Cl\square H_2O$ complex was prepared, and the influence of the IL anion nature on luminescent spectra and lifetimes of europium complex was investigated. Therefore the presented Eu-containing ILs can be considered as potential perspective components for new optical materials and devices.

Nockemann et al. detailedly checked the speciation of europium complexes in task-specific ionic liquid betainium bis(trifluoromethylsulfonyl)imide ([Hbet][Tf_2N]) using multiple-technique approach including luminescent spectra at 77 K [43]. Clear changes in the luminescent spectrum of $[Eu_2(bet)_8(H_2O)_4][Tf_2N]_6$ occur upon dissolution in the ionic liquids [Hbet][Tf_2N] and [C_4mim][Tf_2N], but ultimately luminescent spectroscopy alone cannot unequivocally discriminate between dimeric and monomeric Eu^{3+} betaine complexes, and as such, it remains unclear whether the dimeric compound $[Eu_2(bet)_8(H_2O)_4][Tf_2N]_6$ stays intact upon dissolution in the ionic liquids [Hbet][Tf_2N] and [C_4mim][Tf_2N] or if it dissociates into monomers.

Li et al. prepared the soft material by dissolving Eu_2O_3 and organic ligand (2-thenoyltrifluoroacetone (TTA)) and 1,10-phenanthroline (phen) to a task-specific ionic liquid containing a carboxylate group (3-(5-carboxypropyl)-1-methylimidazoliumbromide) [44]. Consequently, the obtained soft material shows high luminescence and could find potential applications in emission displays and laser dyes despite the low concentration of Eu^{3+} complexes in the ionic liquid (ca. 3 mol%).

Ionic liquids are used as solvents to disperse luminescent rare earth-doped phosphors such as rare earth fluoride nanocrystals. Binnemans's group studied the dispersion of LaF_3:RE^{3+} nanocrystals (RE = Eu, Nd) in 1-butyl-1-methylpyrrolidinium bis(trifluoromethylsulfonyl)imide [C_4mpyr][Tf_2N], 1-butyl-1-methylpyrrolidinium trifluoromethanesulfonate [C_4mpyr][TfO], and 1-butyl-3-methylimidazolium bis(trifluoromethylsulfonyl)imide [C_4mim][Tf_2N] [45]. To increase the solubility of the inorganic nanoparticles in the ionic liquids, the nanocrystals were prepared with different stabilizing ligands such as citrate, N,N,N-trimethylglycine (betaine), and lauryl dimethyl glycine (lauryl betaine). Red photoluminescence and near-infrared luminescence are observed for the nanoparticles doped with Eu^{3+} and Nd^{3+}, respectively.

Yan's group also realized the dispersion of some complex rare earth fluorides with down-/up-conversion fluoride nanocrystals in different ionic liquid media [46, 47]. Firstly, two typical kinds of fluoride nanocrystals codoped with rare earth ions (Eu^{3+} and Tm^{3+}/Er^{3+}, Yb^{3+}) in ionic liquid compound with alkoxyl group 1-chlorohexane-3-methylimidazoliumchloride. Assisted by agarose, the transparent and uniform luminescent hydrogels are prepared, which presents the down-/up-conversion luminescence of the dispersed fluoride nanocrystals. The results provide a strategy to prepare luminescent (especially up-conversion luminescent) hydrogels with ionic liquid to disperse rare earth fluoride nanocrystals. The down-/up-conversion luminescence is checked for Eu^{3+} and Yb^{3+} and Er^{3+}/Tm^{3+} systems, respectively, which is beneficial for further development and application of luminescent (especially up-conversion luminescent) rare earth fluoride nanocrystals in practical fields. Moreover, they realized the dispersion of rare earth-doped fluorides ($BaMgF_4$, $NaYF_4$, and $BaYF_5$/$BaLuF_5$) in an ionic liquid compound, (3-triethoxysilyl) propyl-3-methylimidazolium chloride. Through the cohydrolysis and copolycondensatoin reaction between the alkoxy group (3-triethoxysilyl) of IM^+ and tetraethoxysilane in the presence of carboxylic acids (formic acid) as catalyst and water source, transparent and uniform luminescent hybrid ionogels form subsequently. These hybrid ionogels exhibit the

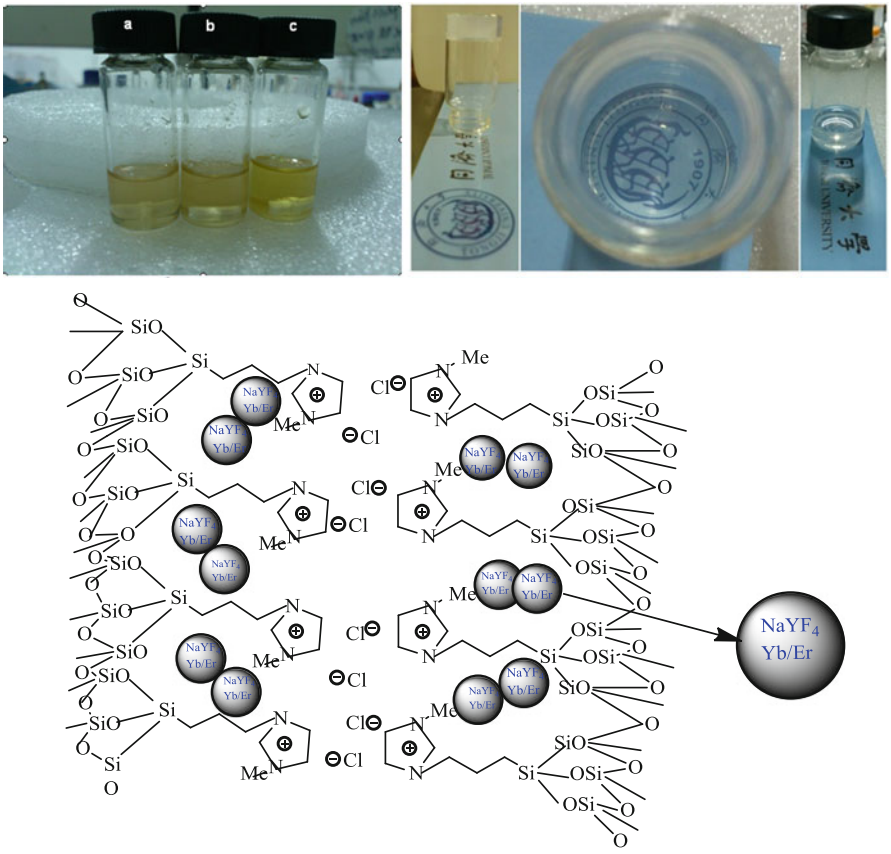

Fig. 8.2 Photograph for dispersions of fluoride nanocrystals in ionic liquid: $NaYF_4$ (a), $BaYF_5$/$BaLuF_5$ (b), $BaMgF_4$ (c) (*left*); the photos of hybrid ionogels from different angles (*right*); and the scheme for the possible structure of the ionogels (*bottom*) (Reproduced from Ref. [46] with permission from John Wiley and Sons)

up-conversion luminescent properties of immobilized rare earth-doped fluoride nanocrystals Er^{3+}/Tm^{3+} and Yb^{3+}. It is worth mentioning that the decentralized good samples are placed after a long period of about one month, which indicates that fluoride has been stably dispersed in the ionic liquids (see Fig. 8.2, top, left). The stable dispersion can be the product of interest, although it may also need to be studied further as hybrid material. The scheme for the possible structure of the soft ionogels is shown in Fig. 8.2 (bottom). Our research group tries to develop it into soft materials, ionogels, owning a good transparency as shown in Fig. 8.2 (top, right). Target gel is formed through these processes: carboxylation, etherification, hydrolysis, and condensation. The three fluorides are considered as up-conversion host for ion pairs of Yb^{3+}/Er^{3+} and Yb^{3+}/Tm^{3+}, as for photo-up-conversion among the near-infrared, visible light, the ultraviolet, and near-infrared regions. Because these three kinds of fluoride nanocrystals

Fig. 8.3 Photograph for up-conversion luminescence of rare earth-doped fluoride nanocrystals dispersed in (3-triethoxysilyl) propyl-3-methylimidazolium chloride under the excitation wavelength of 980 nm: from left to right, $NaYF_4$:Yb^{3+}/Er^{3+}(20, 2 mol%), $NaYF_4$:Yb^{3+}/Tm^{3+}(20, 2 mol %), $BaYF_5$:Yb^{3+}/Er^{3+} (20, 2 mol%), $BaYF_5$:Yb^{3+}/Tm^{3+} (20, 2 mol%) (Reproduced from Ref. [46] with permission from John Wiley and Sons)

are well distributed in ionic liquids, we can get room-temperature up-conversion luminescent spectra. For Yb^{3+}/Er^{3+} (20, 2 mol %) system, the energy transitions, $^2H_{11/2}$ to $^4I_{15/2}$, $^4S_{3/2}$ to $^4I_{15/2}$, and $^4F_{9/2}$ to $^4I_{15/2}$, are corresponded to three main emission peaks centered at ~520, ~550, and ~655 nm, respectively. Yb^{3+}/Tm^{3+} (20, 1 mol %) nanocrystals are under the 980 nm excitation. It can be clearly shown that the emission spectra have five peaks at 450, 477, 646, 693, and 800 nm, which attributed to $^1D_2 \rightarrow {}^3F_4$, $^1G_4 \rightarrow {}^3H_6$, $^1G_4 \rightarrow {}^3F_4$, $^3F_3 \rightarrow {}^3H_6$, and $^3H_4 \rightarrow {}^3H_6$ transitions, respectively. Figure 8.3 shows the photograph of the hybrid systems.

8.4 Photofunctional Rare Earth Hybrid Materials Based on Ionic Liquid with Organically Modified Siloxane

Binnemans's group prepared luminescent ionogels based on Eu^{3+} tetrakis β-diketonate complex-doped imidazolium ionic liquids confined within silica-derived networks by a non-hydrolytic method as perfect monoliths featuring both the transparency of silica and the ionic conductivity of ionic liquids (80 vol.%) [48]. The organic–inorganic hybrid materials show a very intense red photoluminescence with very high color purity under ultraviolet irradiation. They showed that RE^{3+} complexes can be efficiently confined in the ionic liquid component of solid-state ionogels to construct luminescent organic–inorganic hybrid materials, which is a powerful alternative for the immobilization of the complexes by covalently linking to the silica network (Fig. 8.4).

Carlos's group studied the structural and photoluminescence of a Eu^{3+} tetrakis (β-diketonate) complex with $[NBu_4]^+$; 1-butyl-3-methylimidazolium, $[C_4\ mim]^+$, and 1-butyl-3-methylpyridinium, $[C_4mpyr]^+$ counterions [49]. Under ligand

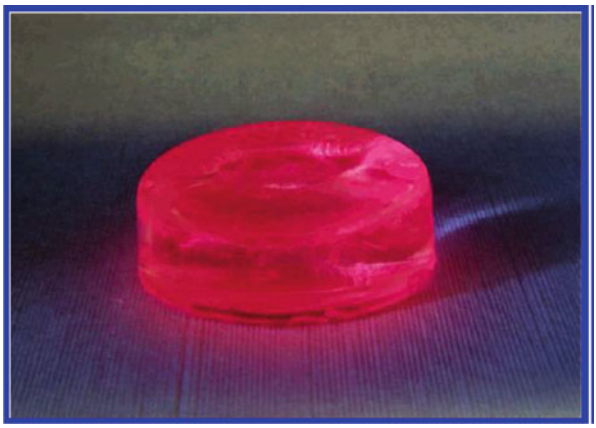

Fig. 8.4 Luminescence of Eu^{3+}-doped ionogel under ultraviolet irradiation (Reprinted with permission from Ref. [48], copyright 2006, American Chemical Society)

excitation (λ_{ex} = 290–395 nm), the quantum yields (room temperature) are in the range of 0.72–0.77 for the 1-butyl-3-methylimidazolium salt. An immobilized analogue of this complex is prepared by supporting $[Eu(NTA)_4]^-$on ordered mesoporous silica derived from 1-propyl-3-methylimidazolium groups. The disappearance of the intra-$4f^6$ lines in the excitation spectrum of the supported material indicates an increase in the ligand's sensitization process of the Eu^{3+} ions, which is related to the direct intra-$4f^6$ excitation. The emission quantum yield measured for the supported material (0.32–0.40, for excitations between 265 and 360 nm) is the highest so far reported for rare earth-containing ordered mesoporous silica.

Li and Zhang presented a facile method to prepare a transparent and luminescent ionogel monolith by hydrolysis and condensation of the silylated bipyridine and carboxyl-functionalized ionic liquid coordinating to Eu^{3+} ions [50, 51]. Excitation and emission spectra verified that the energy transfer from the bipyridine groups (covalently bound to silica) to Eu^{3+} ions occurs. The $^5D_0$ quantum efficiency value and the number of water molecules coordinated to Eu^{3+} ions in the ionogel have been estimated. Due to the versatility of the silylated sensitizer and the Eu^{3+} ions, ionogels displaying different emission lines both in the visible region and near-infrared region can be obtained by this facile method (Fig. 8.5).

Our group mainly focuses on the photofunctional rare earth hybrid materials with ionic liquid 1-methyl-3-[3-(trimethoxysilyl)propyl]imidazolium chloride as double chemical linker to assemble rare earth complex and organically modified silica host with versatile aggregation [52–56]. The ionic liquid 1-methyl-3-[3-(trimethoxysilyl)propyl]imidazolium chloride is incorporated into mesoporous SBA15 framework by an in situ sol-gel processing. Then, an anion metathesis processing is performed for introducing the rare earth β-diketonate complex anion. Four kinds of commercially available β-diketonates are used for SBA15-$IM^+[Eu(L)_4]^-$ (L = TTA, BTA, HTA, or TAA), which are benzoyltrifluoroacetone (BTA), hexafluoroacetylacetone (HTA), thenoyltrifluoroacetone (TTA), and trifluoroacetylacetone (TAA), respectively. Figure 8.6 shows the possible

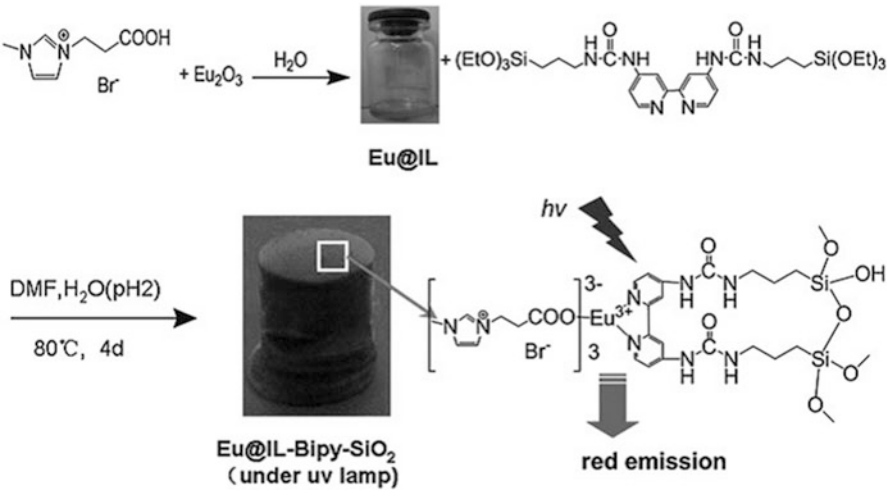

Fig. 8.5 The procedure used to obtain the transparent and luminescent ionogel (Reproduced from Ref. [50] with permission from The Royal Society of Chemistry)

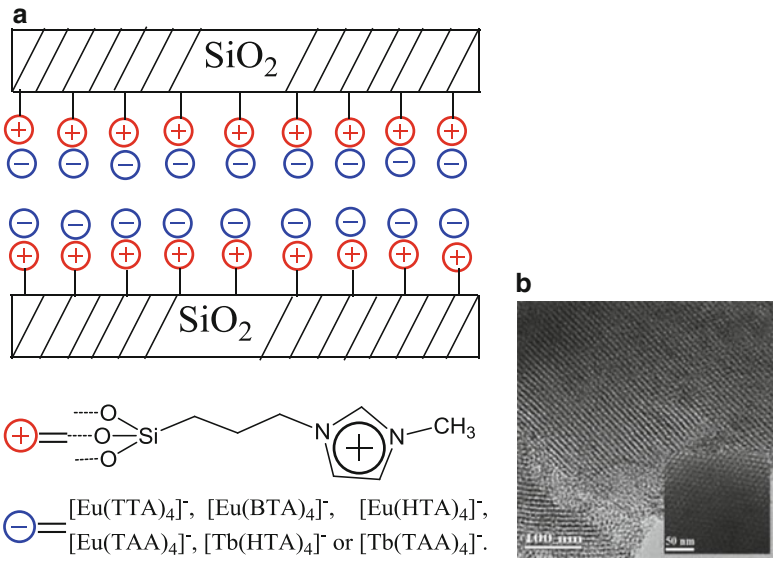

Fig. 8.6 Possible composition structure of the mesoporous hybrid materials and the selected TEM images of SBA15-IM$^+$Cl$^-$ (**a**) and SBA15-IM$^+$[Eu(TTA)$_4$]$^-$ (**b**) (Reproduced from Ref. [52] with permission from The Royal Society of Chemistry)

composition structure of the resulted materials and the selected TEM images for SBA15-IM$^+$Cl$^-$ and SBA15-IM$^+$[Eu(TTA)$_4$]$^-$ [52]. It can be observed that of SBA-15 the well-ordered hexagonal mesostructure is preserved in both SBA15-

IM^+Cl^- and SBA15-$IM^+[Eu(TTA)_4]^-$. There is a regular hexagonal array of uniform two-dimensional channels, which also indicates that the mesostructure of SBA15 can be substantially conserved after the introduction of ionic liquid and the subsequent anion exchange reaction. In addition, the distance between the contiguous centers of the mesopore is estimated to be about 10 nm. It is found that the luminescent intensities of SBA15-$IM^+[Eu(TAA)_4]^-$ and SBA15-$IM^+[Eu(HTA)_4]^-$ are weaker than those of SBA15-$IM^+[Eu(TTA)_4]^-$ and SBA15-$IM^+[Eu(BTA)_4]^-$, indicating that the TTA and BTA ligands are the favorable sensitizer for Eu^{3+} probably because they possess a more asymmetry molecular structure than TAA and HTA. The luminescent lifetimes of SBA15-$IM^+[Eu(TTA)_4]^-$ and SBA15-$IM^+[Eu(BTA)_4]^-$ are longer than those of SBA15-$IM^+[Eu(TAA)_4]^-$ and SBA15-$IM^+[Eu(HTA)_4]^-$, which is consistent with the results of their emission spectra. It can be clearly seen that the luminescent quantum efficiencies of SBA15-$IM^+[Eu(TTA)_4]^-$ (55.9 %) and SBA15-$IM^+[Eu(BTA)_4]^-$ (62.3 %), suggesting that this method is preferable for constructing europium-based luminescent mesoporous materials. Meanwhile, the relatively high quantum efficiency of these materials shows that the SBA15 is an excellent host for the europium complexes.

Besides, the rare earth functionalized polymers are conveniently prepared from hydroxyl groups containing polymer (Wang resin) and copolymer (Poly (St-HEMA)) through three steps of chlorination, quaterization, and anion exchange reaction, whose scheme is outlined in Fig. 8.7 [53]. Firstly, the chlorination reaction is accomplished by the reaction of hydroxyl groups containing polymers with thionyl chloride. The functionalization of chlorine substituent groups containing polymers with imidazolium salt molecular bridge could be easily achieved through the ordinary quaterization reaction method. And then, through a mild anion exchange reaction between the chloride ion of the imidazolium moieties and the

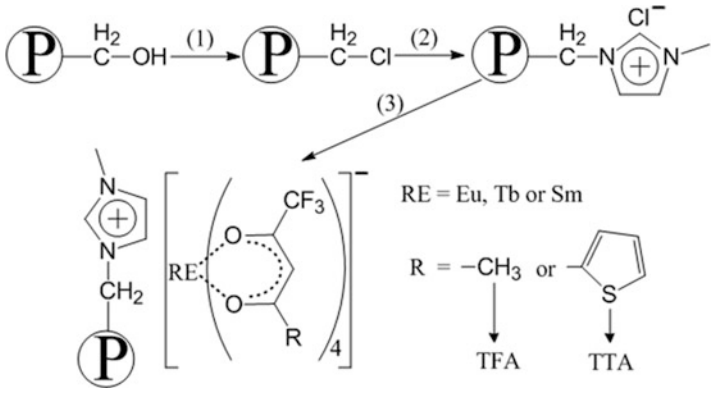

Fig. 8.7 Synthesis of the rare earth tetrakis(β-diketonate) complex functionalized polymers (or copolymers). Conditions: (*1*) thionyl chloride, reflux for 12 h, (*2*) 1-methylimidazole, 100 °C for 48 h, (*3*) rare earth tetrakis(β-diketonate) complexes, ethanol, room temperature for 48 h (Reproduced from Ref. [53] with permission from the European Society for Photobiology, the European Photochemistry Association, and The Royal Society of Chemistry)

rare earth complex anions within the as-prepared $Na_4(REL_4)$ solution, we succeeded in anchoring rare earth tetrakis(β-diketonate) complexes onto the modified hydroxyl groups containing polymers. Moreover, in order to demonstrate the feasibility of the method used here, we repeated the doping procedures using the rare earth tetrakis(TAA) complexes and the unmodified Poly(St-HEMA) under the identical conditions. Luminescent emission spectra of the resulted materials are measured under the same conditions as its corresponding materials derived from the imidazolium-modified Poly(St-HEMA); however, only very weak luminescent emission originating directly from the Poly(St-HEMA) matrices is observed, suggesting that the imidazolium modification is necessary here.

We also realized the covalent functionalization of GaN surfaces with imidazolium salt IL, which bears an organosilane group and can silanize the hydroxylated surfaces of GaN and then can adsorb the tetrakis β-diketonate europium complex anion through the electrostatically driven anion exchange reaction. The aim of the work described herein [54] is to explore the way of constructing GaN-based luminescent materials using the IL and research their photophysical properties [54]. Figure 8.8 shows the detailed synthetic pathways to obtain the luminescent materials. The resulting material is denoted as GaN-IM^+-$[Eu(TTA)_4]^-$. The X-ray photoelectron spectroscopy (XPS) analysis of samples before and after anion exchange reaction is provided as a complement to FTIR. The emerging peak of F 1 s appearing at 692 eV in GaN-IM^+-$[Eu(TTA)_4]^-$ is a positive evidence for the

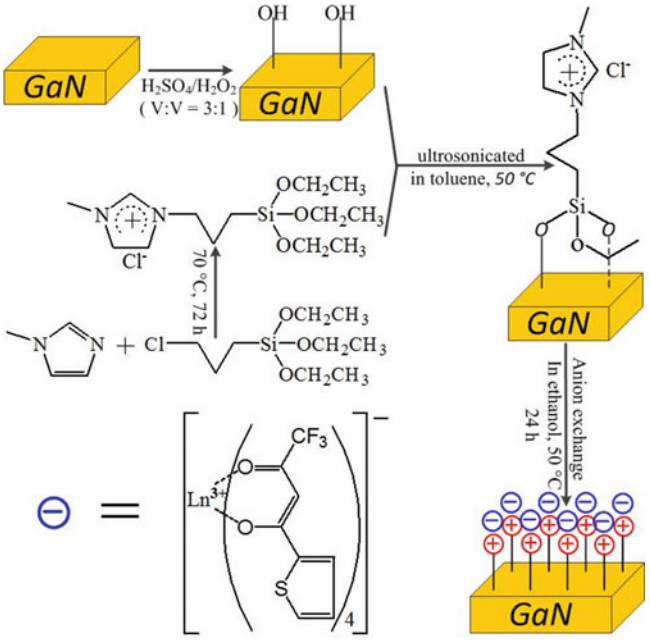

Fig. 8.8 Synthetic scheme for the preparation of rare earth complex functionalized GaN (Reproduced from Ref. [54] with permission from The Royal Society of Chemistry)

success of anion exchange. The O 1 s core-level XPS spectra of IL-modified GaN could be attributed to the O-H, O-Ga, and O-Si constituent. Thus, for the materials after anion exchange, the new component (around 536.3 eV) could be attributed to the introduction of coordinated oxygen within the resonating structures of chelated β-diketonate ligands. The intensity ratio $I(^5D_0 \rightarrow {}^7F_2)/I(^5D_0 \rightarrow {}^7F_1)$ of the red/orange intensities is approximately 16.1, indicating that the Eu^{3+} ions are located in an asymmetric environment. The lifetime value is calculated as 316 μs. Furthermore, based on the emission spectra and the lifetime(τ) of GaN-IM^+-$[Eu(TTA)_4]^-$, the emission quantum efficiency (η) of the $^5D_0$ excited state of europium(III) ion is determined as 26.3 %. The photoluminescent properties reveal that GaN is a favorable matrix for constructing luminescent rare earth hybrid materials. Moreover, this achievement provides a new approach to design novel functional GaN materials.

The silica-based matrix is prepared through an ionic liquid-mediated non-hydrolytic sol-gel route, using a mixture of tetramethoxysilane, formic acid, 1-hexyl-3-mexylimidazolium bis[(trifluoromethyl)sulfonyl]imide, and 1-methyl-3-[3-(triethoxysilyl)propyl]-imidazolium chloride [55]. The formic acid used here serves as solvent, water source, and catalyst for both hydrolysis and condensation. After the completion of gelation, the confined ionic liquid was removed by Soxhlet extraction. During the synthesized process, silica-based matrix is prepared through an ionic liquid-mediated non-hydrolytic sol-gel route in advance, and then the rare earth complex anion is assembled into the matrix through electrostatic interactions after a simple anion metathesis reaction. The intensity ratios $I(^5D_0 \rightarrow {}^7F_2)/I(^5D_0 \rightarrow {}^7F_1)$ (red/orange ratio) of the two emission peaks are about 14.8 and 9.5 for Gel-$Im^+[Eu(TTA)_4]^-$ and Gel-$Im^+[Eu(NTA)_4]^-$, respectively, suggesting that the Eu^{3+} is not at the center of an asymmetric coordination field. In addition, we have found that the Gel-$Im^+[Eu(TTA)_4]^-$ shows better luminescent properties than Gel-$Im^+[Eu(NTA)_4]^-$ under the same test conditions, which is in coincidence with the results of luminescent lifetimes and quantum efficiencies. The outer luminescent quantum efficiencies for $^5D_0$ energy level of Eu^{3+} and $^5D_4$ energy level of Tb^{3+} are determined and are coincident with the values of integration ratio of transition red/orange ratio and luminescent lifetimes.

The rare earth tetrakis β-diketonate complex functionalized silica spheres are conveniently prepared by a one-pot synthesis method which is based on the modified Stöber process [56]. The resulted luminescent nanoparticles are shown schematically in Fig. 8.9 (top). Because the introduction of siloxy-bearing rare earth complex precursor can result in coagulation, a step-by-step approach is adopted to implement the synthesis of uniform silica sphere. The rare earth complex precursors added into the reaction system in the second step can ensure the size uniformity of the nanoparticles furthest. As a result, the rare earth chelate mainly lies in the outer layer of the silica sphere, which has been shown schematically in Fig. 8.9 [55]. As shown in Fig. 8.9 (bottom), the nanoparticles obtained are uniform spheres, approximately 61 ± 5 nm in diameter. And there is no obviously change in the particle size or morphology. All nanoparticles show relatively high luminescent lifetimes. Among the quantum efficiencies, the experiment values of Eu-TTA-SS (34.8 %)

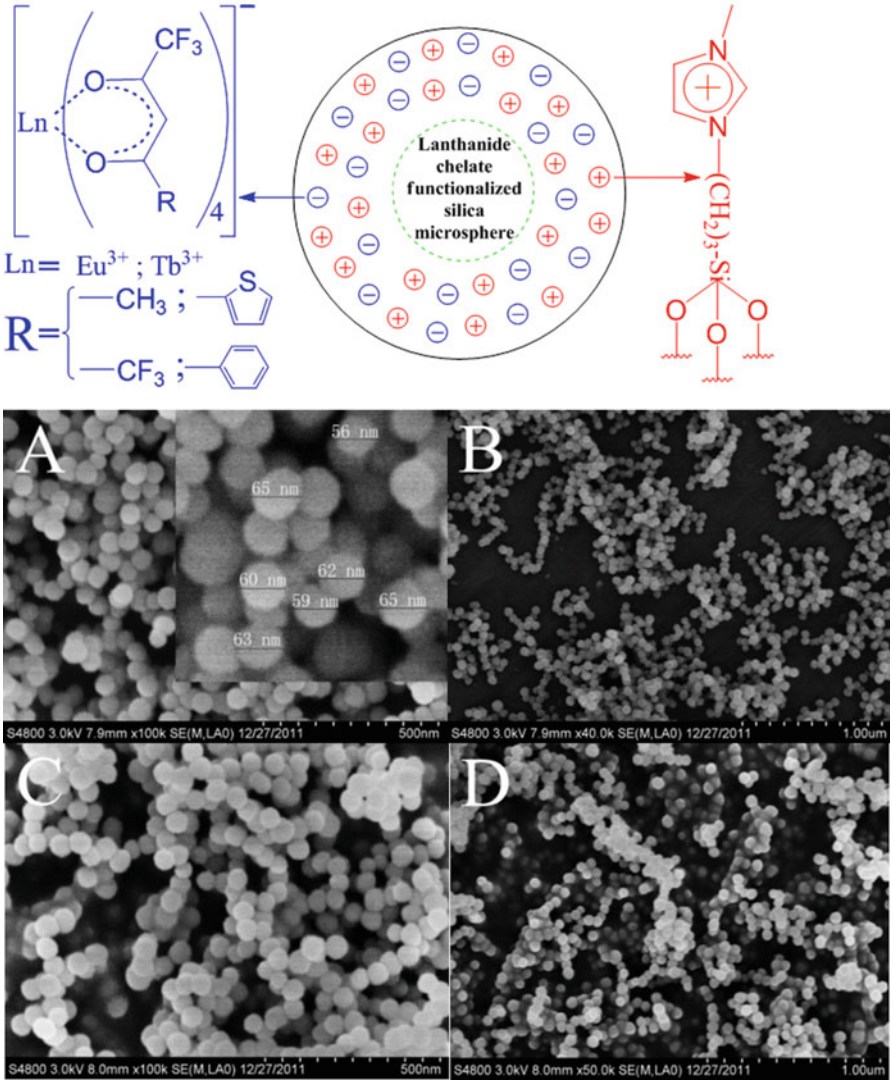

Fig. 8.9 Schematic diagram and selected SEM images of rare earth chelate functionalized Eu-TTFA-SS (a, b) and Tb-TFAA-SS (c, d) silica sphere (Reproduced from Ref. [56] with permission from Springer)

and Tb-HFA-SS (54.7 %) are at a relatively high level, which suggests ligand TTA is the most appropriate one for sensitizing the luminescent properties of Eu^{3+}, and so does the HAA to Tb^{3+}. We also have noticed that values of the theoretical quantum efficiency are generally much higher than the ones in quantum efficiency experiment. The resulted silicon spheres would retain much of its outstanding luminescent properties of rare earth chelates, such as high quantum efficiency,

long luminescent lifetime, and line-like emission. This makes the resulted silicon spheres have great potential as luminescent nanoparticle.

For rare earth hybrid materials themselves, the tendency is shifted to introduce the inorganic crystalline building block into hybrid system to further improve their physical and chemical properties. Polyoxometalates are inorganic metal oxide clusters with nanometer dimension, whose crystalline framework structure and versatile function are favorable for the hybrid materials. Especially decatungstoeuropate (9-) anion as a potassium salt is worthy of attention, whose sodium salt ($Na_9EuW_{10}O_{36}\cdot 32H_2O$, EuW_{10}) possesses long luminescent lifetime and high luminescent quantum yield for its crystalline structure. Our group designed a series of photofunctional hybrid materials with POMs and different building units [57–59]. Figure 8.10 (left) shows the scheme for the synthesis and basic

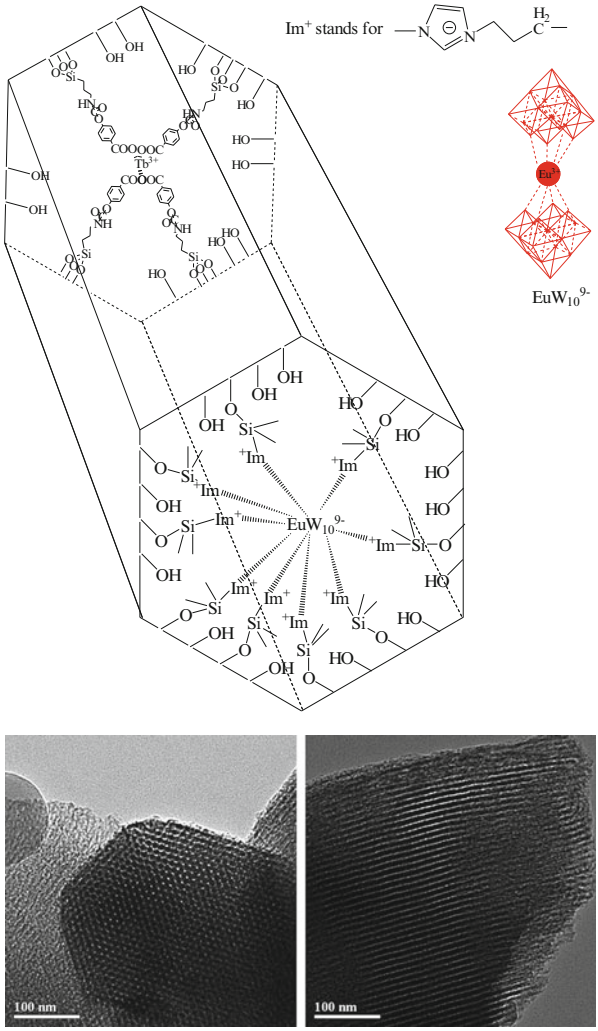

Fig. 8.10 The selected scheme for the synthesis process and basic composition of O-Si-IL (EuW_{10}, Tb)-SBA15 mesoporous hybrids (*left*) and selected transmission electron micrographs of O-Si-IL(EuW_{10})-SBA-15 mesoporous hybrids along the [100], [110] zone axes (*right*) (Reproduced from Ref. [57] with permission from The Royal Society of Chemistry)

composition of whole hybrid systems [57]. Organically modified silanes (ORMOSILs) are firstly synthesized with three benzoate derivatives and TEPIC. In the presence of surfactant template P123, the organically functionalized mesoporous silica SBA-15 materials can be prepared. On the other hand, ILs can be grafted onto organically functionalized mesoporous silica SBA-15 for its alkoxy group to form Si–O linkage. Further, ILs can interact with the PMOs through ion exchange with electrostatic force. Here ILs behave as double functional linkages both from Si–O covalent bond and static electricity interaction. The selected TEM micrographs of O-Si-IL(EuW_{10})-SBA-15 and N-Si-IL(EuW_{10})-SBA-15 along [100] and [110] zone axes are shown in Fig. 8.10 (right), respectively. It can be seen the highly ordered mesostructures are reserved, and the hexagonal symmetry of the space group P_{6mm} is shown clearly. There is no phase separation observed in the TEM micrographs, which indicates that the homogeneous and uniform ordered materials are obtained. This is due to the covalent bonds between the organic compound and the framework of SBA15. The value orders of the I_{02}/I_{01} for europium hybrids are as follows: O-Si-IL(EuW_{10})-SBA15 > N-Si-IL(EuW_{10})-SBA15 > pure $Na_9EuW_{10}O_{36}$ > S-Si-IL(EuW_{10})-SBA15. This is mainly caused by the difference of the energy transfer in the environment of Eu^{3+}. After the introduction of Tb^{3+} in the hybrid system, the overlapping peak regions of both $EuW_{10}O_{36}^{9-}$ and Tb^{3+} in hybrids of N-Si-IL(EuW_{10},Tb)-SBA15 and O-Si-IL(EuW_{10},Tb)-SBA15 change the original ratios of I_{02}/I_{01} compared to that N-Si-IL(EuW_{10})-SBA15 and O-Si-IL(EuW_{10})-SBA15, which are reflected by their decreasing values. The value orders of the I_{02}/I_{01} are as follows: S-Si-IL(EuW_{10}, Tb)-SBA15 > N-Si-IL(EuW_{10},Tb)-SBA15 > O-Si-IL(EuW_{10},Tb)-SBA15. Comparing the data for the hybrids without Tb^{3+} and with Tb^{3+}, it is discovered that the benzoate groups (O-Si, N-Si, S-Si) of the hybrid system may sensitize the emission of Tb^{3+}. And we get the CIE chromaticity diagrams from the emission spectra (CIE stands for the International Commission on Illumination). And seeing from the CIE chromaticity diagrams of the hybrids with Tb^{3+}, the emissions are almost close to white light. The data of Luminescent Decay Times (τ) of the Eu^{3+} first excited level ($^5D_0$) can be analyzed directly, and the emission quantum efficiency (η) of the $^5D_0$ excited state can be determined. The quantum efficiency of pure EuW_{10} is 52.8 %, and the quantum efficiency of materials S-Si-IL(EuW_{10},Tb)-SBA15-encapsulated $Na_9EuW_{10}O_{36}$ can reach 74.5 %; this shows us the potential of organic–inorganic hybrids to promote the luminescent performance relative to the pure inorganic rare earth polytungstate. This suggests that the mercapto benzoate-modified SBA15 is a rather good host as the main energy donor for EuW_{10}.

Besides, we designed another kind of the multicomponent hybrids with europium polyoxometalates EuW_{10}, ionic liquid linker, polymer unit, and its functionalized silica or mesoporous silica [58]. As shown in Fig. 8.11 (left), TEPIC firstly is grafted onto the three polymers (P1, P2, and P3) through addition reaction between inter ester group of TEPIC and the hydroxyl groups of polymers under the reaction conditions. Secondly, IM-functionalized EuW_{10} are prepared with ion exchange reaction between IM^+Cl^- and EuW_{10}. Finally, the whole multicomponent hybrid systems consisting of EuW_{10} and polymer-functionalized

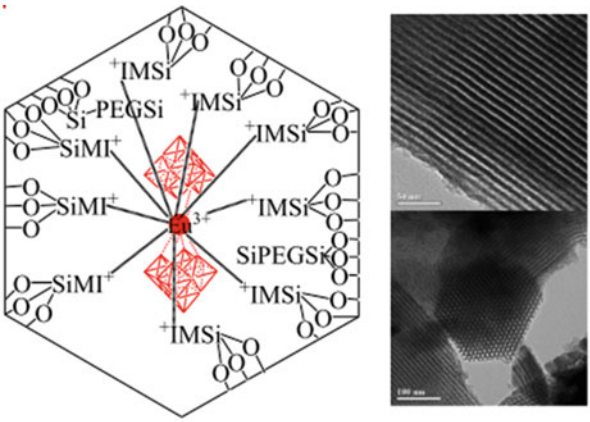

Fig. 8.11 Scheme of synthesis process of the precursor and the composition of the hybrid systems (*left*) and selected TEM images of Eu-SBA15-P1 hybrids along the [100] (A), [110] (B) zone axes (Reproduced from Ref. [58] with permission from The Royal Society of Chemistry)

silanes (P1-Si, P2-Si, and P3-Si) are linked with Si–O bond after the cohydrolysis and copolymerization process between their alkoxy groups (TEPIC unit and IM^+). Here we name the hybrids as Eu-Si-P1(2,3). For the functionalized mesoporous silica (SBA15) hybrids, the reaction process adopts the similar procedure as above except for the use of P123 as template. We name these hybrids as Eu-SBA15-P1 (2,3). Here it needs to be mentioned that the concentration of EuW_{10} in Eu-Si-P1 (2,3) is more than that in Eu-SBA15-P1(2,3), which will have an influence on the corresponding luminescent properties. In Fig. 8.11 (right), the selected TEM micrographs of Eu-SBA15-P1 hybrids along [100] and [110] zone axes also show the homogeneous and uniform ordered microstructure. The absolute luminescent quantum yield of Eu-Si-P1(2,3) hybrids is higher than that of Eu-SBA15-P1(2,3) hybrids, which is in agreement with the order of their lifetimes for the distinction of effective concentration of EuW_{10}. Among them Eu-Si(SBA15)-P1(2,3) possess the quantum efficiency over 50 %, which is comparable to the data of parent EuW10 compound. But the effective concentration of EuW_{10} species is much lower than that of EuW_{10} itself. The favorable luminescent performance (long lifetimes and high quantum yields) is favorable for the further practical application. Furthermore, it can be found that the four hybrid systems (Eu-Si-P2(3) and Eu-SBA15-P2(3)) emit close white luminescence, whose CIE coordinates ((0.3941, 0.4035), (0.3767, 0.4061), (0.3847, 0.4039), and (0.3799, 0.4046)) are in the cool-white region, close to sunlight, which is useful for the lighting.

EuW_{10}, polymer resin unit and rare earth (Eu, Gd) aromatic carboxylate complexes, and MPTMS-functionalized mesoporous silica can also be assembled through ionic liquid linkage, respectively (see the scheme in Fig. 8.12) [59]. Three benzoate derivatives are grafted onto resin (MR or WR) with their substituted groups (−OH, −SH, $-NH_2$) through the condensation reaction, and three carboxylates can occupy chemically equal six coordination spots of Eu^{3+} or Gd^{3+} ion. IL behaves as the linkage to both interact with EuW_{10} ion through ion exchange interaction and chemically bond with functionalized mesoporous silica (MPTMS-S15) after the cohydrolysis and copolymerization process between their alkoxy

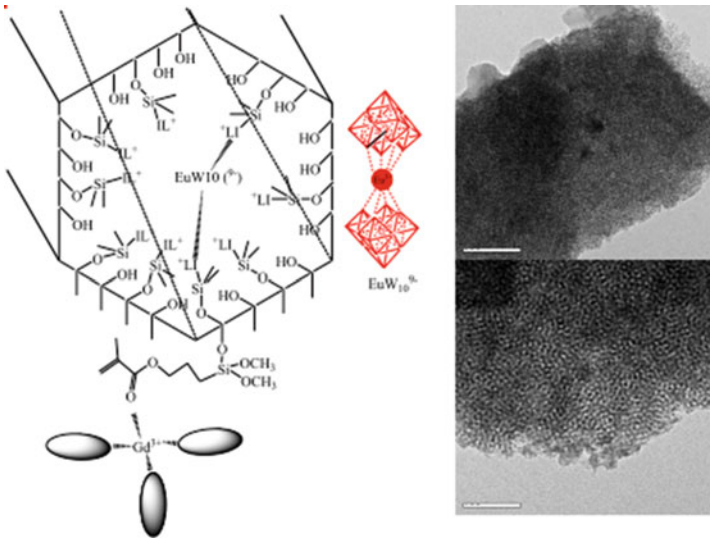

Fig. 8.12 The selected scheme for the synthesis process and basic composition of MR-O-Gd-S15 hybrids; for other hybrids, the scheme is similar except for MR, O, and Gd which are replaced by WR, N or S, and Eu, respectively (*left*), and selected TEM images of WR-O-Eu-S15 along the [100] and [110] zone axes (Reproduced from Ref. [59] with permission from Elsevier)

groups (MPTMS-S15 unit and IL) in the presence of P123 as template. Besides, rare earth (Eu^{3+} or Gd^{3+}) complexes with three benzoate derivatives are easily understood for rare earth coordination chemistry principle. Here we name these hybrids as MR(WR)-O(S, N)-Gd(Eu)-S15. The structures and changes of the uniformly ordered mesoporous SBA15 can be observed more intuitively from the selected micrographs (TEM) in Fig. 8.12 (right). The lifetimes of the hybrids are all shorter than that of EuW_{10} (about 3 ms). The order of luminescent quantum yields is consistent with that of luminescent lifetimes. They are all lower than the parent EuW_{10} compound (over 60 %) for the lower effective concentration of EuW_{10} species in the hybrid system than parent EuW_{10}. Besides, the quantum yields of the hybrids with MR polymer resin are higher than those of the hybrids with WR polymer resin, suggesting that MR-S15 is superior to WR-S15 as the matrix for EuW_{10}. Except for MR-N-Gd-S15 and MR-N-Eu-S15 emitting orange or yellow light, the emitted light colors of other seven hybrid systems almost all locate at the nearly white light region (cool light), which is close to sunlight and should be more useful in practical applications for lighting or optical devices.

Binnemans's group prepared Eu^{3+} complex-doped luminescent poly(methyl methacrylate) films using ionic liquid 1-hexyl-3-methyl imidazolium bis(trifluoromethylsulfonyl)imide ($[C_6mim][Tf_2N]$) as plasticizer [51]. Different europium (III) complexes have been incorporated in the polymer/ionic liquid matrix: $[C_6mim][Eu(NTA)_4]$, $[C_6mim][Eu(TTA)_4]$, $[Eu(TTA)_3(phen)]$, and $[choline]_3[Eu(dpa)_3]$. Bright red photoluminescence was observed for all the films upon

irradiation with ultraviolet radiation. The luminescent films have been investigated by high-resolution steady-state luminescent spectroscopy and by time-resolved measurements. The polymer films doped with β-diketonate complexes are characterized by a very intense $^5D_0$–$^7F_2$ transition (up to 15 times more intense than the $^5D_0$–$^7F_1$), whereas a marked feature of the PMMA films doped with $[choline]_3[Eu(dpa)_3]$ is the long lifetime of the $^5D_0$ excited state (1.8 ms). The ionic liquid also enhances the solubility of the europium(III) complexes in the PMMA matrix. Although we have illustrated here the performance of PMMA/ionic liquid films doped with europium(III) β-diketonate complexes and $[choline]_3[Eu(dpa)_3]$, the applicability of our system is of course not limited to europium(III) or to these types of ligands. The luminescent color of the flexible PMMA films can be tuned by a suitable choice of the RE^{3+} ion, ranging from blue for Tm^{3+} over green for Tb^{3+} and near-infrared emission for ions such as Nd^{3+}, Er^{3+}, and Yb^{3+}.

Our group assembled the hybrids involving rare earth polyoxometalates (REW_{10} unit), ionic liquid linkage (IM^+), and inorganic polymeric gel matrices (alumina, zirconia, titania) [60]. IL (IM^+) behaves as the linkage to both interact with $EuW10^{9-}$ ion through ion exchange interaction and coordinate to zirconia, alumina, and titania matrices with carboxylate groups after the hydrolysis and copolymerization process. Here we name these hybrids as RE-IL-M (RE = Eu, Tb, Sm, Dy, M = Ti, Zr, Al). Besides, it needs to be pointed out that the hydrolysis and polycondensation reaction of tetraisopropoxytitanium is much faster than the other two alkoxyl precursors (aluminum isopropylate and zirconium butoxide), which is too quick to produce the lower encapsulating content of REW_{10} in titania than the other two systems (alumina and zirconia). This will affect the luminescent performance of the corresponding hybrid xerogels. Photoluminescent comparisons of polyoxometalate-encapsulated hybrids in different inorganic matrices are discussed. The R/O ratios of three EuW_{10}-assembled hybrids, Eu-IL-Al, Eu-IL-Zr, and Eu-IL-Ti, are 0.73, 1.04, 1.21, respectively, compared with 0.68 of EuW10. The interaction between EuW_{10} and ionic liquid-functionalized matrix probably influences EuW_{10} through the static electronic force. Zirconia and alumina matrices are more suitable matrices for the luminescence of EuW10 than titania. The lifetimes of EuW_{10}-incorporating alumina, zirconia, and titania can reach millisecond time scale which are above 2 ms. At the same time, hybrids Eu-IL-Al and Eu-IL-Zr display longer decay lifetime than the Eu-IL-Ti, which is consistent with the analysis results of their emission spectra. Decay lifetime values of Tb-IL-Al, Tb-IL-Zr, and Tb-IL-Ti are 0.84 ms, 0.81 ms, 0.704 ms, correspondingly. The values are lower than these inorganic host matrices encapsulating EuW_{10}. The lifetime values of Sm-IL-Al, Sm-IL-Zr, Sm-IL-Ti, Dy-IL-Al, Dy-IL-Zr, and Dy-IL-Ti are 91, 90, 82, 83, 76, and 59 μs, respectively, far below the lifetime of EuW_{10} hybrids. When EuW10 is encapsulated into matrices of alumina and zirconia, the values of η increase significantly which can approach 96 % and 89 % correspondingly. Furthermore, the CIE chromaticity diagrams of polyoxometalate-derived hybrids show that Eu-IL-Ti, Tb-IL-Zr, Tb-IL-Ti, Dy-IL-Ti, Dy-IL-Zr, and Dy-IL-Al are located at warm white light regions, displaying favorable luminescent performance for practical applications.

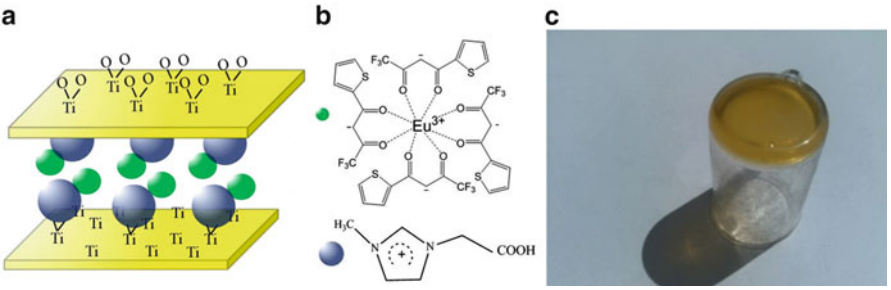

Fig. 8.13 The fabrication scheme of the synthesis process of hybrid soft xerogel material [Eu $(L)_4$]-IM^+-Ti: (**a**) the scheme for synthesis, (**b**) the scheme for sandwich composition and structure. (**c**) the photograph for soft gels [$RE(L)_4$]-IM^+-Ti1. Here we only set $[Eu(TTA)_4]^-IM^+$-Ti as an example, and for other [$RE(L)_4$]-IM^+-Ti (RE = Eu, Tb, Sm; L = TTA or TAA) systems, the scheme is similar except for Eu that is replaced by Tb or Sm, TTA is replaced by TAA, and titania (Ti) is replaced by alumina (Al) (Reproduced from Ref. [61] with permission from the Centre National de la Recherche Scientifique (CNRS) and The Royal Society of Chemistry)

Figure 8.13 shows the scheme for the synthesis and basic composition of whole hybrid systems. Ln^{3+} tetrakis β-diketonate complexes are introduced to replace Br^- of the above system, resulting in the hybrid system by the static electric interaction of the positive (IM^+) and negative charge ($[RE(\beta\text{-diketonate})_4]^-$) [61]. On the other hand, the IM^+ fragment can link alumina and titania xerogel matrices through the coordination interaction between its carboxylic groups and Al^{3+} or Ti^{4+}. So the ionic liquid compound behaves as the double functional linker to connect rare earth complexes and xerogels, just like sandwich mode (see Fig. 8.13b). Figure 8.13c presents the selected photograph of the final xerogels of [$RE(L)_4$]-IM^+-Ti hybrids, revealing the formation of transparent and stable xerogel forms. For samarium hybrid soft xerogels, the luminescent color can be adjusted and the white luminescent integration can be realized.

Ionic liquid compound with -SH group such as SH-IL has the ability to link semiconductor for the affinity between S and metal component of semiconductor. So SH-IL can be used as effective medium to disperse II–VI group semiconductor. Meanwhile, it can as well interact with rare earth complexes through the ion exchange. Under this strategy, some inorganic oxide, metal, or sulfide nanoparticles such as ZnO, ZnS, Ag_2S, and rare earth tetrakis complexes can be used to construct multicomponent composite material system. The photoluminescence, especially the white luminescent integration, is discussed in detail [62–65].

With the different molar ratio of ZnO component and europium complex, the luminescent intensity ratio of violet–blue emission to red one can be adjusted. As a result, the blue for ZnO-SH-IL-Eu2.5 composites and white luminescence for ZnO-SH-IL-Eu5.0 composites can be observed in CIE coordinate diagraphs, whose CIE coordinate is (0.2968, 0.2207). So the white luminescence for ZnO-SH-IL-Eu5.0 composites can be integrated with double components of ZnO

unit and Eu^{3+} complex through SH-IL linkage in the composite system. Further, we introduce Tb^{3+} complex species ($Eu(TTA)_4^-$, $Tb(AA)_4^-$) to the ionic liquid-functionalized composite systems. From the CIE chromaticity diagram of SH-IL-Eu2.5-Tb1 composites, its CIE coordinate is (0.3146, 0.2702) in the white area. The white luminescence can be achieved by integrating three components of blue (ZnO), green (Tb^{3+}), and red (Eu^{3+}) light. The absolute quantum yields are determined by the integrating sphere for all the rare earth composite systems, which covers the emission of ZnO-SH-IL, europium, and terbium beta-diketonates. ZnO-SH-IL-Eu2.5 and ZnO-SH-IL-Eu5.0 possess luminescent quantum yield of 15.5 % and 11.2 %, respectively, while ZnO-SH-IL-Eu1.5-Tb1 and ZnO-SH-IL-Eu2.5-Tb1 present luminescent quantum yield of 14.1 % and 12.0 %, respectively. So the different composition has influences on the luminescent performance of these soft composite materials.

Mercapto-ion liquid compound such as 3-(2-(2-mercaptoacetoxy)ethyl)-1-methyl-1H-imidazol-3-ium bromide (SHIL) has the ability to link semiconductor for the chemical affinity between S and metal element component (Zn, Cd) of semiconductor sulfides [61]. Both two europium tetrakis β-diketonates ($Eu(TTA)_4^-$, $Eu(TAA)_4^-$) and two metal sulfides (ZnS, CdS) can be linked with SHIL in its dispersion process. As a result, close white luminescence for the two soft hybrids can be observed in CIE coordinate diagraphs, whose CIE coordinates are (0.2935, 0.3390) for ZnS-SHIL-$Eu(TAA)_4$ and (0.2730, 0.3237) for ZnS-SHIL-$Eu(TAA)_4$, respectively. So the slight blue (blue–white) luminescence for these soft hybrids can be easily integrated with double components of ZnO unit and Eu^{3+}. The absolute luminescent quantum yields of ZnS-SHIL-$Eu(TAA)_4$ and ZnS-SHIL-$Eu(TAA)_4$ are 24.1 % and 40.5 %, respectively, which is determined with integrating sphere to overlap both ZnS-SHIL unit and europium beta-diketonates. Unlike soft hybrids with CdS nanoparticles, the CIE coordinates of CdS-SHIL-$Eu(TAA)_4$ and CdS-SHIL-$Eu(TTA)_4$ are (0.3715, 0.3220) and (0.3390, 0.3102), respectively, both locating in the white region. Especially CdS-SHIL-$Eu(TTA)_4$ possess the pure white luminescence. Therefore, the white luminescence can be achieved by integrating the two components of CdS-SHIL and $Eu(L)_4$. CdS-SHIL-$Eu(TAA)_4$ and CdS-SHIL-$Eu(TTA)_4$ present luminescent quantum yields of 27.5 % and 36.2 %, respectively. The luminescent performance of Ag-SHIL-$3Eu(TAA)_4$ and Ag-SHIL-$Sm(DBM)_4$ soft hybrids with thiol-functionalized ionic liquid bridge possesses tunable luminescent behavior [62]. The luminescent color of Ag_2S-SHIL-$Eu(TTA)_4$ soft material is in white region. To the Ag nanoparticle-based hybrid material, the luminescent color can be controlled through adjustment of each component, even to get white light quite conveniently. To the Ag_2S nanoparticle-based hybrid material, white light can be tuned out only with strong luminescent europium β-diketonate complexes. The result provides the strategy to obtain the white luminescence of soft materials.

SHIL is also linked with resin through condensation reaction between its thiol group and the alkyl chloride of polymer resins (MR, WR) [63]. Both rare earth beta-diketonates and two resins (Merrifield resin (MR) or Wang resin (WR)) can be linked with SHIL. Europium hybrid materials containing terbium ion even reached

28 %. Europium ion can reach higher quantum efficiency bonded with Merrifield resin than with Wang resin which provides clues for the further study on how to improve the luminescent properties of rare earth ions in different substrate or doped system. By changing the form of the rare earth ions and the adjustment of hybrid composition, we can obtain better luminous performance of hybrid materials. Considering the reactivity of mercapto group of SHIL, we try to assemble rare earth polyoxometalate with polymer resin, in which SHIL behaves as linkage through both the exchange reaction with REW_{10} (RE = Eu, Sm) and covalent bonding (condensation reaction) with MR or WR. The CIE diagram of combined excitation and emission spectrum for EuW_{10}-SHIL-WR hybrids shows white luminescence with coordinate (0.3339, 0.2399), which is close to white luminescence. This means that the hybrids under excitation in visible region can obtain the orange/red emission. For the excitation is in visible region, we can observe the close white light from the hybrid system.

8.5 Conclusion and Outlook

In conclusion, recent research progress on the photofunctional rare earth materials based on ionic liquids has been summarized, which mainly consist of two important classes: one is the rare earth compounds dispersed or dissolved in ionic liquids, even including the rare earth compounds of ionic liquids with exact crystal structures; the other is the photofunctional rare earth hybrid materials using ionic liquids both as the chemical linkers and host. However, some problems still exist in the field of photofunctional rare earth materials based on ionic liquids. The first problem is the controlled preparation and fabrication of thin film materials of ionic gels based on luminescent rare earth compounds, which is important and necessary for the further applications in optical devices. The second problem is luminescent enhancement and functional integration of the photofunctional rare earth materials based on ionic liquids. Here it is worth pointing out that it is important to develop visible-excitation lanthanide hybrid system and obtain white luminescence through multicomponent assembly of rare earth species and ionic liquids.

References

1. Binnemans K (2005) Ionic liquid crystals. Chem Rev 105:4148–4204
2. Greaves TL, Drummond CJ (2008) Ionic liquids as amphiphile self-assembly media. Chem Soc Rev 37:1709–1726
3. Plechkova NV, Seddon KR (2008) Applications of ionic liquids in the chemical industry. Chem Soc Rev 37:123–150
4. Parvulescu VI, Hardacre C (2007) Catalysis in ionic liquids. Chem Rev 107:2615–2665
5. Binnemans K (2007) Lanthanides and actinides in ionic liquids. Chem Rev 107:2592–2614

6. Hallett JP, Welton T (2011) Room-temperature ionic liquids: solvents for synthesis and catalysis. 2. Chem Rev 111:3508–3576
7. Nunez NO, Ocana M (2007) An ionic liquid based synthesis method for uniform luminescent lanthanide fluoride nanoparticles. Nanotechnology 18:455606
8. Jacob DS, Bitton L, Grinblat JC et al (2006) Are ionic liquids really a boon for the synthesis of inorganic materials? A general method for the fabrication of nanosized metal fluorides. Chem Mater 18:3162–3168
9. Liu XM, Zhao JW, Sun YJ et al (2009) Ionothermal synthesis of hexagonal-phase $NaYF_4$:Yb^{3+}, Er^{3+}/Tm^{3+} upconversion nanophosphors. Chem Commun 6628–6630
10. Zhang C, Chen J, Zhou YC et al (2008) Ionic liquid-based "all-in-one" synthesis and photoluminescence properties of lanthanide fluorides. J Phys Chem C 112:10083–10088
11. Li CX, Lin J (2010) Rare earth fluoride nano-/microcrystals: synthesis, surface modification and application. J Mater Chem 20:6831–6847
12. Eliseeva SV, Bunzli JCG (2010) Lanthanide luminescence for functional materials and bio-sciences. Chem Soc Rev 39:189–227
13. Le Bideau J, Viau L, Vioux A (2011) Ionogels, ionic liquid based hybrid materials. Chem Soc Rev 40:907–925
14. Li M, Pham PJ, Pittman CU et al (2009) SBA-15-supported ionic liquid compounds containing silver salts: novel mesoporous pi-complexing sorbents for separating polyunsaturated fatty acid methyl esters. Microporous Mesoporous Mater 117:436–442
15. Nakashima T, Nonoguchi Y, Kawai T (2008) Ionic liquid-based luminescent composite materials. Polym Adv Technol 19:1401–1405
16. Feng J, Zhang HJ (2013) Hybrid materials based on lanthanide organic complexes: a review. Chem Soc Rev 42:387–410
17. Hines CC, Cocalia VA, Rogers RD (2008) Using ionic liquids to trap unique coordination environments: polymorphic solvates of $ErCl_3(OH_2)_4$□2([C_2mim]Cl). Chem Commun 226–228
18. Maggini L, Traboulsi H, Yoosaf K et al (2011) Electrostatically-driven assembly of MWCNTs with a europium complex. Chem Commun 47:1626–1628
19. Mudring AV, Tang S (2010) Ionic liquids for lanthanide and actinide chemistry. Eur J Inorg Chem 2569–2581
20. Jensen MP, Neuefeind J, Beitz JV (2003) Mechanisms of metal Ion transfer into room-temperature ionic liquids: the role of anion exchange. J Am Chem Soc 125:15466–15473
21. Guillet E, Imbert D, Scopelliti R et al (2004) Tuning the emission color of europium-containing ionic liquid-crystalline phases. Chem Mater 16:4063–4070
22. Nockemann P, Breuer E, Driesen K et al (2004) Photostability of a highly luminescent europium β-diketonate complex in imidazolium ionic liquids. Chem Commun 4354–4356
23. Babai A, Mudring AV (2005) Anhydrous praseodymium salts in the ionic liquid [bmpyr][Tf_2N]: structural and optical properties of [bmpyr]$_4$[PrI_6][Tf_2N] and[bmyr]$_2$[Pr(Tf_2N)$_5$]. Chem Mater 17:6230–6238
24. Arenz S, Babai A, Binnemans K et al (2005) Intense near-infrared luminescence of anhydrous lanthanide(III) iodides in an imidazolium ionic liquid. Chem Phys Lett 402:75–79
25. Mudring AV, Babai A, Arenz S (2006) Strong luminescence of rare earth compounds in ionic liquids: luminescent properties of lanthanide(III) iodides in the ionic liquid 1-dodecyl-3-methylimidazoliumbis(trifluoromethanesulfonyl)imide. J Alloys Compd 418:204–208
26. Samikkanu S, Mellem K, Berry M et al (2007) Luminescence properties and water coordination of Eu^{3+} in the binary solvent mixture water/1-butyl-3-methylimidazolium chloride. Inorg Chem 46:7121–7128
27. Tang S, Babai A, Mudring AV (2008) Europium-based ionic liquids as luminescent soft materials. Angew Chem Int Ed 47:7631–7634
28. Mallick B, Balke B, Felser C et al (2008) Dysprosium room-temperature ionic liquids with strong luminescence and response to magnetic fields. Angew Chem Int Ed 47:7635–7638

29. Getsis A, Balke B, Felser C et al (2009) Dysprosium-based ionic liquid crystals: thermal, structural, photo- and magnetophysical properties. Cryst Growth Des 9:4429–4436
30. Tang S, Cybinska J, Mudring AV et al (2009) Luminescent soft material: two new europium-based ionic liquids. Helv Chim Acta 92:2375–2386
31. Tang S, Mudring AV (2009) Terbium β-diketonate based highly luminescent soft materials. Eur J Inorg Chem 2769–2775
32. Getsis A, Tang S, Mudring AV et al (2010) A luminescent ionic liquid crystal: $[C_{12}mim]_4[EuBr_6]Br$. Eur J Inorg Chem 2172–2177
33. Getsis A, Mudring AV (2011) Switchable green and white luminescence in terbium-based ionic liquid crystals. Eur J Inorg Chem 3207–3213
34. Lunstroot K, Nockemann P, Hecke KV et al (2009) Visible and near-infrared emission by samarium(III)-containing ionic liquid mixtures. Inorg Chem 3018–3026
35. Pandey S, Baker GA, Sze L et al (2013) Ionic liquids containing fluorinated β-diketonate anions: synthesis, characterization and potential applications. New J Chem 37:909–919
36. Wang D, Wang H, Li H (2013) Novel luminescent soft materials of terpyridine-containing ionic liquids and europium(III). ACS Appl Mater Interfaces 5:6268–6275
37. Driesen K, Nockemann P, Binnemans K (2004) Ionic liquids as solvents for near-infrared emitting lanthanide complexes. Chem Phys Lett 395:306–310
38. Brandner A, Kitahara T, Beare N et al (2011) Luminescence properties and quenching mechanisms of $Ln(Tf_2N)_3$ complexes in the ionic liquid bmpyr Tf_2N. Inorg Chem 50:6509–6520
39. Hopkins T, Goldey M (2009) Tb^{3+} and Eu^{3+} luminescence in imidazolium ionic liquids. J Alloys Compd 488:615–618
40. Getsis A, Mudring AV (2010) Lanthanide containing ionic liquid crystals: $EuBr_2$, $SmBr_3$, $TbBr_3$ and$DyBr_3$ in C_{12}mimBr. Z Anorg Allg Chem 636:1726–1734
41. Devi SV, Maji S et al (2011) Novel room temperature ionic liquid for fluorescence enhancement of Eu^{3+} and Tb^{3+}. J Lumin 131:739–748
42. Puntus LN, Pekareva IS, Lyssenko KA et al (2010) Influence of ionic liquid anion nature on the properties of Eu-containing luminescent materials. Opt Mater 32:707–710
43. Nockemann P, Thijs B, Lunstroot K et al (2009) Speciation of rare-earth metal complexes in ionic liquids: a multiple-technique approach. Chem Eur J 15:1449–1461
44. Li H, Shao H, Wang Y et al (2008) Soft material with intense photoluminescence obtained by dissolving Eu_2O_3 and organic ligand into a task-specific ionic liquid. Chem Commun 18:5209–5211
45. Lunstroot K, Baeten L, Nockemann P et al (2009) Luminescence of LaF_3: Ln^{3+} nanocrystal dispersions in ionic liquids. J Phys Chem C 113:13532–13538
46. Yan Z, Yan B (2013) Luminescent hybrid ionogels functionalized with rare earth fluoride up-conversion nanocrystals dispersing in ionic liquid. Photochem Photobiol 89:1262–1268
47. Yan Z, Yan B, Jia L (2014) Hydrogels immobilized by doped rare earth fluoride nanocrystals: ionic liquid dispersion and down/up-conversion luminescence. Spectro chim Acta A 121:732–736
48. Lunstroot K, Driesen K, Nockemann P et al (2006) Luminescent Ionogels based on europium-doped ionic liquids confined within silica-derived networks. Chem Mater 18:5711–5715
49. Bruno SM, Ferreira RAS, Almeida Paz FA et al (2009) Structural and photoluminescence studies of a europium(III) tetrakis(β-diketonate) complex with tetrabutylammonium, imidazolium, pyridinium and silica-supported imidazolium counterions. Inorg Chem 48:4882–4895
50. Feng Y, Li H, Gan Q et al (2010) A transparent and luminescent ionogel based on organosilica and ionic liquid coordinating to Eu^{3+} ions. J Mater Chem 20:972–975
51. Lunstroot K, Driesen K, Nockemann P et al (2010) Ionic liquid as plasticizer for europium (III)-doped luminescent poly(methyl methacrylate) films. Phys Chem Chem Phys 12:1879–1885

52. Li Q, Yan B (2012) Luminescent hybrid materials of lanthanide β-diketonate and mesoporous host through the covalent and ion bonding with anion metathesis. Dalton Trans 41:8567–8573
53. Li Q, Yan B (2012) Luminescent GaN semiconductor based on surface modification with lanthanide complexes through an ionic liquid bridge. RSC Adv 2:10840–10843
54. Li Q, Yan B (2013) Novel luminescent hybrids by incorporating rare earth β-diketonates into polymers through ion pairing with an imidazolium counter ion. Photochem Photobiol Sci 12:1628–1635
55. Li Q, Yan B (2014) Photophysical properties of lanthanide (Eu^{3+}, Tb^{3+}) hybrid soft gels of double functional linker of ionic liquid modified silane. Photochem Photobiol 90:22–28
56. Li Q, Yan B (2014) Luminescent hybrid nanoparticles prepared by encapsulated lanthanide chelates to the silica microsphere. Colloid Polym Sci 292:1385–1393
57. Cuan J, Yan B (2013) Multi-component assembly and photophysical property of europium polyoxometalates and polymer functionalized (mesoporous) silica through double functional ionic liquid linker. Dalton Trans 42:14230–14239
58. Cuan J, Yan B (2013) Cool-white light emitting hybrid materials of resin-mesoporous silica composite matrix encapsulating europium polyoxometalates through ionic liquid linker. RSC Adv 3:20077–20084
59. Cuan J, Yan B (2014) Photofunctional hybrid materials with polyoxometalates and benzoate modified mesoporous silica through double functional imidazolium ionic liquid linkage. Microporous Mesoporous Mater 183:9–16
60. Yan Z, Yan B (2014) Luminescent lanthanide-polyoxometalates assembling zirconia/alumina/titania hybrid xerogels through task-specified ionic liquid linkage. RSC Adv 4:1735–1743
61. Yan Z, Yan B (2014) Novel photoactive lanthanide complex functionalized hybrid soft xerogels through ionic liquid linkage. New J Chem 38:2604–2610
62. Mei Y, Lu Y, Yan B (2013) Multi-component hybrid soft gels containing Eu^{3+} complexes and MS (M = Zn, Cd) nanoparticles assembled with mercapto- ion liquid linkage: adjustable color and white luminescence. New J Chem 37:2619–2623
63. Mei Y, Yan B (2014) White hybrid soft materials of lanthanide (Eu^{3+}, Sm^{3+}) beta-diketonates and Ag/Ag_2S nanoparticles based with thiol-functionalized ionic liquid bridge. Inorg Chem Commun 40:39–42
64. Mei Y, Lu Y, Yan B (2014) Soft materials composed with lanthanide (Eu^{3+}, Tb^{3+}) beta-diketonates and ZnO nanoparticles through thiol-functionalized ionic liquid bridge to integrate white luminescence. J Photochem Photobiol A Chem 280:1–4
65. Mei Y, Yan B (2014) Photoactive hybrid materials of lanthanide (Eu^{3+}, Tb^{3+}, Sm^{3+}) beta-diketonates and polymer resin through ionic liquid bridge. Photochem Photobiol 90:1462–1466

Chapter 9
Ionic Liquid-Assisted Hydrothermal Synthesis of Rare Earth Luminescence Materials

Yanhua Song, Yuefeng Deng, Ji Chen, and Haifeng Zou

Abstract The shape control of nano- and microcrystals has received considerable attention because the morphology, dimensionality, and size of materials are well known to have great effects on their physical and chemical properties, as well as on their applications in optoelectronic devices. Ionic liquids were found to be very advantageous in synthetic nanochemistry, especially as templates and capping agents. Their particular phase behavior and unique physicochemical properties, including complex solvation interactions with organic and inorganic compounds, can provide various growth pathways for nanocrystals with novel morphologies and properties. This chapter gives an overview of existing ionic liquid-assisted hydrothermal method for the synthesis of rare earth luminescence materials. Particular attention is given to synthesis mechanism and the role of ionic liquids in the formation of specific morphology, as well as the effect of morphology on the luminescent properties.

Keywords Ionic liquids • Hydrothermal synthesis • Rare earth • Luminescent materials

9.1 Introduction

In recent years, rare earth (RE) ion-doped luminescent materials have been extensively investigated due to the fascinating optical characteristics based on their unique intra 4f transitions, which are weakly dependent on the coordination environment

Y. Song (✉) • H. Zou
College of Chemistry, Jilin University, Changchun 130012, China
e-mail: yhsong@jlu.edu.cn

Y. Deng • J. Chen
State Key Laboratory of Rare Earth Resources Utilization, Changchun Institute of Applied Chemistry, Chinese Academy of Sciences, 5625 Renmin Street, Changchun 130022, China

J. Chen (ed.), *Application of Ionic Liquids on Rare Earth Green Separation and Utilization*, Green Chemistry and Sustainable Technology,
DOI 10.1007/978-3-662-47510-2_9

or crystal field (due to the shielding of the 4f orbits by the 5 s and 5p orbits) leading to sharp emission and narrow band [1]. Due to the abundant emission colors based on their $4f \rightarrow 4f$ or $5d \rightarrow 4f$ transitions, RE ions have been playing an irreplaceable role in modern lighting and display fields [2]. The conventional method to prepare luminescent materials is high temperature solid-state reaction. The operation for this method is simple and the cost is relatively low. But this method has some shortcomings, such as energy consumption, irregular morphology, and regrinding leading to the decrease of luminescence and so on. Another commonly used method is chemical precipitation method. The advantage of this method is that the agglomeration of crystal particles can be reduced through controlling the precipitation speed. Thus, nano-/micro-materials with high purity can be prepared. This method is an important method for the synthesis of inorganic powder luminescent materials, but it is not suitable for multicomponent complex system. The third commonly used method is sol-gel method. Compared with the traditional solid-state method, this technique can reduce the temperature dramatically. In addition, some other methods have been created to realize the morphology controllable synthesis of nano-/micro-materials, such as hydro-/solvothermal method, microemulsion, electrostatic spinning, spray pyrolysis, and so on. In these methods, organic additives are usually used to control the structure, which may have negative effects on the environment, and some of the methods are complex. So it is significant to develop more facile and environmentally friendly method to fabricate nano-/micro-luminescent materials. Ionic liquids (ILs) as "environmentally friendly" solvents with designable structures have attracted worldwide attention due to their potential applications in synthesis, catalysis, separation, electrochemistry, and nanochemistry. Owing to their excellent physicochemical properties and multiple functions, they play key roles in the fields of chemistry and materials science. For the synthetic chemistry, ILs mainly play the following roles: solvent, template, reactant, and surface modification reagent. Sometimes, ILs play multiple roles and the synthesis system can be simplified. Microwave synthesis is the most efficient and least time-consuming procedure. In that context, ionic liquids are specifically advantageous. Ionic liquids are highly susceptible to microwave irradiation because of their ionic character and high polarizability. Due to the direct energy transfer to the reactive species, improved yields, cleaner products, and even different reaction outcomes and thus new materials can be obtained [3]. So some nano-/micro-materials were prepared through ionic liquid-assisted microwave methods [3, 4]. Hydrothermal treatment as a typical solution approach has proven to be an effective and convenient process in preparing various inorganic materials with a variety of controllable morphologies and architectures [5]. Combined with the advantages of hydrothermal method and ionic liquids, a large number of rare earth materials with various morphologies and novel luminescent properties have been synthesized.

9.2 "All-in-One" Synthesis and Photoluminescence Properties of Rare Earth-Related Materials

Nanocrystals of lanthanide fluoride and lanthanide-doped fluoride (LaF_3, EuF_3, CeF_3, $NaYF_4$, $NaYF_4$:Er,Yb, CeF_3:Tb, LaF_3:Eu, CaF_2:Ce,Mn, etc.) arouse intense interest because of their potential applications in amplifiers for fiber optics communication, light sources for zero-threshold lasers, displays, light-emitting diodes (LEDs), lubricants, biological fluorescence labeling, NMR and MRI relaxation agents, catalysis field, and so on. In previous reports, the main synthesis routes were wet chemical routes including the hydrothermal method, microemulsion, the microwave method, the single-source precursor route, the ultrasonic method, and so on. The fluorine sources commonly used were HF, NaF, or NH_4F, so additional templates or structure directors were necessary. Although high-quality products can be obtained from thermal decomposition of the precursors, the rigorous reaction conditions must be considered. Although some meaningful work in these fields has been reported, there are still great efforts to make to simplify the route and improve the yields and quality. It was also important to obtain lanthanide fluoride nanostructures with interesting luminescent properties. In this "all-in-one" system, the ILs act as solvents and templates, as well as a fluorine source. Uniform and novel LaF_3, CeF_3, PrF_3, NdF_3, SmF_3, EuF_3, LaF_3:Eu^{3+}, CeF_3:Tb^{3+} nanodisks, and donut-shaped nanostructures were successfully synthesized in these systems with a large scale (Fig. 9.1). In that work, 1-octyl-3-methylimidazolium hexafluorophosphate ($OmimPF_6$), 1-octyl-3-methylimidazolium tetrafluoroborate ($OmimBF_4$), and 1-butyl-3-methylimidazolium hexafluorophosphate ($BmimPF_6$) were introduced to prepare uniform RE fluoride nanocrystals [6].

Research on the phase behavior of binary mixtures of ILs with alcohols has attracted much attention for the further applications of ILs [7, 8]. In this work, ethanol was used as a cosolvent to promote the solubility of Ln^{3+} and then formed macroscopic homogeneous solution with the ILs. Although ethanol was not a reaction agent, it did affect the morphologies and dispersility of the products. It was found that the uniformity and dispersility of the products decreased with the increasing of the volume ratios of ethanol to ILs. Figure 9.2 exhibits the morphologies of the products synthesized with different ratios of ethanol to ILs. As can be seen, the morphology of as-prepared CeF_3 nanocrystals changes from uniform disk-like shape to distort and aggregate with the increase of the ratio. Although the same reaction and collection processes were performed, the sample shown in Fig. 9.2a was difficult to disperse well. When the ratio was further improved to 0.3, aggregated flower-like nanostructures (Fig. 9.2b) formed. It could be clearly seen that they were derived from the regular and irregular nanodisks. It was found that, at a value of about 0.08, the as-prepared nanocrystals exhibited regular disk-like shapes and good dispersility.

ILs have designer properties due to their alterable structures. It was well known that the alkyl chain on an imidazole ring greatly affects the physical and chemical properties of dialkylimidazolium-based ILs, such as hydrophobicity, viscosities,

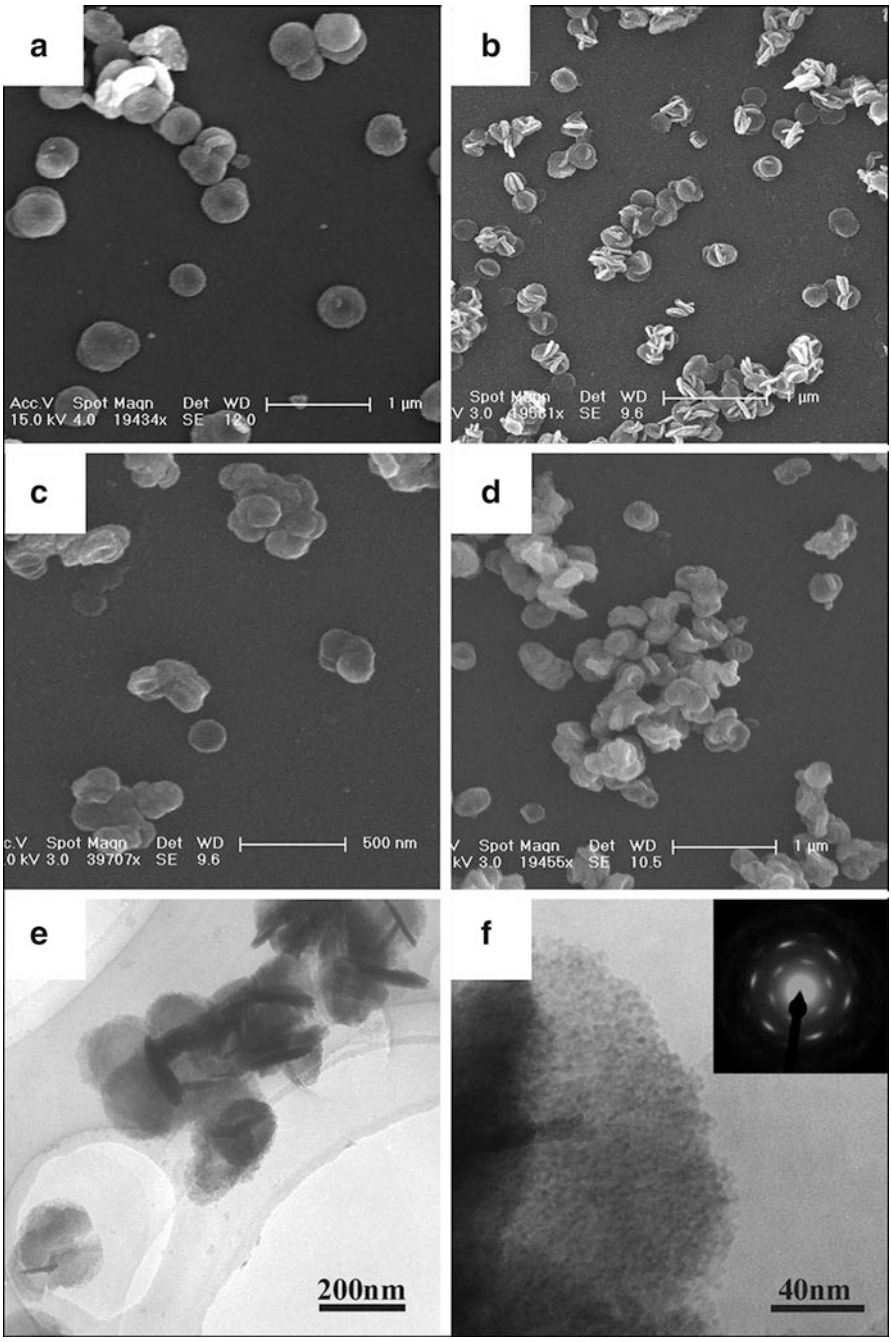

Fig. 9.1 SEM images of the as-prepared nanocrystals: LaF_3 (**a**), CeF_3 (**b**), NdF_3 (**c**), EuF_3 (**d**), and TEM images of CeF_3 (**e**, **f**) (Reprinted with the permission from Ref. [6]. Copyright 2008 American Chemical Society)

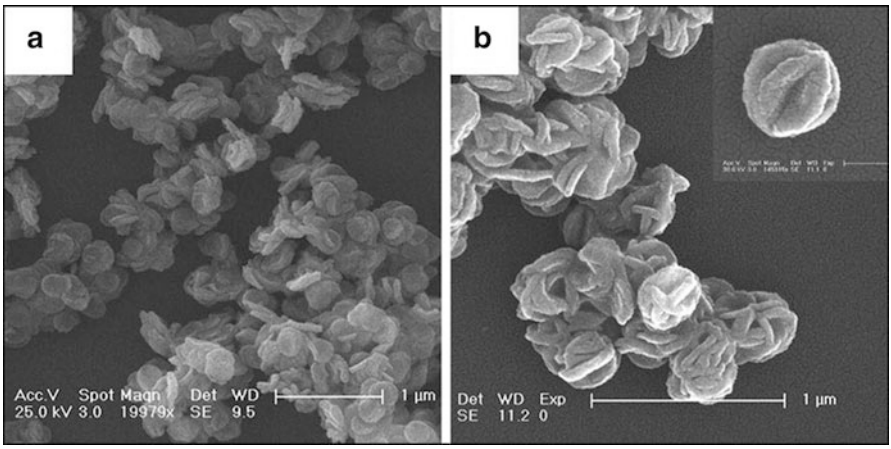

Fig. 9.2 SEM images of CeF_3 prepared in different ethanol volumes: 2 mL (**a**); 3 mL (**b**) (Reprinted with the permission from Ref. [6]. Copyright 2008 American Chemical Society)

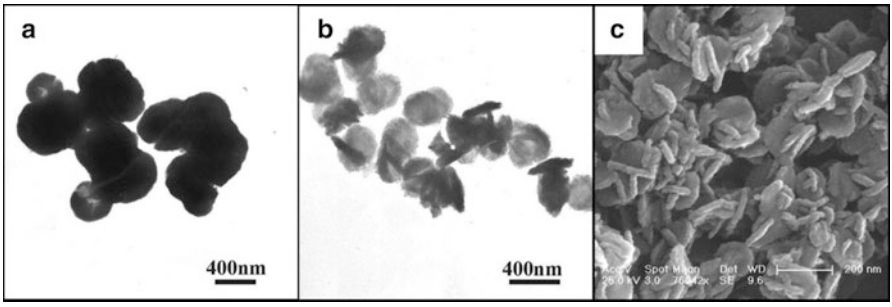

Fig. 9.3 LaF_3:Eu^{3+} nanocrystals prepared in $BmimPF_6$ (**a**), $OmimPF_6$ (**b**), and CeF_3 nanodisks prepared in $OmimBF_4$ (**c**) (Reprinted with the permission from Ref. [6]. Copyright 2008 American Chemical Society)

densities, conductivities, and so on. The phase behavior of binary mixtures of ILs and ethanol was also influenced by the length of alkyl chains. In this work, the morphologies of the final nanocrystals made in the ILs with different alkyl chain lengths were varied. Figures 9.3a, b display the TEM and SEM images of LaF_3:Eu^{3+} nanocrystals synthesized in $BmimPF_6$ and $OmimPF_6$ under the same conditions. In $BmimPF_6$ systems, the as-prepared nanocrystals were donut shaped with the sizes from 200 to 600 nm. It seems that the longer alkyl chains of the cations are in favor of the uniformity of the nanocrystals in their work.

Dialkylimidazolium-based tetrafluoroborate and hexafluorophosphate were the most studied ILs because of their facile preparation and purification process. It was well known that these anions would be degraded when contacted with moisture or exposed to microwaves, heat, and so on. Although the two anions all could produce F^- in the process of degradation, there was still a difference in the final products.

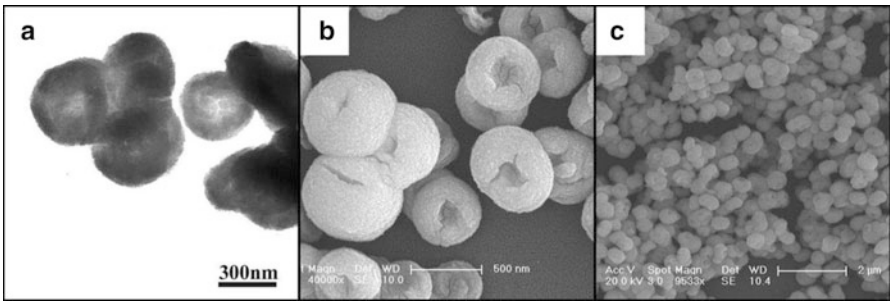

Fig. 9.4 TEM and SEM images of CeF_3:Tb^{3+} nanocrystals prepared in $OmimPF_6$ (Reprinted with the permission from Ref. [6]. Copyright 2008 American Chemical Society)

Figure 9.3c displays the morphologies of CeF_3 nanocrystals synthesized in $OmimBF_4$. Contrasted to those synthesized in $OmimPF_6$ (shown in Fig. 9.1b), the uniformity of them remarkably decreased. The most products were aggregated fragments of nanodisks.

Figure 9.4a–c displays the TEM and SEM images of Tb^{3+}-doped CeF_3 nanocrystals with interesting donut shapes. Observation from the TEM images indicates that the uniform donut-shaped nanostructures also consisted of little nanoparticles. In contrast to the CeF_3 nanodisks, the donut-shaped CeF_3: Tb^{3+} nanocrystals were much larger.

Ji Chen et al. also discussed the formation mechanism of rare earth florides in ionic liquid system. It was well known that PF_6^- hydrolyzes to produce F^-, HF, POF_3, and so on [9]; BF_4^- hydrolyzes to form F^-, $HOBF_3^-$, HF, and H_3BO_3 [10–12] under proper conditions. Although no additional water was added into the system, the anions in the mixture were also hydrolyzed as a result of the trace water and hydration water of $Ln(NO_3)_3 \cdot 6H_2O$. Contrasted to the simple experimental processes, the situations of the Ln^{3+} located in the systems were quite complex. In the systems, coulombic force, van der Waals interaction, and hydrogen bonds were coexistent [8, 13]. Molecular dynamic simulations of ILs gave many valuable conclusions about the salvation of Ln^{3+} in RTILs [14, 15]. The behavior of the lanthanide ions and ILs has been studied through quantum calculations. PF_6^- can coordinate the metal in a monodentate or polydentate faction fashion [8]. When the ethanol solution containing RE (III) ions was dispersed in the ILs, the Ln^{3+} ions were surrounded first by the PF_6^- or BF_4^- anions, and the first shell was surrounded by imidazolium cations. At the same time, the NO_3^- ions were surrounded by a rigid "cage" of imidazolium cations [8, 12]. Thus, all the Ln^{3+} ions were in the same chemical environments, and the ILs acted as a coordinate solution. When the vials containing the mixture were heated continuously, some PF_6^- ions were degraded and brought F^- and then formed LnF_3 grains. Subsequently, the IL-stabled particles aggregated to form secondary structures through the "nonclassical crystallization" processes.

Subtle diversifications emerged when Ce^{3+} and Tb^{3+} coexisted in the reaction systems because of their different sizes and coordinations. After the homogeneous nucleation, the IL-stabled Tb^{3+}-doped CeF_3 nanoparticles exhibited quite different self-assembly behaviors from the IL-stabled pure CeF_3 nanoparticles. In this situation, the disk-shaped nanostructures became bent and stacked layer by layer, and the stack structures could still be observed among the final products. A donut-shaped structure could be developed because of the stacking efficiency, where an inner field effect within the crystal proposed by Colfen may take effect. Ethanol, as the cosolvent, indeed affected the assemble process. The viscosities of the systems decreased greatly with the increase of ethanol contents. It seemed that the self-assembly was strongly affected by the viscosities and then affected the final morphologies. The viscosities of $BmimPF_6$, $OmimPF_6$, and $OmimBF_4$ at 20 °C were 308.3, 857.4, and 135.0 mPa · s, respectively [16]. Improving the systems' viscosities seemed to favor the formation of uniform nanodisks.

The photoluminescent properties of LaF_3:Eu^{3+} and CeF_3:Tb^{3+} have been discussed. Figure 9.5 shows the room temperature emission spectra of Eu^{3+}-doped LaF_3 nanodisks synthesized in $BmimPF_6$ systems with different doped concentrations (5, 10, 12.5 %). The emission intensity increased along with the doped concentrations from 5 to 12.5 % and reached the maximum at 12.5 %. Above the doped concentration of 12.5 %, concentration quenching occurred. The weak emission peak located near 550 nm was due to $^5D_1$ to ^7F_j levels. The La^{3+} ion in LaF_3 was at a site of $C2$ symmetry, because electric and magnetic dipole transitions were both allowed. Both $^5D_0$-$^7F_1$ and $^5D_0$-$^7F_2$ can be observed. It is well known that the $^5D_0$-$^7F_2$ transition is sensitive to the lattice environment, while the $^5D_0$-$^7F_1$

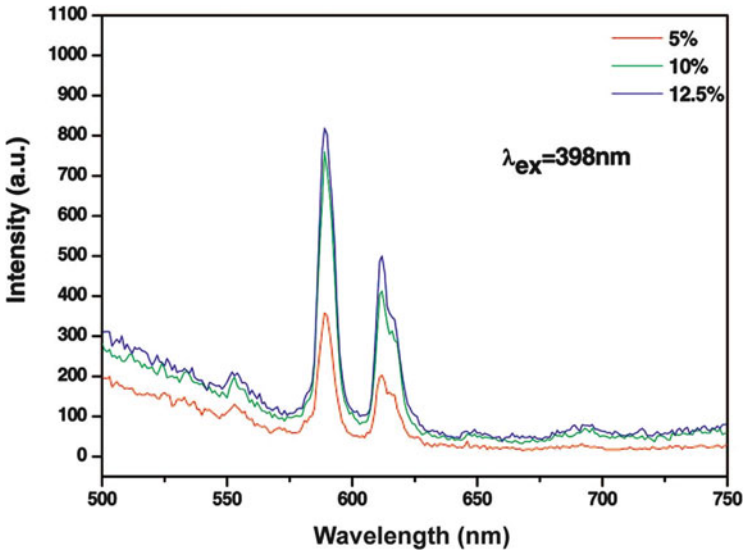

Fig. 9.5 Emission spectra of Eu^{3+}-doped LaF_3 nanocrystals synthesized in $BmimPF_6$ (Reprinted with the permission from Ref. [6]. Copyright 2008 American Chemical Society)

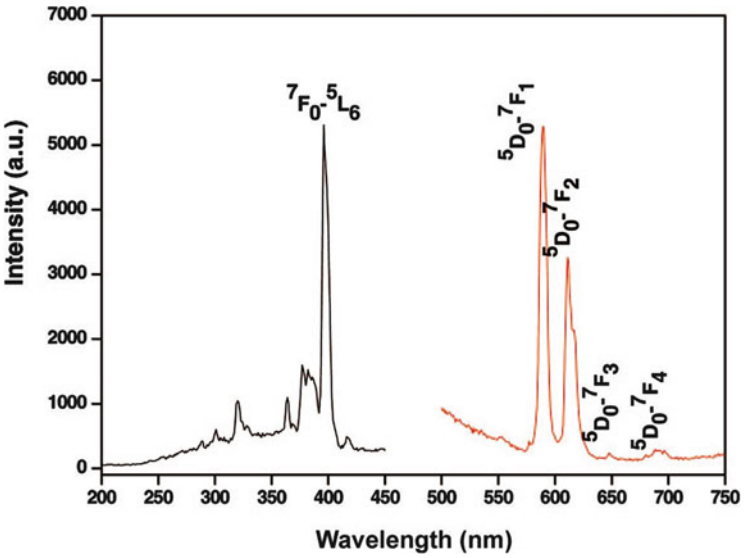

Fig. 9.6 Excitation and emission spectra of $La_{0.9}Eu_{0.1}F_3$ nanocrystals synthesized in $OmimPF_6$ (Reprinted with the permission from Ref. [6]. Copyright 2008 American Chemical Society)

transition is not. The ratio of the two intensities was a good measure for the symmetry of the Eu^{3+} site. The relative intensities of the $^5D_0$-$^7F_1$ and $^5D_0$-$^7F_2$ peaks were similar to those of previous articles, confirming that Eu^{3+} ions were located in the La^{3+} crystal site with C_2 symmetry [17, 18].

Figure 9.6 shows the excitation and emission spectra of the $Eu_{0.1}La_{0.9}F_3$ nanocrystals synthesized in the $OmimPF_6$ systems. In the excitation spectrum, the characteristic absorption peaks of Eu^{3+} are ascribed to the direct transition from the ground state of europium into the higher state of f electrons. The most intense peak was located at 396 nm. Although they had different morphology sizes than that synthesized in $BmimPF_6$, there were no notable shifts in the positions of the emission peaks compared to the Eu^{3+}-doped systems, because of the crystal field shield effect of $5s^25p^6$. There were distinct differences in the relative intensity ratios of the $^5D_0$-$^7F_1$ to $^5D_0$-$^7F_2$ transition between the nanocrystals synthesized from the two systems. The intensity ratio of $^5D_0$-$^7F_2$ to $^5D_0$-$^7F_1$ transition changed in contrast to those prepared in $BmimPF_6$ systems. Their difference could also be observed when they were exposed to UV irradiations. It was known that structures, sizes, shapes, and capping agents of the nanocrystals affected the luminescence properties. It is also believed that the surface of the nanocrystals had a major influence on the luminescence properties due to the large surface to volume ratio. Relative to the nanocrystals synthesized in $BmimPF_6$, the nanodisks synthesized in $OmimPF_6$ had higher surface Eu^{3+} concentrations and resulted in less symmetry and increasing $^5D_0$-$^7F_2$ transition intensity. Just as that shown in Figure 9.6, the

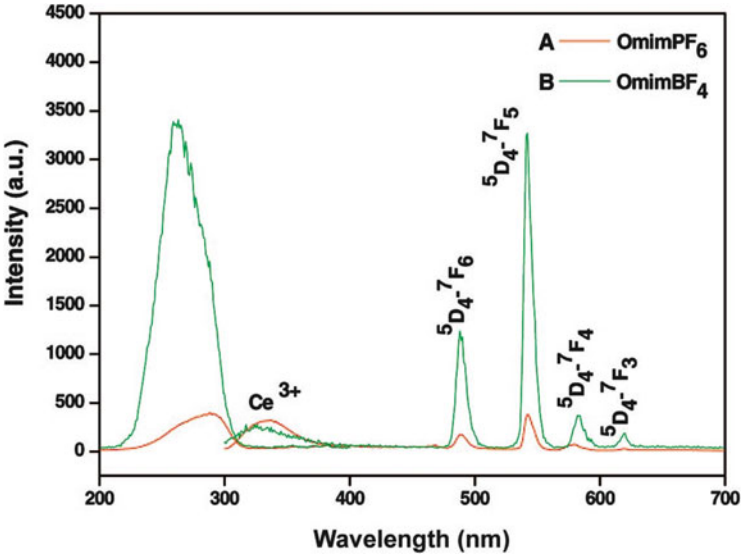

Fig. 9.7 Excitation and emission spectra of $Ce_{0.9}Tb_{0.1}F_3$ nanocrystals synthesized in $OmimPF_6$ and $OmimBF_4$ (Reprinted with the permission from Ref. [6]. Copyright 2008 American Chemical Society)

nanocrystals synthesized in $OmimPF_6$ systems had relatively higher R/O ratios and narrower half-maximum widths.

Figure 9.7 displays the excitation and emission spectra of $Ce_{0.9}Tb_{0.1}F_3$ nanocrystals prepared in $OmimPF_6$ (A) and $OmimBF_4$ (B), respectively. In the emission spectra of B, observed characteristic emission (486, 542, 587, and 619 nm) of Tb^{3+} ions between the excited $^5D_4$ state and the ^7F_J ($J = 6, 5, 4, 3$) ground state was in accordance with previous reports [19–21]. The weak emission peak of Ce^{3+} indicated the energy transfer from Ce^{3+} to Tb^{3+}. However, for the nanocrystals prepared in $OmimPF_6$, the luminescence properties were quite different. In contrast to that of B, the excitation spectrum had notable red shift. The emission intensity of Tb^{3+} was not stronger than that of Ce^{3+}. In contrast to that of B, the emission intensity of Tb^{3+} was much lower. It was speculated that a very small quantity of Ce^{3+} and Tb^{3+} could be oxidized to Ce^{4+} and Tb^{4+} in the $OmimPF_6$ system, which was the killer of the emission. But in the $OmimBF_4$ system, the Ce^{4+} and Tb^{4+} were suppressed by the H_3BO_3 stem from the BF_4^-. Therefore, the two nanocrystals synthesized in $OmimPF_6$ and $OmimBF_4$ systems exhibited different luminescent properties. The donut-shaped CeF_3:Tb^{3+} nanostructures were also new candidates for redox luminescent switches [22].

X. Kong et al. reported the controlled synthesis, formation mechanism, and upconversion luminescence of $NaYF_4$:Yb,Er nano-/submicrocrystals via ionothermal approach, where hydrophilic ionic liquids ([Emim][BF_4], [Bmim]

[BF_4], and [Omim]BF_4) were used as solvents, templates, as well as fluorine source. They illustrated that the morphology and size of the product can be tuned by the properties of ILs, such as viscosities, polarity, solvency, and interfacial tension [23].

Yanhua Song et al. synthesized CaF_2:Ce^{3+}/Mn^{2+} submicrocubes and nanospheres through an ionic liquid-based hydrothermal method. OmimPF_6 and OmimBF_4 were utilized to introduce a new fluoride source and act as templates. The effects of ionic liquid amount and species on the morphologies and sizes of the nanocrystals have been studied [24].

The typical SEM and TEM images for CaF_2 synthesized with OmimPF_6 show that the CaF_2 sample consists of a large quantity of submicrocubes with good uniformity and monodispersity. These submicrocubes have a length between 300 and 400 nm. The SAED pattern of a submicrocube shows the regular diffraction spots and rings, confirming that the uniform submicrocubes are polycrystalline. The effects of volume ratios of OmimPF_6 to ethanol on the morphology of samples were discussed. The product synthesized with 2 mL OmimPF_6 exhibits nonuniform distribution and agglomerates to some extent. When 10 mL OmimPF_6 are introduced into the reaction system, the products are monodispersed quasi submicrocubes with length between 300 and 400 nm. The edge of the cube is not very clear. When the amount of OmimPF_6 increases to 15 mL, the component of the structure is mainly cubes with edge length of about 300 nm. The OmimPF_6 is expected to be decomposed into some chemical species under the hydrothermal reaction conditions. Therefore, OmimPF_6 and their decomposed products could selectively absorb onto the surfaces of CaF_2 seeds, facilitating the preferential growth of some specific crystalline planes. With low amount of OmimPF_6, the micro-environment for the CaF_2 nuclei might be isotropic or the effect of the absorbed species is not significant, which facilitates the isotropic growth of CaF_2 particles, leading to the formation of irregular particles. When the amount of OmimPF_6 increases, the role of absorbed species on the crystalline planes is significant, leading to the anisotropic growth; hence, the submicrocubes are formed. In order to check the influence of the ionic liquid in the synthesis of CaF_2 particles, ILs with different anions have been used. Besides the hexafluorophosphate, the tetrafluoroborate anion is able to release fluoride in heat or in the presence of water. The sample synthesized with OmimBF_4 is composed of uniform nanospheres with average diameter about 30 nm. The surface roughness observed may be caused by the irritation of the high-energy electron beam because the adsorbed organic groups are quite unstable. Comparing the FT-IR spectra of the samples synthesized with OmimPF_6 and OmimBF_4, it is shown that there are additional two absorption bands at 1,564 and 1,464 cm^{-1} for the sample synthesized with OmimBF_4 as F^- source, which are attributed to the vibration of imidazolium ring, confirming that the surface of the CaF_2 nanospheres is coated by imidazolium compounds.

Figure 9.8 shows the excitation and emission spectra of the Ce^{3+} and Mn^{2+} co-doped CaF_2 phosphor. The excitation spectrum monitored by the Mn^{2+} emission is consistent with the excitation band monitored by Ce^{3+} emission, which means that an efficient energy transfer occurs from the Ce^{3+} to Mn^{2+} ions. Excitation into

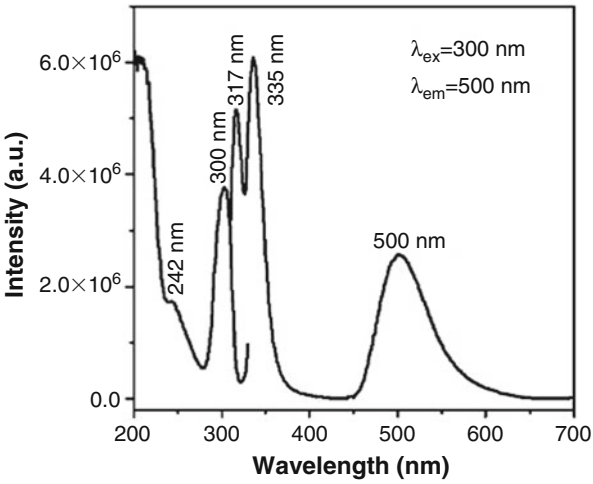

Fig. 9.8 Excitation and emission spectra of CaF_2: Ce^{3+},Mn^{2+} (Reprinted from Ref. [24], with permission from Springer Science + Business Media)

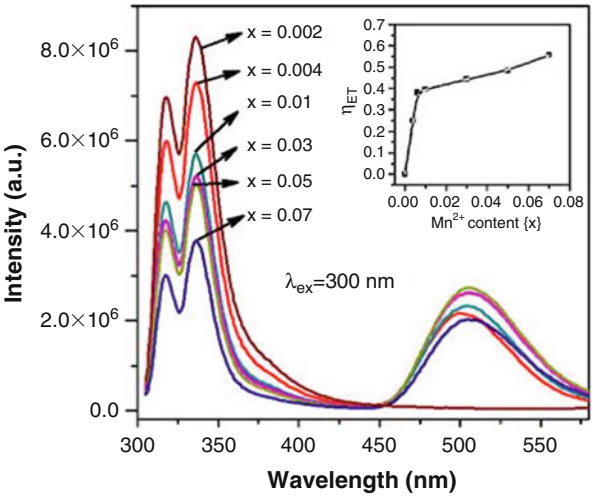

Fig. 9.9 Emission spectra of CaF_2: $0.01Ce^{3+}$,xMn^{2+} ($\lambda_{ex} = 300$ nm). Inset is the dependence of the energy transfer efficiency η_{ET} on Mn^{2+} content(x) (Reprinted from Ref. [24], with permission from Springer Science + Business Media)

the Ce^{3+} band at 300 nm yields both the emissions of Ce^{3+} (300–350 nm) and Mn^{2+} (500 nm) ions, which is a further indication of energy transfer from Ce^{3+} to Mn^{2+} ions in CaF_2:Ce^{3+}, Mn^{2+} submicrocubes.

Figure 9.9 shows the emission spectra of CaF_2:$0.01Ce^{3+}$, xMn^{2+} measured under the excitation wavelength of 300 nm. With the Mn^{2+}-concentration increasing, the emission intensity of the Mn^{2+} ions increases systematically and reaches saturation when x is 0.05, whereas the intensity of the Ce^{3+} ions simultaneously decreases from $x = 0.002$ to 0.07. These results indicate that the efficient energy transfer

occurs from the Ce^{3+} to Mn^{2+} ions. The emission intensity decrease of the Mn^{2+} ions beyond $x = 0.05$ can be attributed to the concentration quenching of the Mn^{2+} ions. The energy transfer efficiency from Ce^{3+} to Mn^{2+} ions can be calculated according to the formula $\eta_{ET} = 1 - I_S/I_{S0}$, where I_S and I_{S0} are the corresponding integrated luminescence intensities of the donor (Ce^{3+}) in the presence and the absence of the acceptor (Mn^{2+}), respectively. The η_{ET} was calculated as a function of Mn^{2+} concentration x and represented in inset of Fig. 9.9. The energy transfer efficiency (η_{ET}) increases gradually from $x = 0$ to 0.07 and reaches to 0.62 when Mn^{2+} content is 0.07.

$Ca_5(PO_4)_3Cl$:Ce,Tb straw-like sheaves and microrods were synthesized via an ionic liquid-based hydrothermal method. The ionic liquid [Omim]Cl was utilized to introduce a new chloride source. The influences of the ionic liquid amount and reaction time on the final products were investigated in detail [25].

The representative SEM images of the samples synthesized with different amounts of [Omim]Cl show that when the amount of [Omim]Cl was 5 mL, the products are of a bundle of filamentary crystals banded in the middle and fanned out from the middle to two ends to form sheaf-like morphology with a length of 2.0 μm. As the content of [Omim]Cl was increased to 7 and 9 mL, besides the sheaves, another morphology, microrods appeared. When the content of [Omim]Cl increased to 10 mL, the sheaves disappeared. The SEM image reveals that the sample was composed on a large scale of $Ca_5(PO_4)_3Cl$:Ce,Tb microrods in nearly 100 % morphological yield. The high-magnification SEM image illustrates that the microrods have an average size of 200 nm in diameter and 1.5 μm in length.

The XRD patterns of the products corresponding to different reaction stages reveal that the samples display distinctively different XRD patterns at different reaction times. The sample obtained before $t = 2$ h shows a unique XRD pattern due to pure triclinic $CaHPO_4$ phase (JCPDS No. 090080). When the reaction time increased to 6 h, a new $Ca_5(PO_4)_3Cl$ phase emerged in addition to the $CaHPO_4$ phase. This indicated that the samples transformed partially from $CaHPO_4$ to $Ca_5(PO_4)_3Cl$ phase with reaction time prolongation. With the further reaction, from 6 to 24 h, the fraction of $Ca_5(PO_4)_3Cl$ phase increased remarkably. As the reaction time extended to 24 h, the $CaHPO_4$ phase disappeared completely, and only the $Ca_5(PO_4)_3Cl$ phase existed. The FT-IR spectra also confirmed the transformation process. For the sample synthesized at $t = 30$ min, the broad band at 3,410 cm^{-1} is assigned to ν (O–H). Furthermore, three broad bands between 3,000 and 1,500 cm^{-1} can be attributed to hydrogen bridge bonds. The bands at 1,132, 1,071, 999, and 896 cm^{-1} arising from PO stretches localize mainly in the PO_3 fragment. The band at 896 cm^{-1} is attributed to the P–O(H) stretch. With the prolongation of the reaction time, the absorption peaks of PO_3 group and P–O (H) become weaker and disappeared when the reaction time is 24 h. These characterized FT-IR spectra further confirm the transformation from $CaHPO_4$ to $Ca_5(PO_4)_3Cl$.

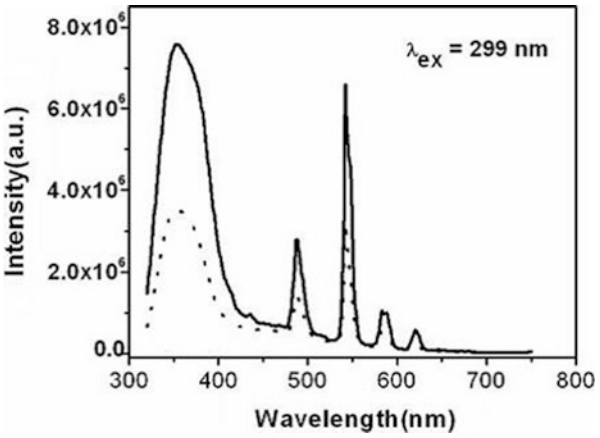

Fig. 9.10 Emission spectra of the $Ca_5(PO_4)_3Cl:Ce^{3+}$, Tb^{3+} sheaves and microrods obtained under the same reaction conditions (Reprinted from ref. [25], with permission from Springer Science + Business Media)

From the comparative emission spectra of the as-obtained $Ca_{4.96}(PO_4)_3Cl:Ce^{3+}{}_{0.02},Tb^{3+}{}_{0.02}$ sheaves and the microrods (Fig. 9.10), it can be seen that the two samples show similar spectral patterns without any emission band shift, but one can clearly observe that the nanorods have a higher PL intensity than sheaves. It is well known that surface area of materials increases along with decrease in size. The larger the surface area is, the more defects will be introduced into the phosphor crystal. Defects have a serious drawback in PL intensity for phosphors as they provide nonradiative recombination routes for electrons and holes. In addition, the complication of the morphology of the sheaf-like hierarchical architectures reduces the luminescence efficiency by reflecting part of the luminescence in the inner part of the architectures, which leads to the absorption of the defects in the sheaf-like hierarchical architectures. So the luminescence intensity of $Ca_{4.96}(PO_4)_3Cl:Ce^{3+}{}_{0.02},Tb^{3+}{}_{0.02}$ microrods is higher than that of the $Ca_{4.96}(PO_4)_3Cl:Ce^{3+}{}_{0.02}$, $Tb^{3+}{}_{0.02}$ sheaves.

Furthermore, there were some other literatures reporting the nano- or micro-fluoride materials with versatile morphology synthesized through ionic liquid-based hydrothermal method [26, 27].

9.3 Ionic Liquid Microemulsion

Microemulsions, isotropic liquid mixtures of oil, water, and surfactant, frequently in combination with a cosurfactant, were stable. In the binary systems (water/surfactant or oil/surfactant), different types of self-assembled structures can be formed, providing excellent templating systems to synthesize monodispersed nanocrystals with controllable size and morphology [28]. Recently, imidazolium-based ILs had been explored and used as solvents of the inner phase, or continuous

outer phase, or surfactants in the formation of microemulsion systems [29–33]. Research was also conducted to study the behavior of ILs in microemulsion systems [34–36]. As an example, the aggregation of some imidazolium-based ILs in aqueous solutions was observed, indicating the similarity to surfactants [37, 38]. The polarity and solvation properties of ILs could be easily modified due to their diverse functional groups and structures, facilitating the formation of microemulsions with desired properties.

Ji Chen et al. reported a novel tributylphosphate/1-octyl-3-methylimidazolium halide/water (TBP/[Omim]Cl/H_2O) microemulsion system, and this system was used to synthesize RE phosphate nanocrystals. Uniform nanoparticles and one-dimensional nanowires of $REPO_4$, $REPO_4{\cdot}xH_2O$(RE = La, Ce, Pr, Nd, Sm, Eu, Gd, Tb), and RE ion-doped $REPO_4{\cdot}xH_2O$ were successfully made. Moreover, the surfaces of the as-prepared nanocrystals were capped with TBP, leading to the enhancement of their luminescence and facilitation of their dispersion in some imidazolium-based ILs [39]. This is the first "oil-in-water" microemulsion system with ILs as surfactant and without any cosurfactants for the formation of nanocrystals. This strategy is expected to be applicable for the synthesis of other RE salt nanocrystals, like vanadates and fluorides.

Both hexagonal and monoclinic phase of RE phosphates can be controllably synthesized when changing the reaction temperature. The hexagonal phase of $REPO_4{\cdot}xH_2O$ (RE = La-Tb) nanocrystals was obtained at 100 °C. When the reaction temperature was raised to 150 °C, monoclinic $REPO_4$ nanocrystals were obtained. The XRD patterns shown in Figs. 9.11 and 9.12 indicate that the $REPO_4{\cdot}xH_2O$ (RE = La-Nd and Sm-Tb) nanocrystals were in pure hexagonal phase (their JCPDS numbers are 46-1439, 35-0614, 23-1202, 50-0620, 34-0537, 20-1044, 39-0232, and 20-1244, respectively). No peaks of any other phases or impurities were detected. Compared to light RE phosphates (RE = La-Nd), the XRD patterns of $REPO_4{\cdot}xH_2O$ nanocrystals (Sm-Tb) exhibited sharp and narrow peaks, indicating their highly crystalline nature.

The size and morphologies of the as-prepared structures were studied using SEM and TEM. Figure 9.13a shows the low-magnification TEM images of the $CePO_4 \cdot H_2O$ nanowires. The HRTEM image (shown in Fig. 9.13b) taken from a single nanowire showed the lattice spacing of 2.82 Å, which can be indexed to the (102) lattice space of $CePO_4 \cdot H_2O$. Under HRTEM (shown in Fig. 9.13c), the $CePO_4 \cdot H_2O$ nanowires appear as a single crystal with a lattice spacing of 3.01 Å between two adjacent lattice planes parallel to the long axis, which was in good agreement with the theoretical d-spacing for (200) planes of hexagonal $CePO_4 \cdot H_2O$. The HRTEM image shown in Fig. 9.13d displayed the clearly resolved planes of (200) and (102). The inset was the fast Fourier transform (FFT) analysis over the nanowire. The long axis of the nanowire was parallel to the {200} facets with an angle of 27.8° to the [102] direction, indicating the nanowires growing along the c axis. This is in very good agreement with the strong intensity of the (200) peak and (102) peak in the XRD patterns. According to the same hexagonal phase structures and synthetic conditions, it can be speculated that the other seven $REPO_4 \cdot xH_2O$ nanowires grew along the c axis.

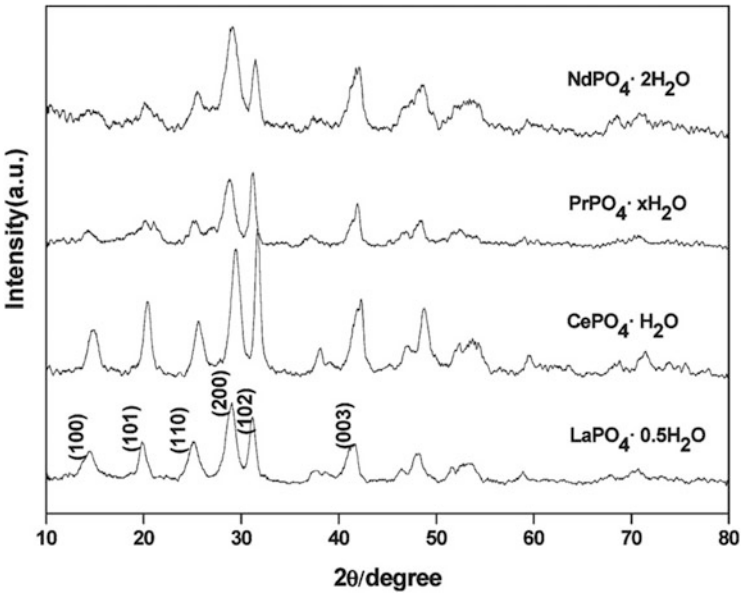

Fig. 9.11 XRD patterns of $REPO_4 \cdot xH_2O$ nanocrystals (RE = La to Nd) (Reprinted with the permission from Ref. [39]. Copyright 2009 American Chemical Society)

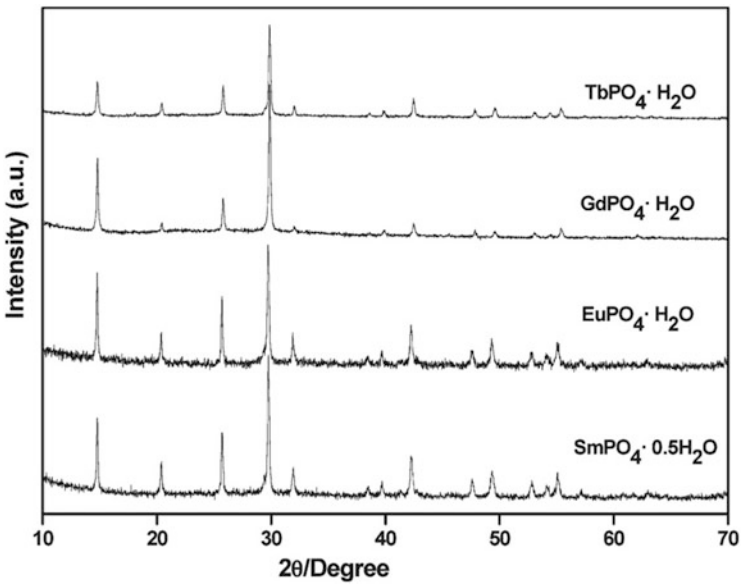

Fig. 9.12 XRD patterns of $REPO_4 \cdot xH_2O$ nanocrystals (RE = Sm to Tb) (Reprinted with the permission from Ref. [39]. Copyright 2009 American Chemical Society)

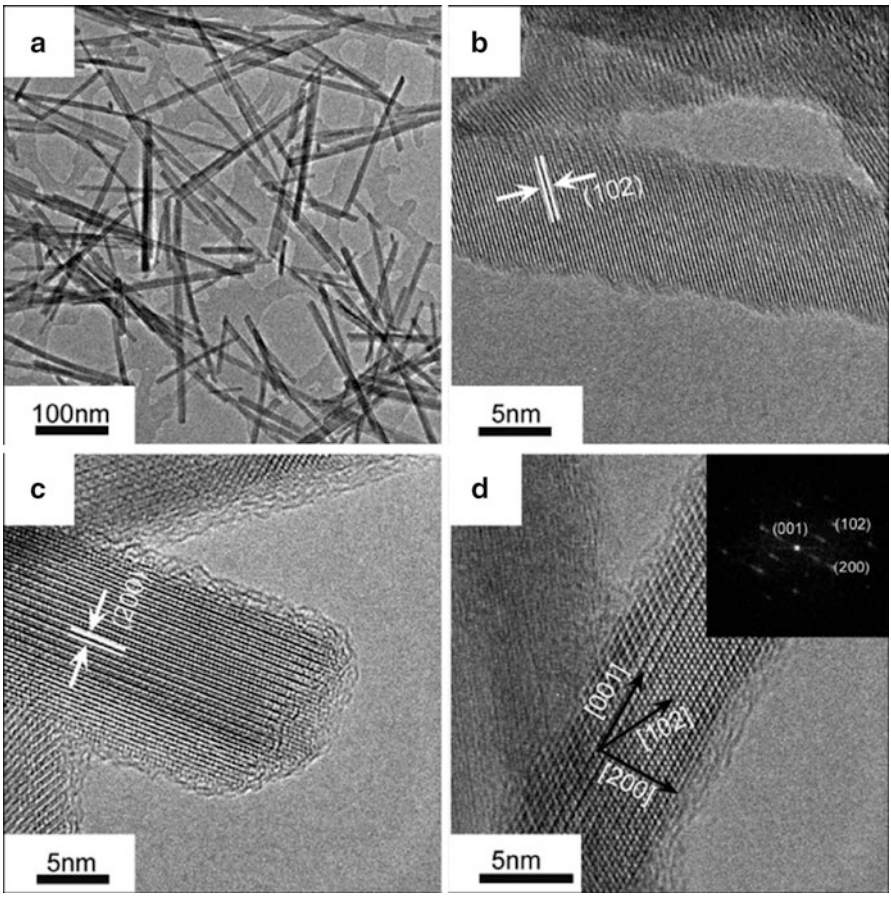

Fig. 9.13 TEM and HRTEM images of $CePO_4 \cdot H_2O$ nanowires: (**a**) low-magnification image and (**b**, **c**, **d**) HRTEM images of an individual nanowire (Reprinted with the permission from Ref. [39]. Copyright 2009 American Chemical Society)

Figure 9.14 showed the SEM images of hexagonal phase $LaPO_4 \cdot 0.5H_2O$, $CePO_4 \cdot H_2O$, $SmPO_4 \cdot 0.5H_2O$, $EuPO_4 \cdot H_2O$, $GdPO_4 \cdot H_2O$, and $TbPO_4 \cdot H_2O$, respectively. As shown in Fig. 9.14a, b, the uniform $LaPO_4 \cdot 0.5H_2O$ and $CePO_4 \cdot H_2O$ nanowires were about 200–500 nm in length, and their diameters were about 5–15 nm. From La to Nd, the RE phosphate hydrate nanowires had similar sizes and morphologies. But from Sm to Tb, the nanowires (shown in Fig. 9.14c–f) had different sizes. Compared to the light RE phosphate hydrates (La to Nd), $SmPO_4 \cdot 0.5H_2O$ and $EuPO_4 \cdot H_2O$ nanowires (shown in Fig. 9.14c, d) had similar diameters to those of $LaPO_4 \cdot 0.5H_2O$ nanowires but were much longer (up to 10 μm). $GdPO_4 \cdot H_2O$ and $TbPO_4 \cdot H_2O$ (shown in Fig. 9.14e, f) nanowires were about 3–10 μm in length with diameters of 10–30 nm.

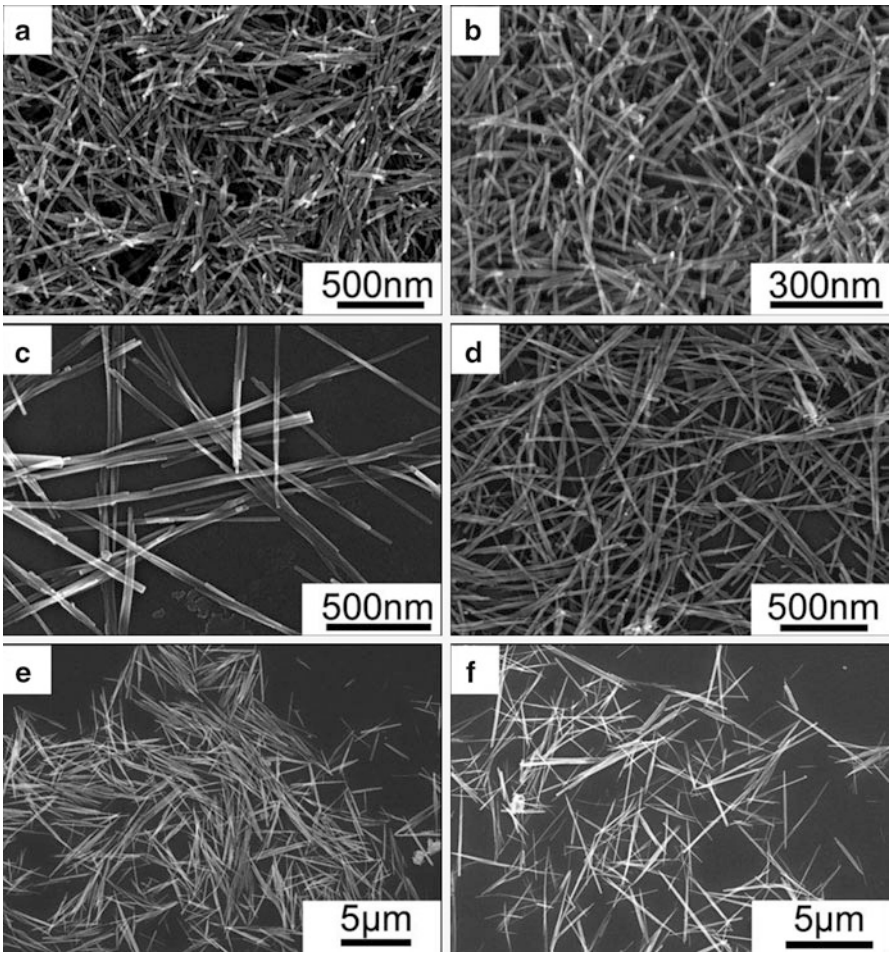

Fig. 9.14 SEM images of as-prepared nanowires: (**a**) $LaPO_4 \cdot 0.5H_2O$ (**b**) $CePO_4 \cdot H_2O$ (**c**) $SmPO_4 \cdot 0.5H_2O$, (**d**) $EuPO_4 \cdot H_2O$ (**e**) $GdPO_4 \cdot H_2O$, and (**f**) $TbPO_4 \cdot H_2O$ (Reprinted with the permission from Ref. [39]. Copyright 2009 American Chemical Society)

Figure 9.15 shows an IR spectrum of the $CePO_4$ nanowires. Pure TBP had a $\nu(P=O)$ stretch at 1282 cm^{-1} and a ν(P-O-C) stretch between 950 and 1050 cm^{-1} but was heavily overlapped by the strong and broad peaks of PO_4^{3-} in our systems. But the peaks at 2928, 2856, and 2962 cm^{-1}, assigned to the antisymmetric and symmetric methylene stretches ($\nu_{as}(CH_2)$, $\nu_s(CH_2)$) and antisymmetric methyl stretches ($\nu_{as}(CH_3)$) of the TBP molecule, indicated the presence of the TBP molecules on the surfaces of the nanowires. The presence of TBP made the nanocrystals more easily dispersed in some imidazolium-based ILs, such as [Omim]Cl, [Omim]BF_4, [Omim]PF_6, and [Omim]Tf_2N.

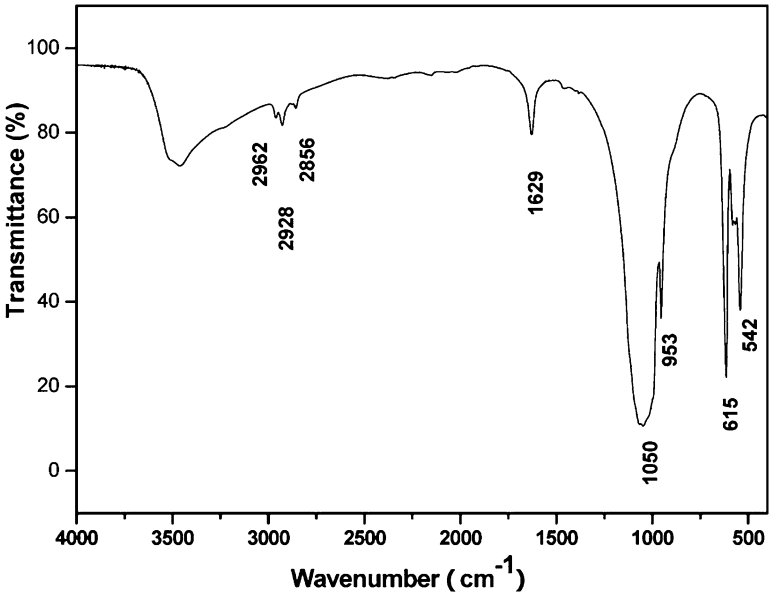

Fig. 9.15 FT-IR spectrum of $CePO_4{\cdot}H_2O$ nanowires capped with TBP molecules (Reprinted with the permission from Ref. [39]. Copyright 2009 American Chemical Society)

The surface, phase, and aggregation behaviors of ILs in solutions and mixtures with traditional solvents had attracted much research attention. Some molecular level-based study had been brought forward in recent investigations. The aggregation behavior of 1-methyl-3 alkylimidazolium salts in aqueous solution had been studied [40]. The amphiphilic nature of IL cations can lead to nano-in-homogeneity. The critical micelle concentrations (CMC) and micelle structures of [Omim]Cl had been revealed by several groups [30, 32]. It had been found that at concentrations just above the CMC, small near-spherical aggregates exist in aqueous [Omim]Br solutions, and the radius increases when increasing the concentration [32]. TBP was a well-known neutral organophosphorus extractant and had been extensively used in industrial extraction of RE ions for about half a century [41]. When extracting RE ions in a HNO_3 medium, $RE(NO_3)_3 \cdot 3TBP$ was formed as the extracted species [34]. Meanwhile, TBP was also a perfect solvent and capping agent in the synthesis of II–VI semiconductors [42, 43]. On the basis of the above results, a primary understanding of the nucleation and growth mechanism of the nanocrystals was proposed, as shown schematically in Fig. 9.16. Both [Omim]Cl and TBP played key roles in the formation of the nanowires. On the basis of the proposed mechanism, when TBP containing RE ions was added to the mixture of water and [Omim]Cl, a micelle system was generated. TBP as the inner phase was confined by aggregated ILs with the hydrophobic carbon chains penetrating into the inner TBP phase and the imidazole rings pointing to the outer water phase. It was known that hydrophilic ILs existed in the form of ions in dilute aqueous solution instead of ion pairs. The coulomb interactions

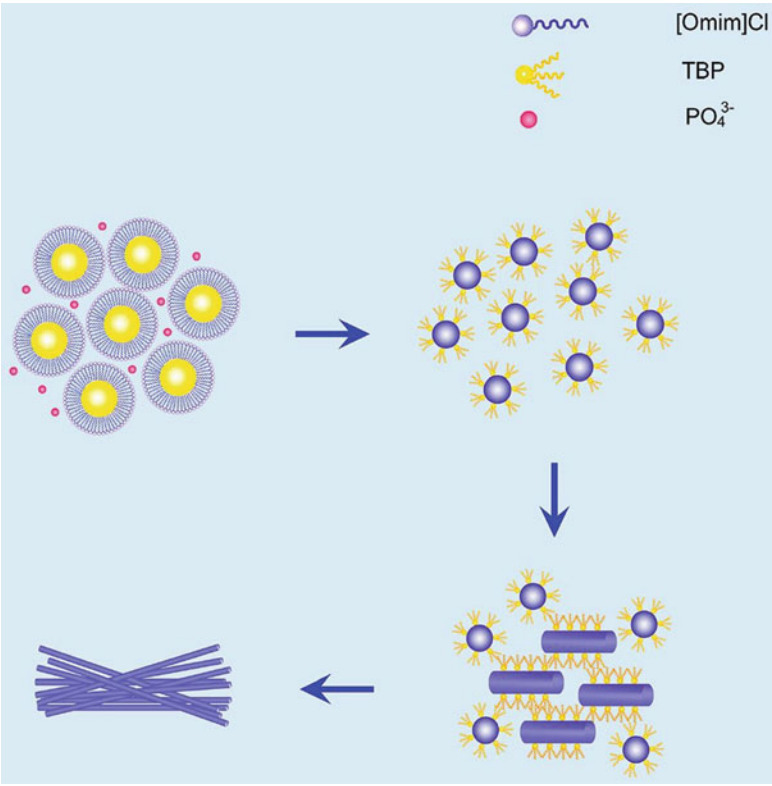

Fig. 9.16 Schematic diagram showing the formation and growth processes of $REPO_4{\cdot}xH_2O$ nanowires (Reprinted with the permission from Ref. [39]. Copyright 2009 American Chemical Society)

between PO_4^{3-} and imidazole rings make the ILs the buffer shell that suppresses the quick penetration of PO_4^{3-} into the micelles. After the injection of PO_4^{3-}, a homogeneous nucleation process would start in the micelles, thus producing uniform $REPO_4$ nanoparticles capped by TBP. In the following step, the nanoparticles with larger sizes would be able to grow into short nanorods at the expense of smaller ones through Ostwald ripening. It had been found the three carbon chains of TBP can facilitate the anisotropic growth of $REPO_4$ nanocrystals [44]. As a result of the different surface energies of different facets, the interaction between TBP and certain facets would be much stronger than others. Conjecturably, in the synthesis of $REPO_4 \cdot xH_2O$ nanowires, the newly formed side surfaces, {100} facets and {010} facets, might be stabilized by their interactions with the oxygen atoms of P = O groups in TBP. Meanwhile, the interaction between TBP and the two ends of the nanorods should be much weaker so as to enable the two ends of the nanorods to grow continuously through Ostwald ripening. Thereby, after 48 h of reaction, uniform nanowires were generated as the products.

Figure 9.17 shows the excitation and emission spectra of hexagonal $LaPO_4$:Eu (10 %) nanocrystals, including the uncapped nanoparticles and nanoparticles and nanowires capped with TBP. The broad charge-transfer band (CTB) centered at 254 nm, generated by electron delocalization from the filled 2p shell of O^{2-} to the partially filled 4f shell of Eu^{3+} was in agreement with the previous reports on the bulk materials. The Eu^{3+}-doped $LaPO_4$ nanocrystals exhibited orange-red luminescence ($\lambda = 570$–700 nm), assigned to transitions from the excited $^5D_0$ to the ^7F_J ($J = 1$–4) levels. It was well known that the $^5D_0$-$^7F_1$ lines originate from magnetic dipole transition, while the $^5D_0$-$^7F_2$ lines originate from electric dipole transition. The electric dipole transition was allowed only on the condition that the europium ion occupied a site which was not an inversion center and was sensitive to local symmetry. When Eu^{3+} ions occupied an inversion center, the $^5D_0$-$^7F_1$ transition should be relatively strong, while the $^5D_0$-$^7F_2$ transition should be relatively weak. In Fig. 9.24, the intensity ratios of $^5D_0$-$^7F_2$ to $^5D_0$-$^7F_1$ in uncapped nanowires, TBP-capped nanoparticles, and TBP-capped nanowires were 0.61, 0.69, and 0.64, respectively. Compared to the nanoparticles, the TBP-capped and uncapped nanowires had fewer surface atoms, and more Eu^{3+} occupied the site with inversion center and thus enhanced the $^5D_0$-$^7F_1$ transition [45]. Compared to the uncapped nanowires, the TBP-capped nanoparticles and nanowires have higher emission intensity. Possible reasons might be that the capping TBP suppressed the quenching

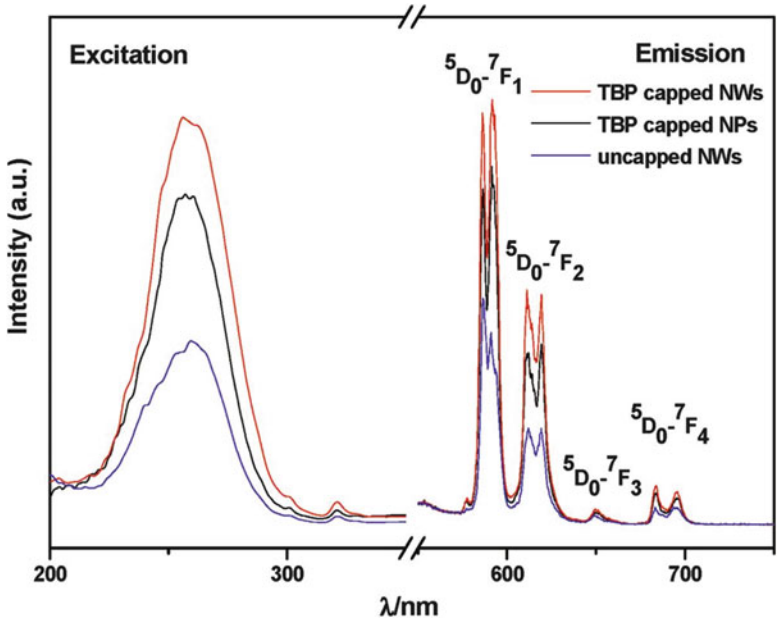

Fig. 9.17 Emission spectrum (λ_{ex}: 254 nm) and excitation spectrum (λ_{em}: 591 nm) of $LaPO_4 \cdot 0.5H_2O$ nanocrystals doped with 10 % Eu^{3+}: uncapped nanowires (*blue*), TBP-capped nanoparticles (*black*), and nanowires (*red*) (Reprinted with the permission from Ref. [39]. Copyright 2009 American Chemical Society)

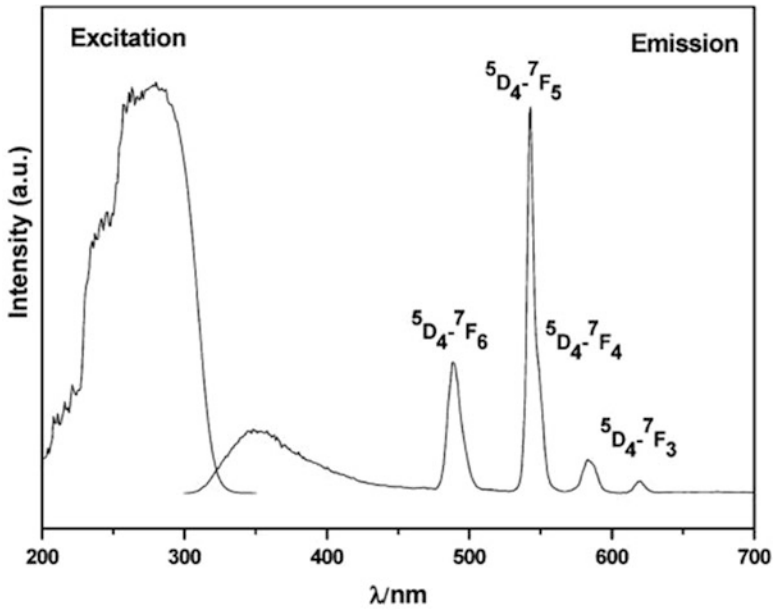

Fig. 9.18 Emission spectrum (λ_{ex}: 285 nm) and excitation spectrum(λ_{em}:542 nm) of $CePO_4 \cdot H_2O$ nanowires doped with 5 % Tb^{3+} (Reprinted with the permission from Ref. [39]. Copyright 2009 American Chemical Society)

effect of the OH groups on the surfaces and the influences from the effective index of refraction change. The nanowires capped with TBP had fewer surface defects than the nanoparticles, which contributed to the higher emission intensity. The $^5D_0$ lifetimes of Eu^{3+} in uncapped nanowires, TBP-capped nanoparticles, and TBP-capped nanowires were 2.85, 3.70, and 3.50 ms, respectively, indicating that the capping of TBP improved both the emission intensity and the lifetime of Eu^{3+}-doped $LaPO_4$ nanocrystals.

Figure 9.18 gives the excitation and emission spectra of $CePO_4$ nanowires doped with 5 % Tb^{3+}. The excitation spectrum was monitored by the $^5D_4$-$^7F_5$ emission. The broad excitation spectrum showed three peaks with maxima at 245, 263, and 280 nm, which corresponded to the transitions from the ground state of $^2F_{5/2}$ of Ce^{3+} to the different components of the excited Ce^{3+} 5d states split by the crystal field. Excitation in the Ce^{3+} absorption band at 285 nm yielded both the weak broad emission between 300 and 400 nm which arises from the 5d-4f emission of Ce^{3+} and the strong emission of Tb^{3+} (370–700 nm: $^5D_4$-^7F_J, J = 6, 5, 4, 3), showing the efficient energy transfer from Ce^{3+} to Tb^{3+}. In contrast to the f electrons of terbium, the d electrons of cerium strongly coupled to the lattice photons, resulting in broad overlapping bands and a significant Stokes shift. The luminescence decay curve of Tb^{3+} in Tb^{3+}-doped $CePO_4$ nanowires can be fitted to a single exponential function, and the lifetime of Tb^{3+} emission was 3.04 ms.

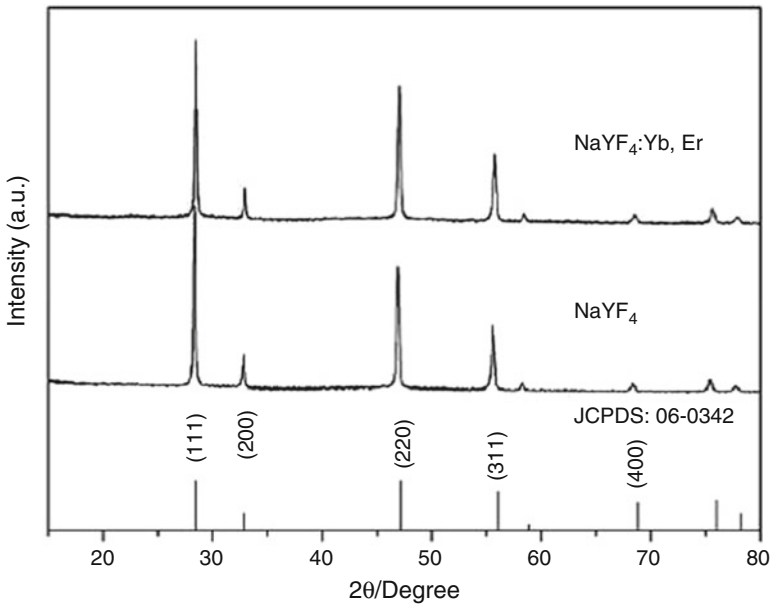

Fig. 9.19 XRD pattern of the nanocubes of $NaYF_4$ and $NaYF_4$:18 %Yb^{3+}, 2 % Er^{3+} (Reproduced from Ref. [46] by permission of The Royal Society of Chemistry)

9.4 Two Phase Synthesis of Luminescence Materials

Ji Chen et al. reported a facile mild ethylene glycol (EG)/1-methyl-3-octylimidazolium hexafluorophosphate ($[C_8mim]PF_6$) interfacial synthesis strategy to fabricate high-quality monodispersed Yb^{3+}, Er^{3+}/Tm^{3+}/Ho^{3+}-doped $NaYF_4$ nanocubes with $[C_8mim]PF_6$ acting as both templates and reagents [46].

The UC nanocubes were prepared via an EG/$[C_8mim]PF_6$ interfacial reaction method. In the two-phase system, RE nitrate and sodium nitrate were dissolved in EG solution in the top phase, and $[C_8mim]PF_6$ was the bottom phase. The PF_6^- anions were partly decomposed and brought F^- to the interface area under the reaction temperature of 80 °C, thus resulting in the formation of $NaYF_4$ nanoparticles. During a ripening period of 24 h, with the aid of the ILs, the nanoparticles grew into nanocubes and finally transformed into ionogels.

The XRD pattern of undoped $NaYF_4$, Yb^{3+}/Er^{3+}-doped $NaYF_4$ nanocubes is shown in Fig. 9.19. The peak positions and intensities agreed well with the single-phase cubic $NaYF_4$ crystals (JCPDS: 06–0342), and no peaks of other phases or impurities were detected. The sharp and narrow peaks indicated the highly crystalline nature of these nanocubes despite the low reaction temperature (80 °C). The results show that well-doped α-$NaYF_4$ nanocubes can be obtained by this route, and the nanocubes, comprising of various dopants and dopant concentrations, exhibit essentially the same crystal phase.

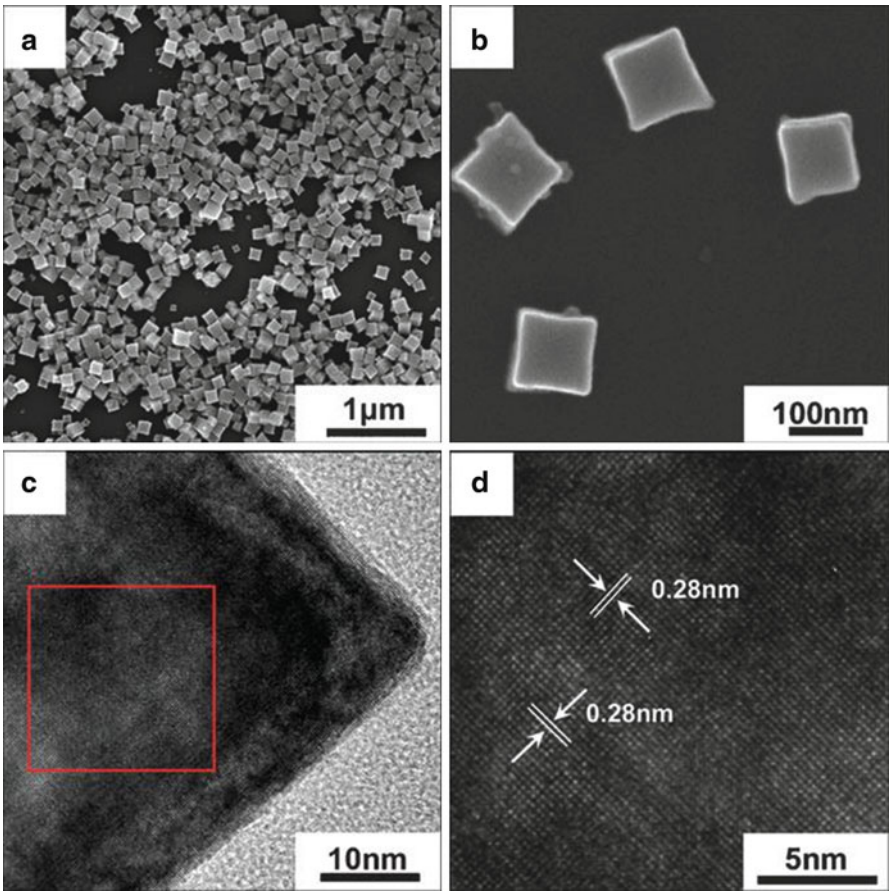

Fig. 9.20 (**a**, **b**) SEM images of $NaYF_4$: 18 % Yb^{3+}, 2 % Er^{3+} nanocubes, (**c**) HRTEM images of a single nanocube, (**d**) enlarged image of the selected area in Fig. 9.20c (Reproduced from Ref. [46] by permission of The Royal Society of Chemistry)

As shown in the scanning electron microscopy (SEM) and transmission electron microscopy (TEM) images in Fig. 9.20, all the $NaYF_4$: Yb^{3+}/Er^{3+} nanocubes exhibit cubic morphologies and edge length of around 100 nm. It was also found that some distortion occurred on the surfaces of these nanocubes, and it agreed well with the XRD patterns, where the (200) plane was not the dominating peak. Under the high-resolution TEM (Fig. 9.20c, d), the nanocube appears as a single crystal with a lattice spacing of about 0.28 nm, which is very close to the theoretical d-spacing value of the (200) plane and can be indexed to the d_{200} spacing of α-$NaYF_4$. These results indicate that highly crystalline products can be fabricated in this system under mild conditions.

It is interesting that no obvious morphology changes of the products can be observed at varied RE concentrations from 0.05 to 0.2 mmol and the volume ratios

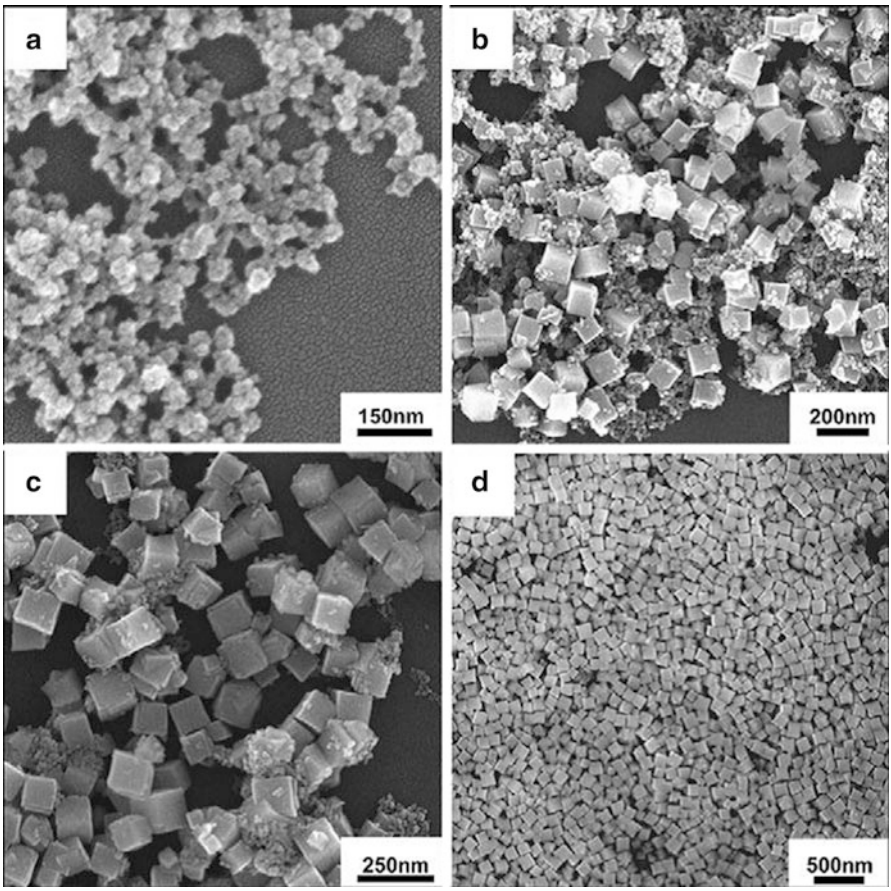

Fig. 9.21 SEM images of $NaYF_4$ nanocrystals under different reaction times (**a**) 2 h, (**b**) 6 h, (**c**) 12 h, (**d**) 24 h (Reproduced from Ref. [46] by permission of The Royal Society of Chemistry)

of EG to $[C_8mim]PF_6$ from 1:10 to 1:1. To understand the roles of the IL on the evolution of the nanocubes, the growth process was investigated by time-dependent experiments. The SEM images of the corresponding products are shown in Fig. 9.21. Figure 9.21a shows the SEM image of the nanoparticles under the reaction time of 2 h. In the earlier stage, only small nanoparticles of $NaYF_4$ which were heavily aggregated can be obtained at the two-phase interface area, and only two broad peaks can be observed in their XRD pattern, revealing their amorphous nature. As time passed by, nanocubes began to appear along with depletion of the amorphous nanoparticles. As shown in Fig. 9.21b, c, nanocubes appeared with the existence of nanoparticles after 6 h and became dominant with the increasing ripening time. In this stage, the sizes of nanocubes were in the range of 50–120 nm. Figure 9.21d shows that almost all the nanoparticles grew into nanocubes with a final size distribution of around 100 nm.

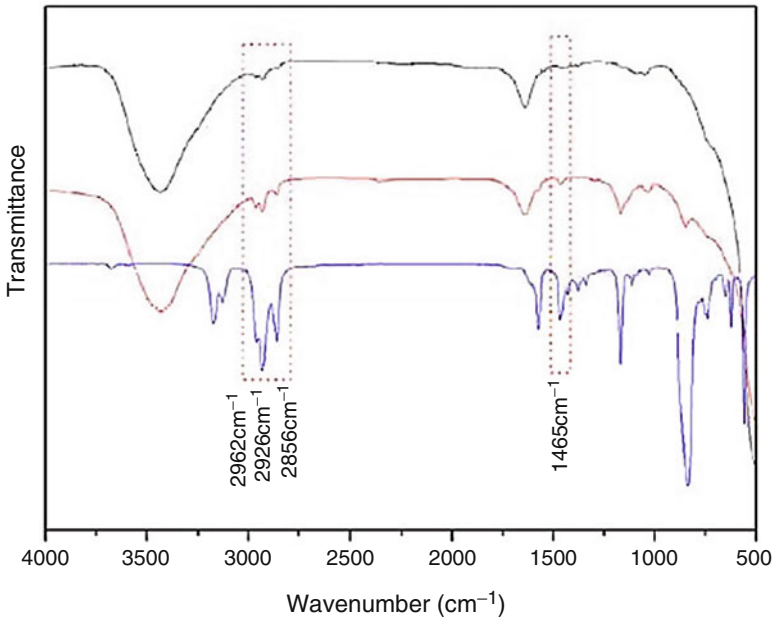

Fig. 9.22 FT-IR spectra of the nanocubes, nanoparticles, and the pure $[C_8mim]PF_6$ (Reproduced from Ref. [46] by permission of The Royal Society of Chemistry)

The IR spectra of the as-prepared nanoparticles and nanocubes are shown in Fig. 9.22. The peaks at 2856, 2928, and 2962 cm^{-1} were assigned to the antisymmetric stretches, symmetric methylene stretches ($\nu_{as}(CH_2)$, $\nu_s(CH_2)$), and antisymmetric methyl stretches (ν_{as} (CH_3)) of 1-methyl-3-octylimidazolium cations. The peak at 1465 cm^{-1} was assigned to ring in-plane asymmetry stretches and CH_3 (N) stretches. These results identified the presence of alkylimidazolium cations on the surfaces of the amorphous nanoparticles and the nanocubes.

Based on the above experimental results, a primary understanding of the nucleation and growth mechanism for the nanocubes in the two-phase system was proposed, as shown schematically in Fig. 9.23. In the EG/$[C_8mim]$ PF_6 two-phase system, EG dissolving the RE^{3+} and Na^+ was the top phase, whereas the immiscible $[C_8mim]PF_6$ was the bottom phase. Pure $[C_8mim]PF_6$ was stable under heat, but the small quantity of some impurities, such as water, ethanol, or NO_3^-, would decompose the ILs quickly and produce F^-. Firstly, a portion of $[C_8mim]PF_6$ began to degrade under heat and then formed amorphous $NaYF_4$ nanoparticles at the two-phase interfacial area. Due to coulomb interactions, the ILs were adsorbed on the surface of the nanoparticles. At the second stage of evolution, the IL-wrapped nanoparticles began to aggregate and dropped into the bottom phase slowly. At this stage, nanocubes began to appear and grew with the depletion of the nanoparticles. It was speculated that the anisotropic adsorption of 1-methyl-3-octylimidazolium cations on the $NaYF_4$ crystal facets conducted the formation of nanocubes. Under a

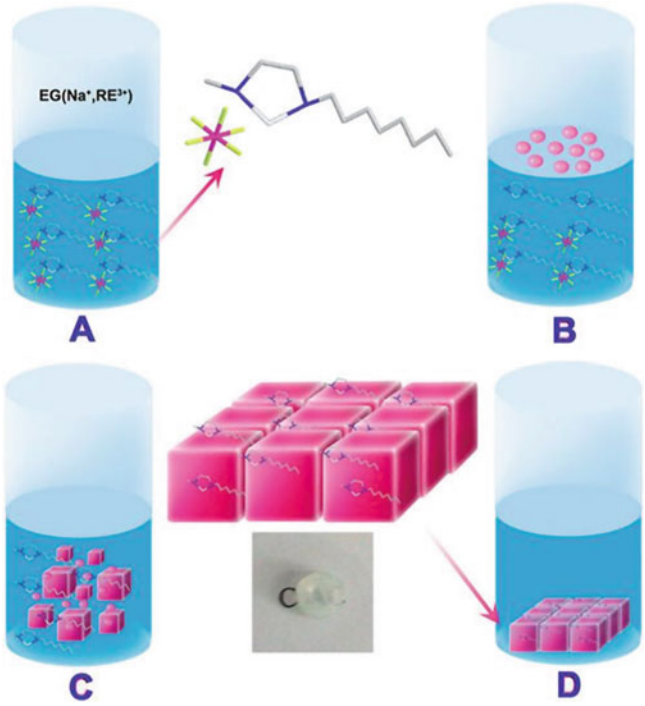

Fig. 9.23 Schematic diagram showing the formation and evolution of the $NaYF_4$ nanocubes (Reproduced from Ref. [46] by permission of The Royal Society of Chemistry)

long period of ripening, almost all the products grew into nanocubes of similar size. Finally, the IL-wrapped nanocubes transformed into ionogels of nanocubes and ILs (inset in Fig. 9.23) through the p–p interactions among ILs. In this process, $[C_8mim]PF_6$ played the role of capping agents and induced the assembly and evolution of the nanocrystals.

Multicolor UC fluorescence can be observed in the as-prepared RE^{3+} ion-doped nanocubes. The visible luminescent spectra of α-$NaYF_4$ co-doped Yb^{3+}, Er^{3+} nanocubes displayed two emission bands under NIR excitation, which can be assigned to the 4f–4f transitions of the Er^{3+}. For the nanocrystals obtained under reaction time of 2, 12, and 24 h, their UC emission intensity increased along with the reaction time (shown in Fig. 9.24). Figure 9.25 shows the UC emission spectra of Yb^{3+}, Er^{3+} co-doped a-$NaYF_4$ nanocubes with different doped concentrations of 18 % Yb^{3+}, 2 % Er^{3+}; 28 % Yb^{3+}, 2 % Er^{3+}; and 38 % Yb^{3+}, 2 % Er^{3+} under a 980 nm NIR excitation. The emission peaks can be attributed to $^2H_{11/2}$, $^4S_{3/2}$–$^4I_{15/2}$, and $^4F_{9/2}$–$^4I_{15/2}$ transitions of Er^{3+}, thus resulting in the yellow green color output. In their experiments, the ratios of the red to green emission were found to be influenced by the doped concentrations of Yb^{3+}. With the increasing Yb^{3+} concentrations, the relative intensity of the $^4F_{9/2}$–$^4I_{15/2}$ transitions was enhanced. The relative intensity ratios of the red to green emission of the three samples are 0.79,

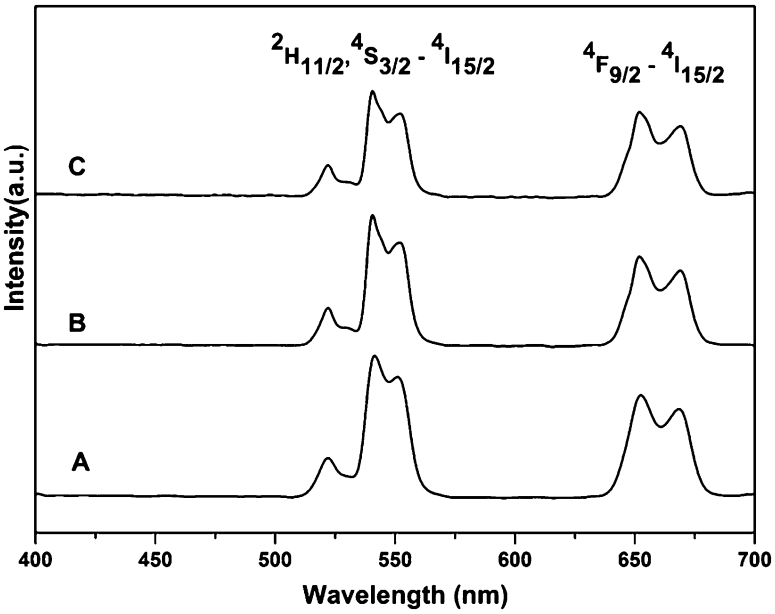

Fig. 9.24 Upconversion emission spectra of $NaYF_4$: 18 %Yb^{3+}, 2 % Er^{3+} nanocrystals obtained under different reaction times: nanoparticles (2 h), nanoparticles and nanocubes (12 h), and nanocubes (24 h) (Reproduced from Ref. [46] by permission of The Royal Society of Chemistry)

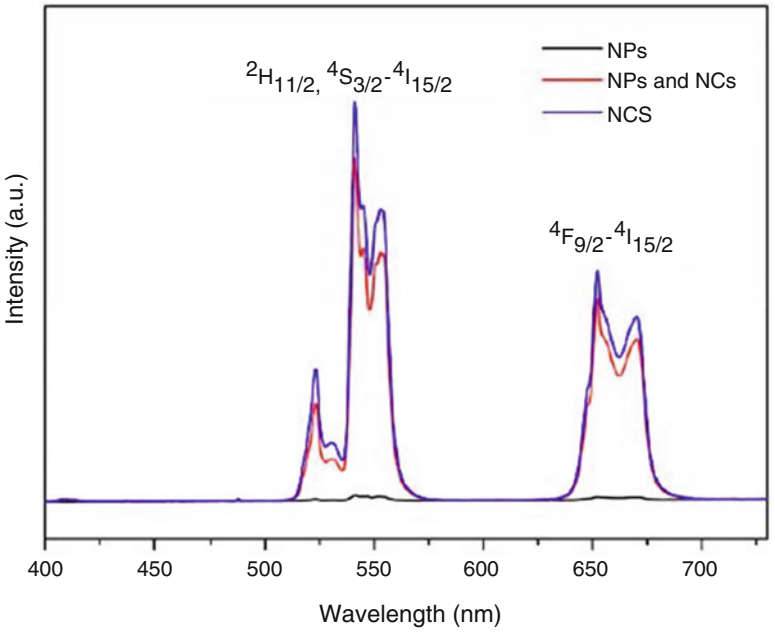

Fig. 9.25 Upconversion emission spectra of Yb^{3+}, Er^{3+} co-doped $NaYF_4$ nanocubes with different doped concentrations: (**a**) 18 %Yb^{3+}, 2 % Er^{3+}; (**b**) 28 % Yb^{3+}, 2 % Er^{3+}; and (**c**) 38 % Yb^{3+}, 2 % Er^{3+} (Reproduced from Ref. [46] by permission of The Royal Society of Chemistry)

0.83, and 0.95, respectively. The results indicate that with the increasing Yb^{3+} concentrations, the reverse energy transfer from Er^{3+} to Yb^{3+} was improved, and the red emission was enhanced. The different color output can also be accomplished by adjusting the doped ions. Yb^{3+}, Ho^{3+} co-doped $NaYF_4$ nanocubes displayed green emission under a 980 nm NIR excitation. In the emission spectra, the dominating green emission from $^5F_4$, $^5S_2$–$^5I_8$ transitions and the weak red emission from $^5F_5$–$^5I_8$ transition and $^5F_4$, $^5S_2$–$^5I_7$ transition can be observed.

Different mesocrystals of YF_3 hierarchical nanostructures were synthesized in the two-phase system of ethylene glycol and four different ILs, [Omim]PF_6, [Omim]BF_4, [Bmim]PF_6, and Cyphos IL111. The SEM and TEM images show that the product was composed of rhombic leaves. The high-magnified SEM images show that these leaves are further composed of nanoparticles (Fig. 9.26) [47].

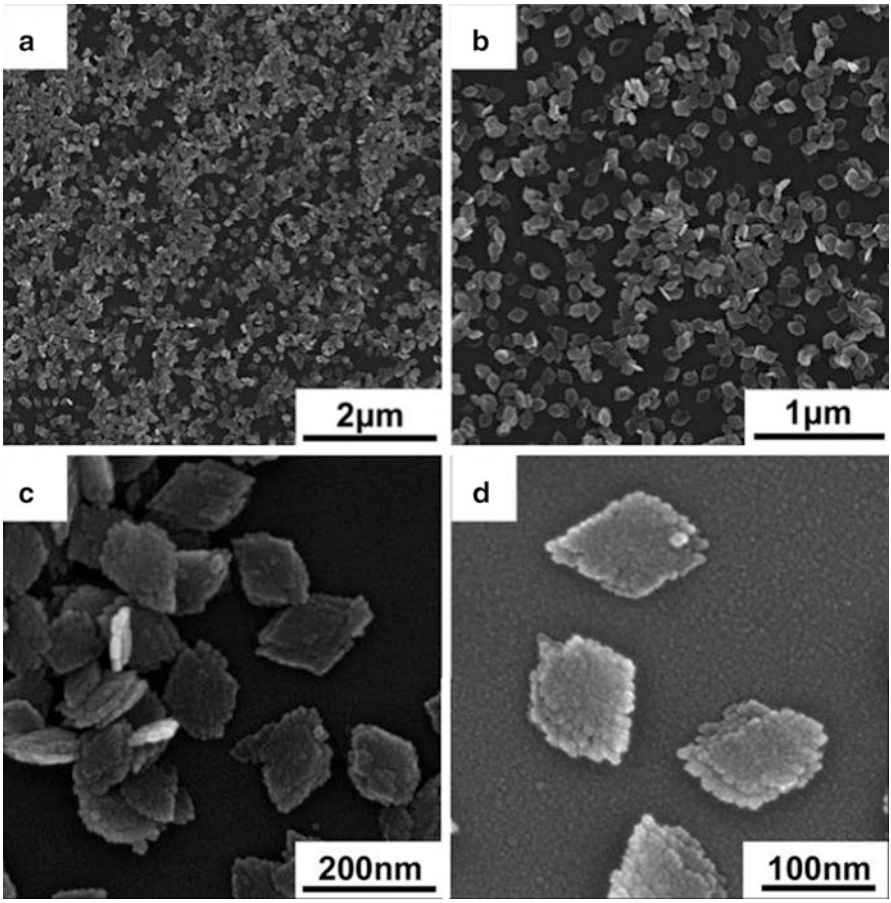

Fig. 9.26 SEM images of YF_3 synthesized in the two-phase system of ethylene glycol and four different ILs

In order to explore the effect of ionic liquids on the morphology of YF_3, different ionic liquids were introduced to the two-phase system. When [Omim]PF_6 was replaced by [Bmim]PF_6 with shorter carbon chain, the size and morphology of the product almost have no change, as shown in Fig. 9.27. When the anion of the ionic liquid was replaced by tetrafluoroborate, the obtained products were not leaf-like structures, but nanoparticles that formed aggregates. When the ionic liquids were changed to Cyphos IL111, the product was rodlike aggregates with bigger size. The TEM and HRTEM images (Fig. 9.28) show that these bundles were composed of nanoparticles through oriented lapping.

First of all, in the system of [Omim]PF_6 and EG, the anions will decompose into F^- ions rapidly when the system is heated, and then YF_3 nuclei formed. These nuclei grow quickly to become rhombic nanoparticles. Then, the ionic liquid can adsorb on the nanoparticle surface to reduce the surface-free energy. Ionic liquids will selectively adsorb on the crystal surface due to the surface energy differences. With the effect of π–π bond between imidazole ring and hydrogen bonds, these nanoparticles assembled along [101] and [−101] direction. In the longitudinal direction, these nanoparticles overlap along [020] direction. Finally, the multilayer rhombic aggregations formed. In this growth process, the initial formation of a regular shape of nanoparticles is the key to further assembly. Only when the ionic liquid anion is BF_4^-, or the ionic liquid is quaternary phosphonium salt, the obtained product is spherical nanoparticle with irregular geometric profile.

Under the excitation of 394 nm, all the YF_3 nanostructures synthesized in different ionic liquids exhibit red emission between 500 and 700 nm, which can be ascribed to the $^5D_0$-^7F_n ($n = 1, 2, 3, 4$) transition of Eu^{3+} ions. The bundle-like YF_3:Eu^{3+} synthesized with Cyphos IL 111 exhibits strongest emission, but the sample synthesized with [Omim]BF_4 shows lowest emission. The reason may be that in the leaf-like and bundle-like structures, nanostructures lap together through orientation, and that reduces the surface defects and appearance of europium in the surface (Fig. 9.29).

As an important approach to offer effect on the self-assembling process by nanoparticles (NPs), the liquid–liquid interfaces are attracting more and more interests [48–51]. The highly dynamic of the NPs offered by aqueous–organic interfaces allows reversible assembly of them, and the emulsions or microemulsions stabilized by NPs make the modification of the particles by functional molecules accessible [52]. Although the assembly of NPs at the liquid–liquid is well explored, researches on the preparation of NPs and their assemblies at the liquid–liquid interface are still rare. Rao et al. proved that the liquid–liquid interfaces could generate ultrathin films of crystallined Au and CdS [53]. And the organic phases used in this work were prepared by dissolving liposoluble precursors in organic solvents. But the liposoluble precursors are often expensive; compared with the above organic phase, the loaded phases of the extraction process are more abundant and unexpensive. Therefore, the organic loaded phases are well suitable as the organic phases to form aqueous–organic interfaces for producing

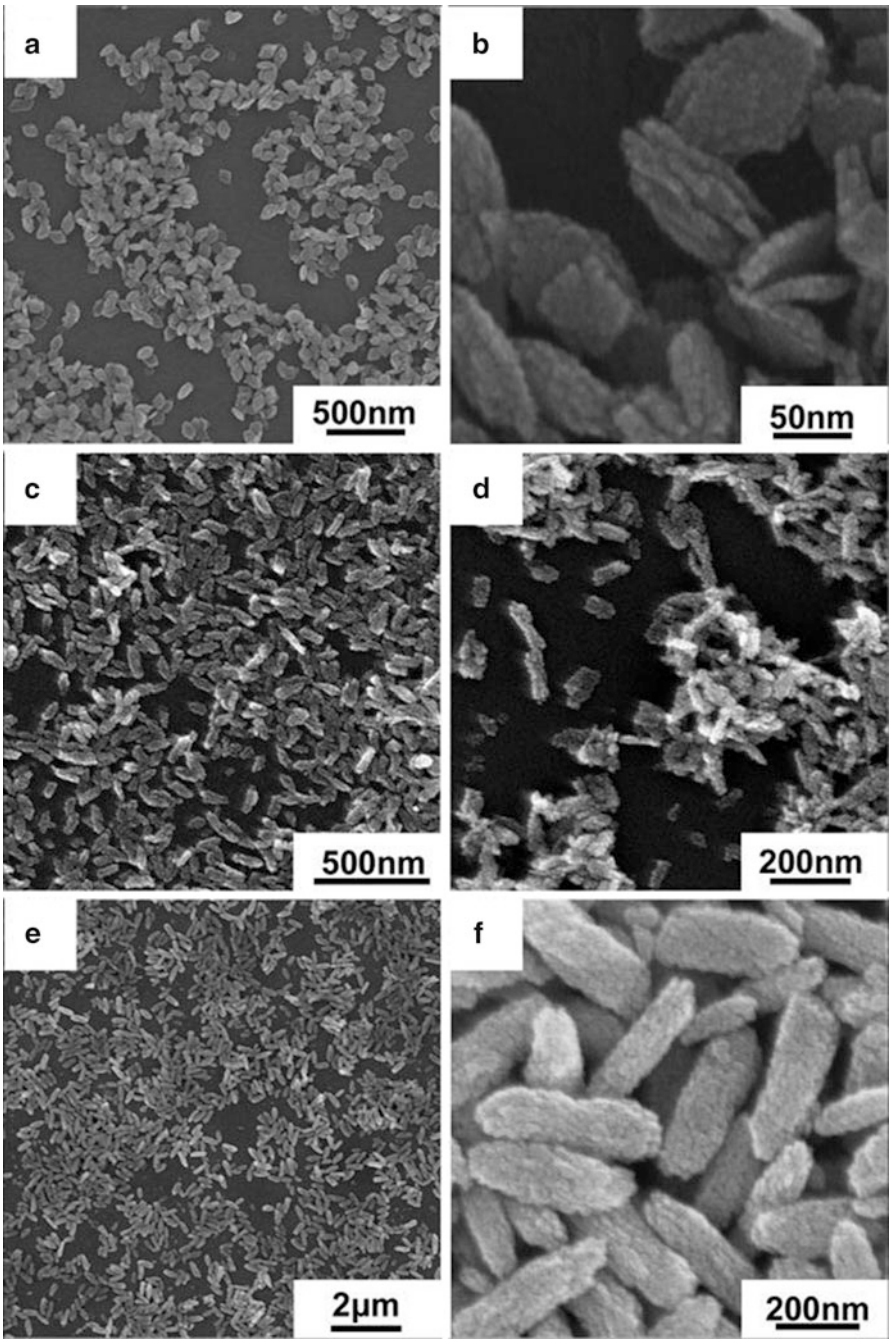

Fig. 9.27 SEM images of YF_3 synthesized in two-phase system with different ionic liquids. (**a**, **b**) [Bmim]PF_6; (**c**, **d**) [Omim]BF_4; (**e**, **f**) Cyphos IL 111

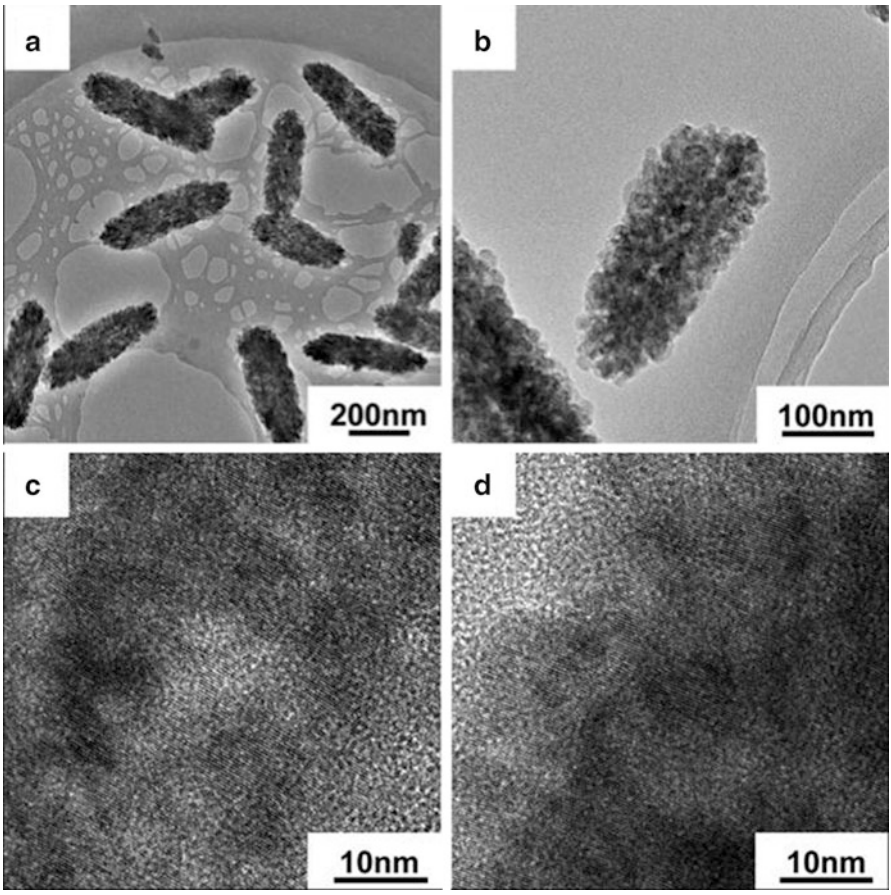

Fig. 9.28 TEM and HRTEM images of bundle-like YF_3 synthesized in the system of Cyphos IL 111 and EG

nanomaterials. In this work, self-assembled 3D-hierarchical flower-like $CePO_4$ nanostructures were prepared at the aqueous–organic interface formed by the third phase from an ionic liquid extraction process and the aqueous solution of K_3PO_4. Different interfaces formed by the same aqueous and other two loaded phases were also examined in this work, their interfacial tensions were measured, and a relationship between the morphologies and crystallinities of the products and the interfacial tensions was found [54].

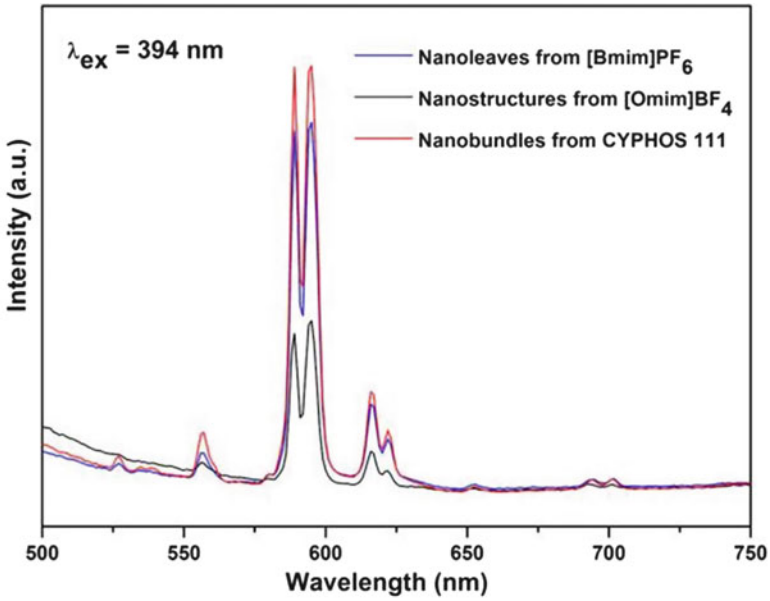

Fig. 9.29 Emission spectra of $YF_3:Eu^{3+}$ synthesized with different ionic liquids. $[Bmim]PF_6$ (*blue*); $[Omim]BF_4$ (*black*); Cyphos IL111 (*red*)

In order to explain the formation of the third phase in the liquid–liquid extraction process, the phase behavior was investigated. The phase volumes versus the initial concentrations of H^+ in the bottom phases ($C_H{}^+$) were given in Fig. 9.30. It showed that the third phase did not appear in the systems until $C_H{}^+$ reached 0.3 mol/l, and the volume of the third phase (V_m) decreased gradually from 2.45 ml to 2.0 ml while $C_H{}^+$ changing from 0.3 mol/l to 1 mol/l. The phase volumes versus the initial concentrations of [A336][Cyanex272] in the extract phase ($C_{Bif\text{-}ILE}$) were shown in Fig. 9.31. It can be seen that the V_m increased with the increasing of $C_{Bif\text{-}ILE}$ throughout the whole rage. From above, it was concluded that with the aggregation of the extracted complex, they did not dissolve in the n-heptane anymore; thus, a new phase with higher density was formed. While $C_{Bif\text{-}ILE}$ was increasing, more extracted complexes were aggregated, forming more volume of third phase. This observation well proved our previous conjecture about the forming reason of the third phase.

The size and morphology of the products with different reaction times were observed by SEM with the images shown in Fig. 9.32. Their reaction time was 1 min, 3 min, 5 min, 10 min, 30 min, and 60 min, respectively. The images showed that after about 1 min, the generated NPs self-assembled into 3D-hierarchical flower-like $CePO_4$ nanostructures; it was also indicated that the products with their reaction time longer than 10 min had similar sizes and morphologies; thus, the self-assembling process reached equilibrium stage quickly. A HRTEM image (Fig. 9.32g) of an individual nanostructure showed the lattice spacing of 3.0 Å and

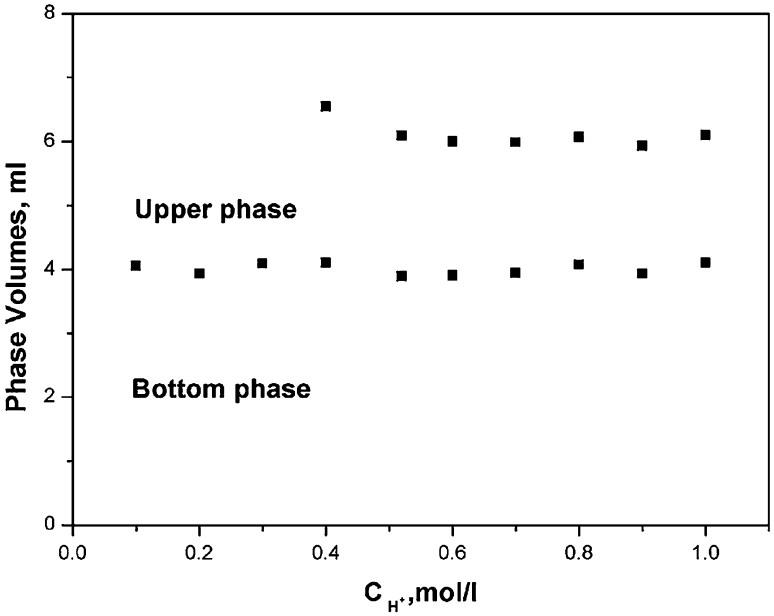

Fig. 9.30 Relationship between the phase behavior and C_H^+ (the regime between two plots is the third phase (Reprinted from Ref. [54], copyright 2014, with permission from Elsevier)

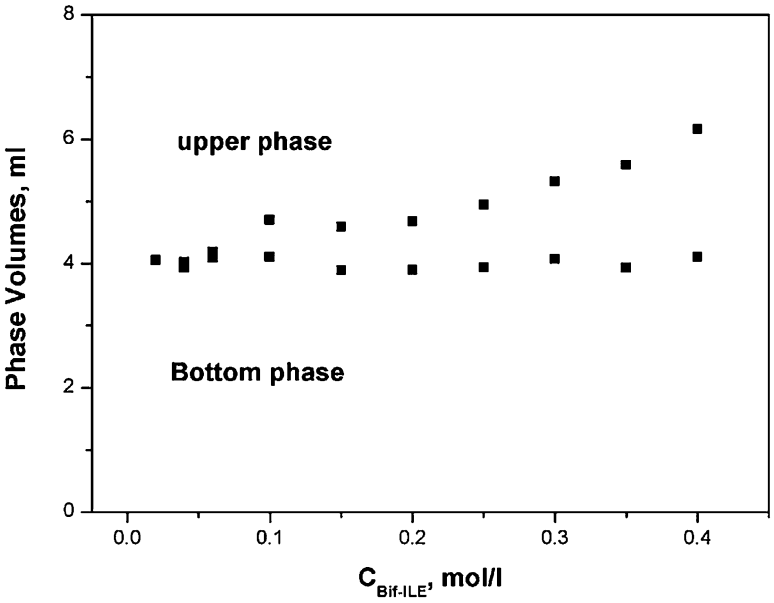

Fig. 9.31 Relationship between the phase behavior and $C_{Bif\text{-}ILE}$ (Reprinted from Ref. [54], copyright 2014, with permission from Elsevier)

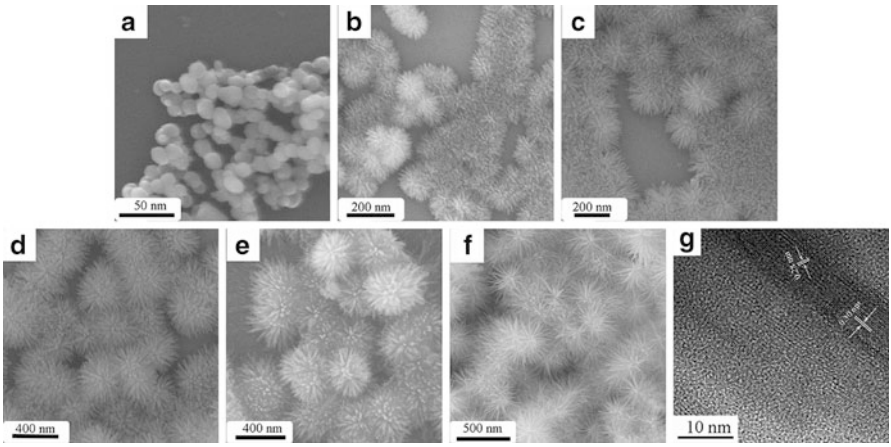

Fig. 9.32 SEM images of $CePO_4$ nanostructures prepared with different times: (**a**) 1 min, (**b**) 3 min, (**c**) 5 min, (**d**) 10 min, (**e**) 30 min, (**f**) 60 min, and (**g**) TEM image (Reprinted from Ref. [54], copyright 2014, with permission from Elsevier)

2.8 Å, which can be indexed to the (2 0 0) and (1 0 2) lattice space of $CePO_4$. The observation agreed well with the strong intensity peaks of (2 0 0) and (1 0 2) lattices in XRD patterns.

The influence of concentration of the K_3PO_4 (C_P) and $CeNO_3$ (C_{Ce}) solutions were studied. C_P was changed to 0.01 mol/l, 0.05 mol/l, 0.5 mol/l, and 1.0 mol/l, respectively. The obtained nanostructures were shown in Fig. 9.33; it was shown that the morphology was similar with the product of typical conditions, but the size increased with the increase of C_P. From above, the size of the products can be controlled by varying C_P. C_{Ce} was varied to 0.01 mol/L, 0.05 mol/L, and 0.2 mol/L, respectively. But it was noteworthy that the products made from different C_{Ce} had similar size and morphology. Thus, it was concluded that C_{Ce} could not affect the final products, and the C_P could only influence the size, but the morphology was mainly determined by the nature of the interface.

The third phase in [A336][Cyanex272] system was eliminated as the reference method to integrate it with the upper phase [55]. In addition, 50 % (v/v) TBP was dissolved in n-heptane as the organic phase in the extraction process, and there was no third phase in the resulting loaded phase. These two loaded phases were applied to prepare the products, too. The XRD results of the products were shown in Fig. 9.34. It was indicated that the products generated from the interface between the third phase and the aqueous solution of K_3PO_4 were well crystallized as mentioned above, the products from TBP loaded phase and the same aqueous phase were almost amorphous, and the crystallinity of the ones generated from the third phase-eliminated phase and the same aqueous phase was between the other

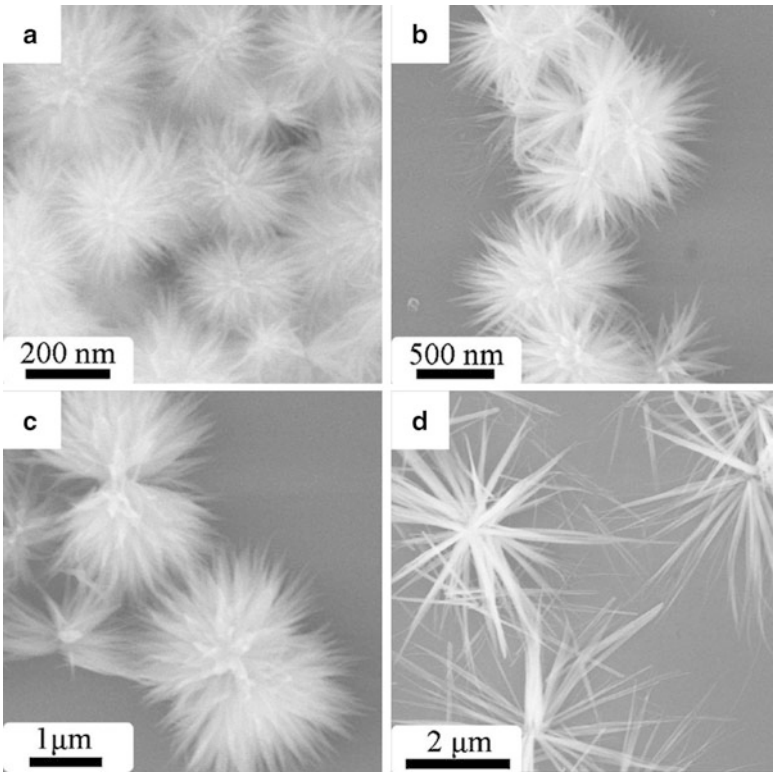

Fig. 9.33 SEM images of $CePO_4$ nanostructures prepared through different C_P: (**a**) $C_P = 0.05$ mol/l, (**b**) $C_P = 0.5$ mol/l, (**c**) $C_P = 1.0$ mol/l, and (**d**) $C_P = 5.0$ mol/l (Reprinted from Ref. [54], copyright 2014, with permission from Elsevier)

two. Their SEM images were shown in Fig. 9.35a, b respectively. The images showed the products formed at the interface with TBP loaded phase as its organic phase had a spherical morphology; this observation agreed with other literature that concluded the amorphous material tended to show a spherical morphology. And the interface between the third phase-eliminated loaded phase and the same aqueous phase generated fractal networks; this was consistent with the behavior of the assembled Au particles generated from a surfactant-assisted liquid–liquid interface.

Because the precipitates formed at the interface interrupted the measurement of the interfacial tensions, the solution of K_3PO_4 was replaced by water with the same pH value in the measurement. Combined with the above observations, this result indicated that the crystalline nanostructures preferred to form at the interface with lower tension, and spherical amorphous products were likely to generate at the interface with higher tension, and the fractal networks tended to occur at the

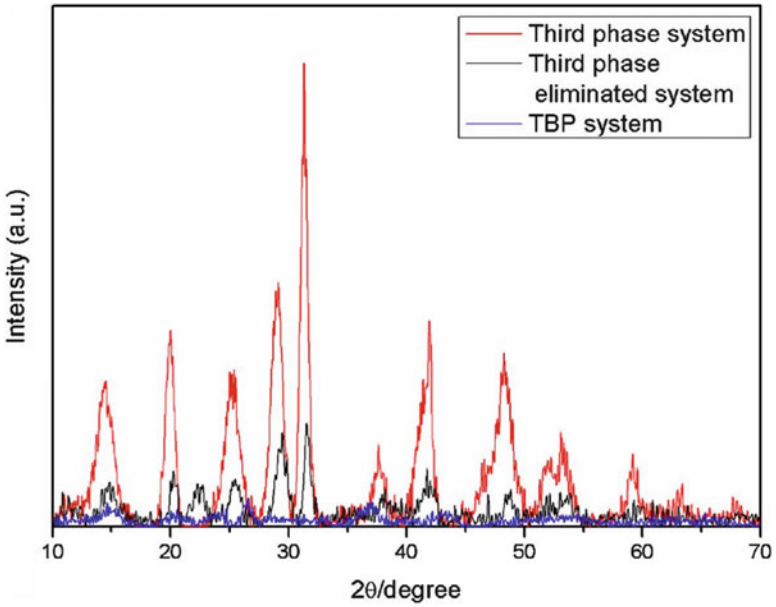

Fig. 9.34 XRD patterns of $CePO_4$ nanostructures (Reprinted from Ref. [54], copyright 2014, with permission from Elsevier)

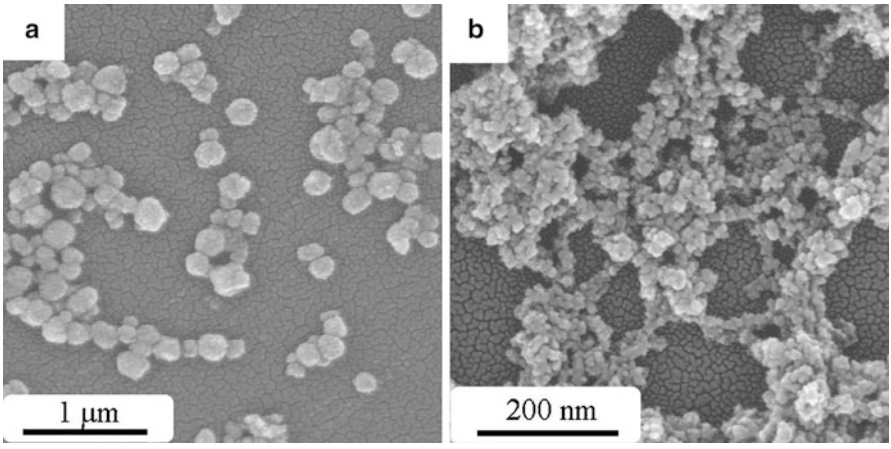

Fig. 9.35 SEM image of products prepared with the loaded phase from the (**a**) TBP system and (**b**) middle-phase-eliminated system (Reprinted from Ref. [54], copyright 2014, with permission from Elsevier)

interface whose tension was between the above two. A possible reason for this phenomenon was proposed: as it was known to all that bigger particles stabilized the interface more efficient than the small ones, the NPs generated at the interface

with high surface energy were compelled by the strong tendency of lowering the surface energy to form big assemblies quickly. And because of the quick assembling, the anisotropy was not shown; thus, the assembly was amorphous and spherical. While the NPs formed at the interface with low tension assembled more slowly, this tended to generate crystalline structures.

From the above results, a possible mechanism to explain the growth process of the products was proposed and shown schematically in Fig. 9.36. At the beginning of the reaction, the Ce^{3+} of the extracted complex from the organic phase and the PO_4^{3-} from the aqueous phase encountered at the aqueous–organic interface, the nuclei of $CePO_4$ generated, and then the nuclei grew into NPs. After that, the NPs assembled into small flower-like nanostructures. With the reaction time extended, more NPs assembled onto the nanostructures, and the nanostructures grew bigger. When the equilibrium was reached, the nanostructures stopped growing. It can be seen that during the entire growth process, the bifunctional ionic liquid extractants (Bif-ILEs) played key roles in the formation of the 3D-hierarchical $CePO_4$ nanostructures. At first, the Bif-ILEs acted as extractants that extracted Ce^{3+} from aqueous solution. Then, they were stripped by precipitate agents. Once the nuclei generated, the stripped ILs capped on the surface of the nuclei and played the role of structure directors. Finally, the Bif-ILEs stabilized the nanostructures from aggregating.

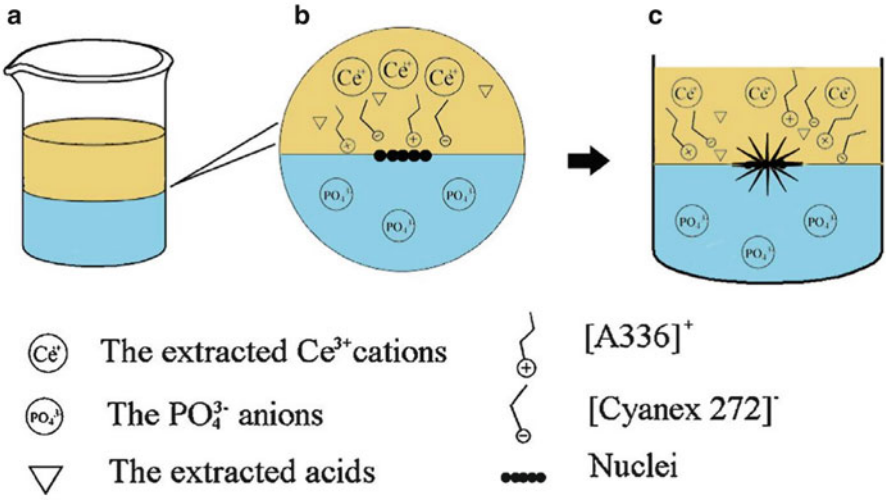

Fig. 9.36 Schematic diagram of the interface strategy: (**a**) the form of aqueous–organic interface, (**b**) the nuclei generated into NPs, (**c**) NPs self-assembled into flower-like 3D-hierarchical nanostructures (Reprinted from ref. [54], copyright 2014, with permission from Elsevier)

Daxiang Cui et al. reported a general strategy to synthesize highly uniform and monodisperse rare earth fluoride nanocrystals through a novel OA/ionic liquid two-phase system [56–58]. They adopt the notion of liquid–liquid two-phase reaction and devise a novel oleic acid (OA)/1-butyl-3-methylimidazolium tetrafluoroborate ($BmimBF_4$) two-phase system, which combines the merits of thermal decomposition (size and morphology control) and IL-based strategy (mild conditions, user-friendly reagents, and direct water solubility). Highly uniform and monodisperse REF_3 and $NaREF_4$ (RE = La, Gd, Yb, and Y) nanocrystals with small size (< 25 nm) and different morphologies were synthesized in the OA phase of the OA/IL two-phase system for the first time. Moreover, water-soluble Ln^{3+}-doped $NaREF_4$ (RE = Gd and Y) nanocrystals with a hexagonal phase were obtained in the IL phase by adding a certain volume of n-octanol (Fig. 9.37).

Furthermore, they upgraded their previously reported OA/$BmimBF_4$ two-phase system by employing 1-butyl-3-methylimidazlium hexafluorophosphate ($BmimPF_6$) as the IL. They developed a new OA/IL two-phase system and n-octanol-induced OA/IL two-phase system to successfully synthesize high-quality hexagonal RE (RE = La, Gd, and Y) fluoride nanocrystals with uniform morphologies (mainly spheres and elongated particles) and small sizes (<50 nm) (Fig. 9.38) [59].

They also illustrate the possible formation mechanism of REF_3 and $NaREF_4$ and the role of ILs in the formation process in detail [50].

A. V. Mudring et al. made use of the multifunctional properties of ionic liquids by employing them as a fluoride resource and hydrophilic phase; they have grown small, monodisperse, highly luminescent Ln^{3+}-doped $NaGdF_4$ nanorods at the interface between octadecene and the reactive ionic liquid 1-butyl-3-methylimidazolium tetrafluoroborate (Fig. 9.39). The obtained nanocrystals could further be endowed with functional groups and rendered water dispersible, which allows them to be used for biodetection [60].

A. V. Mudring et al. reported the phase-selective synthesis of trivalent lanthanide-doped $NaGdF_4$ nanocrystals, capped by ionic liquid cations bearing long alkyl chains, succeeded via a one-step interface-assisted ionothermal route. Owing to the existence of an interface formed between hydrophobic ionic liquids ($[P_{66614}][PF_6]$) and ethylene glycol, selectively either pure cubic or hexagonal phase $NaGdF_4$ could be obtained by changing the amount of the added surfactant, polyethyleneimine. Utilizing the fact that the $NaGdF_4$ NC surface was capped by the hydrophobic IL cation, the obtained NCs could be easily modified by an amphiphilic polymer to allow for transfer from an organic to an aqueous environment (Fig. 9.39). The surface-modified NCs show nearly no toxicity to cells, indicating their potential as bioprobes. The surface-modified NCs could be further conjugated with biomolecules to bind the specific target via a simple TR-FRET route. These new findings may open a new avenue for the application of ILs for the novel synthesis of inorganic NCs for bioapplications (Fig. 9.40) [61].

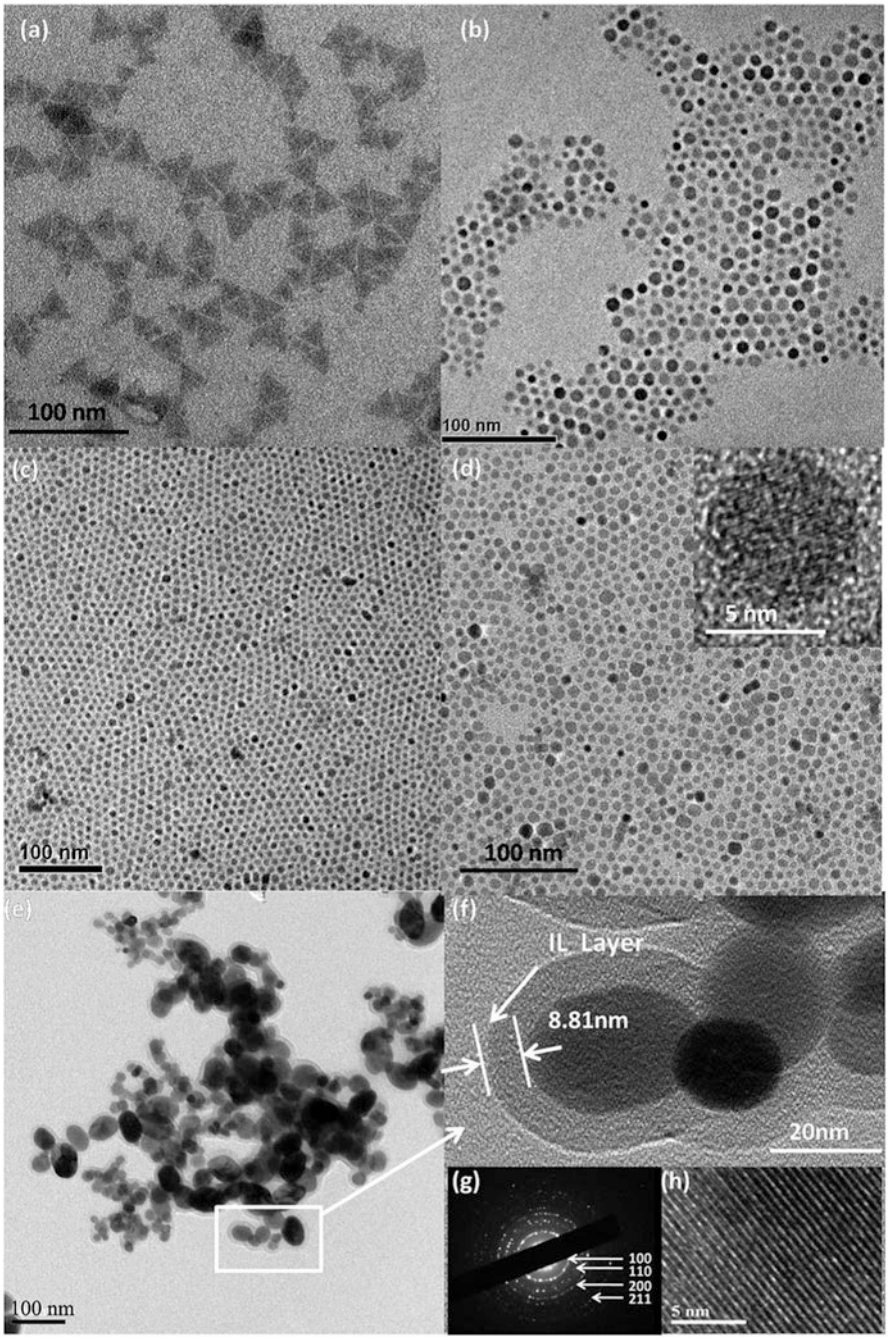

Fig. 9.37 (**a**–**d**) TEM images of RE fluoride nanocrystals in OA phase: (**a**) LaF_3, (**b**) GdF_3, (**c**) $NaYbF_4$, (**d**) $NaYF_4$. Inset: HRTEM image of (**d**); (**e**, **f**) TEM images with different magnifications of water-soluble $NaYF_4$: 20 %Yb, 2 %Er nanocrystal in IL phase. (**g**, **h**) The corresponding SAED pattern and HRTEM image of (**e**, **f**) (Reproduced from Ref. [56] by permission of The Royal Society of Chemistry)

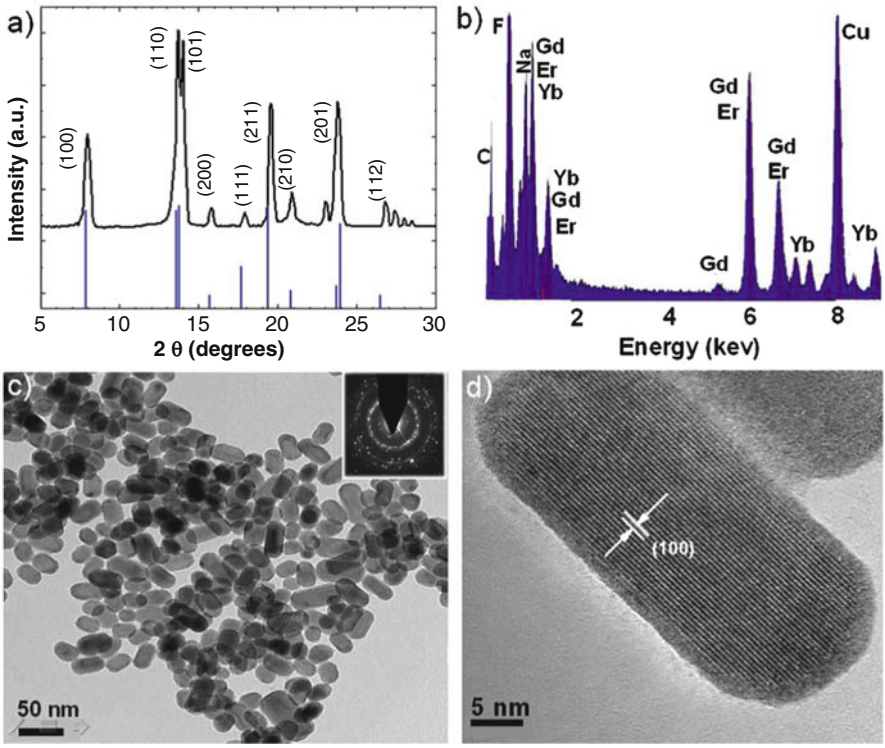

Fig. 9.38 (**a**) XRD pattern, (**b**) EDX pattern, and (**c**) TEM and (**d**) HRTEM images of $NaGdF_4$:Er-Yb NCs. The inset of (**c**) shows the SAED pattern (Reproduced from Ref. [60] by permission of The Royal Society of Chemistry)

The lower lines in Fig. 9.39a, c correspond to the standard data from JCPDS 027–699 (hexagonal) and JCPDS 027–697 (cubic), respectively. The inset of (a) shows the $NaGdF_4$ dispersed in dichloroethane, and the insets of (b) and (d) show the size distribution of NCs, respectively.

9.5 Ionic Liquid as Template

As one of typical soft chemical methods, ionic liquid-assisted hydrothermal technique is widely applied to overcome the problems because of the following advantages. First, ionic liquids have unique characteristics such as good thermal stability, wide liquid temperature range, and low volatility, which make them as good solvents in hydrothermal reactions. Secondly, hydrogen bonds form between the H atom of the imidazole ring in ionic liquids and the O atoms located in the outside plane of the muticomponent oxide, making it useful for producing the uniformly adsorbed nuclei at the initial stage of reaction. Moreover, the number

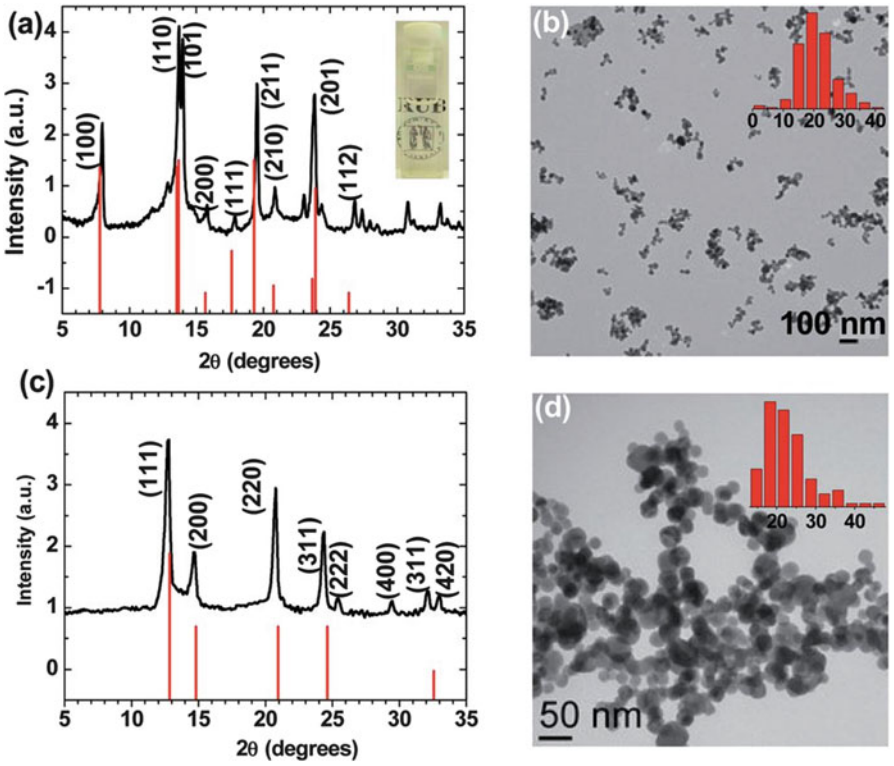

Fig. 9.39 (**a**) XRD pattern and (**b**) TEM image of hexagonal $NaGdF_4$ NCs; (**c**) XRD pattern and (**d**) TEM image of cubic $NaGdF_4$ NCs (Reproduced from Ref. [61] by permission of The Royal Society of Chemistry)

of hydrogen bonds absorbed on the certain surface of crystals is determined by the amount of ionic liquid. In addition, hydrogen bond and *co*-p–p stack interaction of ionic liquids can induce the preferential growth of crystals along 2D direction at a certain condition and is crucial to monitor the phases and shapes of desired nanostructures [62]. W. Zheng et al. reported the synthesis of ultrathin $SmVO_4$ nanosheets through a simple and facile ionic liquid-assisted hydrothermal approach (Fig. 9.41), in which process ionic liquid [BMIM] can vertically adsorb on the (001) plane of *t*-$SmVO_4$ crystal to control its 2D-oriented growth. The phase composition, structure, and morphology of the products were readily adjusted by varying the reaction parameters, such as the amount of ionic liquid [BMIM]Br, pH value, and temperatures (Fig. 9.42).

Flower-like Y_2O_3 nano-/microstructured phosphors have successfully been fabricated by an ionic liquid-assisted method involving temperature (600 °C) annealing [63]. The ionic liquids play a crucial role in the formation of various morphologies of Y_2O_3. The results suggested that the morphology of the Y_2O_3 sample prepared by the solution-phase reactions is influenced by adding IL. The

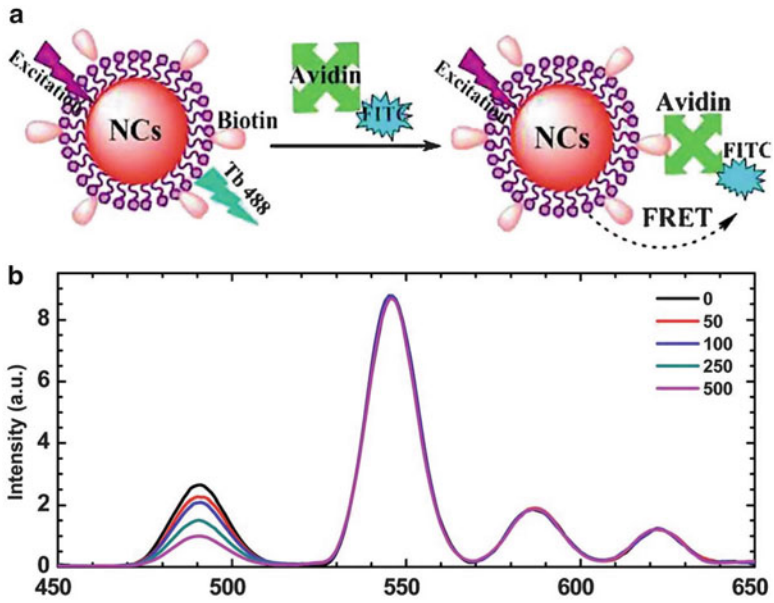

Fig. 9.40 (**a**) Schematic illustration of FRET detection of avidin and (**b**) TR-FRET spectra of the bioassays at different concentrations of avidin as indicated (nM) using the biotinylated $NaGdF_4$: Ce^{3+}, Tb^{3+} as bioprobes (Reproduced from Ref. [61] by permission of The Royal Society of Chemistry)

$[C_{17}mim]^+$ cation of $[C_{17}mim]^+[H_2PO_4^-]$ has a hydrophobic chain which, under proper experimental conditions $[C_{17}mim]^+$, could form micelles with the positive ends stretching to the outside.

After the $Y(NO_3)_3$ is solved in water in the absence of $[H_2PO_4]^-$, which is an IL anion, there is the possibility of formation of $[Y(H_2O)_2(NO_3)_3\ H_2PO_4]^-$. Then, $[C_{17}mim]^+$, which is IL cation, can interact with precursor $[Y(H_2O)_2(NO_3)_3\ H_2PO_4]^-$ ions through electrostatic attraction. Therefore, flower-like Y_2O_3 architecture can be obtained by hydrothermal route by adding a small amount of $[C_{17}mim] + [H_2PO_4]$.

As shown in Fig. 9.43a–c, in high concentration IL (0.045 mmol), the Y_2O_3 sample is irregular and crossed microsheets which overlap each other. When 0.012 mmol of IL is added in hydrothermal solution, the Y_2O_3 sample is shaped as a uniform flower-like architecture, as shown in Fig. 9.43e. The formation mechanism of Y_2O_3 flowers is obviously due to the templating effect in the present ionic liquid–water reaction system. The inset SEM images in Fig. 9.43e offer a clear view of the morphology from which it can be seen that the flower-like Y_2O_3 architecture is built up from Y_2O_3 nanoflakes. The results suggested that the morphology of the Y_2O_3 sample prepared by the solution-phase reactions is influenced by adding IL. $[C_{17}mim]^+$ cation of $[C_{17}mim]^+[H_2PO_4^-]$ has a

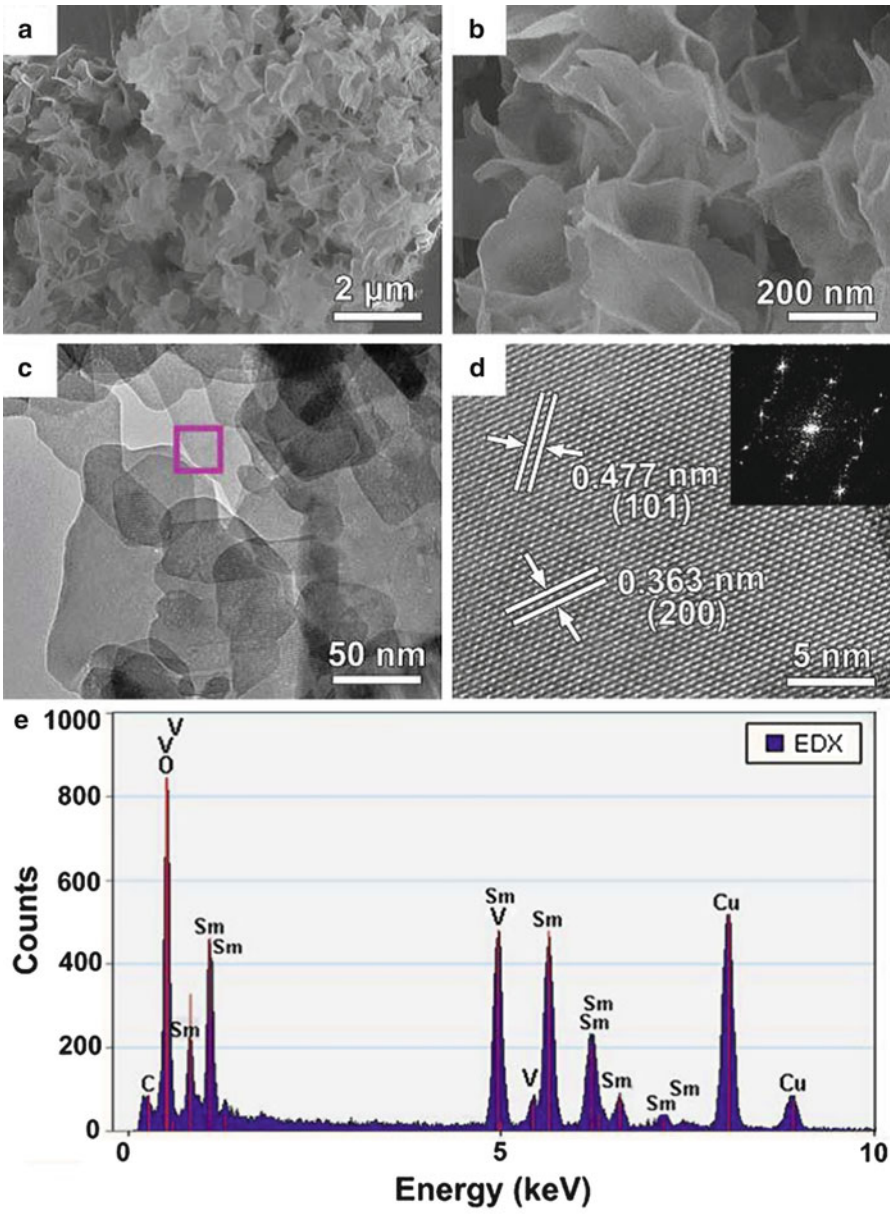

Fig. 9.41 The size and shape of *t*-$SmVO_4$ nanosheets obtained by an ionic liquid-assisted hydrothermal method (1.5 mL of 0.01 M [BMIM]Br, 180 °C, 48 h, pH = 11). (**a**, **b**) SEM, (**c**) TEM, and (**d**) HRTEM image of the selected area marked with a *pink square* in (**c**). The inset is the fast Fourier transformation (FFT) pattern (Reproduced from Ref. [62] by permission of The Royal Society of Chemistry)

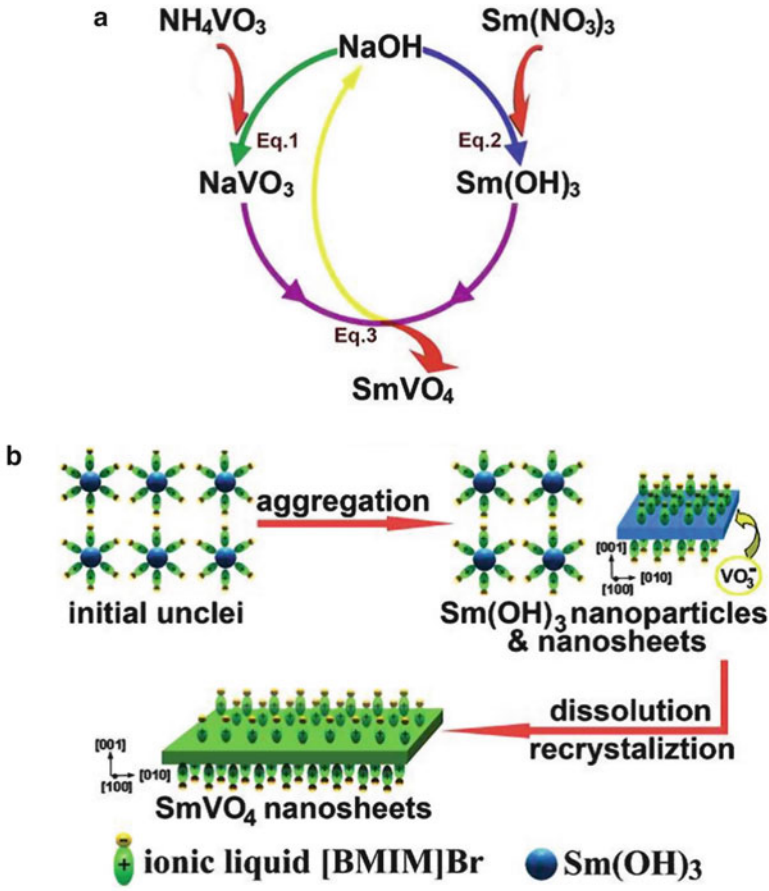

Fig. 9.42 Schematic illustration of the "reaction circle" process of chemical reactions (**a**) and the growth mechanism of *t*-$SmVO_4$ nanosheets (**b**) (Reproduced from Ref. [62] by permission of The Royal Society of Chemistry)

hydrophobic chain which, under proper experimental conditions $[C_{17}mim]^+$, could form micelles with the positive ends stretching to the outside. After the $Y(NO_3)_3$ is solved in water in the absence of $[H_2PO_4]^-$, which is an IL anion, there is the possibility of forming $[Y(H_2O)_2(NO_3)_3\ H_2PO_4]^-$. Then, $[C_{17}mim]^+$, which is an IL cation, can interact with precursor $[Y(H_2O)_2(NO_3)_3\ H_2PO_4]^-$ ions through electrostatic attraction. Therefore, flower-like Y_2O_3 architecture can be obtained by hydrothermal route by adding a small amount of $[C_{17}mim]^+[H_2PO_4^-]$.

In this study, some Y_2O_3 nanostructures were prepared in the presence of other ILs with different cations. The effect of the ILs cation and the counter anions on the Y_2O_3 morphology of these nanostructures was studied experimentally. It was observed that Y_2O_3 morphology and PL of these nanostructures were strongly influenced by the type of cation and anion. As the length of the subsidiary chain

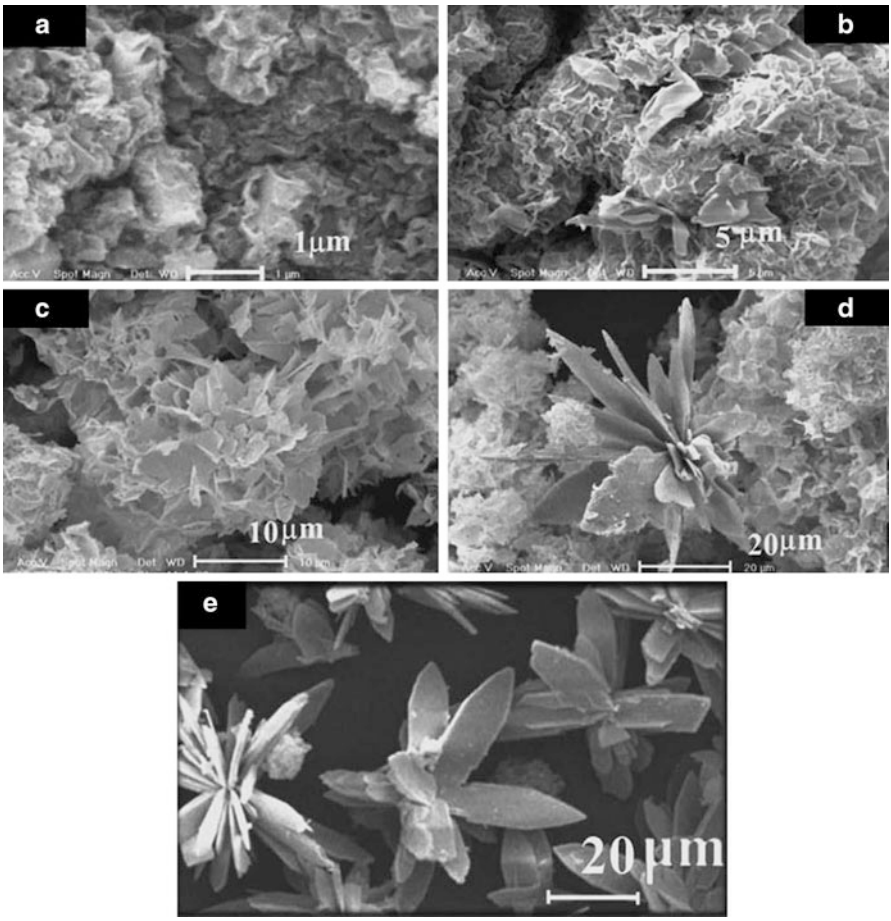

Fig. 9.43 SEM images showing the morphological evolution of Y_2O_3 samples with different concentrations of IL1: (**a**) 0.045 M, (**b**) 0.036 M, (**c**) 0.027 M, (**d**) 0.018 M, and (**e**) 0.012 M (Reprinted from Ref. [63], copyright 2010, with permission from Elsevier)

of cation section of IL (imidazole ion) reduces, the thickness of the nanosheets increases. And as anion section of IL changes ($H_2PO_4^-$ to HSO_4^-), as shown in Fig. 9.44e, morphology changes from a nanosheet-like structure to a coral-like one.

An ionic liquid-assisted solvothermal method is employed to prepare single-phase, oxygen-free, hexagonal $NaGdF_4:Eu^{3+}$ nanorods with a visible quantum efficiency of 187 %, where 1-ethyl-3-methylimidazolium bromide (C_2mimBr) was used as template (Fig. 9.45). Most importantly, the presence of the ionic liquid additive is mandatory as only in that case phase pure hexagonal material is obtained that shows the exceptionally high quantum yields [64].

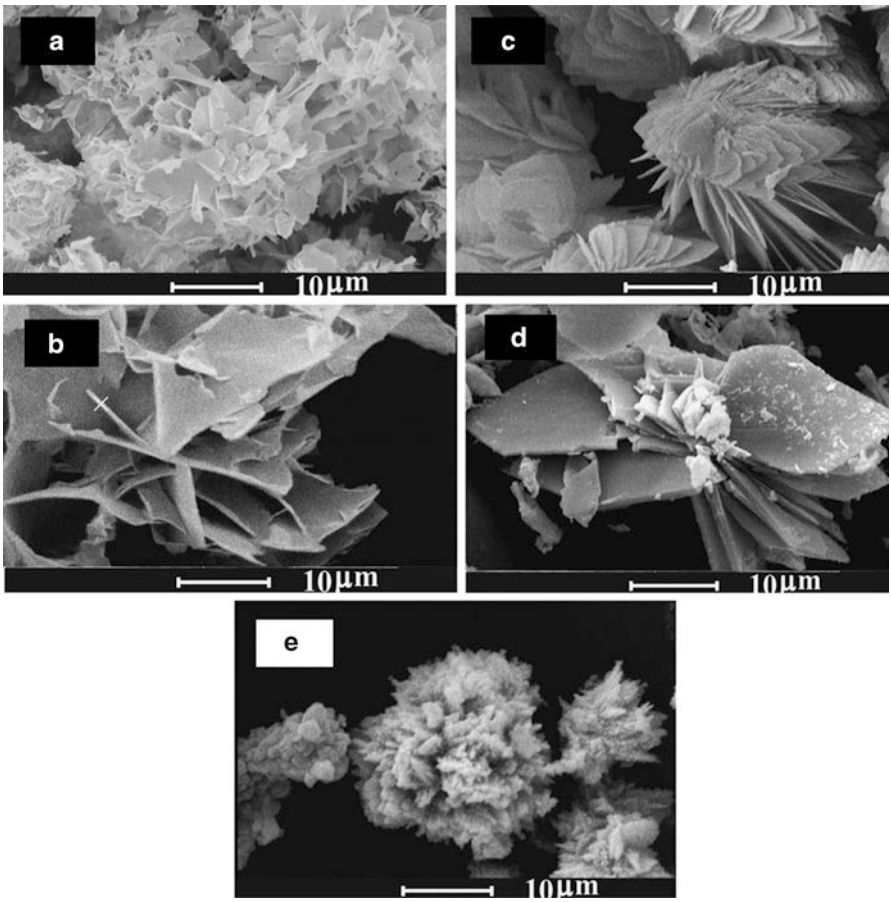

Fig. 9.44 SEM images showing the morphological evolution of Y_2O_3 samples with different cation and anion of ILs [concentrations of IL = 0.027 M]: (**a**) [C_{17}mim][H_2PO_4], (**b**)[C_{10}mim][H_2PO_4], (**c**) [C_8mim][H_2PO_4], (**d**) [C_4mim][H_2PO_4], and (**e**) [C_{17}mim][HSO_4] (Reprinted from Ref. [63], copyright 2010, with permission from Elsevier)

9.6 Conclusions and Prospect

Ionic liquids, with special properties, have been commonly used in the synthesis of inorganic materials. Compared with traditional solvent, the nano-/micro-materials synthesized with ionic liquids have more abundant morphology and more uniform particle size. Especially for luminescent materials, ionic liquids are good solvents, templates, or reagents because this system can suppress the production of amorphous materials like hydrates and hydroxides which will reduce the luminescence intensity. Ionic liquid-assisted hydrothermal method combined with other methods, such as microemulsion and two-phase system, opens a new route for the synthesis

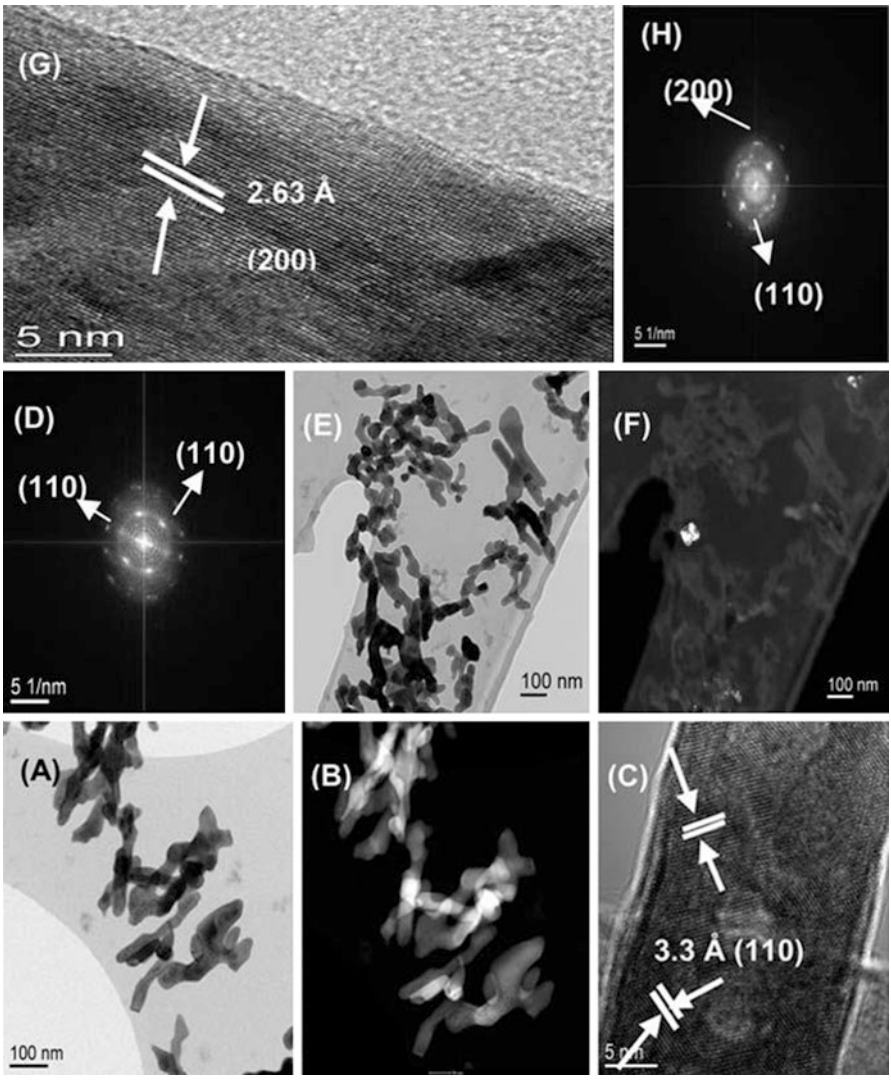

Fig. 9.45 (**a**–**d**) Low-magnification TEM, high-angle annular dark-field (HAADF), and scanning transmission electron microscopy (STEM) images and HRTEM and FFT pattern of $NaGdF_4:Eu^{3+}$ nanocrystals prepared in the presence of IL. (**e**–**h**) TEM, dark-field images, HRTEM and FFT pattern of hexagonal $NaGdF_4:Eu^{3+}$ nanocrystals prepared in the absence of IL (Reproduced from Ref. [64] by permission of The Royal Society of Chemistry)

of luminescent materials and is expected to facilitate the synthesis of nano- or micro-luminescent materials with special properties.

The special inner structure and lower interface energy of ionic liquids make them easier to connect with a variety of organic and inorganic groups. So, ionic liquids can be used in different synthesis systems and work as solvents, templates,

or reactants. Therefore, there is much work to be done to develop ionic liquid-based methods to synthesize luminescent materials, such as ionic liquid-based microemulsion, ionic liquid-based two-phase method, and so on. Although some work has been done, the mechanism is not very clear, and it may be one of the research directions in the future. Another area of research focus may be the recycle of ionic liquids. Moreover, exploiting new methods and synthesizing novel luminescent materials based on the unique properties of the ionic liquids may become an important research topic.

References

1. Blasse G, Grabmaier BC (1994) Luminescent materials. Springer, Berlin
2. Huang CH, Chen TM (2011) A novel single-composition trichromatic white-light $Ca_3Y(GaO)_3(BO_3)_4:Ce^{3+}$, Mn^{2+}, Tb^{3+} phosphor for UV-light emitting diodes. J Phys Chem C 115:2349–2355
3. Lorbeer C, Cybińska J, Mudring AV (2011) Europium(III) fluoride nanoparticles from ionic liquids: structural, morphological, and luminescent properties. Cryst Growth Des 11:1040–1048
4. Lorbeer C, Cybińska J, Mudring AV (2010) Facile preparation of quantum cutting $GdF_3:Eu^{3+}$ nanoparticles from ionic liquids. Chem Commun 46:571–573
5. Li C, Quan Z, Yang J, Yang P, Lin J (2007) Highly uniform and monodisperse β-$NaYF_4:Ln^{3+}$ (Ln = Eu, Tb, Yb/Er, and Yb/Tm) hexagonal microprism crystals: hydrothermal synthesis and luminescent properties. Inorg Chem 46:6329–6337
6. Zhang C, Chen J, Zhou Y, Li D (2008) Ionic liquid-based "all-in-one" synthesis and photoluminescence properties of lanthanide fluorides. J Phys Chem C 112:10083–10088
7. Crosthwaite JM, Muldoon MJ, Aki SN, Maginn EJ, Brennecke JF (2006) Liquid phase behavior of ionic liquids with alcohols: experimental studies and modeling. J Phys Chem B 110:9354–9361
8. Crosthwaite JM, Aki SN, Maginn EJ, Brennecke JF (2004) Liquid phase behavior of imidazolium-based ionic liquids with alcohols. J Phys Chem B 108:5113–5119
9. Swatloski RP, Holbrey JD, Rogers RD (2003) Ionic liquids are not always green: hydrolysis of 1-butyl-3-methylimidazolium hexafluorophosphate. Green Chem 5:361–363
10. Jacob DS, Bitton L, Grinblat J, Felner I, Koltypin Y, Gedanken A (2006) Are ionic liquids really a boon for the synthesis of inorganic materials? A general method for the fabrication of nanosized metal fluorides. Chem Mater 18:3162–3168
11. Miao Z, Liu Z, Ding K, Han B, Miao S, An G (2007) Controlled fabrication of rare earth fluoride superstructures via a simple template-free route. Nanotechnology 18:125605–125609
12. Zhu L, Li Q, Liu X, Li J, Zhang Y, Meng J, Cao X (2007) Morphological control and luminescent properties of CeF_3 nanocrystals. J Phys Chem C 111:5898–5903
13. Jiang W, Wang T, Voth GA (2007) Molecular dynamics simulation of nanostructural organization in ionic liquid/water mixtures. J Phys Chem B 111:4812–4818
14. Chaumont A, Wipff G (2005) Solvation of fluoro and mixed solvation of fluoro and mixed fluoro/chloro complexes of EuIII in the [BMIM][PF_6] room temperature ionic liquid. A theoretical study. Phys Chem Chem Phys 7:1926–1932
15. Chaumont A, Wipff G (2003) Solvation of M^{3+} lanthanide cations in room-temperature ionic liquids. A molecular dynamics investigation. Phys Chem Chem Phys 5:3481–3488
16. Branco LC, Rosa JN, Ramos JJM, Afonso CAM (2008) Preparation and characterization of new room temperature ionic liquids. Chem Eur J 8:3671–3677

17. Stouwdam JW, van Veggel FCJM (2002) Near-infrared emission of redispersible Er^{3+}, Nd^{3+}, and Ho^{3+} doped LaF_3 nanoparticles. Nano Lett 2:733–737
18. Wang F, Zhang Y, Fan X, Wang M (2006) Facile synthesis of water-soluble LaF_3:Ln^{3+} nanocrystals. J Mater Chem 16:1031–1034
19. Wang L, Li P, Li Y (2007) Down- and up-conversion luminescent nanorods. Adv Mater 19:3304–3307
20. Wang ZL, Quan ZW, Jia PY, Lin CK, Luo Y, Chen Y, Fang J, Zhou W, O'Connor CJ, Lin J (2006) A facile synthesis and photoluminescent properties of redispersible CeF_3:Tb^{3+}, and CeF_3:Tb^{3+}/ LaF_3(core/shell) nanoparticles. Chem Mater 18:2030–2037
21. Wang L, Li Y (2006) $Na(Y_{1.5}Na_{0.5})F_6$ single-crystal nanorods as multicolor luminescent materials. Nano Lett 6:1645–1649
22. Li Q, Yam VWW (2007) Redox luminescence switch based on energy transfer in $CePO_4$:Tb^{3+} nanowires. Angew Chem Int Ed 46:3556–3559
23. Liu J, Liu X, Kong X, Zhang H (2012) Controlled synthesis, formation mechanism and upconversion luminescence of $NaYF_4$: Yb, Er nano-/submicrocrystals via ionothermal approach. J Solid State Chem 190:98–103
24. Song Y, Deng Y, Zhou H, Zhang H, Zou H, Chen J (2012) Ionic liquid-based hydrothermal synthesis and luminescent properties of CaF_2:Ce^{3+}/Mn^{2+} nanocrystals. J Nanoparticle Res 14:1258–1266
25. Zou H, Song Y, Deng Y, Zhang H, Sheng Y, Zheng K, Zhou X, Chen J (2013) Ionic liquids assisted synthesis and luminescence properties of $Ca_5(PO_4)_3Cl$:Ce^{3+}, Tb^{3+} nanostructures. J Nanoparticle Res 15:1973–1981
26. Guo H, Zhang T, Qiao YM, Zhao LH, Li ZQ (2010) Ionic liquid-based approach to monodisperse luminescent LaF_3:Ce, Tb nanodiskettes: synthesis, structural and photoluminescent properties. J Nanosci Nanotechnol 10:1913–1919
27. Kundu S, Kar A, Patra A (2012) Morphology dependent luminescence properties of rare-earth doped lanthanum fluoride hierarchical microstructures. J Lumin 132:1400–1406
28. Pileni MP (2003) The role of soft colloidal templates in controlling the size and shape of inorganic nanocrystals. Nat Mater 2:145–150
29. Rodill E, Aldous L, Hardacre C, Lagunas MC (2008) Preparation of AgX (X = Cl, I) nanoparticles using ionic liquids. Nanotechnology 19:105603–105610
30. Eastoe J, Gold S, Roger SE, Paul A, Welton T, Heenan RK, Grillo I (2005) Ionic liquid-in-oil microemulsions. J Am Chem Soc 127:7302–7303
31. Hao J, Zemb T, Opin C (2007) Self-assembled structures and chemical reactions in room-temperature ionic liquids. J Colloid Interface Sci 12:129–137
32. Cheng S, Zhang J, Zhang Z, Han B (2007) Novel microemulsions: ionic liquid-in-ionic liquid. Chem Commun 24:2497–2499
33. Gao Y, Zhang J, Xu H, Zhao X, Zheng L, Li X, Yu L (2006) Structural studies of 1-butyl-3-methylimidazolium tetrafluoroborate/TX-100/p-Xylene ionic liquid microemulsions. ChemPhysChem 7:1554–1561
34. Moniruzzaman M, Kamiya N, Nakashima K, Goto M (2008) Formation of reverse micelles in a room-temperature ionic liquid. ChemPhysChem 9:689–692
35. Patrascu C, Gauffre F, Nallet F, Bordes R, Oberdisse J, Lauth-Viguerie ND, Mingotaud C (2006) Micelles in ionic liquids: aggregation behavior of alkyl poly (ethylene glycol)-ethers in 1-butyl-3-methyl-imidazolium type ionic liquids. ChemPhysChem 7:99–101
36. Blesic M, Marques MH, Plechkov NV, Seddon KR, Rebelo LSPN, Lopes AN (2007) Self-aggregation of ionic liquids: micelle formation in aqueous solution. Green Chem 9:481–490
37. Singh T, Kumar A (2007) Aggregation behavior of ionic liquids in aqueous solutions: effect of alkyl chain length, cations, and anions. J Phys Chem B 111:7843–7851
38. Goodchild I, Collier L, Millar SL, Prokes I, Lord JCD, Butts CP, Bowers J, Webster JRP, Heenan RK (2007) Structural studies of the phase, aggregation and surface behaviour of 1-alkyl-3-methylimidazolium halide + water mixtures. J Colloid Interface Sci 307:455–468

39. Zhang C, Chen J, Zhu X, Zhou Y, Li D (2009) Synthesis of tributylphosphate capped luminescent rare earth phosphate nanocrystals in an ionic liquid microemulsion. Chem Mater 21:3570–3575
40. Remsing RC, Liu Z, Sergeyev I, Moyna G (2008) N′-Dialkylimidazolium ionic liquids: a multinuclear NMR spectroscopy and molecular dynamics simulation study. J Phys Chem B 112:7363–7369
41. Marcus Y (1963) Solvent extraction of inorganic species. Chem Rev 63:139–170
42. Peng X, Schlamp MC, Kadavanich AV, Alivisatos AP (1997) Epitaxial growth of highly luminescent CdSe/CdS core/shell nanocrystals with photostability and electronic accessibility. J Am Chem Soc 119:7019–7029
43. Peng ZA, Peng X (2001) Mechanisms of the shape evolution of CdSe nanocrystals. J Am Chem Soc 123:1389–1395
44. Sapra S, Poppe J, Eychmuller A (2007) CdSe nanorod synthesis: a new approach. Small 3:1886–1888
45. Yu L, Song H, Lu S, Liu Z, Yang L, Kong X (2004) Luminescent properties of $LaPO_4$:Eu nanoparticles and nanowires. J Phys Chem B 108:16697–16702
46. Zhang C, Chen J (2010) Facile EG/ionic liquid interfacial synthesis of uniform RE^{3+} doped $NaYF_4$ nanocubes. Chem Commun 46:592–594
47. Zhang C (2009) Preparation of rare earth nanomaterials in ionic liquids-based multiple phases systems. Changchun Institute of Applied Chemistry, Chinese Academy of Sciences, P. R. China
48. Binder WH (2005) Supramolecular assembly of nanoparticles at liquid–liquid interfaces. Angew Chem Int Ed 44:5172–5175
49. Glaser N, Adams DJ, Böker A, Krausch G (2006) Janus particles at liquid–liquid interfaces. Langmuir 22:5227–5229
50. Lin Y, Skaff H, Emrick F, Dinsmore A, Russell T (2003) Nanoparticle assembly and transport at liquid-liquid interfaces. Science 299:226–229
51. Dai LL, Sharma R, Wu CW (2005) Self-assembled structure of nanoparticles at a liquid–liquid interface. Langmuir 21:2641–2643
52. Gu H, Yang Z, Gao J, Zhang C, Xu B (2005) Heterodimers of nanoparticles: formation at a liquid–liquid interface and particle-specific surface modification by functional molecules. J Am Chem Soc 127:34–35
53. Rao C, Kalyanikutty K (2008) The liquid-liquid interface as a medium to generate nanocrystalline films of inorganic materials. Acc Chem Res 41:489–499
54. Zhang Y, Chen J (2014) Interface mechanism of a rapid and mild aqueous–organic method to prepare $CePO_4$ nanostructures. Colloids Surf A Physicochem Eng 444:246–251
55. Yang H, Wang W, Cui H, Zhang D, Liu Y, Chen J (2012) Recovery of rare earth elements from simulated fluorescent powder using bifunctional ionic liquid extractants (Bif-ILEs). J Chem Technol Biotechnol 87:198–205
56. He M, Huang P, Zhang C, Chen F, Wang C, Ma J, He R, Cui D (2011) A general strategy for the synthesis of upconversion rare earth fluoride nanocrystals via a novel OA/ionic liquid two-phase system. Chem Commun 47:9510–9512
57. He M, Huang P, Zhang C, Hu H, Bao C, He R, Cui D (2011) Dual phase-controlled synthesis of uniform lanthanide-doped $NaGdF_4$ upconversion nanocrystals via an OA/ionic liquid two-phase system for in vivo dual-modality imaging. Adv Funct Mater 21:4470–4477
58. Zhou N, Qiu P, Wang K, Fu H, Gao G, He R, Cui D (2013) Shape-controllable synthesis of hydrophilic $NaLuF_4$:Yb, Er nanocrystals by a surfactant-assistant two-phase system. Nanoscale Res Lett 8:518
59. He M, Huang P, Zhang C, Ma J, He R, Cui D (2013) Phase- and size-controllable synthesis of hexagonal upconversion rare-earth fluoride nanocrystals through an oleic acid/ionic liquid two-phase system. Chem Eur J 18:5954–5969
60. Ju Q, Murdring AV (2013) Phase and morphology selective interface-assisted synthesis of highly luminescent Ln^{3+}-doped $NaGdF_4$ nanorods. RSC Adv 3:8172–8175

61. Ju Q, Campbell PS, Murdring AV (2013) Interface-assisted ionothermal synthesis, phase tuning, surface modification and bioapplication of Ln^{3+}-doped $NaGdF_4$ nanocrystals. J Mater Chem B 1:179–185
62. Sun Y, Zheng W (2010) Ultrathin $SmVO_4$ nanosheets: Ionic liquid–assisted hydrothermal synthesis, characterization, formation mechanism and optical property. Dalton Trans 39:7098–7103
63. Kowsari E, Faraghi G (2010) Synthesis by an ionic liquid-assisted method and optical properties of nanoflower Y_2O_3. Mater Res Bull 45:939–945
64. Ghosh P, Tang S, Mudring AV (2011) Efficient quantum cutting in hexagonal $NaGdF_4:Eu^{3+}$ nanorods. J Mater Chem 21:8640–8644